The Evolution of Solar Wind Strahl

Georgina Alessandra Graham

A dissertation submitted in partial fulfillment
of the requirements for the degree of
Doctor of Philosophy
of
University College London.

Department of Space & Climate Physics
University College London

18th May 2018

I, Georgina Alessandra Graham, confirm that the work presented in this thesis is my own. Where information has been derived from other sources, I confirm that this has been indicated in the work.

Please note that some of the contents of this thesis have been previously reported in the following two journal papers:

- Graham et al. (2017), *The evolution of solar wind strahl with heliospheric distance*, Journal of Geophysical Research: Space Physics, 122(4), pp.3858-3874.

- Graham et al. (2018), *Investigating the Effect of IMF Path Length on Pitch-angle Scattering of Strahl within 1 AU*, The Astrophysical Journal, 855(1), p.40.

Abstract

Suprathermal electrons are an important kinetic feature of the solar wind; however, their origin and evolution is yet to be fully understood. Suprathermal electrons are divided into two component populations: the field-aligned, beam-like 'strahl' and the approximately isotropic 'halo'. Observations have revealed that the strahl component cannot be subject solely to expansion effects as it travels away from the Sun along the Interplanetary Magnetic Field (IMF). Thus, strahl scattering processes must occur within the solar wind and may be at least partly responsible for the existence of the isotopic halo. In this thesis, strahl evolution is examined, in order to constrain the possible strahl scattering mechanisms and investigate strahl utility as an IMF probe. Novel analysis methods are applied to strahl observations to obtain the largest radial range of strahl width observations to date; examine the effect of distance travelled along the IMF on strahl width; and provide estimates of IMF orientation. It is found that strahl scattering likely occurs throughout the solar wind, to at least to 5.5 AU, and strahl electrons are most likely scattered to form part of the halo population by 9 AU. It is also concluded that strahl scattering occurs quasi-continuously and results indicate that scattering may be more intense closer to the Sun, particularly for higher energy electrons. The increase in strahl beamwidth with distance is also greater for higher energy strahl, suggesting that there is a dominant scattering mechanism with an inherent energy relation, most likely explained by resonant wave-particle interactions. Finally, observing relatively narrow strahl beams at 1 AU using high resolution Cluster data allowed estimations of strahl width that generally lie within 20° of the magnetometer observations.

Impact Statement

In this thesis, the beam-like solar wind electron population known as strahl is investigated. The evolution of solar wind electrons is a key aspect of Sun-solar wind science. In particular, with regard to understanding solar wind and interplanetary magnetic field source regions; uncovering the mechanisms that heat the corona and accelerate the solar wind; and determining the sources and evolution of solar wind turbulence. These areas of heliophysical research are especially pertinent as the launch of Parker Solar Probe (2018) and Solar Orbiter (2020) will provide new, unprecedented observations within the inner heliosphere. Much of the research within this thesis focuses on obtaining the maximum solar wind physics return from available missions by developing novel methods that expand their scientific utility. These techniques will be applied to additional existing datasets in order to further investigate the evolution of solar wind electrons. This analysis will be scientifically advantageous in its own right, and will also provide valuable information for the upcoming Solar Orbiter mission. In particular, understanding strahl electron interactions and transport will aid investigations into the heliospheric magnetic field topology and solar wind conditions that Solar Orbiter encounters. This information is crucial to linking in-situ measurements with remote sensing observations and therefore an important aspect of Solar Orbiter science. The potential topology and connectivity information obtained from strahl observations can also contribute to the understanding of the internal structure and solar connectivity of interplanetary coronal mass ejections - a key aspect of space weather research. Finally, the beam-fitting methodology presented in this thesis can also be developed to provide a magnetic field orientation tool for other beam like particle populations, such as those observed within magnetospheres.

Acknowledgements

First, and most definitely foremost, I am grateful to my supervisors, Jonny Rae and Chris Owen, who are both brilliantly informative, perceptive and supportive. As a student studying field-aligned electrons who still routinely misspells 'field', I think that I am lucky to have two supervisors who gave so much of their time to helping me with the smaller things as well as the big picture science discussions. Jonny - thank you for keeping me on track, I know I have the tendency to wander down rabbit holes. Chris - thank you for unfaltering insight, you always ask the best questions.

I am also indebted to my ESA supervisor-in-law Andrew Walsh. I am in no doubt that my work is better because of his input and I am very glad to have had the opportunity to work with such an intelligent and helpful person. Particularly one who could be kidnapped, dropped off in the middle of nowhere and still lead everyone to the best pub in the area.

I would like to thank everyone in the Plasma Group (past and present). I have yet to suffer a question unanswered, a code un-fixed or a coffee mug un-full thanks to all of you. Andrew Fazakerley, Rob Wicks and Daniel Verscharen - thank you for your sharp minds and kind words. Colin Forsyth - as my masters supervisor you played a big role in my decision to pursue science further, so thank you very much. Ali Varsani, Nadine Kalmoni, Licia Ray and Zhonghua Yao - thank you all so much for your help and advice. Allan Macneil - thank you for talking about the solar wind with me. Our discussions, both science and Bob's Burgers related, definitely made my PhD experience a good one. Lloyd Woodham, Marina Georgiou, Michaela Mooney, Frankie Staples, George Nicolaou and Hong Hong Wu - I very much hope that our paths cross repeatedly in the future (thank you for looking after my frogs).

Mayur Bakrania - you where great to work with as a summer student and I am really glad you are joining the plasma group next year.

I am very grateful to all the members of the Planetary Group. Thank you for sharing your data, insight, research and delicious cakes. Geraint Jones - thank you for all your help with Cassini. Will Dunn - thank you for involving me in your research into Jovian aurora and your extensive outreach endeavours. You are brilliant to work with and an even better friend. Ollie Price - I am very glad that I got to work with you planning work experience week and even gladder to have stolen a few of your recipes. I am also very grateful to the Solar Group, firstly for letting me have a desk in their office while I wrote up my thesis but mostly for being such a lovely group of people. Dave Long - thank you for involving me in your research into EUV waves. Magnus Woods, Alex James, Jack Jenkins and Jenny O'Kane - thank you for helping me with thesis madness.

I most definitely would not have got very far if it wasn't for the Cassini and PEACE Operations teams. In particular, I would like to thank Lin Gilbert, Gethyn Lewis and Gill Watson. I would also like to thank Chris Arridge for his help using the Cassini electron data. Nor would I have made much progress without the help of the Computing Group or everyone in the Main Office, particularly during work experience week. For which I would like to say thank you to everyone that got involved and, in particular, Libby Daghorn, Philippa Elwell, Sue Ford, Paul Prior and Martin de la Nougerede.

I would also like to thank my family and friends outside of MSSL. Particularly my mum, dad and sister, each of whom has been incredibly supportive. David Milne - I suspect you have had to listen to me talk about strahl more than any other person on the planet.

Finally, I would like to acknowledge the University College London IMPACT scheme and the European Space Agency for financial support over the course of my PhD.

Contents

List of Figures

List of Tables

Glossary

3DP 3D Plasma. 18, 112–114

ACE Advanced Composition Explorer. 13, 14, 101, 111, 117, 118, 138–141

ASPERA-3 Analyzer of Space Plasmas and Energetic Atoms - 3. 18, 124, 125, 215, 231, 232, 245, 246

CAPS Cassini Plasma Spectrometer. 13, 18, 103, 105, 108–110, 127, 128, 138, 140, 144, 146–149, 153, 157, 158

CME coronal mass ejection. 79, 80, 187

EESA Electron Electrostatic Analysers. 14, 18, 112–114, 165

EESA-H high energy Electron Electrostatic Analyser. 113, 114

EESA-L low energy Electron Electrostatic Analyser. 113, 114

EIT Extreme ultraviolet Imaging Telescope. 76

ELS Electron Spectrometer. 13, 14, 16, 18, 103, 105, 107–110, 124, 125, 127–129, 137, 138, 140, 141, 143–149, 153, 157, 215–217, 220–223, 225–228, 231, 232, 235

EPACT Energetic Particles: Acceleration, Composition, and Transport. 18, 112, 115, 116

FGM Fluxgate Magnetometer. 18, 103, 105, 109, 110, 120, 121, 137, 140, 145, 148, 189

FOV field-of-view. 13, 15, 16, 107–110, 113, 114, 120, 122, 125, 127, 128, 140, 145, 158, 190–211, 213, 214, 216, 220–223, 225–229, 231, 232, 235, 243, 245

FWHM full-width-half-maximum. 110, 120, 126, 127, 143, 146, 156, 168, 190, 191, 223, 229, 231, 243

GGS Global Geospace Science. 111

GSE Geocentric Solar Ecliptic. 22, 139, 188

HCI Heliocentric Inertial. 22

HCS heliospheric current sheet. 77, 78

HEEA High Energy Electron Analyser. 120–122

ICME interplanetary coronal mass ejection. 79, 99, 138, 161

IMF Interplanetary Magnetic Field. 4, 12, 14, 23, 24, 70, 72, 74–76, 81, 82, 88, 94–96, 99, 100, 127, 130, 132–134, 136, 146, 148, 150, 152, 158, 160–174, 176–181, 184, 186–188, 215, 229–233, 235, 236, 238–241, 243–250

ISTP International Solar Terrestrial Physics. 111

KAW kinetic Alfvén waves. 86, 98, 184, 242

L1 1st Lagrange point. 111, 117, 138

LASCO Large Angle Spectrometric Coronagraph. 76

LEEA Low Energy Electron Analyser. 120–122, 188, 189

LEMT Low Energy Matrix Telescopes. 112, 115, 116

MAG Magnetometer (or Dual Technique Magnetometer on-board Cassini). 103, 105, 109, 110, 117

MCP micro-channel plates. 107

MEX Mars Express. 123, 124, 215–218, 220–223, 225–228, 231, 232, 245, 246

MFI Magnetic Field Investigation. 18, 112, 115

MHD Magnetohydrodynamics. 18, 39, 42–46, 54–57, 71, 83, 85, 129

MMS Magnetospheric Multiscale. 86

PEACE Plasma Electron And Current Experiment. 15, 16, 121, 122, 188, 190–196, 198, 199, 201–208, 210, 211, 213, 214, 216, 229, 231, 243, 245

PSD Phase Space Density. 48, 190, 191, 203

PVI partial variance of increments. 14, 130, 131, 169, 175, 176

RTN Radial Tangential Normal. 22, 141

SEP solar energetic particle. 13, 14, 113, 132–134, 162–166, 168–173, 175–179, 239, 245

SI stream interface. 78, 79

SIR stream interaction region. 78, 80

SoHO Solar and Heliospheric Observatory. 76

SST Solid State Telescopes. 14, 18, 112–114, 164, 165

STEREO Solar TErrestrial RElations Observatory. 133

SWEPAM Solar Wind Electron, Proton, and Alpha Monitor. 117

SWOOPS Solar Wind Observations Over the Poles of the Sun. 76

VDA velocity dispersion analysis. 134, 164, 166, 169–173, 177, 178, 239

VDF velocity distribution function. 50, 51

VEX Venus Express. 232, 246

Coordinate Systems

Geocentric Solar Ecliptic (GSE)

Earth-centred system: x-axis towards the Sun, z-axis perpendicular to the plane of the Earth's orbit around the Sun (positive North), and y-axis completes the right-handed triad (ecliptic plane, positive dusk). N.B. Earth rotates East to West.

Heliocentric Inertial (HCI)

Sun-centred system: x-axis is the solar ascending node of the J2000 epoch, z-axis is the Sun's rotational axis (positive North), and y-axis completes the right-handed triad.

Radial Tangential Normal (RTN)

Spacecraft-centred system: R points from the Sun to the spacecraft, T $=$ $(\Omega \times R)/\Omega R$, where Ω is the Suns rotation vector (positive north), and N completes the right-handed triad. N.B. Sun rotates counterclockwise when viewed from North.

Chapter 1

Introductory Material

1.1 Motivation

The suprathermal electron populations of the solar wind are a fascinating component of heliospheric physics. Observations of these suprathermals can provide details on range of phenomena at different scales, from the kinetic physics of their interactions with plasma waves and turbulence, to their role in the thermodynamics of the solar wind, or even their use as signatures of solar connectivity. Suprathermal electrons can supply clues as to the nature of individual events, such as the folding of IMF or intense wave activity at a shock front, as well as the overall environment of the solar wind, such as origins and evolution of slow and fast streams. However, although solar wind suprathermal electrons are well documented and used frequently within solar wind investigations, the formation of these electron populations and their development within the heliosphere is yet to be fully understood.

Suprathermal electrons are typically divided into two constituent populations: an approximately isotropic 'halo' and a beam-like population known as 'strahl'. It is this latter population that is the focus of this thesis. Firstly, because the high-velocity, field-aligned nature of strahl electrons means that, not only is strahl generally the primary carrier of heat flux into the heliosphere, but it is also the electron population which can be used to investigate IMF topology and connectivity. Secondly, because scattering of the strahl electrons has significant implications for the evolution of both the strahl and the halo. Suprathermal solar wind electrons which are solely subjected to the effects of global expansion should narrow in pitch-angle space with distance from the Sun. However, observations reveal that this is not the

case, as average strahl beam width increases with distance and the halo is present at all pitch-angles. Investigations have also found that the fractional density of strahl relative to total electron density decreases with distance, while that of the halo increases. These factors imply that strahl electrons must be subject to in-transit scattering, and that some or all of the halo is formed from the strahl.

In Chapter 1 of this thesis, a number of core plasma physics concepts are summarised. In Chapter 2, further details into our current understanding of the solar wind and a literature review of historical and recent key findings with regard to the solar wind electrons are presented. Chapter 3 focuses on the spacecraft, instrumentation and datasets used to complete the investigations within this thesis. It also contains explanations of the scientific methods used and developed within these studies. In Chapter 4 an investigation of the evolution of strahl beams from 1 to 9 AU using Cassini-Huygens' observations is presented. Findings include a strahl width broadening which continues out to at least 5.5 AU and and an energy relation that differs significantly from previous Ulysses observations. In Chapter 5 a novel analysis method that makes use of solar energetic particles is developed and used to investigate the effect of IMF length on strahl evolution within 1 AU. The resulting observations suggest that scattering of strahl within the solar wind is at least quasi-continuous and that strahl scattering may be more intense closer to the Sun. Chapter 6 focusses less on the understanding of strahl itself and more on the applicability of strahl as a tool for determining IMF orientation. Key findings include the effect of strahl beam width and the angular and time resolution of the instrument used on the reliability of the predicted IMF orientation. Finally, in Chapter 7, the implications of the observations presented in this thesis and the focus of future investigations, particularly with regard to the upcoming NASA Solar Parker Probe and ESA Solar Orbiter observations, are discussed.

1.2 What is a Plasma?

A plasma is an ionized gas made up of ions and electrons that exhibit collective behaviour and has an overall net charge of zero. For simplicity, a plasma can be considered to be made of electrons (charge $-e$, mass m_e) and ions (usually protons, charge $+e$, mass m_i) with equal number densities ($n = n_i = n_e$). This assumption requires that the distance between particles is much smaller than the spatial scale L of the system considered. The average distance r between plasma particles is given by

$$< r > \quad = \quad n^{-1/3} \quad \ll \quad L \tag{1.1}$$

The temperature of a plasma, T, characterizes the agitation of the particles and, in thermal equilibrium, the particle velocities in each space coordinate are Gaussian distributed around zero (in the bulk rest frame). Thus, the mean square velocities for each space coordinate are given by

$$< v_x^2 > \quad = \quad < v_y^2 > \quad = \quad < v_z^2 > \quad = \quad \frac{k_B T}{m} \tag{1.2}$$

where x, y and z are the three space co-ordinates, k_B is Boltzmann's constant and m is the mass of a particle species. The average kinetic energy per particle is given by

$$\frac{m < v^2 >}{2} \quad = \quad \frac{3 k_B T}{2} \tag{1.3}$$

It is important to note that space plasmas are frequently not in thermal equilibrium; particle velocities are not always Gaussian distributed and the different particle species often have different bulk velocities and temperatures. However, Equation 1.3 can be used to define a kinetic temperature for each species, even if it is not a thermal equilibrium temperature (Meyer-Vernet, 2007).

1.2.1 Quasi-Neutrality

Even though the net charge of a plasma is zero, individual charged particles will produce and experience electric potentials. The electric potential (ϕ) experienced by a test charge due to a single-point charge in a vacuum is given by

$$\phi_C = \frac{q}{4\pi\varepsilon_0 r} \tag{1.4}$$

where q is particle charge, ε_0 is the the permittivity of free space and r the distance from the source of the potential. This is known as the Coulomb potential. However, in a plasma, the particles are sufficiently numerous to shield this potential and therefore a test charge will experience a potential of a different form. This is known as the Debye potential and it is given by

$$\phi_D = \frac{q}{4\pi\varepsilon_0 r} exp\left(-\frac{r}{\lambda_D}\right) \tag{1.5}$$

where λ_D is the Debye length, the distance over which a Coulomb potential is reduced by a factor of e due to the presence of shielding particles. λ_D is affected by the number density and temperature of the shielding particles. Assuming a proton-electron plasma ($n = n_i = n_e$), it is given by

$$\lambda_D = \left(\frac{\varepsilon_0 k_B T_e}{n q_e^2}\right)^{1/2} \tag{1.6}$$

where T_e is the electron temperature, q_e electron charge and k_B is Boltzmann's constant. Electrons have much higher mobility than the ions and so T_e is considered as opposed to T_i.

The Coulomb force (see Eqution 1.22) which results from electric potentials tends to establish charge neutrality, as like charges repel whereas unlike charges attract. However, the random motion of the particles tends to perturb this neutrality. The Debye length is the distance over which a balance is obtained between the Coulomb force and random motions. In other words, plasmas can be considered quasi-neutral when their characteristic length scale is much larger than the Debye length ($L \gg \lambda_D$).

1.2.2 Charged Particle Collisions

In a neutral gas, particles interact via collisions and the collisionality of the medium determines the transport coefficients that control its response to gradients macroscopic quantities (listed in Table 1.1). In diffuse solar wind plasma, particle-particle collisions are negligible and collective behaviour effectively take on the role that collisions would play in a neutral gas. That is to say, the motion of charged particles in solar wind plasma is controlled by large-scale electromagnetic forces, which in turn are modified by the currents generated by particle motion.

Transport Coefficients	
Diffusion Coefficient	Transport of particles in response to concentration gradient
Viscosity	Transport of momentum in response to velocity gradient
Thermal Conductivity	Transport of heat in response to temperature gradient
Electric Conductivity	Transport of electric charge in response to an electric field

Table 1.1: Transport coefficients influenced by particle-particle collisions.

The mean-free-path for a particle in a neutral gas is typically defined as the average distance a particle has to travel for a collision to occur. A particle with a collisional cross-section σ_{col}, travelling a distance l will encounter all the particles within a cylinder with volume $l\sigma_{col}$, i.e., a total of $nl\sigma_{col}$ particles. The mean-free-path is therefore given by

$$l_{mfp} = (n\sigma_{col})^{-1} \tag{1.7}$$

A major difference between plasmas and neutral gasses is the collisional cross-section, as charged particles interact via the Coulomb force (see Eqution 1.22). If plasma particles come within a Debye length of each other then the particles will deviate from their trajectories. A large perturbation in trajectory occurs when the potential energy of the interaction is equal to or greater than the average kinetic energy (i.e., $q^2/4\pi\varepsilon_0 r \geq k_B T$).

In other words, any distance closer than the Landau radius r_L, which is given by

$$r_L = \frac{q^2}{4\pi\varepsilon_0 k_B T} \tag{1.8}$$

The effective cross section for interactions is thus approximately πr_L^2 and the mean free path can be written as

$$l_{mfp} = \left(n\pi r_L^2\right)^{-1} \tag{1.9}$$

If the particles being considered are not in equilibrium, then the kinetic energy of the particle can be substituted for the thermal energy. This yields the effective distance for collisions which is given by

$$r_{eff} = \frac{q^2}{2\pi\varepsilon_0 m v^2} \tag{1.10}$$

Both l_{mfp} and r_{eff} only account for large perturbations. A charged particle moving in a plasma will experience numerous smaller perturbations and therefore a charged particle will have a larger collisional cross-section. Consider an electron with velocity $\boldsymbol{v}_e$ that experiences a small perturbation in trajectory when passing an ion (assumed to be at rest). Most of the deviation will occur in the region of closest approach to the ion i.e., during the time $\delta t = 2r_c/v_e$ where r_c is the distance of closest approach. In this section of the electron's trajectory it will experience a force approximately perpendicular to the its initial velocity, $F_\perp \approx q^2/4\pi\varepsilon_0 r_c^2$. The change in velocity during time δt is given by

$$\delta v_\perp \approx \frac{F_\perp \delta t}{m_e} = \frac{v_e r_e}{r_c} \tag{1.11}$$

where r_e is given by

$$r_e = \frac{q^2}{2\pi\varepsilon_0 m_e v_e^2} \tag{1.12}$$

Statistically, the perturbations in an electron's trajectory could be in either sense with equal probability and thus, the individual deviations are not necessarily cumulative. However, the squares of the deviations are cumulative, as in a ran-

dom walk. The mean total deviation ($< v_\perp^2 >$) during a time Δt can therefore be calculated by integrating over encounters of various r_c that occur during this time. Each encounter at r_c produces a $\delta v_\perp$ as defined in Equation1.11. The number of encounters in the range r_c to $r_c + dr_c$ during time Δt is given by

$$\Delta N \quad = \quad n v_e \quad \times \quad 2\pi r_c dr_c \quad \times \quad \Delta t \tag{1.13}$$

where $2\pi r_c dr_c$ is the area for the range r_c to $r_c + dr_c$. Thus, $< v_\perp^2 >$ is given by

$$< v_\perp^2 > \quad = \int \delta v_\perp^2 dN \quad = \quad 2\pi n r_e^2 v_e^3 \Delta t \int \frac{dr_c}{r_c} \tag{1.14}$$

If $r_c < r_e$ then the deviation is large, if $r_c > \lambda_D$ then the charges do not interact because of Debye shielding, Equation1.13 is thus intergrated over this range. The collision frequency is the inverse of the Δt needed to produce a large enough deviation so that $< v_\perp^2 > \sim v_e^2$. Substituting this into Equation 1.14, and solving, gives the collision frequency between electrons and singly-charged ions:

$$f_{ei} \quad = \quad 2\pi n v_e r_e^2 ln \frac{\lambda_D}{r_e} \tag{1.15}$$

where the collisional free path is given by:

$$l_{mfp} \quad = \quad \left(2\pi n r_e^2 ln \frac{\lambda_D}{r_e} \right)^{-1} \tag{1.16}$$

The mean value at equilibrium can thus be obtained by substituting $\frac{1}{2} m_e v_e^2$ with average kinetic energy and the values for λ_D and r_e, yielding:

$$l_{mfp} \quad = \quad \left(\frac{4}{3} \pi r_L^2 ln \frac{n^{1/3} q^2}{4\pi \eta_0 k_B T} \right)^{-1} \tag{1.17}$$

Using this equation and typical values for the solar wind at 1 AU from the Sun (e.g., $n \sim 5 \times 10^6 \mathrm{m}^{-3}$, $T \sim 10^5 \mathrm{K}$), the mean free path is approximately 1 AU. Thus the dynamics of solar wind plasma are determined,not by interactions between particles, but by the system as a whole.

1.3 Plasma Oscillations

If a plasma is subjected to an external perturbation that disturbs its quasi-neutrality then the particles will move so that the charge density imbalance is corrected. Consider a volume of plasma, initially quasi neutral, in which the elections are displaced by a distance x. This displacement results in non-charge-neutral slabs at the volume edges, each with charge per unit volume of $\pm nq$, see Figure 1.1.

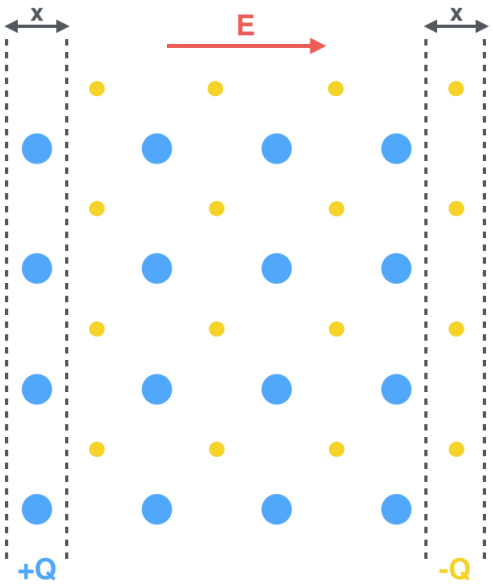

Figure 1.1: An initially quasi neutral volume of plasma (with blue ions and yellow electrons), in which the elections are displaced by a distance x. This displacement results in non-charge-neutral slabs (assumed infinite in y- and z- directions) at the volume edges, each with charge per unit volume of $\pm nq$, and an electric field E between the two slabs.

The electric field between the two slabs is given by

$$E = \frac{nqx}{\varepsilon_0} \tag{1.18}$$

Each displaced electron is thus subject to a force in the x-direction given by

$$F = m_e \frac{\partial^2 x}{\partial t^2} = -qE \tag{1.19}$$

and hence,

$$\frac{\partial^2 x}{\partial t^2} = -\left(\frac{nq^2}{\varepsilon_0 m_e}\right) x \tag{1.20}$$

This is the equation for a simple harmonic oscillator ($-\omega^2\dot{\mathbf{x}} = \ddot{\mathbf{x}}$) with a frequency given by

$$\omega_p = \left(\frac{nq^2}{\varepsilon_0 m_e}\right)^{1/2} \tag{1.21}$$

This oscillation frequency is called the plasma frequency. The electrons have much higher mobility than the ions, and so ion oscillation can generally be ignored as they will oscillate much more slowly than the plasma frequency.

Oscillating behaviour requires two conditions. Firstly, collisions between particles should not suppress oscillations, in other words the collision frequency must be smaller than the plasma frequency. Secondly, the electrons must move as a whole, i.e., random agitation is negligible. This means bulk oscillations can only occur at distances greater than the Debye length.

1.4 Single Particle Dynamics

A plasma is made up of dynamic charged particles. If particle-particle interactions are negligible and particle-field interactions do not significantly affect the external magnetic or electric field, then the collective behaviour of plasma particles can be neglected and the motion of each individual particle can be considered independently. Single particle dynamics is the simplest method of describing a plasma. However, methods of describing the collective behaviour of these particles, such as magnetohydrodynamics or kinetics physics, are built upon the basic principals of single particle motion.

A charged particle in the presence of an electric field experiences a force. Positively charged particles are accelerated in the field-aligned direction and negatively charged particles are accelerated in the anti-field-aligned direction. This is called the Coulomb force $\boldsymbol{F}_C$ and is given by

$$\mathbf{F}_C \quad = \quad q\mathbf{E} \quad = \quad m\frac{d\mathbf{v}}{d\mathbf{t}} \tag{1.22}$$

where q is particle charge, $\boldsymbol{E}$ is electric field, m is particle mass and $\boldsymbol{v}$ is particle velocity. A charged particle will also experience a force if it is moving in the presence of a magnetic field. This is called the Lorentz force $\boldsymbol{F}_L$ and is given by

$$\mathbf{F}_L \quad = \quad q\left(\mathbf{v}\times\mathbf{B}\right) \quad = \quad m\frac{d\mathbf{v}}{d\mathbf{t}} \tag{1.23}$$

where $\boldsymbol{B}$ is magnetic field. The Lorentz force results in centripetal acceleration of a particle in the plane perpendicular to the field-aligned direction; left-handed for a positively charged particle and right-handed for a negatively charged particle. This is shown in the simple illustration shown in Figure 1.2.

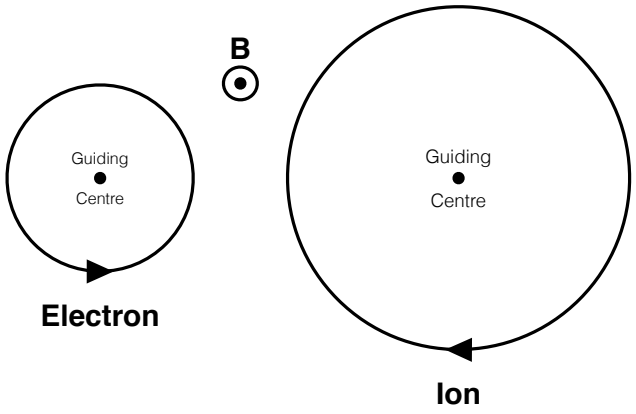

Figure 1.2: Gyration of charged particles in the presence of a magnetic field. The centre of the particle orbit is called the guiding centre. The negatively charged electron is accelerated in the right-handed direction in the plane perpendicular to the background magnetic field. The positively charged ion is accelerated in the left-handed direction in the plane perpendicular to the background magnetic field.

The two combined forces ($\boldsymbol{F}_C + \boldsymbol{F}_L$) describe the motion of a single charged particle due to the presence of external magnetic and electric fields. This is given by

$$q(\mathbf{E} + \mathbf{v} \times \mathbf{B}) = m\frac{d\mathbf{v}}{d\mathbf{t}} \tag{1.24}$$

If the electric field is assumed to be zero and the magnetic field is assumed to be uniform and constant, then differentiating Equation 1.23 with respect to time yields

$$-\left(\frac{qB}{m}\right)^2 \mathbf{v} = \frac{d^2\mathbf{v}}{d\mathbf{t}^2} \tag{1.25}$$

This is the equation for a simple harmonic oscillator ($-\omega^2\dot{\mathbf{x}} = \ddot{\mathbf{x}}$) with a frequency given by

$$\omega_g = \frac{|q|B}{m} \tag{1.26}$$

This is known as the gyrofrequency (also referred to as cyclotron frequency or Larmour frequency).

The gyration of a charged particle around a magnetic field also has a gyroradius (or Larmour radius) given by

$$r_g = \frac{mv_\perp}{|q|B} \tag{1.27}$$

where $v_\perp$ is the velocity of the particle in the plane perpendicular to the magnetic field direction.

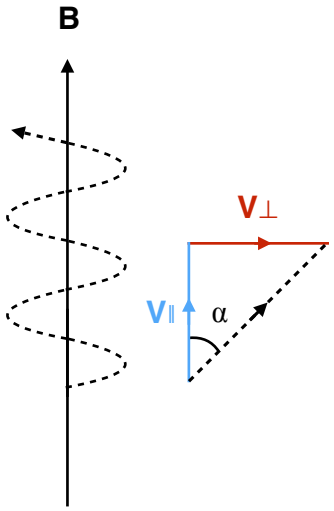

Figure 1.3: 2D projection, in the plane parallel to the magnetic field direction, of a helical trajectory of charged particle in a magnetic field, with $v_{total} = v_\parallel + v_\perp$

It should be noted that the component of a particle's velocity parallel to the magnetic field $v_\parallel$ remains constant ($v_\parallel \times \boldsymbol{B} = 0$). Thus, the full motion of a moving charged particle in the presence of a magnetic field consists of a combination of gyromotion and parallel motion. The angle between the total velocity vector of the particle ($v_{total} = v_\parallel + v_\perp$) and the magnetic field direction is known as pitch angle α, and is defined as

$$\alpha = arctan(\frac{v_\perp}{v_\parallel}) \tag{1.28}$$

The motion of a particle with 0° or 180° pitch angle is entirely along the magnetic field in the field-aligned or anti-field-aligned direction, the motion of a charged particle with 90° is purely gyrational, and other pitch angle values have a helical trajectory, as shown in the 2D projection presented in Figure 1.3.

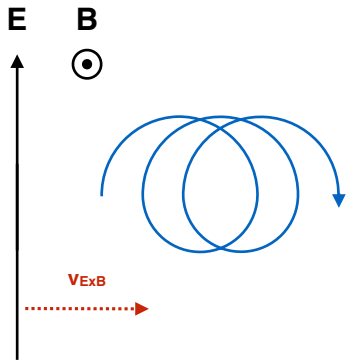

Figure 1.4: Trajectory of a positively charged particle in the presence of a uniform, constant magnetic and electric field.

If the presence of a constant electric field is now considered, then differentiating Equation 1.24 with respect to time yields

$$-\omega_g^2\left(\mathbf{v}-\frac{\mathbf{E}\times\mathbf{B}}{B^2}\right) = \frac{d^2\mathbf{v}}{d\mathbf{t}^2} \tag{1.29}$$

The electric field component that is perpendicular to the magnetic field direction accelerates the particle in the plane of its gyromotion. This has the effect of increasing its velocity on one side of a gyration, and decreasing it on the other. Hence, for half a gyration, the gyroradius is increased and for the other half, the gyroradius is decreased. This is the equivalent of superposing a further velocity component upon the gyromotion of the particle, given by

$$\mathbf{v}_d = \frac{\mathbf{E}\times\mathbf{B}}{B^2} \tag{1.30}$$

and thus,

$$-\omega_g^2\left(\mathbf{v}-\mathbf{v}_d\right) = \frac{d^2\mathbf{v}}{d\mathbf{t}^2} \tag{1.31}$$

This additional velocity component is perpendicular to both the electric and magnetic fields and represents the drift of a particle's guiding centre, it is known as $\boldsymbol{E}\times\boldsymbol{B}$ drift. This concept is illustrated in Figure 1.4.

Drift motions can result from any additional force $\boldsymbol{F}$ applied to a particle in a magnetic field. The general equation for guiding centre drift is given by

$$\mathbf{v}_F = \frac{\mathbf{F} \times \mathbf{B}}{qB^2} \tag{1.32}$$

All particle drifts can be described in this manner, provided the drift velocity is much smaller than the gyrovelocity. Additional forces experienced by particles are frequently the result of a non-uniform magnetic field, i.e., with some gradient or curvature, or a non-constant electric field. Drift motion may also result from the presence of a gravitational field, although, gravitational force is generally comparatively weak and can usually be neglected. Force terms for the gradient ($\mathbf{F}_\nabla$, $\nabla \mathbf{B} \neq 0$), curvature ($\mathbf{F}_R$, $\nabla \times \mathbf{B} \neq 0$, R_C = local radius of curvature), polarisation ($\mathbf{F}_P$, $d\mathbf{E}/dt \neq 0$) and gravitational ($\mathbf{F}_G$) drift are given below.

$$\mathbf{F}_\nabla = -\frac{mv_\perp^2}{2}\frac{\nabla B}{B} \tag{1.33}$$

$$\mathbf{F}_R = mv_\parallel^2 \frac{\mathbf{R}_c}{R_c^2} \tag{1.34}$$

$$\mathbf{F}_P = -m\frac{d\mathbf{E}}{dt} \tag{1.35}$$

$$\mathbf{F}_G = -m\mathbf{g} \tag{1.36}$$

1.4.1 Adiabatic Invariants

Adiabatic invariants are the characteristic constants of a particle in an electromagnetic field associated with each type of particle motion i.e., gyromotion, longitudinal motion and perpendicular drift. Unlike absolute constants, such as energy or total momentum, an adiabatic invariant may change in space and time. However, adiabatic invariants change over much longer periods or distances than typical particle time- or length- scales (e.g., ω_g or r_g). The 1st adiabatic invariant, called magnetic moment μ, is associated with particle gyration. It is the ratio of a particle's perpendicular energy $W_\perp$ to external magnetic field strength.

$$\mu = \frac{mv_\perp^2}{2B} = \frac{W_\perp}{B} \tag{1.37}$$

The magnetic moment can also be written in terms of pitch angle (α), using the definition given in Equation 1.28,

$$\mu = \frac{mv^2 sin^2(\alpha)}{2B} \tag{1.38}$$

Thus it can be seen that, since magnetic moment is invariant and total energy remains constant, only the sine of the pitch angle changes if magnetic field strength increases or decreases along the guiding centre trajectory. Hence, a particle moving into converging magnetic field will experience an increase in $sin(\alpha)$ and a particle moving into diverging magnetic field will experience a decrease in $sin(\alpha)$.

Magnetic mirror points occur when a particle in a converging magnetic field reaches $\alpha = 90°$. The particle no longer has any parallel velocity, cannot penetrate any further and is pushed back by the gradient force (Equation 1.33, $\mathbf{F}_\nabla = -\mu\nabla B$). If the magnetic field has mirror symmetry where the field line converges on both sides, such as in a dipole field, then the particle will oscillate between mirror points. The 2nd adiabatic invariant J is associated with the motion of a particle oscillating along such a magnetic field. It is defined by

$$J = \oint mv_\parallel ds \tag{1.39}$$

Where ds is an element of the guiding centre path (see Figure 1.2) and the integral

is taken over a full oscillation between mirror points. The consequence of the 2nd adiabatic invariant is that particles undergoing bounce motion in a dipole field will remain confined to a particular force line, provided any external changes occur at a slower rate than the time period associated with bounce frequency.

A particle ocillating in a dipole field will also experience drift orbits around the magnetic field axis (Equation 1.34, $\mathbf{v}_R \propto \mathbf{R}_c \times \mathbf{B}$). The 3rd adiabatic invariant (Φ) is defined as the conserved magnetic flux enclosed within the perpendicular drift orbit of a particle trapped in an axisymmetric mirror magnetic field configuration. It is defined by

$$\Phi = \oint v_d r d\psi \tag{1.40}$$

where v_d is the sum of all perpendicular drift velocities, $d\psi$ is an element of the azimuthal angle of the circular drift path and the integration is taken over a full drift path. The consequence of the 3rd adiabatic invariant is that particles remain trapped in drift 'shells'. For example, if the magnetosphere was gradually compressed, then charged particles within drift shells would move radially inwards to conserve the magnetic flux enclosed by their drift orbits.

1.5 Magnetohydrodynamics

Considering the dynamics of individual particles is not always appropriate when describing plasma particles in large numbers. It is also not always necessary to treat the plasma in a statistical sense, as is done in kinetic physics (see Section 1.6), in which the distribution functions of plasma particle motion are considered. For large systems, with scale sizes much larger than particle gyroradius and time scales much longer than associated with the gyrofrequency, the plasma can be treated as an electrically conducting fluid and only the macroscopic, bulk quantities need to be considered.

Magnetohydrodynamics (MHD) is the study of electrically conducting fluid in the presence of electromagnetic fields (Alfvén, 1942, 1945; Alfvén and Lindblad, 1947). MHD equations are a combination of Maxwell's equations of electrodynamics and the Navier-Stokes equations of fluid dynamics. The former taking into account the effects of electric and magnetic fields and the latter taking into account the laws for conservation of mass, momentum and energy. Maxwell's equations and the Navier-Stokes equations are given in Table 1.2 and Table 1.3 respectively.

Name	Equation	Implication
Gauss' law	$\nabla.\mathbf{E} = \frac{\rho}{\varepsilon_0}$	Conservation of charge
Gauss' law for magnetism	$\nabla.\mathbf{B} = 0$	No magnetic monopoles
Faraday's law	$\nabla \times \mathbf{E} = -\frac{\partial \mathbf{B}}{\partial t}$	Time varying **B** fields give rise to **E** fields
Ampère's law	$\nabla \times \mathbf{B} = \mu_0 \mathbf{j} + \mu_0 \varepsilon_0 \frac{\partial \mathbf{E}}{\partial t}$	Currents or time varying **E** fields give rise to **B** fields

Table 1.2: Differential form of Maxwells Equations and their implications. Where $\boldsymbol{B}$ is magnetic field, $\boldsymbol{E}$ is electric field, $\mathbf{j}$ is current density, ρ is charge density, ε_0 is vacuum dielectric permittivity and μ_0 is vacuum magnetic permeability.

Name	Equation
Motion	$\rho_m \frac{\partial \mathbf{v}}{\partial t} + \rho_m (\mathbf{v}.\nabla)\mathbf{v} = -\nabla P + \mathbf{j} \times \mathbf{B} + \rho \mathbf{E} + \rho_m \mathbf{g} + \mathbf{F}$
Continuity	$\frac{\partial n}{\partial t} + \nabla.(n\mathbf{v}) = 0$ $\frac{\partial \rho_m}{\partial t} + \nabla.(\rho_m \mathbf{v}) = 0$ $\frac{\partial \rho}{\partial t} + \nabla.(\rho \mathbf{v}) = 0$
Energy	$\frac{\partial P}{\partial t} + \mathbf{v}.\nabla P \gamma P (\nabla \mathbf{v}) = E_L$
Equation of State (Ideal Gas)	$P = R\rho_m T = nk_B T$
Equation of State (Adiabatic)	$\frac{\partial (P\rho_m^{-\gamma})}{\partial t} + (\mathbf{v}.\nabla)\left(P\rho_m^{-\gamma}\right) = 0$
Ohm's Law (general)	$\mathbf{E} + \mathbf{v} \times \mathbf{B} = \eta \mathbf{j} + \frac{1}{ne}(\mathbf{j} \times \mathbf{B}) - \frac{1}{ne}(\nabla.P_e) + \frac{m_e}{ne^2}\frac{\partial \mathbf{j}}{\partial t}$
Ohm's Law (simplified)	$\mathbf{j} = \sigma(\mathbf{E} + \mathbf{v} \times \mathbf{B})$

Table 1.3: The Navier-Stokes Equations for a Plasma. $\boldsymbol{B}$ is magnetic field, $\boldsymbol{E}$ is electric field, $\boldsymbol{g}$ is gravitational acceleration, $\boldsymbol{j}$ is current density, P is pressure, T is temperature, n is number density, ρ is charge density, ρ_m is mass density, e is electron charge, P_e is electron pressure, m_e is electron mass, η is resistivity, σ is the electrical conductivity, E_L the is the total energy loss function, R is the universal gas constant, k_B is Boltzmanns constant, γ is the ratio of specific heat at constant pressure to specific heat at constant volume (usually assumed to be 5/3).

The equation of motion and equations of continuity that form part of the Navier-Stokes Equations, given in Table 1.3, imply that momentum, mass and charge are conserved. The associated energy equation describes the net heat loss/gain due to energy sources/sinks. The terms on the right hand side of the equa-

tion of motion (from left to right) are the plasma pressure gradient, the Lorentz force per unit volume, the Coulomb force per unit volume, the gravitational force per unit volume and any additional forces (F). The ideal gas equation of state is for a system where plasma particles have random motion and interact through elastic collisions. The adiabatic equation of state is for a system with no heat exchange. Ohm's law is required to close the system consisting of Maxwell's and Navier-Stokes equations. In the general form of Ohm's law, the terms on the right hand side include (from left to right) the resistive term ($\eta \boldsymbol{j}$), the 'Hall Effect', possible anisotropic electron pressure, and the contribution of electron inertia to the current. The simplified version of Ohm's law is acceptable when the 2nd, 3rd and 4th terms are considered small enough to be negligible.

1.5.1 Ideal MHD and 'Frozen-in Flow'

Ideal MHD assumes that the plasma is a perfect conductor (i.e., very low resistivity, $\eta \to 0$) and that processes occurring within the plasma are able to convert magnetic energy into kinetic energy without magnetic dissipation. Table 1.4 and Table 1.5 provide a list of Ideal MHD assumptions, implications and equations.

Assumption	Implication
The plasma is approximately charge neutral.	$qE \to 0$, charge conservation becomes irrelevant.
Electrons and ions behave collectively.	The plasma consists of a single fluid of ions and electrons.
The macroscopic time scale of the system is greater than any microscopic plasma time scales, such as ion gyrofrequency and collision frequency.	The plasma is in thermodynamic equilibrium with distribution functions close to Maxwellian.
The plasma flow speeds/velocities are all much less than the speed of light	No relativistic effects. The displacement current in Ampère's law can be ignored ($\varepsilon_0\mu_0 = 1/c^2 \to 0$).
The dielectric permittivity and magnetic permeability are constant and have the same values as in a vacuum.	$\varepsilon = \varepsilon_0$ and $\mu = \mu_0$
The plasma behaves like an ideal gas.	Equation of state for an ideal gas can be used. Maxwellian distribution functions are appropriate.

Table 1.4: Ideal MHD asumptions and implications. N.B., an inertial frame of reference is used.

In the simplified version of Ohm's Law given in Table 1.3, $\mathbf{j}$ and $\mathbf{E}$ can substituted using Ampère's and Faraday's Laws respectively. Rearranging and applying vector identities yields

$$\frac{\partial \mathbf{B}}{\partial t} = \nabla \times (\mathbf{v} \times \mathbf{B}) + \frac{1}{\mu_0 \sigma} \nabla^2 \mathbf{B} \tag{1.41}$$

This equation describes the motion of magnetic field in a plasma in terms of convection with the plasma (1st term on the right) and diffusion through the plasma

(2nd term on the right). The ratio between these terms is known as the magnetic Reynolds number and is given by

$$R_m = \frac{|\nabla \times (\mathbf{v} \times \mathbf{B})|}{|(\mu_0 \sigma)^{-1} \nabla^2 \mathbf{B}|} \tag{1.42}$$

R_m is a measure of the relative importance of convection and diffusion. Equation 1.42 can also be rewritten in simple dimensional terms as follows

$$R_m = \mu_0 \sigma L V \tag{1.43}$$

Where L represents the spatial scale over which the magnetic field varies, V is the convection velocity of the plasma and the conductivity term σ is a measure of the frequency of collisions in the plasma. If $R_m \ll 1$ then diffusion dominates over convection and the magnetic field will diffuse across the plasma in such a way as to smooth out any local inhomogeneities. If $R_m \gg 1$ then convection dominates over diffusion and the magnetic field is 'frozen-in' to the plasma.

The frozen-in flow approximation is a key part of ideal MHD and is described by

$$\frac{\partial \mathbf{B}}{\partial t} = \nabla \times (\mathbf{v} \times \mathbf{B}) \tag{1.44}$$

This equation implies that the magnetic field lines are constrained to move with the plasma. In other words, when the plasma particles move, the magnetic field will change shape so that the particles remain on the same field line, and vice versa. Hence, the 'frozen-in' magnetic field lines can be identified by their associated plasma - this phenomenon is also referred to as 'frozen-in flux'. It can also be helpful to consider the concept of 'flux tubes' which are generalized cylinders containing a constant amount of magnetic flux. For the frozen-in approximation, a flux tube will always contain the same particles and magnetic flux regardless of any motion of the flux tube or change in shape of the bounding surface.

Name	Equation
Gauss' law	$\nabla.\mathbf{E} = 0$
Gauss' law for magnetism	$\nabla.\mathbf{B} = 0$
Faraday's law	$\nabla \times \mathbf{E} = -\frac{\partial \mathbf{B}}{\partial t}$
Ampère's law	$\nabla \times \mathbf{B} = \mu_0 \mathbf{j}$
Motion	$\rho_m \frac{\partial \mathbf{v}}{\partial t} + \rho_m (\mathbf{v}.\nabla)\mathbf{v} = -\nabla P + \mathbf{j} \times \mathbf{B} + \rho_m \mathbf{g} + \mathbf{F}$
Continuity	$\frac{\partial \rho_m}{\partial t} + \nabla.(\rho_m \mathbf{v}) = 0$
Energy	$\frac{\partial P}{\partial t} + \mathbf{v}.\nabla P \gamma P (\nabla \mathbf{v}) = E_L$
Equation of State	$P = R\rho_m T = nk_B T$
Ohm's Law	$\mathbf{E} + \mathbf{v} \times \mathbf{B} = 0$

Table 1.5: Ideal MHD equations. The ideal MHD form of Ohm's law describes the 'frozen-in' flow approximation.

1.5.2 Further Consequences of MHD

1.5.2.1 Magnetic Tension and Magnetic Pressure

Magnetic tension and magnetic pressure are two additional properties associated with MHD theory. From Ampère's law it can be seen that,

$$\mathbf{j} \times \mathbf{B} = \frac{1}{\mu_0} (\nabla \times \mathbf{B}) \times \mathbf{B} \tag{1.45}$$

This can be rewritten in the form,

$$\mathbf{j} \times \mathbf{B} = -\nabla \left(\frac{B^2}{2\mu_0} \right) + \frac{1}{\mu_0} (\mathbf{B}.\nabla) \mathbf{B} \tag{1.46}$$

Thus the $\boldsymbol{j} \times \boldsymbol{B}$ force has two components. The first term on the right represents a force resulting from a gradient in magnetic flux density – the magnetic pressure. This force acts to oppose the compression of field lines and expel plasma from regions of high magnetic field strength. The second term on the right is the force exerted by the magnetic field as it changes shape to reach its minimum energy state – the magnetic tension force. This tends to oppose the curvature of field lines and to shorten them and it is analogous to the tension in an elasticated string.

1.5.2.2 Plasma Beta and Alfvén speed

The equilibrium and dynamics of a magnetized plasma are determined by three key terms (Meyer-Vernet, 2007):

- Inertia, which corresponds to the density of bulk kinetic energy ($\rho V^2/2$ where V is the bulk velocity of the plasma).
- Thermal (or kinetic) pressure, which corresponds to the density of random kinetic energy (nk_BT/m).
- Magnetic forces, which correspond to the density of magnetic energy ($B^2/2\mu_0$).

The relationship between the second and third term yields another parameter commonly used to describe a magnetised plasma, known as plasma beta β. It is defined as the ratio of plasma thermal pressure to plasma magnetic pressure (Mullan and Smith, 2006).

$$\beta = \frac{2\mu_0 n k_B T}{B^2} \tag{1.47}$$

Plasma beta describes the relative importance of plasma particle and magnetic field pressures. If $\beta>1$ then the particle pressure dominates over the magnetic pressure, whereas for $\beta<1$ the reverse applies. Anisotropic plasma betas can be split into parallel and perpendicular components, Equation 1.47 assumes a plasma in equilibrium, that is isotropic and quasi-neutral.

Finally, if the first and last of these terms are equated, the following speed can be found,

$$v_A = \frac{B}{(\mu_0 \rho)^{1/2}} \tag{1.48}$$

This is known as the Alfvén speed and it is the typical speed to which the magnetic field can accelerate the plasma.

1.5.3 Magnetic Reconnection

As described in Section 1.5.1, a consequence of ideal MHD and the frozen-in approximation is that magnetic fields with different sources and their associated particle populations cannot readily mix. However, when the magnetic Reynolds number (see Equation 1.42) is of order unity or lower, magnetic diffusion becomes significant and magnetic reconnection, the process by which magnetic field lines break and reconnect with each other, can occur.

Put in very simple qualitative terms, if two regions of anti-parallel magnetic field separated by a thin current sheet are pushed together (e.g., due to the frozen-in flow of the plasma frozen-in to one or both of the field regions) then the importance of resistivity becomes such that the plasma in the region near the boundary can becomes such that magnetic field lines diffuse though the current sheet and vanish at a particular point. This produces an X-type configuration, where the magnetic

field is zero at the centre of the X or 'neutral point', see Figure 1.5. This results in pairs of field lines reconnecting with each other and creating new pairs of highly bent field lines. Magnetic tension forces then act to straighten these field lines, causing them to become expelled from the reconnection site and allowing the next pair of field lines to reconnect. It is important to note that magnetic reconnection is a method by which magnetic energy can be transferred to particle kinetic energy, as bent field lines being pulled from the reconnection site via magnetic tension will accelerate the particles frozen to the expelled field lines.

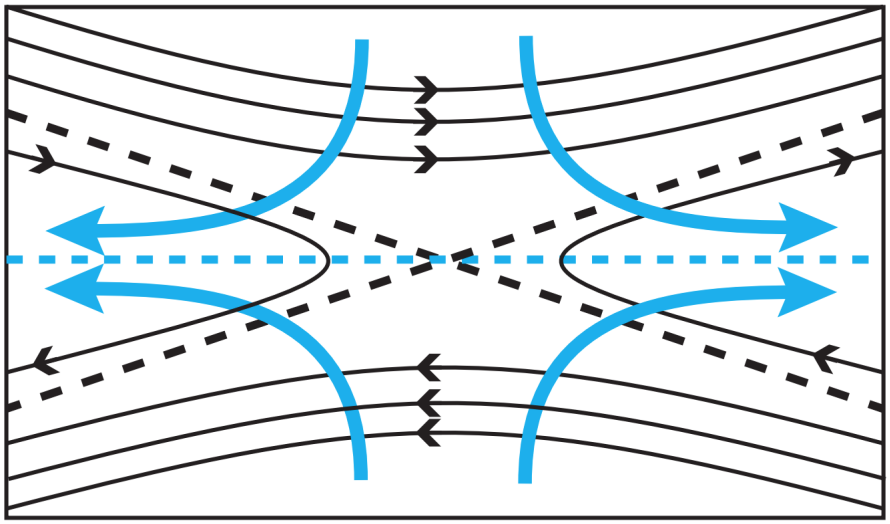

Figure 1.5: Illustration of the geometry of simple reconnection (Eastwood et al., 2013). Magnetic field lines are shown in black, plasma flow is shown by the blue arrows and the current sheet is shown by the blue dashed line. The X-type configuration is shown by black dashed lines, for which the centre of the X or 'neutral point' has zero magnetic field.

1.6 Kinetic Description of a Plasma

The kinetic model of a plasma considers the collective behaviour of individual particles. However, a system of many individual dynamic plasma particles, each generating its own electrostatic field and reacting to the fields of others, results in very complex behaviour. Therefore, rather than attempting to account for the complete particle dynamics, kinetic theory consists of approximate statistical descriptions of the plasma by defining a distribution function of particles. It is assumed that the plasma consists of very strongly interacting particles, each with its own time dependant position and velocity. The configuration of a system at a given time can be thus be fully described by six quantities for each particle within the system: three positions (x,y,z) and three velocities (v_x,v_y,v_z). Each of these quantities is a coordinate in a six-dimensional phase space. By following particle trajectories in phase space it is possible to study the changes of the system with time (see Figure 1.6).

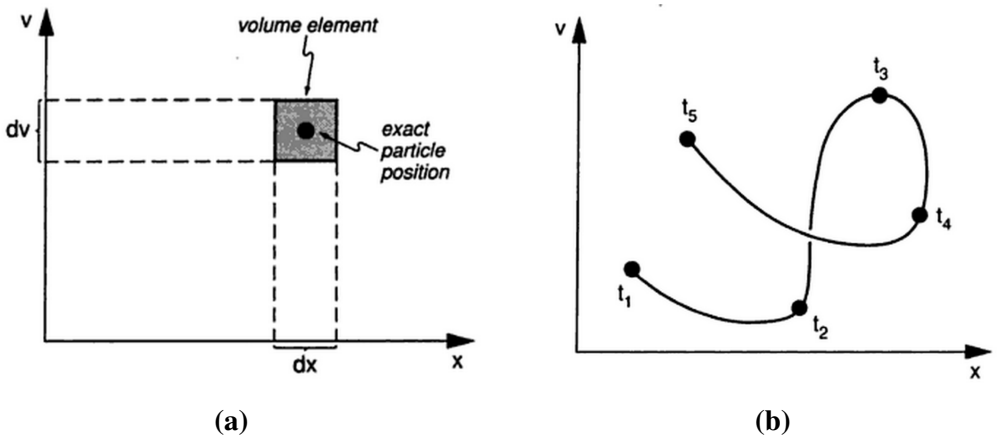

Figure 1.6: Illustration of the basic concepts of phase space (Treumann and Baumjohann, 1997). (left) At certain time t_0, a particle exists within the phase space volume element $dxdv$. (right) A particle with position $\boldsymbol{x}_i(t)$ and velocity $\boldsymbol{v}_i(t)$, plotted in phase space for subsequent times ($t1$, $t2$... $t5$).

It can be assumed that the plasma particles within a system are statistically correlated in time, space and velocity due to their mutual interactions and therefore, that averaging over large number of particles is appropriate when describing a plasma. This ensemble average of a variable does not distinguish between single particles but instead, only accounts for their dependence on space and velocity (Treumann and Baumjohann, 1997). The Equations related to ensemble average Phase Space Density (PSD) are given in Table 1.6.

Name	Equation
Ensemble Average Phase Space Density	$\langle \mathscr{F}(\mathbf{x},\mathbf{v},t)\rangle = f(\mathbf{x},\mathbf{v},t)$
Exact Phase Density	$\mathscr{F}(\mathbf{x},\mathbf{v},t) = f(\mathbf{x},\mathbf{v},t) + \delta\mathscr{F}(\mathbf{x},\mathbf{v},t)$
	where $\langle \delta\mathscr{F}\rangle = 0$
Electric Fields	$\mathbf{E}_{micro}(\mathbf{x},\mathbf{v},t) = \mathbf{E}(\mathbf{x},\mathbf{v},t) + \delta\mathbf{E}(\mathbf{x},\mathbf{v},t)$
	where $\langle \partial\mathbf{E}_{micro}\rangle = 0$
Magnetic Fields	$\mathbf{B}_{micro}(\mathbf{x},\mathbf{v},t) = \mathbf{B}(\mathbf{x},\mathbf{v},t) + \delta\mathbf{B}(\mathbf{x},\mathbf{v},t)$
	where $\langle \partial\mathbf{B}\rangle = 0$

Table 1.6: Equations for ensemble average phase space density. Where **x** is position, **v** is velocity, $\boldsymbol{B}_{micro}$ is the microscopic magnetic field, $\boldsymbol{E}_{micro}$ is the microscopic electric field, $\mathscr{F}$ is the exact phase density which accounts for the phase space density of all particles within the system and f is the ensemble average phase space density.

The kinetic equation for the ensemble average assumption is given by

$$\frac{\partial f}{\partial t} + \mathbf{v}.\nabla_x f + \frac{q}{m}(\mathbf{E}+\mathbf{v}\times\mathbf{B}).\nabla_v f = -\frac{q}{m}\langle(\partial\mathbf{E}+\mathbf{v}\times\partial\mathbf{B}).\nabla_v\delta\mathscr{F}\rangle \tag{1.49}$$

which describes the distribution function of the plasma particles in phase space under average electric and magnetic fields. As the exact position of each particle is now unknown, the distribution function is interpreted as the probability of a particle to be found in a certain phase space volume element ($d\mathbf{x}d\mathbf{v}$). However, the averaged term on the right-hand side contains all the particle and field correlations and, as a consequence, its calculation is complex. Simplification of the kinetic equation can be achieved by neglecting the correlations between the fields and, in the case of space plasmas, it is often appropriate to assume that the plasma is completely collisionless. The right-hand side of Equation 1.49 can thus be entirely ignored, resulting in the so-called Vlasov Equation (Hénon, 1982) given by

$$\frac{\partial f}{\partial t} + \mathbf{v}.\nabla_x f + \frac{q}{m}(\mathbf{E}+\mathbf{v}\times\mathbf{B}).\nabla_v f = 0 \tag{1.50}$$

The assumption that collisions are negligible implies that the phase space density remains constant under all plasma and field interactions. This behaviour forms the basis of Liouvilles Theorem, which states that the phase space volume can be deformed but that phase space density remains constant during the dynamic evolution of a plasma system.

1.6.1 Velocity Distributions

An aspect of kinetic physics that is commonly used in the study of space plasmas is the velocity distribution function (VDF). This function provides the dependence of the distribution on velocity for a fixed point in configuration space $f(\mathbf{v})$. A plasma that is in equilibrium can be described using a Maxwellian VDF. For a Maxwellian plasma, the velocities of the particles are distributed randomly around the average velocity – they have a Gaussian distribution. The VDF for an equilibrium, isotropic plasma that is streaming with bulk velocity v_0 is given by

$$f(v) = n\left(\frac{m}{2\pi k_B T}\right)^{3/2} exp\left(-\frac{m(\mathbf{v}-\mathbf{v}_0)^2}{2k_B T}\right) \tag{1.51}$$

However, not all space plasmas are isotropic. In particular, the presence of a magnetic field can lead to different particle velocities in the parallel and perpendicular field direction, for example the temperature anisotropies commonly observed in solar wind electrons (see Section 2.2.2). In this case the VDF can be given by

$$f\left(v_\perp, v_\parallel,\right) = \frac{n}{T_\perp T_\parallel^{1/2}}\left(\frac{m}{2\pi k_B}\right)^{3/2} exp\left(-\frac{mv_\perp^2}{2k_B T_\perp} - \frac{mv_\parallel^2}{2k_B T_\parallel}\right) \tag{1.52}$$

VDFs of this form are the most common for space plasmas (Baumjohann and Treumann, 2012).

Observed space plasma VDFs also often display non-Maxwellian suprathermal tails. These VDFs can be represented by a Kappa distribution given by

$$f_\kappa(v) = \frac{n}{\left(\pi\kappa v_\kappa^2\right)^{3/2}} \frac{\Gamma(\kappa+1)}{\Gamma(\kappa-1/2)} \left(1+\frac{v^2}{\kappa v_\kappa^2}\right) \tag{1.53}$$

where $\Gamma(a) = (a-1)!$ and v_κ is the effective thermal velocity given by

$$v_\kappa = \left(\frac{2\kappa-3}{\kappa}\frac{k_B T}{m}\right)^{1/2} \tag{1.54}$$

For $v \gg v_\kappa$, the Kappa distribution decreases with v as a power law given by $f_\kappa(v) \propto v^{-2(\kappa+1)}$. Additionally, in the limit of $\kappa \to \infty$ the kappa function reduces to a Maxwellian distribution (Zouganelis, 2008).

1.6.2 Moments

The three-dimensional velocity distribution of particles $f(v,r,t)$ can be used to calculate the bulk parameters of plasma by integrating the distribution function over the velocity components of phase space i.e., taking the moments of the distribution function (e.g. Paschmann et al., 1998). There are an infinite number of moments of the distribution function. However, only the first few are discussed within this thesis. The general equation for a moment (the ith moment) is given by

$$M_i(\mathbf{r},t) = f(\mathbf{v},\mathbf{r},t)\,\mathbf{v}^i d^3v \tag{1.55}$$

The zeroth order moment gives the number density of particles and is given by

$$n = \int f(\mathbf{v},\mathbf{r},t)\,d^3v, \tag{1.56}$$

The first order moment is related to the bulk velocity of particles $\boldsymbol{v}_b$ and is given by

$$\mathbf{v}_b(\mathbf{r},t) = \frac{1}{n}\int \mathbf{v} f(\mathbf{v},\mathbf{r},t)\,d^3v, \tag{1.57}$$

The pressure tensor is calculated from the second order moment, given by

$$P = m\int (\mathbf{v}-\mathbf{v}_b)(\mathbf{v}-\mathbf{v}_b) f(\mathbf{v},\mathbf{r},t)\,d^3v, \tag{1.58}$$

Finally, the trace of the third order moment (the heat tensor) yields the heat flux vector, a measure of the transfer of heat through the plasma. This is given by

$$\mathbf{q} \quad = \quad \frac{m}{2}\int |\mathbf{v}-\mathbf{v}_b|^2(\mathbf{v}-\mathbf{v}_b) f(\mathbf{v},\mathbf{r},t)\, d^3v, \tag{1.59}$$

1.7 Plasma Waves

The existence of a plasma necessitates high temperatures and, accordingly, plasma particles have high kinetic energies. This high-speed particle motion generates microscopic charge separations, leading to variation in the plasma's electromagnetic field (Alfvén, 1942). Thus, even for a plasma considered to be in equilibrium, there is always a certain level of background thermal fluctuation. In addition, a plasma may also be subjected to external disturbances imposed on the system. These disturbances are generally considered to be a superposition of linear waves which propagate through the plasma, transporting and dispersing the energy injected into the system. However, unlike thermal fluctuations, plasma waves are not random and there are two basic conditions necessary for their existence (Stix, 1992). Firstly, the wave must be a solution to the appropriate plasma equations and secondly, wave amplitudes must exceed those of the background thermal fluctuations. The former implies that the number of possible plasma wave modes is discrete. The latter implies that a perturbance with an amplitude below the background noise cannot affect the plasma unless it has been amplified by another mechanism.

A simple way to consider a plasma wave disturbance is as a plane wave given by

$$\mathbf{A}(\mathbf{x},t) \quad = \quad \mathbf{A}(\mathbf{k},\omega)\, exp\,(i\mathbf{k}.\mathbf{x} - i\omega t) \tag{1.60}$$

where $\boldsymbol{A}$ is amplitude, $\boldsymbol{x}$ is position, t is time, $\boldsymbol{k}$ is wave vector and $\boldsymbol{\omega}$ is frequency. The phase velocity v_{ph} and group velocity v_{gr} of a wave are then given by Equations 1.61 and 1.62 respectively.

$$\mathbf{v}_{ph} \quad = \quad \frac{\omega \mathbf{k}}{k^2} \tag{1.61}$$

$$\mathbf{v}_{gr} \quad = \quad \frac{\partial \omega}{\partial \mathbf{k}} \tag{1.62}$$

Phase velocity is always parallel to the wave vector and shows the direction of wave propagation. Group velocity not always parallel to the wave vector and describes the speed and direction of the energy flow of the wave.

In this section a number of different possible wave modes will be discussed, ranging from large-scale MHD waves in which the plasma can be treated as a fluid, down to small scale waves for which the characteristic frequencies of the plasma become relevant and plasma particle inertia comes into play.

1.7.1 Waves in an Unmagnetized Plasma

There are two types of wave that can propagate in an unmagnetized plasma (Treumann and Baumjohann, 1997). The first take the form of plasma particle oscillations, as described briefly in Section 1.3. The second are ordinary electromagnetic waves, which are similar to the electromagnetic waves that propagate in a vacuum, except that the electric and magnetic fields of the waves interact with the charged particles in a plasma. In a magnetised plasma, these wave modes are present for frequencies/scales where the MHD treatment of a plasma breaks down i.e., above the plasma and gyro- frequencies of the plasma.

1.7.1.1 Langmuir Waves

The displacement of electrons in a plasma results in oscillations of disturbed electrons relative to the less-mobile ions. These are commonly referred to as Langmuir oscillations and can also be given in terms of variation in density,

$$\frac{\partial^2 \delta n}{\partial t^2} = -\omega_p^2 \delta n \tag{1.63}$$

where ω_p is the plasma frequency as given in Equation 1.21. However, as stated previously, this is a very simple picture of electron displacement. Electrons in a plasma have different velocities and will react differently to a process that acts to displace them from their instantaneous positions. To account for this effect the adiabatic variation of electron thermal pressure ($\delta p_e = \gamma_e k_B T_e \delta n$) must be included in the description. This yields a more precise equation for the variation in density given by

$$\frac{\partial^2 \delta n}{\partial t^2} = \left(\frac{\gamma_e k_B T_e}{m_e}\right) \frac{\partial^2 \delta n}{\partial x^2} - \delta \omega_p \delta n \tag{1.64}$$

This is the equation for a Langmuir wave and, as it has the form of a wave equation, can be solved by introducing $\delta n \propto e^{-i\omega+ikx}$ to give,

$$\omega_l^2 \quad = \quad \omega_p^2 \quad + \quad k^2\gamma_e v_{th}^2 \tag{1.65}$$

Where v_{th} is the thermal velocity ($v_{th} = k_B T_e/m_e$). Equation 1.65 is the Langmuir dispersion relation, which gives the dependence of the frequency of the waves on the wavenumber.

1.7.1.2 Ordinary Electromagnetic Waves

Moving plasma particles can contribute to oscillating plasma currents which can become sources for electromagnetic waves. There are a number of possible electromagnetic modes in an magnetized plasma. However, for an unmagnetized plasma, the wave mode is known as the ordinary electromagnetic mode and its dispersion relation is given by

$$\omega_{om}^2 \quad = \quad \omega_p^2 \quad + \quad c^2k^2 \tag{1.66}$$

This is a transverse wave ($\boldsymbol{k} \perp \boldsymbol{E} \perp \boldsymbol{B}$) similar to light propagating in a vacuum (with the dispersion relation $\omega = ck$).

In a magnetised plasma, the gyromotion of the electrons comes into play. This will effect electromagnetic waves with frequencies of the order of magnitude of the electron gyrofrequency or smaller. In particular, for propagation along the magnetic field, the wave becomes split into two waves for which the electrons and the wave $\boldsymbol{E}$ and $\boldsymbol{B}$ fields gyrate about the background magnetic field. The wave mode that rotates in the same sense as the electrons gyromotion is more easily emitted and absorbed by the electrons - this mode is known as the whistler mode and discussed in more detail in Section 1.7.3.

1.7.2 Magnetohydrodynamic Waves

At large scales, waves described by ideal MHD can be considered. In particular, a magnetised plasma supports transverse waves known as Alfvén waves, which propagate though a plasma via the transverse motion of field lines produced by magnetic tension. In very simple terms, Alfvén waves are analogous to transverse

waves propagating along a stretched string due to the string's tension. A wave on a string has a phase speed of $v_{ph} = (T/\rho)$, where T is the tension force per unit cross-sectional area and ρ is the mass density of the string. In the case of a magnetized plasma, the tension force is equal to B^2/μ_0 and the mass density is given by that of the plasma frozen-in the the field, yielding a phase speed of $v_{ph} = (B/\mu_0\rho)$ (Meyer-Vernet, 2007). This, of course, assumes that the perturbations are perpendicular to the field and propagate along the field direction.

In reality, there are three MHD modes consisting of a generalization of the Alfvén mode that propagates at an angle to the field, and two modes which also include a certain amount of plasma compression thereby introducing the gas pressure gradient into the restoring force along with the magnetic stresses. These two compressive modes are known as the fast and slow magnetosonic waves. The fast mode propagates faster than the slow and has pressure and magnetic restoring forces that act in phase, whereas the slow mode has pressure and magnetic restoring forces that act out of phase.

For a uniform plasma with straight magnetic field lines given by $\mathbf{B}_0$=$\mathrm{B}_0\hat{\mathbf{z}}$ and $\boldsymbol{k}$=$\boldsymbol{k}_{\parallel}$+$\boldsymbol{k}_{\perp}$, the solution of the MHD wave equation, derived using Maxwell's equations, can be found and written in the form

$$\begin{bmatrix} \omega^2 - v_A^2 k_\parallel^2 - c_{ms}^2 k_\perp^2 & 0 & -c_s^2 k_\perp^2 k_\parallel^2 \\ 0 & \omega^2 - v_A^2 k_\parallel^2 & 0 \\ -c_s^2 k_\perp^2 k_\parallel^2 & 0 & \omega^2 - c_s^2 k_\parallel^2 \end{bmatrix} \begin{bmatrix} \delta v_{0x} \\ \delta v_{0y} \\ \delta v_{0z} \end{bmatrix} = 0 \qquad (1.67)$$

Where v_A is the Alfvén speed and c_{ms} is the magnetosonic speed (see Section 2.1.6). It can be seen from the system above that the y-component decouples from the other fields which represents a wave with a linear dispersion relation ($\omega_A = \pm k_\parallel v_A$). This wave propagates parallel to the field and is purely transverse, it is an Alfvén wave.

1.7.3 Cold Electron Plasma Waves

As stated previously, the ideal MHD description of a wave, in which the plasma is treated as a single fluid, is only appropriate at low frequencies (i.e., $\omega \ll \omega_{gi}, \omega_{pi}$). When the characteristic frequencies of the plasma are approached, the difference between the ion and electron dynamics become significant and the waves transform into modes that cannot be described by single-fluid theory. For very high frequency waves (i.e., $\omega \gg \omega_{gi}, \omega_{pi}$) the plasma can be treated as a cold, magnetised electron plasma in which the ions are considered to exist purely as a neutralizing background. The assumptions made for this model are as follows [Auer et al., 1958, Dawson & Oberman, 1959]:

- The plasma consists of zero-temperature, frictionless fluids of ions and electrons.
- The plasma is approximately charge neutral.
- The plasma is homogeneous in space.
- The plasma is immersed in a static, uniform magnetic field.

The 'cold' model for electron dynamics is essentially governed by single-particle motion in a strong background field. It is is important to note that zero-temperature plasma implies that electrons and ions are motionless in the unperturbed state. This assumption is used because, as stated previously, wave amplitude must exceed the thermal noise. Therefore, assuming a cold plasma is equivalent to assuming that all disturbances result in large enough wave amplitudes. This is not true for a real plasma but is useful when deriving possible wave modes. It should also be noted that the 'cold' conditions mean that the magnetic field of the wave is considered to be unaffected by the electron motion.

The cold plasma dispersion relation was originally found by Astrom (1951) and Sitenko and Stepanov (1957). If $\boldsymbol{k}$ is set to be in the x-z plane, the cold plasma dispersion relation can be written as

$$Det\begin{bmatrix} N_{\parallel}^2-\varepsilon_1 & i\varepsilon_2 & N_{\parallel}N_{\perp} \\ -i\varepsilon_2 & N^2-\varepsilon_1 & 0 \\ -N_{\parallel}N_{\perp} & 0 & N_{\perp}^2-\varepsilon_3 \end{bmatrix} = 0 \tag{1.68}$$

Where $\boldsymbol{N}$ is the vectorial refractive index and ε_1, ε_2 and ε_3 are matrix components defined as

$$\begin{aligned} \varepsilon_1 &= 1 + \frac{\omega_{pe}}{\omega^2-\omega_{ge}^2} \\ \varepsilon_2 &= \frac{i\omega_{ge}}{\omega}\frac{\omega_{pe}^2}{\omega^2-\omega_{ge}^2} \\ \varepsilon_3 &= 1 - \frac{\omega_{pe}^2}{\omega^2} \\ \mathbf{N} &= \frac{\mathbf{k}c}{\omega} \\ N^2 &= N_{\perp}^2 + N_{\parallel}^2 \end{aligned} \tag{1.69}$$

For a parallel propagating wave $N_\perp = 0$ and $N_\parallel = N$. Since $\boldsymbol{k}$ is parallel to $\boldsymbol{B}_0$, the dispersion relation splits into parallel ($\varepsilon_3 = 0$) and transverse components. The parallel dispersion relation yields Langmuir electron oscillations due a $\delta\boldsymbol{E}_\parallel$ parallel to $\boldsymbol{k}_\parallel$. The transverse dispersion relation contains the two perpendicular electric field components, which due to the cylindrical geometry of electric wave field components can be written as

$$\sqrt{2}\delta E_{R,L} \quad = \quad \delta E_x \quad \pm \quad i\delta E_x \tag{1.70}$$

These component wave fields describe right-hand R and left hand L circularly polarised waves, where the electric field vector rotates in the positive y-direction for R and in the negative y-direction for L. The transverse dispersion relation splits into two independent relations for R and L modes given by

$$\mathbf{N}^2 \quad = \quad \frac{k^2c^2}{\omega^2} \quad = \quad \varepsilon_{R,L} \tag{1.71}$$

with,

$$\varepsilon_{R,L} \quad = \quad 1 \quad - \quad \frac{\omega_{pe}^2}{\omega\left(\omega \mp \omega_{ge}\right)} \tag{1.72}$$

Examination of the R-mode equation shows that if $\omega_R \to \omega_{ge}$ then $k \to \infty$. Hence, $\omega_R - \omega_{ge} \to -0$ and,

$$\omega_{R,res} \quad = \quad \omega_{ge} \tag{1.73}$$

Which is the electron-cyclotron resonance frequency for the right-hand polarised wave. The implication of $k \to \infty$, is that the resonant wavelength becomes very short ($\lambda = 2\pi/k \to 0$). Additionally, because the frequency of the wave is constant, the phase velocity of the wave also tends to zero, while the wave plasmon momentum (the momentum of a wave-packet, p=h/λ) increases. Hence, the interaction between the electrons and the plasma waves becomes very strong and dramatically effects the electrons' orbits. During such an interaction the wave will either give energy

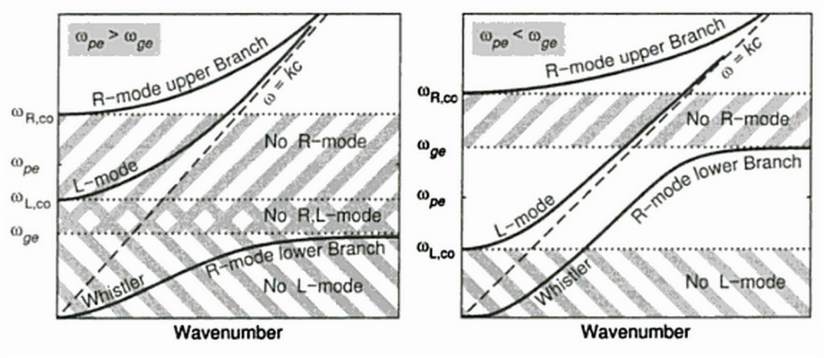

Figure 1.7: Dispersion curves for parallel propagating R- and L- mode waves in a cold elecrton plasma (Treumann and Baumjohann, 1997). The plot on the left is for $\omega_{pe} > \omega_{ge}$ (a dense plasma) and the plot on the right is for $\omega_{pe} < \omega_{ge}$ (a dilute plasma). In both cases, Whistler mode waves are electromagnetic waves with frequencies below the electron gyro-frequency. $\omega_{R,co}$ is the the right-hand cut-off frequency and $\omega_{L,co}$ is the left-hand cut-off frequency. ω_{pe} is the electron plasma frequency and ω_{ge} is the electron gyro-frequency.

and momentum to, or extract energy and momentum from the electrons, resulting in either wave damping or amplification. Similar examination of the L-mode equation reveals that there are no resonant frequencies.

At sufficiently low frequencies the '1' on the right hand side of Equation 1.72 can be neglected to obtain,

$$\omega = \frac{\omega_{ge}}{1+\frac{\omega_{pe}^2}{k^2c^2}} \tag{1.74}$$

In the long-wavelength limit of small k this further simplifies to become,

$$\omega_w = \frac{k^2c^2\omega_{ge}}{\omega_{pe}^2} \tag{1.75}$$

Which is the dispersion relation for electron Whistlers [Stenzel, R. J., 1999]. Whistler wave phase and group velocities are both proportional to k and therefore proportional to $\omega_w^{1/2}$. Thus, waves with higher frequencies have higher associated velocities and observed whistler waves, with the same source location and time, will appear as a falling tone - hence the nomenclature. Figure 1.7 shows the dispersion relation for R- and L- mode electron-cyclotron waves. The plot on the left is for $\omega_{pe} > \omega_{ge}$ and the plot on the right is for $\omega_{pe} < \omega_{ge}$.

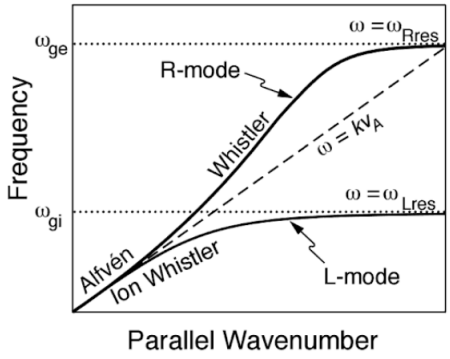

Figure 1.8: Dispersion curves for parallel propagating R- and L- mode waves in a two fluid plasma (Treumann and Baumjohann, 1997). $\omega_{R,res}$ is the the right-hand resonance frequency and $\omega_{L,res}$ is the left-hand resonance frequency. ω_{gi} is the ion gyro-frequency and ω_{ge} is the electron gyro-frequency.

At lower frequencies, near the ion-cyclotron frequency, ion-dynamics can no longer be ignored. The dispersion relations for a two-fluid plasma can be found as above for the electron plasma. In particular, the following relation can be obtained (assuming $\omega \ll \omega_{ge}$),

$$\omega_{lh}^2 = \frac{\omega_{pi}^2 + \omega_{gi}^2}{1 + \frac{\omega_{pe}^2}{\omega_{ge}^2}} \tag{1.76}$$

This is the dispersion relation for a lower-hybrid wave, for which the ion and electron properties mix. This is also the lower limit for election whistlers. Figure 1.8 shows the low frequency dispersion curves for parallel propagation in a two-fluid plasma. In which it can be seen that the dispersion branches of the L- and R- modes separate from the Alfvén curve at frequencies close to the ion-cyclotron resonance.

Within this section, only parallel wave modes have been considered. However, the same methods can be applied to perpendicular propagating waves and also to obliquely propagating waves, for which disperion relations are considered in terms of θ, the angle between the static background magnetic field $\boldsymbol{B}_0$ and the direction of wave propagation $\boldsymbol{k}$. For example, Whistler mode waves can propagate oblique to $\boldsymbol{B}_0$ and the angular limit of this oblique propagation is given by the resonance cone angle, $\theta_{ph,max} = acos\,(\omega/\omega_{ge})$, so called because the whistler mode waves are in resonance with the electron gyro-motion. Figure 1.9 shows a plot of the two resonance frequencies against propagation angle for an electron plasma.

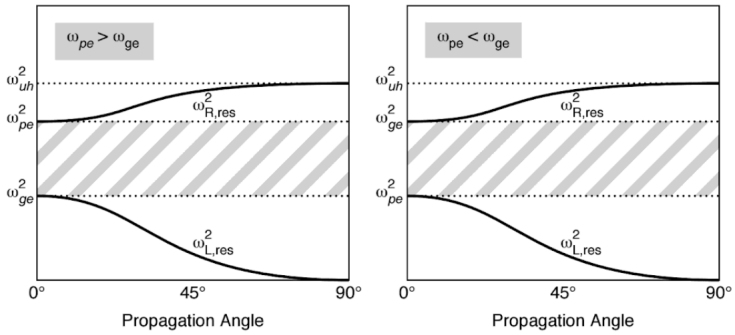

Figure 1.9: Resonance frequencies against propagation angle for an electron plasma (Treumann and Baumjohann, 1997). The plot on the left is for $\omega_{pe} > \omega_{ge}$ (a dense plasma) and the plot on the right is for $\omega_{pe} < \omega_{ge}$ (a dilute plasma). $\omega_{R,res}$ is the the right-hand resonance frequency and $\omega_{L,res}$ is the left-hand resonance frequency. ω_{pe} is the electron plasma frequency and ω_{ge} is the electron gyro-frequency. ω_{uh} is the upper hybrid frequency given by, $\omega_{uh}^2 = \omega_{ge}^2 + \omega_{pe}^2$. ω_{uh} is the frequency at which the plasma and cyclotron properties of the electrons mix and is the resonant frequency for one of the perpendicular wave-modes in a cold electron plasma.

1.8 Turbulence

Plasma and magnetic field fluctuations are ubiquitous in the solar wind. It is an environment in which waves, discontinuities and coherent structures coexist and discriminating between these different phenomenologies and the broad spectrum of fluctuations associated with solar wind turbulence is a challenge. In this section, turbulence in general is discussed. Further details regarding the specifics of solar wind plasma turbulence are discussed in Section 2.1.8.

Turbulence within a fluid is the departure from laminar flow, in other words, departure from velocity that varies smoothly and predictably in space and time. Turbulent flow has two important properties, it is chaotic and it displays intermittency (Meyer-Vernet, 2007, and references within). The chaotic nature of turbulence means that, although the governing fluid equations are deterministic, the long term evolution of turbulence cannot be predicted. This is because a small variation in, or perturbation to, the initial conditions results in a change that increases exponentially with time. Thus, the study of turbulence is reduced to determining its statistical properties. The intermittency of turbulence is displayed by the tendency of turbulent activity to become increasingly localized at smaller scales. In other words, large fluctuations are more probable than expected from Gaussian statistics (the distribution functions for turbulent fluctuations have extended tails) and this effect becomes more pronounced at smaller scales.

Three key assumptions are often used when studying fluid turbulence. The first is that if the bulk flow is fast enough, then the time-variation observed in the fluid corresponds to the spacial-variation in the fluid frame, this is the Taylor hypothesis. The second is that the statistical properties of the turbulent component of the fluid velocity are independent of position and direction i.e., the turbulence is homogeneous and isotropic. Thirdly, the turbulence is incompressible i.e., the density of a parcel of turbulent fluid moving with the bulk flow remains constant. For this incompressible case the continuity equation (Table 1.3) simplifies to become

$\nabla.\boldsymbol{u} = 0$, where $\boldsymbol{u}$ is the turbulent component of the fluid velocity, and thus the equation of motion (Table 1.3) can be given by,

$$\frac{\partial \mathbf{u}}{\partial t} \quad + \quad (\mathbf{u}.\nabla)\,\mathbf{u} \quad = \quad -\frac{\nabla P}{\rho_0} \quad + \quad \nu\nabla^2\mathbf{u} \tag{1.77}$$

Where ν is the kinematic viscosity of the fluid ($\nu \approx v_{th}\lambda_{mfp}$) and $\nu\nabla^2\boldsymbol{u}$ is the term associated with the viscosity force. The importance of viscosity can be quantified by the Reynolds number,

$$R \quad = \quad \frac{VL}{\nu} \tag{1.78}$$

Where V is fluid velocity and L is the characteristic length scale for the variation in V. The Reynolds number is a measure of the ratio of the inertia ($(\mathbf{V}.\nabla)\,\mathbf{V} \approx V^2/L$) of a fluid to its viscosity force ($\approx \nu V/L^2$). Thus, if $V \gg v_{th}$, for the fluid equation of motion to hold then $\lambda_{mfp} \ll L$ and the Reynolds number must be much greater than unity.

If mechanical energy in injected into a fluid at large scales L, then differential motions create shear and eddies; however, the injected energy can not dissipate, as $R \gg 1$ makes viscosity negligible at scale L (Meyer-Vernet, 2007, and references within). The energy can only dissipate at scales so small that the viscosity becomes efficient. At this limiting scale l_d, and given the velocity difference v_d (i.e. the difference in speed between two points separated by l_d), the inertial term $(\mathbf{u}.\nabla)\mathbf{u}$ is approximately v_d^2/l_d and the viscous force is approximately $\nu v_d/l_d^2$. Thus, as viscosity becomes efficient when the latter dominates,

$$l_d \quad \approx \quad \frac{\nu}{v_d} \tag{1.79}$$

The energy injected at scale L cannot dissipate except at scales smaller than l_d where viscous effects become significant (Meyer-Vernet, 2007, and references within). Hence, this energy is transferred via non-linear interactions to smaller and smaller scales, the so-called energy 'cascade'. The range of scales between L and l_d is known as the inertial range and the system can be described by the Euler equations (a more general form of Navier-Stokes equations of fluid dynamics that neglect the

effects of the viscosity). The solution to these equations is scale-invariant and, for a steady, homogeneous and isotropic flow, the relation between l and the velocity difference v_l across an eddy of size l can be determined.

Consider the energy that cascades though an eddy per unit time per unit mass, ε. Energy conservation implies that ε is the rate of energy injection at large scales, the rate of energy cascading though the inertial range and the rate of energy dissipating at small scales. Using dimensional analysis it can be seen that energy per unit mass $\sim v_l^2$ is transferred during time $\sim l/v_l$, yielding $\varepsilon \sim v_l^2/(l/v_l)$. Thus the velocity fluctuation at scale l varies as,

$$v_l \quad \sim \quad (l\varepsilon)^{1/3} \tag{1.80}$$

or, as ε is scale invariant for $l_d < \mathrm{l} < L$,

$$v_l \quad \propto \quad l^{1/3} \tag{1.81}$$

This is the classical Kolmogorov's law. By the same argument, the moments of order n of the velocity differences v_l at at scale l obey,

$$< v_l^n > \quad \propto \quad (l\varepsilon)^{n/3} \tag{1.82}$$

The distribution of energy fluctuations over spacial scales is generally plotted as as the spectral density of the energy fluctuations as a function of wavenumber $W_k(k)$. Using the same principles as above $W_k(k)$ is given by

$$W_k \quad = \quad k^{-5/3} \tag{1.83}$$

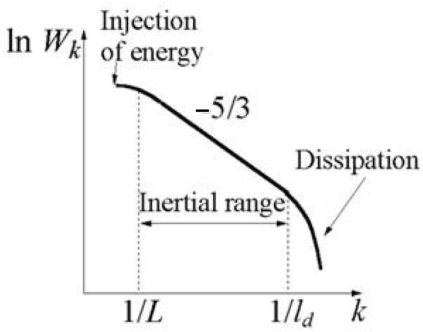

Figure 1.10: Kolmogorov scheme for turbulence (Meyer-Vernet, 2007). The spectral density W_k is plotted as a function of wavenumber k. The energy injection scale is 1/L and energy dissipation occurs after $1/l_d$. Within the inertial range between these two values, energy cascades to smaller and smaller scales.

Chapter 2

Background

2.1 The Solar Wind

The Sun is continuously emitting an enormous quantity of highly-conducting plasma, approximately $10^9 kgs^{-1}$ (Meyer-Vernet, 2007), that flows outwards into space as a result of supersonic expansion of the solar corona. This constant outflow of plasma is called the solar wind. Due to the plasma's high conductivity, the solar magnetic field becomes frozen-in to the plasma and is drawn outwards by the solar wind. This results in the formation of an immense plasma and magnetic field bubble that encompasses the entire solar system and is known as the heliosphere. The environments of all bodies within the solar system are thus shaped by the solar wind, making the study of its heliocentric radial evolution, crucial to our understanding of a wide range multi-scale planetary and interplanetary phenomena.

Traditionally, there are two main approaches to the study of the solar wind: kinetic and hydrodynamic. For the kinetic method, the solar wind is viewed as the evaporation of the hot solar corona into the approximate vacuum of interstellar space. Whereas, for the hydrodynamic method, the solar wind is viewed as a fluid flowing outwards due to the pressure imbalance between the Sun and the interstellar medium. The kinetic description of a plasma takes into consideration the microscopic parameters of individual particles, through the use of statistical distribution functions (see Section 1.6); whereas, the fluid description of a plasma relies on the use of mean macroscopic plasma parameters, such as density, velocity and pressure (see Section 1.5). The hydrodynamic approach also assumes that the plasma is near thermodynamic equilibrium.

2.1.1 Parker's Hydrodynamic Model

Parker (1958) was the first to theoretically demonstrate that the Sun's corona could not be in hydrostatic equilibrium out to large distances and must therefore be continuously expanding. Based on this conclusion, Parker developed a hydrodynamic model for a continuously expanding corona and called it the solar wind. The solar wind assumptions used in this model are as follows:

- Solar wind plasma behaves like an ideal gas.
- Solar wind plasma is isothermal and therefore (using the ideal gas equation of state for a constant temperature) the pressure can be expressed in terms of volume.
- The solar wind flows radially away from the sun.
- The system is spherically symmetric.
- Solar wind mass flux across a spherical surface is constant.
- Electromagnetic forces in solar wind are negligible.
- Changes in the solar wind are slow compared to the solar wind generation time scale.

Using the equations for conservation of mass and momentum, Parker (1958) derived the following equation of motion, which describes how the speed of outflowing plasma changes with distance:

$$\frac{1}{\mathbf{v}}\frac{d\mathbf{v}}{dr}\left(\mathbf{v}^2 - \frac{2k_BT}{m}\right) = \frac{4k_BT}{mr} - \frac{GM_s}{r^2} \tag{2.1}$$

Where $\boldsymbol{v}$ is velocity, r is the radial distance from the Sun, T is temperature, k_B is the Boltzmann constant, G is the gravitational constant and M_S is the mass of the Sun. The critical radius (r_c) is the radius at which the outward pressure gradient becomes dominant over the gravitational forces (i.e., when the two terms on the right hand side of Equation 2.1 are equal).

$$r_c = \frac{GM_sm}{4k_BT} \tag{2.2}$$

There are five possible solution classes for the Parker solar wind equation, these are shown in Figure 2.1. It is clear from observation that class 1 and 2 are not viable solutions, in particular, they are confined to small and large radial distances respectively. Class 3 solutions can also be discounted, as they do not satisfy that, in general, plasma velocities near the Sun are subsonic (as observed). Class 4 and 5 solutions both predict subsonic speeds in the inner corona. However, as r tends to infinity, the class 4 solutions result in a finite pressure that is unlikely to balance that of the near-vacuum of interstellar space. Therefore, Parker concluded that the solar wind must behave as described by class 5, in which the solar wind starts subsonically near the Sun before accelerating to supersonic speeds as radial distances increases. This was later confirmed by observation, the solar wind at 1AU is supersonic and has typical speed of approximately 450 km/s.

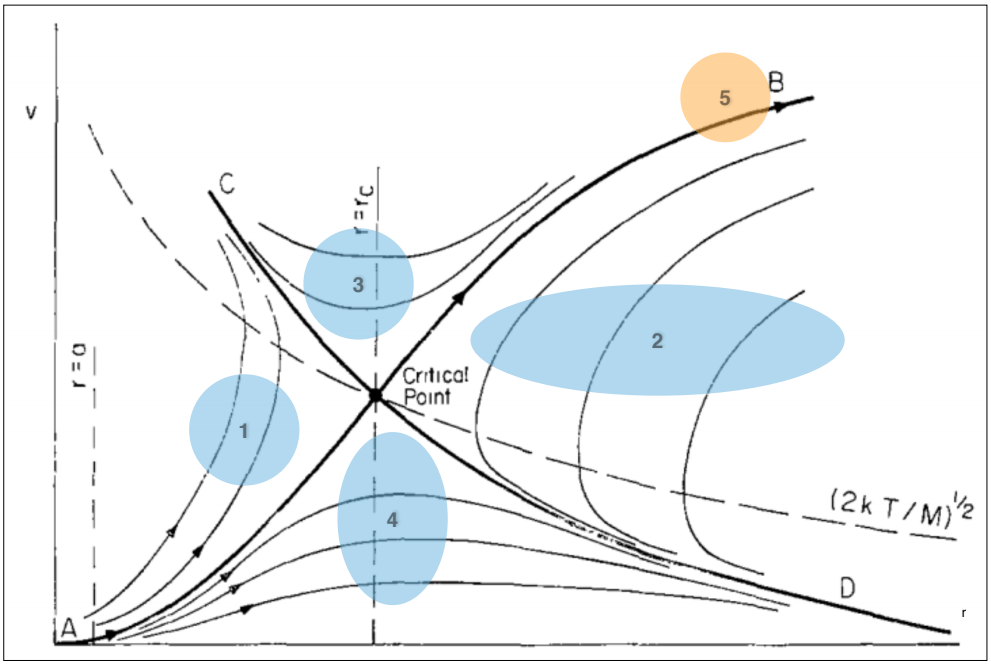

Figure 2.1: Plot of radial distance (r) against solar wind velocity (v) showing the five classes of solution to the Parker solar wind equation (Parker, 1965). The critical point in the centre is the point at which $r = r_c$ and v = sound speed ($v_c^2 = \gamma k_B T/m$). In other words, the critical point is where outward pressure becomes dominant over gravitational forces and the solar wind velocity becomes supersonic.

2.1.2 Exospheric Model of Solar Wind Electrons

The exospheric model is a kinetic model of the solar wind plasma. It was originally proposed by Chamberlain (1960), who claimed that beyond a heliospheric distance of $\sim$ 2.5 solar radii, the solar corona becomes collisionless. This collisionless region then expands outwards into interplanetary space, encompassing the entire solar system, and is referred to as the exosphere. The evolution of particle distributions beyond the base of the exosphere are thus determined only by conservative electric and magnetic fields (Lemons and Feldman, 1983). Primarily, the interplanetary electrostatic potential, which keeps the solar wind plasma approximately charge neutral, and solar magnetic field (or IMF).

In order for an electron to progress past the base of the exosphere it must have sufficient velocity (energy) to escape the electrostatic and gravitational potentials of the Sun. As these energetic solar wind electrons travel radially outwards from the base of the exosphere, they are subject to a gradually decreasing solar magnetic field strength and electrostatic potential. The rate of decrease in field strength is gradual compared to the gyrofrequencies of most particles and so the particle magnetic moment and particle energy can be considered to be conserved. In fact, the relative rate of decrease in field strength and electrostatic potential implies that particle kinetic energy is transferred from velocity perpendicular to the magnetic field to velocity parallel to the magnetic field, faster than the parallel kinetic energy decreases (as energy is transferred from kinetic to potential). Therefore, particle pitch angles are reduced and the exospheric model predicts the development of anisotropic (with $T_{\parallel} > T_{\perp}$) suprathermal particle velocity distribution functions (Lemons and Feldman, 1983).

2.1.3 The Interplanetary Magnetic Field

Thus large scale structure and dynamics of the IMF are governed by solar wind flow, which in turn has its origins in the solar corona. The solar corona is a highly conductive, magnetically dominated plasma and coronal dynamics are dominated by coronal magnetic field motions (which are themselves driven by plasma motions in the photosphere). Temperature is observed to increase with height in the corona, eventually reaching $\sim$ 1-2 million K, see Figure 2.2. Within a few solar radii the

corona is heated to the extent that the plasma flow momentum is comparable to magnetic pressure, resulting in pressure driven supersonic expansion of the corona outwards into space – solar wind outflow.

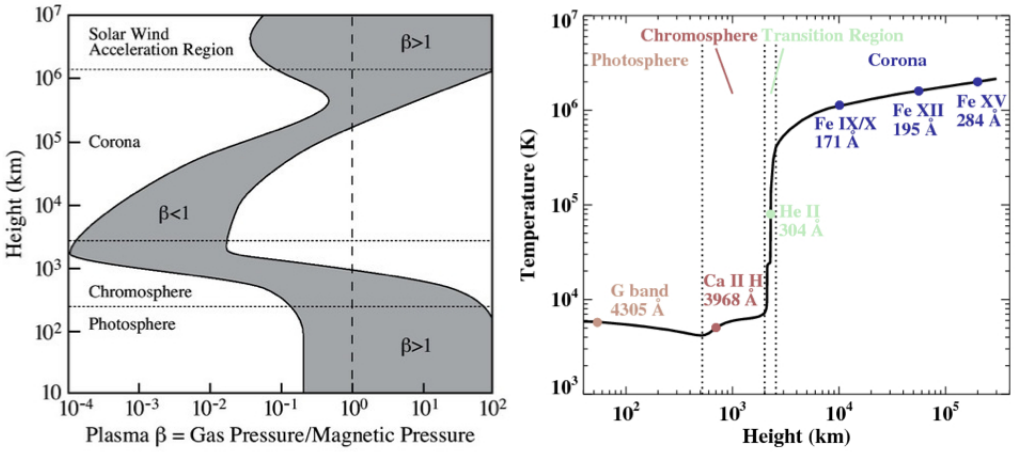

Figure 2.2: (left) Modelled plasma beta as a function of height though different solar regions (Gary, 2001). In the lower corona, magnetic pressure dominates over the plasma pressure, but as height increases the plasma effects begin to dominate over the magnetic effects. (right) Variation of the temperature versus the height for different solar regions (Yang et al., 2009). The temperature can be see to increase rapidly in the transition region between the solar chromosphere and corona, and then continue to increase within the corona.

It should be noted that the exact nature process or processes that heat the corona and accelerate the solar wind remain under debate, with likely candidates generally taking the form of MHD wave/turbulence models or magnetic reconnection models (e.g., Cranmer, 2008; McComas et al., 2007). The former relies on damping of fluctuations driven by jostling of magnetic flux tubes to transform mechanical energy into magnetic and thermal energy. The latter relies on reconnection to supply impulsive bursts of mass, momentum, and energy. It is likely that there are different coronal heating mechanisms governing the active regions, closed loops and the open field lines present on the Sun. These heating mechanisms are inherently intertwined with the possible formation mechanisms related to the origins of fast and slow solar wind streams (see Section 2.1.4).

As temperature increases with height in the corona, so too does the ratio of plasma pressure to magnetic pressure and hence, the plasma effects begin dominate over the magnetic ones, see Figure 2.2. The solar wind is thus subject to the frozen-in effect and drags the coronal magnetic field out into the solar system to form the

IMF. The global geometry of IMF can be understood by considering a steady-state solar wind with a constant radial outflow that is independent of radial and latitudinal distance. The footpoints of the magnetic field lines can be assumed to be fixed in the photosphere and therefore rotate with the surface of the Sun. The result is that the large scale IMF forms an Archimedean spiral, as originally predicted by Parker and thus known as the Parker spiral, see Figure 2.3.

In a constant solar wind flow, the radial component of the interplanetary magnetic field (B_R) must fall off as the inverse square of heliocentric radial distance R due to conservation of magnetic flux (Owens and Forsyth, 2013). For a spherical polar coordinate system B_R is given by:

$$B_R(R,\theta,\phi) = B_R(R_0,\theta,\phi_0)\left(\frac{R_0}{R}\right)^2 \tag{2.3}$$

Where θ is colatitude and ϕ is footpoint longitude on a solar wind source surface at distance R_0 from the centre of the Sun. In the frame of reference co-rotating with the Sun, the plasma stream and the frozen-in field line coincide and thus,

$$\frac{B_\phi(R,\theta,\phi)}{B_R(R,\theta,\phi)} = \frac{V_\phi}{V_\theta} = \frac{-\Omega R sin\theta}{v_R} \tag{2.4}$$

where V_R is the radial component of the solar wind speed and V_ϕ is the azimuthal component of the solar wind speed due to the frame of reference rotating at an angular speed equal to the solar rotation speed Ω (Owens and Forsyth, 2013). The $sin\theta$ term accounts for the decreasing speed of foot point co-rotation with latitude from equator to pole. The assumption of exactly radial solar wind flow gives

$$B_\theta(R,\theta,\phi) = 0 \tag{2.5}$$

Equations 2.3 and 2.4 yield

$$B_\phi(R,\theta,\phi) = -B_R(R_0,\theta,\phi_0)\frac{\Omega R sin\theta}{v_R} \tag{2.6}$$

From which it is clear that the azimuthal component of the magnetic field falls off as $1/R$. These equations show that the field lines gradually become less tightly wound with latitude and that a field line at the Sun's rotational pole should be purely radial.

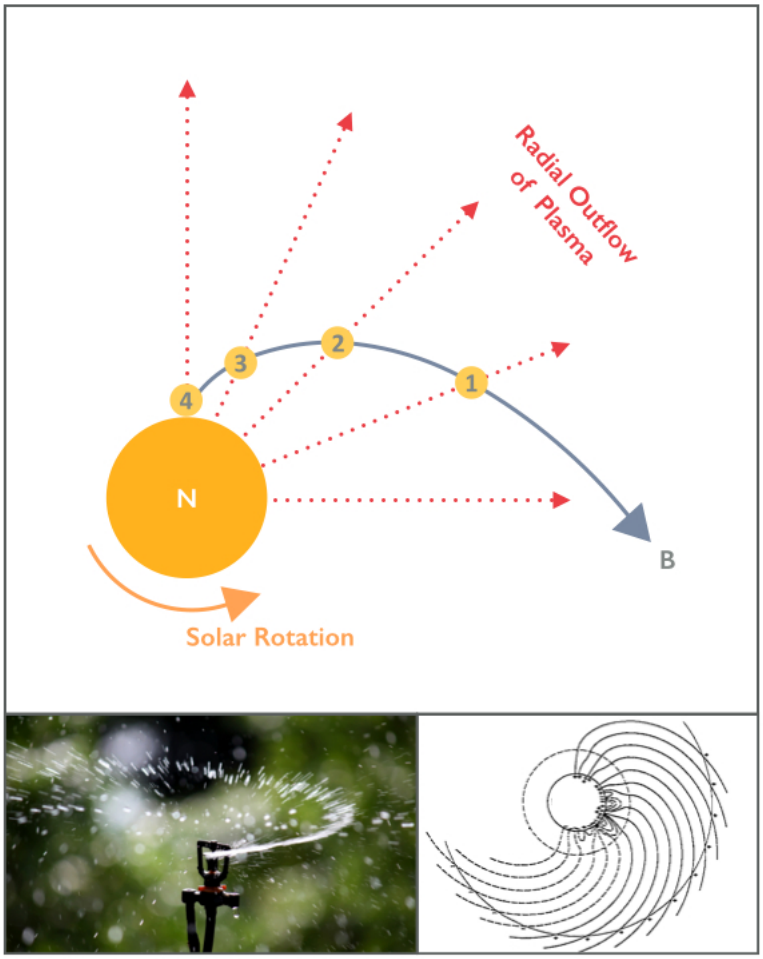

Figure 2.3: Illustration of the formation of a Parker spiral magnetic field line (top). The large yellow circle represents the Sun, viewed from above its north pole. Solar rotation is in the anticlockwise direction. Radial outflow of solar wind plasma for a quadrant of the Sun is represented by the red dashed arrows. 'Parcels' of solar wind plasma which departed the solar surface at times 1, 2, 3 and 4, are represented by the yellow circles and numbered by the order of release. These parcels originate from the same solar source region and are thus frozen-in to the same magnetic field line, represented by the grey line labelled B. The radial flow of plasma in conjunction with a rotating source region and frozen-in flow (see Section 1.5.1) results in a interplanetary magnetic field with spiral geometry. A section of this geometry is shown in the top down view of a Parker spiral field in the ecliptic (lower right). The outer dashed line shows the location of Earth's orbit at ∼1 AU, the inner dashed line represents the source surface at ~ 2.5 R_s. The effect is very similar to the Archimedean spiral that is produced by water droplets dispersed radially by a rotating lawn sprinkler (lower left).

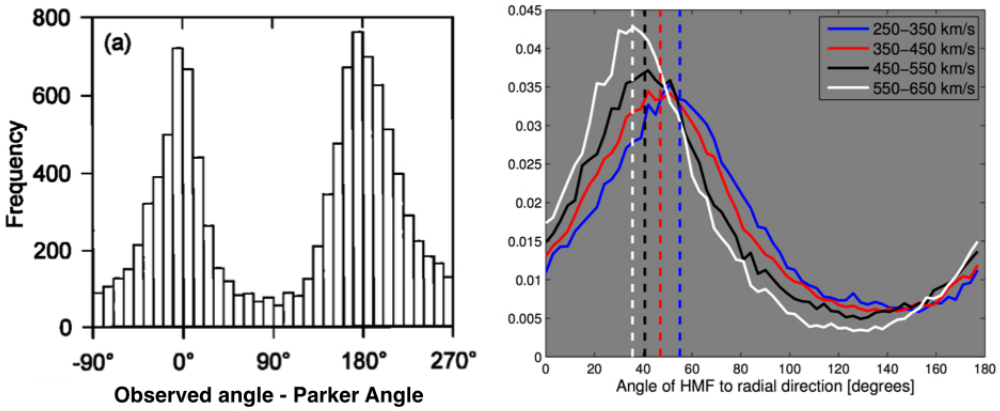

Figure 2.4: (Right) Histograms of the deviation in observed azimuth angle from the expected Parker model magnetic field direction for the in-ecliptic cruise phase of the Ulysses mission, binned into 10° intervals (Forsyth et al., 1996a). (Left) Probability distribution functions of heliospheric magnetic field angles to the radial direction for different solar wind speed intervals. The solid curves show hourly OMNI observations of the near-Earth IMF, covering the period 1965 to 2012. Vertical dashed lines show the equivalent ideal Parker spiral angles for the centre of the speed bins (Owens and Forsyth, 2013).

These equations also show that the IMF spiral angle becomes more tightly wound, tending to 90° at large radial distances. Figure 2.4 shows the probability distribution functions of IMF angle calculated from in-ecliptic observations of the IMF and compared to their equivalent ideal Parker spiral values. Figure 2.4 illustrates that in general, observations are in good agreement with Parker theory but also that there is large variability in the IMF direction. It has also been shown that the Parker model is a good approximation for the large scale IMF both at larger heliospheric distances and out of the ecliptic (e.g, Thomas and Smith, 1980; Burlaga and Ness, 1993; Forsyth et al., 2002).

2.1.4 Fast and Slow Solar Wind

The observed solar wind and associated IMF are at their most simplistic during the minimum of the solar activity cycle when the solar magnetic field is closest to dipolar, see Figure 2.5. Generally there are considered to be three basic types of solar wind: fast, slow and ejecta. The fast solar wind (~ 750 kms^{-1}) flows outwards from regions of open magnetic field lines called coronal holes and fills most of the heliosphere. The slow solar wind ($<$400 kms^{-1}) originates from the closed-field or streamer belt region of the Sun and is typically observed to have $\sim 20^{\circ}$ latitudinal width. Solar Ejecta, also referred to as interplanetary coronal mass ejections are huge bubble-like eruptions of solar plasma and magnetic field that travel though the interplanetary medium at speeds ranging from $<$250 kms^{-1} to $\sim$ 3000 kms^{-1}, see Section 2.1.5.

It is agreed that fast solar wind plasma emanates from the interior of coronal holes, however, the precise origin of the slow solar wind plasma, and how it has come to exist on open magnetic field, is an area of active debate. In general, it is thought that slow solar wind plasma originates from either the edge of a coronal hole near a streamer belt, or the interchange reconnection of open magnetic field with closed streamer belt field. The former is known as the expansion factor model, in which it is postulated that the slow wind and fast wind share the same origins. The heating and acceleration of the slow wind occurs on open flux tubes near the streamer belt boundary, where flux tubes are expected to expand much faster than flux tubes in the central regions of a coronal hole – so-called super radial expansion (Kepko et al., 2016, and references within). The latter is called the interchange model, this postulates that the slow wind plasma source is within the closed field regions of the corona. A process of continuous interchange reconnection is theorized to result in open flux diffusing throughout the closed field region, resulting in the release of closed field plasma into the heliosphere (Kepko et al., 2016, and references within). There is also an intermediate possibility known as the S-Web model (Antiochos et al., 2011), in which closed field plasma is released onto open field lines in a manner similar to an interchange model but only in a limited region about a highly complex boundary between open and closed magnetic flux.

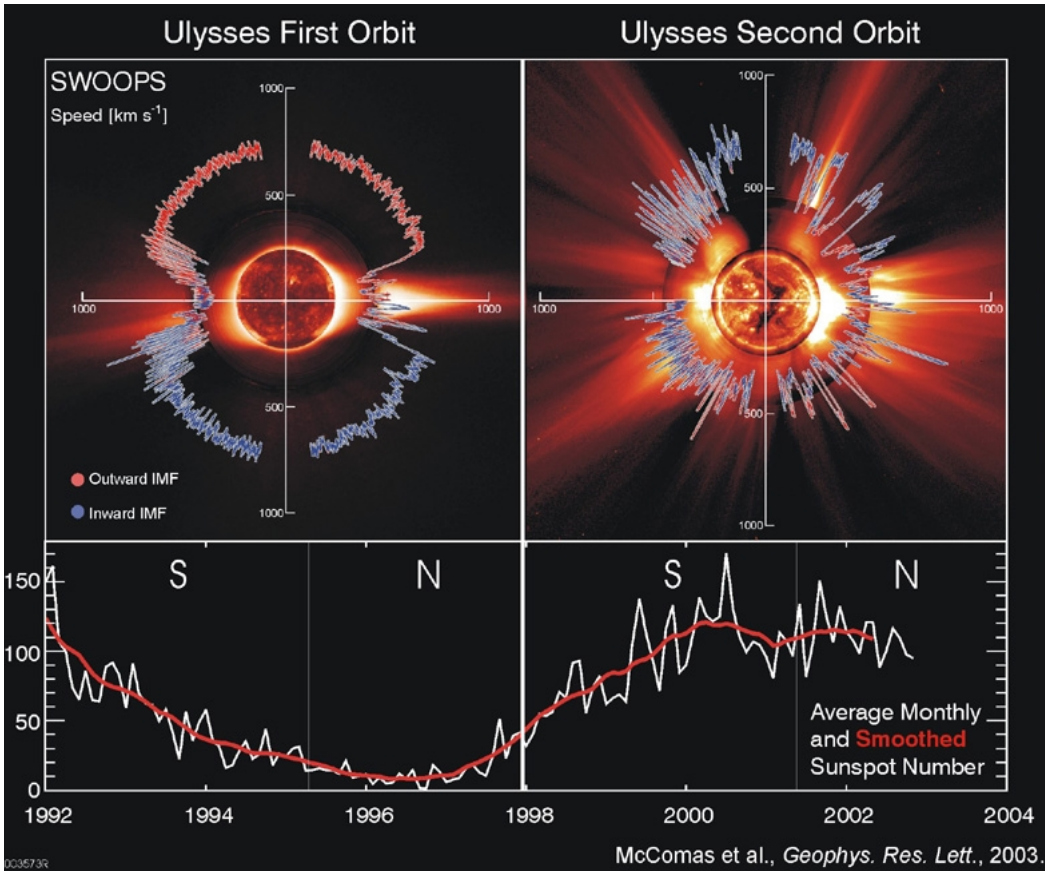

Figure 2.5: Polar plots of solar wind speed as a function of latitude for the Ulysses spacecraft's first two orbits from McComas et al. (2003). The solar wind speed data was obtained using the Solar Wind Observations Over the Poles of the Sun (SWOOPS) instrument observations. The solar wind velocity plots are coloured red or blue for observations of outward or inward directed IMF respectively. The bottom panel shows the sunspot number over the 11 year period in which this data was obtained. The first orbit took place during the declining phase and then minimum of the solar cycle, while the second orbit spanned solar maximum. The solar wind velocity for the first orbit is plotted over solar images characteristic of solar minimum (17 August 1996). The solar wind velocity for the second orbit is plotted over solar images characteristic of solar maximum (7 December 2000). The solar images are composites of (from the center out): a full disk image of the solar corona taken with the Solar and Heliospheric Observatory (SoHO) Extreme ultraviolet Imaging Telescope (EIT, Fe XII at 195 Å); an occulted image of the solar corona from 1.05 to 1.5 solar radii taken by the Mauna Loa K-coronameter (700 to 950 nm), and an occulted image of the solar corona from 1.5 to 6.0 solar radii taken by the SoHO C2 Large Angle Spectrometric Coronagraph (LASCO, white light).

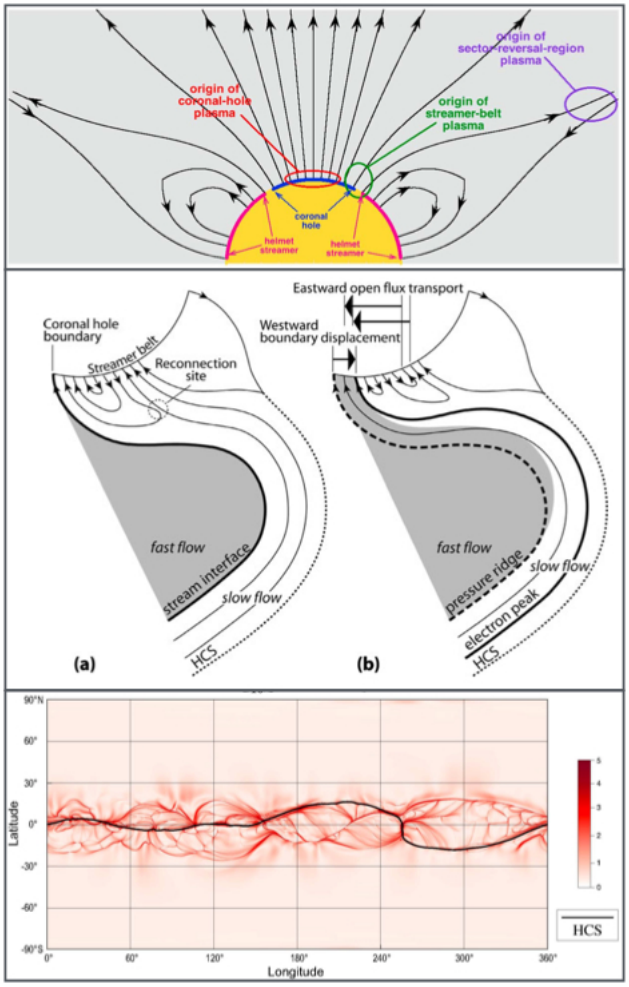

Figure 2.6: (top) An illustration of the Sun (yellow) with a coronal hole surrounded by two helmet streamers (pink labels) from a study of solar wind categorization (Xu and Borovsky, 2015). An additional type of solar wind known as sector-reversal-region plasma or strahl-confusion-zones is proposed. The source locations of three types solar wind of plasma are indicated with the circles: coronal-hole-origin plasma (red), sector-reversal-region plasma (purple), and streamer-belt-origin plasma (green). The streamer belt plasma may come from the edge of the coronal hole near the streamer belt and/or interchange reconnection between open flux and the closed loops of the streamer belt. (middle) Illustration of interchange reconnection of open solar flux with closed solar flux (Crooker and Owens, 2012). Associated phenomena that can be observed in-situ are labelled, including the heliospheric current sheet (HCS). (bottom) Complex structure in Q (colour bar) in the vicinity of the HCS (thick black line) produced by the S-web model (Antiochos et al., 2011). Q, also known as the squashing factor, is a measure of distortion in the magnetic field. The plot of Q in terms of solar latitude and longitude is essentially a map of magnetic separatrices over which reconnection can occur (Antiochos et al., 2011).

2.1.5 The Heliospheic Current Sheet, Corotating Interaction Regions and Coronal Mass Ejections

As described in Section 2.1.4, near solar minimum the Sun's magnetic field can be approximated by a simple dipole. The Heliospheric current sheet (HCS) is formed by open solar flux of opposite polarity from the northern and southern solar hemispheres coming into contact via non-radial expansion (Owens and Forsyth, 2013). The magnetic axis of the Sun is offset from the solar rotation axis and so the current sheet rotates with the Sun, resulting in a HCS with a warped structure often described as a ballerina skirt. In reality, the current sheet is subject to localised warps that result in the observed structure of the HCS being more complex. In addition, as solar activity approaches maximum, the magnetic structure of the Sun increasingly deviates from the simple bipolar structure and the HCS becomes warped further. The HCS maps to the streamer belt region of the Sun and is typically located within slow solar wind.

Inclination of the solar magnetic axis relative to its rotation axis, in addition to warps in the streamer belt, combined with rotating solar wind sources, produces fast and slow solar wind that enter the heliosphere successively at a fixed longitude. Any fast solar wind will catch up with the slow solar wind ahead of it at the same longitude. The region of solar wind compression and deflection brought about by this interaction is referred to as a stream interaction region (SIR), also called corotating interaction regions as SIRs will corotate with the Sun (Owens and Forsyth, 2013). Figure 2.7 shows an illustration of an interface between slow and fast streams, in which a compression and rarefaction regions are observed ahead and behind the stream interface (SI) respectively, and solar wind flow is deflected. The fast wind is deflected in the direction counter to the solar rotation direction and poleward with respect to the heliographic equator. In contrast, the slow wind is deflected along the solar rotation direction and equatorward.

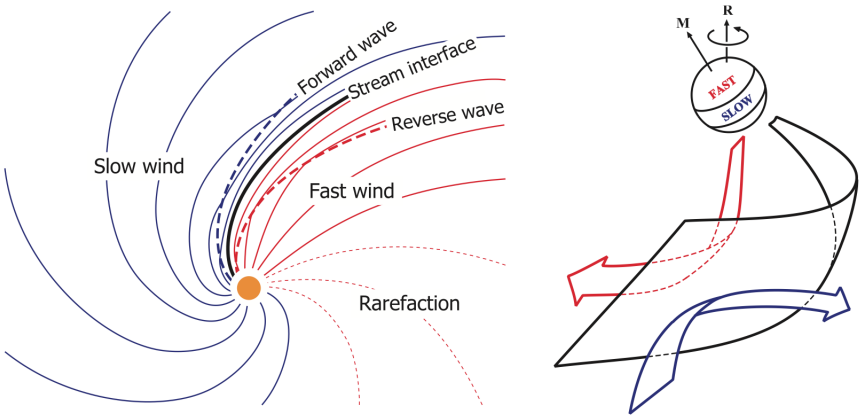

Figure 2.7: Illustration of a stream interaction region adapted by Owens and Forsyth (2013) from Pizzo (1991). (right) View from the perspective of Earth. The solar magnetic axis (M), and therefore the wind speed streams, are inclined relative to the rotation axis (R). The point at which fast wind is able to catch up to the slow wind ahead of it forms a spiral front in the heliosphere called the SI shown as the black-outlined curved surface. In the frame of reference of the SI, both fast and slow wind flow toward the SI. Fast wind (red arrow), is slowed and deflected along the SI in the direction counter to solar rotation. Slow (blue arrow) is accelerated and deflected along the SI in the direction along the solar rotation direction. (left) Looking down on the ecliptic plane. Magnetic field lines within fast (red) and slow (blue) solar wind become aligned with the SI by the reverse (forward) wave. Behind the compressed interaction region, at the trailing end of the high-speed stream, the fast solar wind runs away from the slow solar wind behind it, creating a rarefaction region in which the magnetic field intensity and plasma density are reduced, and the solar wind speed monotonically declines.

As described in Section 2.1.4 coronal mass ejections (CMEs) are huge eruptions of plasma and magnetic field that expand outwards into interplanetary space to become interplanetary coronal mass ejections (ICMEs). CME release frequently involves magnetic reconnection and is often spatially and temporally collocated with solar flares, however the nature of their relation and initiation mechanisms are much debated. As a CME moves upwards through the solar corona and outwards into the heliosphere, it will be accelerated or decelerated towards the ambient solar wind speed depending on its own initial velocity (e.g., Gopalswamy et al., 2000). ICMEs produce the largest deviations from the Parker spiral magnetic field and there are a number of plasma, magnetic field, compositional and charge-state signatures used to identify them. One such signature is lower density and pressure than the bulk solar wind, suggesting ICMEs undergo greater expansion (e.g., Cane and Richardson, 2003). Another form of identification applies to a subset of CME known as mag-

netic clouds, in which a smooth rotation in the magnetic field direction is observed, and is often interpreted and modelled as a magnetic flux rope (e.g., Burlaga, 1988).

2.1.6 Shocks

Due to the supersonic, super-Alfvénic velocity of the solar wind, it is subject to shocking when it encounters an obstacle. In particular, a shock may develop if the flow velocity exceeds the magnetosonic speed (c_{ms}):

$$c_{ms}^2 = c_s^2 + v_A^2 \tag{2.7}$$

Where c_s is the sound velocity ($c_s = \gamma k_B T / m_i$) and v_A^2 is the Alfvén speed. Whenever the fluid velocity exceeds this speed and the flow is distorted due to an obstacle, a shock front will develop across which fluid quantities jump discontinuously and the flow speed will be slowed to a sub-magnetosonic flow. In very simple terms, shocks are essentially non-linear waves, where parameters such as plasma density, plasma temperature, magnetic field strength and flow velocity change abruptly. There are many different types of shock within the heliosphere, including but not limited to those resulting from planetary magnetospheres, CMEs and SIRs, see Figure 2.8. It also should be noted that interplanetary shocks can be an important source of particles acceleration.

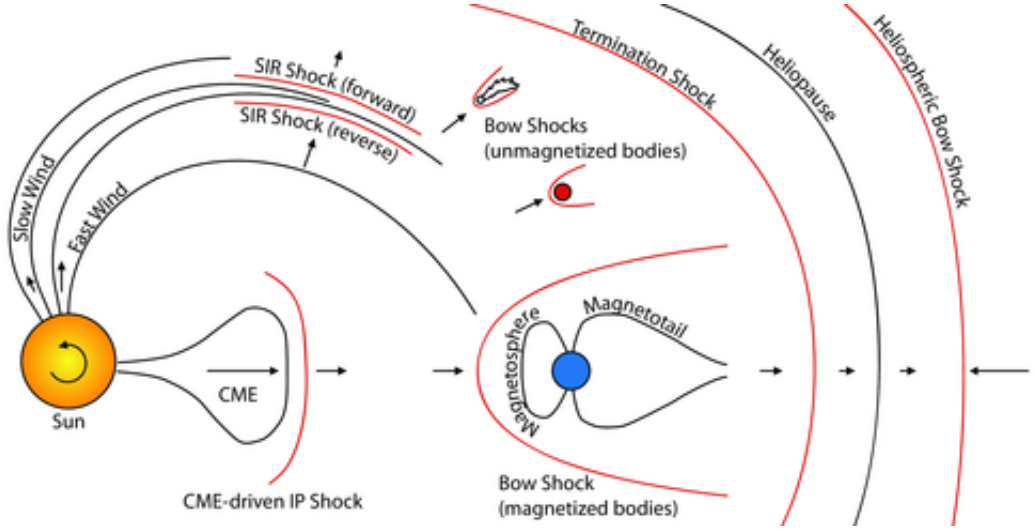

Figure 2.8: Illustration of regions in the heliosphere at which shocks can form. Image Credit: Marc Pulupa

2.1.7 Small Scale IMF Features

In addition to large-scale (global) IMF features, there are also fluctuations in the local IMF at all observable time scales. These spatial and temporal variations are likely due to a combination of waves, shocks and turbulence. There are a large number of wave modes present in the solar wind, some of which are discussed in Section 1.7, many of which directly preturb the magnetic field. For example, the fast solar wind is dominated by Alfvénic fluctuations flowing in the anti-sunward direction in the plasma frame (e.g., Horbury et al., 1995). The solar wind is also highly turbulent, adding a further spectrum of magnetic fluctuations to the mix (Bruno and Carbone, 2013). It is also likely that magnetic structures formed in the solar corona are convected outwards with the solar wind, forming a spaghetti-like, intertwined flux-tube substructure within the solar wind where large discontinuities are boundaries between coherent flux tubes (e.g., Borovsky, 2008). If this is the case then, it is also likely that each of these flux tubes contains its own distinct plasma population (see Section 1.5.1). Figure 2.9 shows an illustration of the two completing, or possibly complementary, turbulent and flux tube substructure theories and their possible associated mechanisms for coronal heating.

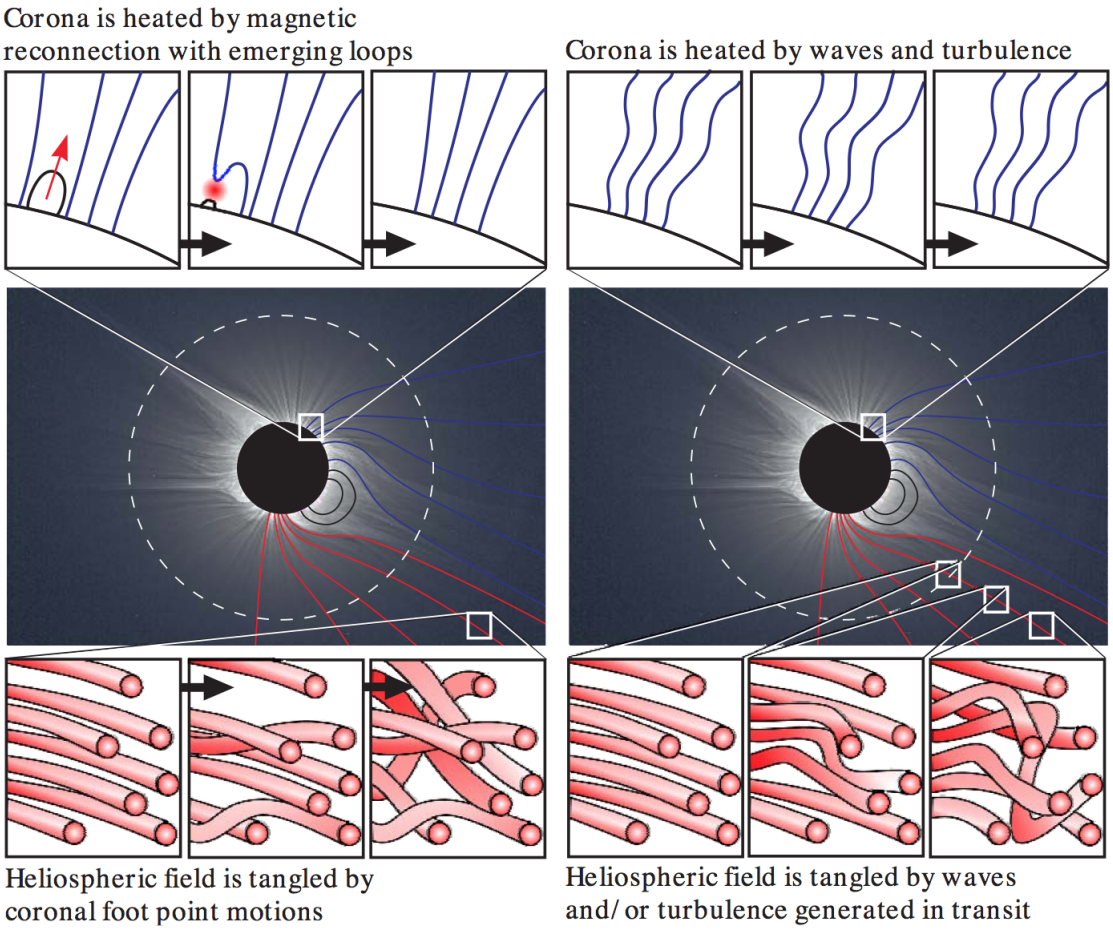

Figure 2.9: Illustration showing two possible mechanisms for coronal heating and subsequent heliospheric magnetic field braiding. (left) Coronal heating is due to reconnection between open solar flux and closed loops emerging through the photosphere. In this model, the IMF is likely to become tangled due to foot point motions. (right) Coronal heating is due to waves or turbulence. In this model, the IMF can then become tangled by turbulent motions, either propagating directly from the corona or generated in transit (Owens et al., 2011).

2.1.8 Turbulence in the Solar Wind

The application of the basic concepts of turbulent theory (Section 1.8) to the solar wind is not a simple task, as solar wind plasma differs from that of an ideal turbulent fluid in a number of different ways (Meyer-Vernet, 2007, and references within). The solar wind has a viscosity which gives a Reynolds number that is not vary large and thus, dissipation is expected to be driven by waves and instabilities rather than by fluid viscosity. In addition, itermittency is observed to be greater than for ordinary fluid turbulence and takes the form of current sheets as opposed to filamentary vortices as in fluid turbulence. Finally, the solar wind is a magnetised plasma which introduces anisotropy and the presence of a magnetic field also introduces additional forces, so that the turbulent 'eddies' in the solar wind take the form of MHD waves (generally Alfvén waves, as the others are typically damped).

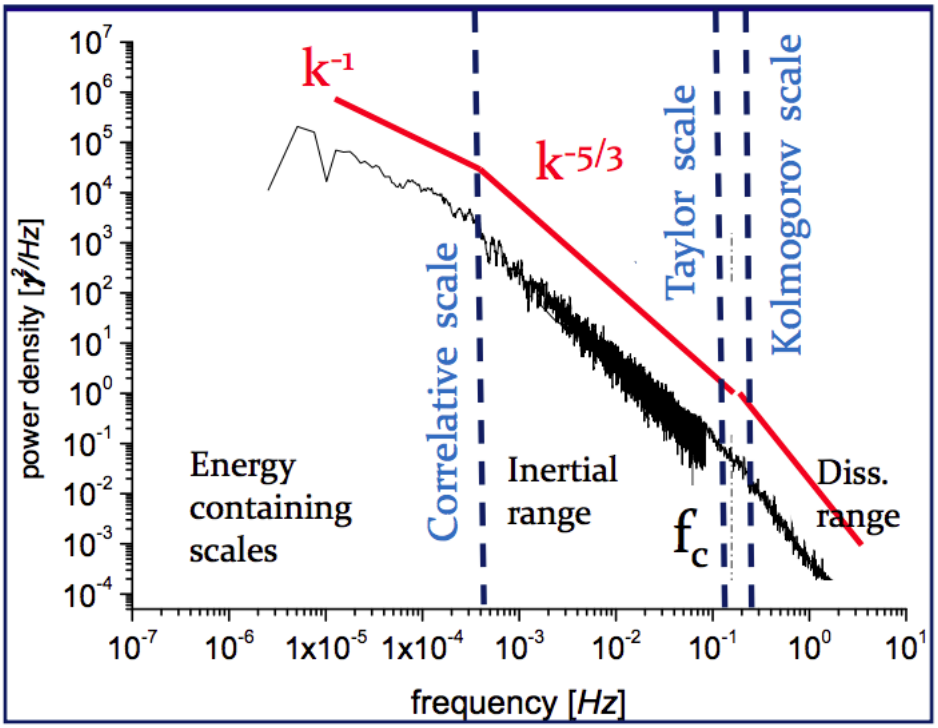

Figure 2.10: Typical interplanetary magnetic field power spectrum at 1 AU (Bruno and Carbone, 2013, and references within). Vertical dashed lines represent the correlation (or inertial) length, the Taylor scale and the Kolmogorov scale. The correlation length is the upper limit for the inertial range or the largest septation distance over which eddies are still correlated, i.e., the largest turbulent eddy size. The Taylor scale is the point at which at which viscous dissipation begins to take effect. The Kolmogorov scale is the point at which the transition from the inertial range to the dissipation range occurs.

Solar wind observations have revealed that the turbulent state, and its radial evolution during solar wind expansion, differs significantly between the slow and fast winds. This difference is likely, at least in part, to be related to the different origins, and thus different different macrostructure, of the slow and fast wind (e.g., Tu and Marsch, 1995a; Goldstein et al., 1995b). One key difference between slow and fast streams is that the fast wind contains more strongly Alfvènic fluctuations i.e., the magnetic field and velocity fluctuations are highly correlated, with $\delta \mathbf{v} \sim \pm \delta \mathbf{B} / \left(\mu_0 \rho\right)^{1/2}$ (Bruno and Carbone, 2013, and references within). Alfvènic fluctuations have also been found to be stronger, and present at increasing lower frequencies, for smaller heliocentric radial distances.

Observations within the ecliptic solar wind have also demonstrated that the spectral index of slow and fast streams are different, see Figure 2.11. The slow wind does not display any radial dependence and can be characterized by a single Kolmogorov-type index. Whereas, the fast wind is characterized by two distinct spectral slopes; the first, a $\sim f^{-1}$ relation at low frequencies and the second, a Kolmogorov-like spectrum at higher frequencies. These two regimes are separated by a knee (or break) in the spectrum which, as the wind expands, moves to lower and lower frequencies. This implies that larger and larger scales become part of the Kolmogorov-like turbulence spectrum, i.e, the inertial range, and that the spectrum of solar wind fluctuations is a function of heliocentric radial distance as well as frequency. Thus observed turbulent evolution is likely influenced by velocity shear, parametric decay (in which large amplitude Alfvén waves are unstable to random field perturbations and decay into two secondary Alfvén modes propagating in opposite directions), and interaction of Alfvénic waves with convected structures (Bruno and Carbone, 2013).

The spectral break has also been observed to move to lower frequencies at greater radial distances within the polar solar wind (e.g., Horbury et al., 1996a). In addition, it was found that the turbulent evolution in the polar wind was slower than that of fast streams in the ecliptic. A key difference between the polar and ecliptic fast wind is that the former has no interactions with slower streams and thus freely flows into interplanetary space. This suggests that, free of co-rotating shear events, the mechanism determining this evolution is an intrinsic property of the turbulence.

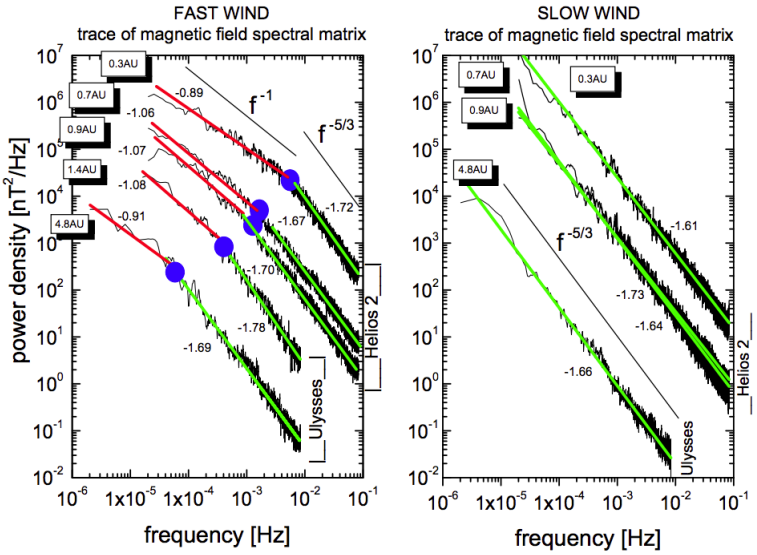

Figure 29: *Left panel:* power density spectra of magnetic field fluctuations observed by Helios 2 between 0.3 and 1 AU within the trailing edge of the same corotating stream shown in Figure 16, during the first mission to the Sun in 1976 and by Ulysses between 1.4 and 4.8 AU during the ecliptic phase. Ulysses observations at 4.8 AU refer to the end of 1991 while observations taken at 1.4 AU refer to the end of August of 2007. While the spectral index of slow wind does not show any radial dependence, the spectral break, clearly present in fast wind and marked by a blue dot, moves to lower and lower frequency as the heliocentric distance increases. Image adapted from Bruno *et al.* (2009).

Figure 2.11: Magnetic field power spectra at different radial distances in the ecliptic plane for slow (right) and fast (left) wind streams (Bruno and Carbone, 2013, and references within). The spectral index of the slow wind does not show any radial dependence. Whereas the spectral breakobserved in the fast wind (marked by blue dots) moves to lower and lower frequency with increasing heliocentric distance.

The solar wind inertial range appears to fit with fluid theory. However, the dissipative behaviour at small scales is very different from that of an ordinary fluid. This is because the solar wind mean free path is so large that the plasma is essentially collisionless and thus viscous dissipation is negligible. In Section 1.7 it was shown that at smaller scales, i.e., the ion gyro-frequency and electron gyro-frequency, the single-fluid MHD approximation breaks down and a more complex description of plasma must be used. In the solar wind, a spectral break at the upper frequency limit of the inertial range is observed close to the ion gyro-scale (see, Figure 2.10), beyond this break the spectrum steepens but the exact nature of the fluctuations beyond this point is much debated.

The region of small scale turbulence beyond this second spectral knee is known as the kinetic turbulence range and it is where dissipation and plasma heating is though to occur. There are two main scenarios for the energy cascade within this

range: dispersion via Whistler-mode waves and dispersion via kinetic Alfvén waves (KAWs). A key difference between the expected spectra of these two forms of turbulence is that whistler turbulence is expected to be steeper than for KAW turbulence (Chen, 2016). A key physical difference between these two forms of turbulence is that KAW turbulence is low frequency, $\omega \ll k_{\perp,i}$, whereas whistler turbulence is high frequency, $\omega \gg k_{\perp,i}$ (Chen, 2016). This means that density fluctuations for KAW turbulence are non-negligible (e.g., Chen et al., 2013b) and it has been shown that, in this case, both the magnetic and density fluctuations within the kinetic range should have the same scaling relation (e.g., Boldyrev et al., 2013). Near-identical scaling relations for magnetic and density fluctuations within the kinetic range have been observed in solar wind turbulence (Chen et al., 2013a). However, the spectral index is also steeper than expected ($\sim k^{-2.8}$ as opposed to $\sim k^{-2.3}$). Modifications to theory, such as including the presence of electron Landau damping (Howes et al., 2012) or the effect of intermittent structures (Boldyrev and Perez, 2012) may explain this difference. However, it should be noted that there have also been observations, , achieved via the very high resolution data provided by the Magnetospheric Multiscale Mission (MMS), of whisltler turbulence at these scales (Narita et al., 2016). Thus the exact nature of turbulence at kinetic scales, and the relative roles of whistler and KAW fluctuations, has yet to be fully resolved. Furthermore, it should be noted that determining the nature of dispersion within this region has significant implications with regard to both solar wind heating (see Section 2.2.2) and the evolution of the strahl (see Section 2.2.6).

2.2 Solar Wind Electrons

Solar wind electrons play a key role in solar wind dynamics; they are responsible for determining the electric field required to maintain zero net charge in the solar wind and for carrying the heat flux conducted into the solar wind from the corona. Solar wind electrons are generally divided three constituent electron populations known as the 'core', 'halo' and 'strahl' (e.g., Feldman et al., 1975; Maksimovic et al., 2005), each of which displays quite different characteristics.

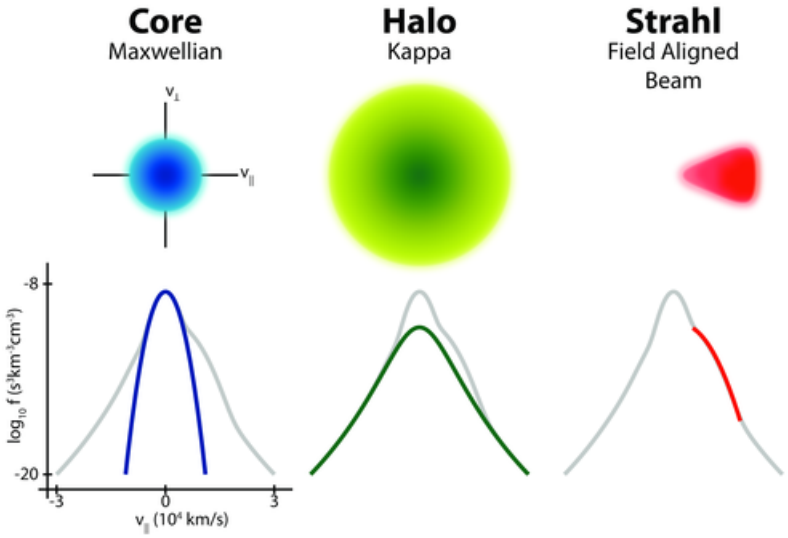

Figure 2.12: Diagram illustrating the different solar wind electrons populations: core, halo, and strahl. Two-dimensional velocity distributions for each population and a cut through in the parallel direction are shown. Image Credit: Marc Pulupa

The distinctions between these three electron populations is clear when their velocity distributions are examined, see Figure 2.12. The core is a thermal population, typically characterized as a bi-Maxwellian, which at $\sim$ 1 AU has a temperature of $\sim 10^5$ K and a temperature anisotropy ($T_{\parallel}/T_{\perp}$) of 1.0-1.5 (Balogh et al., 2001, and references within). It is also the most numerous subset, making up $\sim$95% of the total solar wind electron number density (Maksimovic et al., 2005). The halo population is observed to be a suprathermal tail superposed on the core distribution, typically characterised as a bi-Maxwellian or a kappa distribution, and is faster, higher temperature and lower density than the core (e.g., Feldman et al., 1975). Both the core and the halo drift with respect to the solar wind frame, with $N_{halo}V_{halo} + N_{core}V_{core} = 0$ to maintain zero current and with the $\boldsymbol{V}_{halo} - \boldsymbol{V}_{core}$ vector aligned with the magnetic field direction (Balogh et al., 2001, and references

within). The core and halo often display anisotropies but they are typically present at all pitch-angles and can be considered relatively isotropic when compared to the final population - strahl. This subset of solar wind electrons is a strongly field-aligned beam which is observed to be a bump on the suprathermal tail of the velocity distribution in the parallel or anti-parallel magnetic field direction.

Strahl electrons travel in the anti-sunward direction, along the IMF at high velocities relative to the bulk plasma flow (e.g. Feldman et al., 1978; Pilipp et al., 1987a). Strahl are typically observed in either the parallel or anti-parallel magnetic field direction, depending on the IMF polarity (e.g., Feldman et al., 1978; Pilipp et al., 1987a). However, certain IMF topologies can result in bi-directional strahl, in which electron beams are observed in both the parallel and anti-parallel magnetic field direction simultaneously (e.g., Gosling et al., 1987). It is also possible to observe local sunward strahl due to folded IMF topologies where the field reverses on itself and hence, so to does the strahl flowing along the field (e.g., Owens and Forsyth, 2013, and references within). Finally, it should be noted that there are also times when no clear strahl population is observed in the solar wind (e.g., Anderson et al., 2012), particularly during observations in the slow solar wind (e.g., Gurgiolo and Goldstein, 2017).

2.2.1 Origin of Surathermal Electrons

The current consensus regarding the formation of suprathermal solar wind electrons is that they likely originate in the solar corona (e.g. Viñas et al., 2000; Stverak et al., 2008; Che and Goldstein, 2014). However, there are a number of different mechanisms that can be invoked to explain the generation of election populations and their existence within the solar wind. Hence, a firm agreement on their origin has yet to be reached.

With regard to strahl, it is generally accepted that this population is formed by electrons with sufficient energy to escape the electrostatic potential of the Sun (Pierrard et al., 2001). Once beyond the potential well, the electron collision frequency is reduced to the extent that both electron energy and magnetic moment are conserved (Hammond et al., 1996). Magnetic field strength decreases with distance from the Sun. Hence, as the electrons travel outwards, they experience strong adia-

batic focussing, resulting in the formation of a highly field-aligned electron population (Owens and Forsyth, 2013). In fact, theoretical investigation has demonstrated that, for typical coronal hole conditions, this effect is strong enough to produce a clear strahl signature in the electron distribution function within as little as 10 solar radii (Smith et al., 2012).

With regard to suprathermal electrons in general, it has been found that the suprathermal tails of electron velocity distribution functions can be explained via the velocity filtration model. In this model a pre-existing population of suprathermals in the low corona undergoes velocity filtration in gravitational and electrostatic fields resulting in temperature that increases with height through the solar atmosphere without invoking any local heating source (Scudder, 1992). The velocity filtration model predicts the evolution of the electron velocity distribution function at higher altitudes in the solar wind to form core, halo and strahl like populations, similar to those observed within the solar wind (Viñas et al., 2000). However, this model does not explain how the suprathermals are generated or how they are maintained within the solar wind.

Proposed models for the formation and evolution of electrons within the corona thus frequently invoke a combination of expansion effects, Coulomb collisions and/or wave-particle interactions to explain the formation of a thermal core and a beam-like suprathermal tail (e.g., Pierrard et al., 2001; Vocks et al., 2008; Smith et al., 2012; Landi et al., 2012). The presence of the halo population is then often explained by scattering of suprathermal electrons via further wave-particle interactions within the solar wind or by global reflection in the heliosphere (e.g. Saito and Gary, 2007; Pagel et al., 2007; Smith et al., 2012; Landi et al., 2012; Pavan et al., 2013). However, it has also been shown that it is possible for the halo population to form in the inner corona before subsequent adiabatic focussing results in the formation of a strahl beam (Che and Goldstein, 2014). This process was demonstrated using solar nanoflares as a source for electron acceleration, producing energetic electron beams, which in turn trigger instabilities that generate kinetic Alfvén and whistler wave turbulence and produce a halo population via scattering (Che and Goldstein, 2014). Moreover, it was found that Coloumb collisions were insufficient to thermalise the distribution before the plasma was advected into the solar wind

and thus that the halo feature may be preserved, as long as some form of scattering is present at larger radial distances to counter the effect of adiabatic focussing. It should be noted that all electron evolution models use specific conditions which can be very different. For example the strong magnetic strength gradient presumed for coronal hole wind (as in Smith et al. (2012)) is very unlike the approximations appropriate for the very slow solar wind observed near sector boundaries, where the mean radial magnetic field is near zero (as in Che and Goldstein (2014)).

The solar wind is a weakly collisional plasma. At 1 AU the mean free path is comparable with the typical length scales of the system (Stverak et al., 2008) and electrons should experience negligible Coulomb collisions (e.g. Vocks et al., 2005; Stverak et al., 2008). The magnetic field strength also continues to decrease with distance from the Sun. It thus follows that, in the absence of other influences, the strahl beam should continue to narrow with heliocentric distance, becoming highly collimated within $\sim$ 0.5 AU (Owens et al., 2008), with a beam width $< 1^{\circ}$ by $\sim$ 1 AU (Anderson et al., 2012). Nevertheless, strahl beams observed at 1 AU have pitch angle widths that are often significantly larger than predicted to be due purely to expansion effects and are frequently $> 20^{\circ}$ (e.g., Owens et al., 2008; Anderson et al., 2012). Hence, adiabatic focussing cannot be the sole effect experienced by the suprathermal electrons in the solar wind.

The presence of this broader strahl and the presence of halo electrons at all pitch-angles, implies that suprathermal electrons must be subject to some form of scattering process, or processes, as they travel outwards from the Sun. The negligible collisions experienced by suprathermal electrons suggests that these mechanisms must be some form of wave-particle interaction. This implication is supported by observations of average strahl pitch angle width that continues to increase with heliospheric radial distance beyond 1 AU (Hammond et al., 1996), see Figure 2.14. In addition, it has also been observed that the fractional density of strahl electrons relative to total electron density decreases with heliospheric radial distance, while that of the halo electrons increases (e.g., Maksimovic et al., 2005; Stverak et al., 2009, see also Figure 2.13). This finding implies that not only are strahl electrons indeed subject to some form of in-transit scattering process but also that, eventually, they are likely scattered to form part of the quasi-isotropic halo population. How-

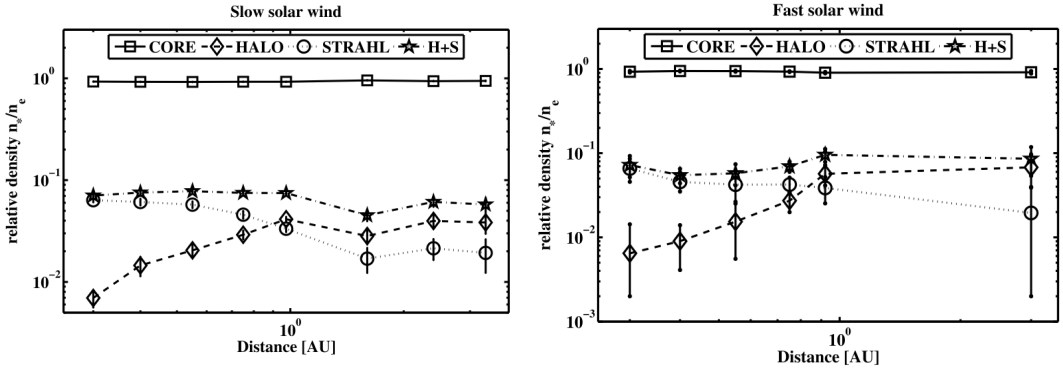

(a) **(b)**

Figure 2.13: Radial evolution of the relative densities of thermal and suprathermal electron populations for (a) slow and (b) fast solar wind observations (Stverak et al., 2009). In both plots, the symbols represents the mean value for the core (squares), halo (diamonds), strahl (circles) and the sum of strahl and halo (stars). Stverak et al. (2009) notes that the sum of suprathermal populations appears to be more variable in the fast solar wind.

ever, it should also be noted that theoretical investigations have demonstrated that there are conditions under which the opposite may be true and strahl is generated by halo electrons. For example, it has been shown that a broad strahl-like feature could be produced by pitch-angle scattering in the solar wind if the halo population has a large enough drift relative to the core (Seough et al., 2015).

Thus, the origins of the both the suprathermal field-aligned strahl and the quasi-isotropic halo remain unclear. In order to better understand the coronal origins of these suprathermal electrons, it is necessary to determine what processes affect the solar wind electrons in-transit.

2.2.2 Radial Evolution of the Core and Halo

Solar wind electron density decreases with heliocentric distance for all electron populations (Stverak et al., 2009). Solar wind electrons are also expected to cool as they travel away from the Sun. Theoretically, for core electrons with purely adiabatic expansion, the temperature should fall off as $R^{4/3}$, whereas for a Coulomb collision dominated plasma, the temperature should fall off as $R^{1/3}$ (Scudder and Olbert, 1979). Observations made of the bulk electron temperature using a number of spacecraft at different heliospheric locations have shown that the actual relationship of temperature with distance is highly variable (between $\sim$ 0.24-1.26) and found significant variation in the properties of solar wind electrons (Balogh et al.,

2001, and references within). Ulysses observations of halo electrons with heliocentric radial distance found that the halo distribution tends towards lower energies with distance. Note that no gap is seen between the core and halo populations (McComas et al., 1992). The so-called breakpoint between these two populations is likely related to the interplanetary electric potential, part of the exospheric model (Section 2.1.2) for solar wind formation. This potential, which accelerates ions and decelerates the more mobile electrons, is a result of the electric field required to keep the net charge of coronal/solar wind plasma neutral. An electron must overcome this potential barrier in order to be accelerated out into interplanetary space and thus the breakpoint between core and halo electrons is a result of the core remaining trapped while the halo electrons are energetic enough to escape. The precise theory and value of the interplanetary potential is still much debated and values calculated using different spacecraft datasets have produced different results. However, Ulysses observations over a wide distance range found that value for the breakpoint energy ($E_B = 7.5 k_B T_{core}$), and its decrease with distance, agree relatively well with the expected value for the basic theory ($E_B = 7 k_B T_{core}$) (McComas et al., 1992).

2.2.3 Heat Flux

The majority of solar wind heat flux (Equation 1.59) is transported by the outflow of suprathermal electrons travelling away from the Sun, into interplanetary space (e.g. Feldman et al., 1975; Scime et al., 1994). This is despite the much lower relative number density of the suprathermal populations ($\sim$ 5% at 1 AU) as compared to the thermal core (Feldman et al., 1975). When a clear strahl beam is observed, the majority of solar wind heat flux is carried by the strahl electrons (Pilipp et al., 1987a); otherwise, the heat flux is carried by the drift of halo electrons relative to the core (Bale et al., 2013). Previous observations at $\sim$ 1 AU have found that the heat flux vector is aligned with the magnetic field direction, as expected theoretically (Feldman et al., 1975; Pilipp et al., 1990). However, the observations of heat flux magnitude, both at 1 AU and for the $\sim$ 0.3-1 AU range observed by the Helios spacecraft, are lower that expected for kinetic models that rely on collisons alone (Pilipp et al., 1990). The solar wind heat flux has also been observed by the Ulysses spacecraft out to $\sim$ 5 AU. It was found that the heat flux drops off with distance

as $\sim R^{-2.9}$, although this value has been found to vary significantly depending on how the data are processed and averaged (Pilipp et al., 1990). For all heliocentric radial distances and latitudes observed by Ulysses, it was found that the heat flux is less than expected for the effects of collisions alone and some process or processes must be acting to limit the heat flux. One such mechanism is the heat flux instability proposed by Gary et al. (1994) which predicts a R^{-3} dependence for the heat flux.

2.2.4 Strahl Evolution in the Solar Wind

In order to separate the effects of in-transit solar wind processing from the original coronal electrons distributions, the evolution of suprathermal electrons with heliospheric radial distance has been examined. As mentioned in Section 2.2.1, it has been found that strahl beam width broadens with heliospheric radial distance from $\sim$ 1 to 2.5 AU (Hammond et al., 1996) and the strahl population has been observed to decrease relative to the halo population with heliospheric distance from $\sim$ 0.3 to 1.5 AU (e.g. Maksimovic et al., 2005; Stverak et al., 2009). These trends indicate that strahl may be scattered to form part of the halo electrons, a theory supported by direct observations of intense strahl scattering events, in which the beam can be seen to form a proto-halo population (Gurgiolo et al., 2012). The cooling down of coronal electrons due to rapid adiabatic expansion into interplanetary space could also be responsible for a decrease in suprathermal electron populations. However, this would effect both the strahl and halo populations at the same time and should also result in an increase in the core population. This is not confirmed by observations, as fractional density of the core population and the sum of the suprathermal populations remain roughly constant with heliocentric distance (see Figure 2.13). Thus, additional processes must be present in the solar wind, to explain strahl scattering and counterbalance the cooling of suprathermals due to expansion. Indications of strahl electrons have also been found as far out as $\sim$ 10 AU by Walsh et al. (2013). It was found that the estimated strahl pitch angle width was narrower than predicted by extrapolation of previous observations from within 2.5 AU and it has been suggested that the rate of scattering may decrease with increasing radial distance. Although, it should be noted that the Walsh et al. (2013) suprathermal electron observations did not cover the full pitch angle range. Hence, it was not possible to fully rule out

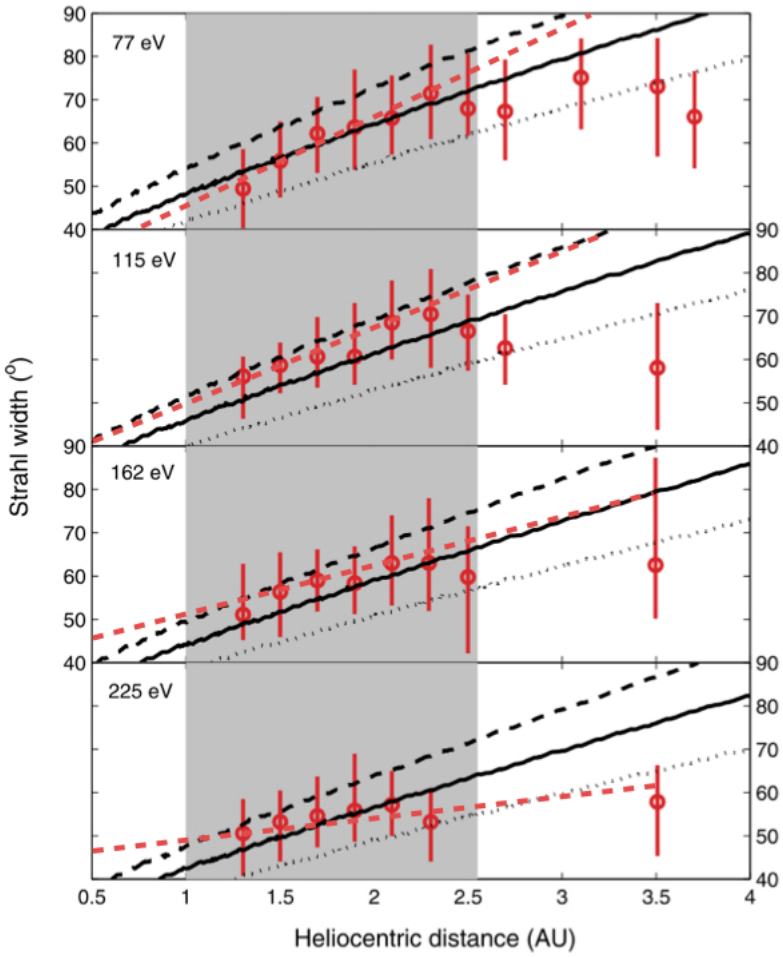

Figure 2.14: Strahl width as a function of heliocentric radial distance for 77, 115, 162 ans 225 eV (Owens et al., 2008). Ulysses observations at different heliocentric distances (adapted from Hammond et al., 1996) are marked by the circles and corresponding error bars. Red dashed lines show the best linear fits to the data. Gray-shaded regions show the range of heliocentric distances at which Hammond et al. (1996) reported that strahl width increases linearly with distance. The solid black lines show the results of the Owens et al. (2008) numerical simulations of electron evolution with pitch-angle scattering to match the 77 eV electron observations. The black dashed and dotted lines represent the results for higher and lower scattering factors respectively. It was found that the scattering rate chosen to for the 77 eV observations matched the majority of the observations within the observational uncertainties, although the modelled gradients of the strahl width-distance relation does not match those observed.

the possibility of the observed electron fluxes being related to an anisotropic halo ($T_{\parallel} > T_{\perp}$) as opposed to a broad strahl beam.

Increase in strahl beam width with heliospheric radial distance has been modelled by Owens et al. (2008), see Figure 2.14. This empirical model assumed a Parker spiral IMF geometry and used an “ad-hoc” pitch-angle scattering rate that

was assumed to be constant with time, distance and electron kinetic energy. The model was constrained by observations of strahl evolution made by Hammond et al. (1996), which were successfully recreated within errors. This model can, to a certain extent, explain the apparent constant increase in strahl width with distance observed out to $\sim$ 2.5 AU. It was found that the geometric effect of a Parker spiral IMF results in adiabatic focussing that dominates closer to the Sun (within $\sim$ 20 R_S) and pitch-angle scattering that becomes more influential at larger heliocentric distances. This is because the Parker spiral IMF becomes less radial at distances further from the Sun and so, for a given unit of time/unit distance along an IMF line, a field-aligned electron further away from the Sun experiences a smaller decrease in magnetic field strength but the same constant scattering rate. This study also suggested that this effect should decrease with increasing helio-latitude, as the Parker IMF becomes less tightly wound for a given radial distance.

2.2.5 Strahl Energy Relations

Previous studies at $\sim$ 1 AU have examined the relationship between strahl width and electron energy to ascertain the nature of the strahl scattering mechanism(s), in particular the role of resonant wave-particle interactions. However, these studies have rendered a number of different, seemingly contradictory, findings, which suggest that there may be multiple scattering mechanisms at play. Strahl beams have been observed to have pitch angle widths that decrease with increasing electron energy (e.g., Feldman et al., 1978; Pilipp et al., 1987a; Fitzenreiter et al., 1998). The opposite relation has also been reported during solar wind intervals with enhanced magnetic field fluctuations (Pagel et al., 2007). In addition, a statistical study completed using 4 years of solar wind data found that, at any given time, it is equally probable for strahl width to increase or decrease with increasing electron energy (Anderson et al., 2012).

The relationship between strahl width broadening per AU and electron energy has also been investigated. For distances beyond 1 AU, it has been shown that the increase in strahl pitch angle width with radial distance is energy dependant and that low energy electrons display greater broadening per AU than higher energies (Hammond et al., 1996). This relationship was also modelled in the Owens et al.

(2008) study (see Section 2.2.4). However, the modelled results displayed a much weaker decease with electron energy than observed by Hammond et al. (1996). The smaller decrease in broadening per AU with electron energy is due to the modelled scattering rate which was chosen to be constant with time, distance and electron kinetic energy. Thus only time-of-flight effects factor into the energy relation, as electrons with greater velocities travel further along an IMF line in a given unit of time, and therefore experience the same quantity of scattering but a larger decrease in magnetic field strength and greater adiabatic focussing effects. The difference between the modelled energy relation for broadening per AU and both the observational results suggests that there may be a dominant scattering mechanism, with an intrinsic energy relation.

Finally, it is also important to consider kinetic modelling investigations of strahl evolution, such as the Lie-Svendsen et al. (1997) and Horaites et al. (2017). The former compared their results to Helios observations at ~ 0.3 AU and the later compared their results to Wind observations at ~ 1 AU. These two studies both demonstrated that the kinetic approach can explain the formation of a strahl beam in fast solar wind streams. In particular, narrow strahl with beam widths of ~ 10 to 50° can be modelled effectively and that the resulting strahl energy relation is a decrease in width with electron energy.

2.2.6 Strahl Scattering Mechanisms

Solar wind plasma is too tenuous for Coulomb collisions to produce the scattering effect necessary to match suprathermal electron observations (e.g. Hammond et al., 1996; Vocks et al., 2005). As a consequence, numerous investigations have concluded that the strahl scattering mechanism(s) must involve electron interaction with plasma waves rather than via collisions (e.g. Saito and Gary, 2007; Pagel et al., 2007). The different energy relations reported in Section 2.2.5 suggest that there may be multiple scattering mechanisms present in the solar wind. However, it is unknown whether there is a scattering mechanism that plays a dominant role in the evolution of strahl, or indeed whether the scattering is a continuous process or intermittently occurring when conditions in the solar wind are favourable. Accordingly, a variety of resonant and non-resonant wave-particle interactions have been

proposed each with different possible drivers for these fluctuations.

Resonant interactions with whistler-mode waves are frequently invoked as a likely scattering mechanism to explain strahl pitch angle width broadening (e.g., Fitzenreiter et al., 1998; Hammond et al., 1996; de Koning et al., 2006; Vocks et al., 2005; Pagel et al., 2007; Anderson et al., 2012). Depending on the driver of the whistler-mode fluctuations, a different energy relation for strahl scattering can be expected (Saito and Gary, 2007, & references therein). For example, a broadband whistler spectrum resulting from turbulent cascade could produce strahl beam width that increases with strahl energy (Saito and Gary, 2007). Alternatively, a core electron temperature anisotropy (where $T_{\perp}/T_{\parallel} > 1$) could lead to the excitation of the whistler anisotropy instability, producing enhanced whistler fluctuations that result in strahl beam width that decreases with strahl energy. Hence, specific properties of the whistler-mode waves may, in part, explain the ostensibly conflicting energy dependence observations. These suppositions are supported by observations of the presence of whistler-like fluctuations in the solar wind up to 10% of the time (e.g., Lacombe et al., 2014). However, another recent study (Stansby et al., 2016), found that the majority of whistler-mode waves propagate in the anti-sunward direction as opposed to the sunward direction required for resonant interaction with anti-sunward propagating strahl.

There have also been numerous investigations in which the strahl itself has driven instabilities that can result in scattering of the strahl beam via a number of different wave-particle interactions. For instance, whistler-mode waves generated by the electron heat flux instability could be a potential source for scattering (Gary et al., 1994). Another possibility is fluctuations resulting from the electron firehose instability (where $T_{\perp}/T_{\parallel} < 1$), for example the Hellinger et al. (2014) study which found non-propagating waves produced by this instability resulted in scattering of the strahl. These standing waves were then transformed into propagating whistler-mode waves that were then rapidly damped, resulting in perpendicular electron heating. It has also been shown that strahl generated Lagmuir waves can produce scattering effects significant enough to broaden the solar wind strahl population (Pavan et al., 2013). Finally, anisotropy of the strahl electron velocity distribution can also result in a core-strahl system that is unstable to lower hybrid waves and results in

pitch-angle diffusion of the strahl (Shevchenko and Galinsky, 2010).

Another frequently evoked candidate for strahl scattering are obliquely propagating KAWs, which may be able to interact with the field-aligned strahl via Landau damping. These suggestions are strongly supported by observations of KAW like fluctuations at small scales (e.g., Salem et al., 2012; Chen et al., 2013b; Kiyani et al., 2012). It should also be noted that intense strahl scattering events have been observed at 1 AU during intervals of oblique KAWs (Gurgiolo et al., 2012). However, we should also note that evidence for resonant scattering of strahl electrons during Whistler-mode intervals have been observed (Kajdič et al., 2016). In a recent investigation into magnetic field turbulence in the solar wind between 1 and 200 Hz, it was found that during intervals that did not contain quasi-parallel Whistler-mode waves, there was a strong correlation between the observed compressibility and the expected compressibility for KAWs (Lacombe et al., 2017).

Finally, indications of strahl electrons have been found as far out at $\sim$ 10 AU by Walsh et al. (2013) using the Cassini spacecraft. Walsh et al. (2013) found that the estimated strahl pitch angle width was narrower than predicted by extrapolation of previous observations from within 2.5 AU. Hence it was concluded that the rate of scattering may decrease with increasing radial distance. It was also suggested that this finding was consistent with whistler-mode wave interaction as the primary strahl pitch angle scattering mechanism, since the effectiveness of whistler-mode scattering depends on the available wave power below the electron gyrofrequency, and both wave power and the electron gyrofrequency decrease with radial distance (Hu et al., 1999; Vocks et al., 2005).

2.2.7 The Effect of Solar Wind Type and Boundaries on Strahl

Narrow strahl features ($< 20^{\circ}$) are most commonly observed in the coronal hole solar wind (e.g., Fitzenreiter et al., 1998; Anderson et al., 2012). Some studies have also observed that strahl pitch angle distributions are generally narrower in the fast solar wind than the slow solar wind (e.g., Feldman et al., 1978; Pilipp et al., 1987b). This suggests that the strahl has either undergone a lesser degree of scattering in-transit within the fast solar wind than the slow, or that the different origins of the slow and fast solar wind result in different electron velocity distributions. It has

also been shown that narrow strahl features are fractionally more likely to occur for counter-streaming strahl within ICMEs than in the solar wind as a whole (e.g., Anderson et al., 2012). ICMEs and the fast solar wind do not generally originate from similar source regions. However, both ICMEs, which frequently experience over-expansion as they propagate (Gosling et al., 1994), and high speed coronal hole wind should have a greater decrease in IMF strength per unit distance along the IMF direction than the slow solar wind (e.g., Gosling et al., 1994; Anderson et al., 2012). This provides a greater adiabatic focusing effect for the strahl scattering mechanism to overcome. Therefore, it seems likely that the topology of the IMF and specifically the path length travelled by the strahl electron, should have a significant effect on the width of the strahl observed at 1 AU.

However, it has also been shown that proximity to IMF sector boundaries may have a more significant effect on strahl width than solar wind speed, with strahl electrons displaying increased width near boundaries for all electron energies (Pilipp et al., 1987b). In addition, observations of whistler waves downstream of interplanetary shocks have been shown to demonstrate a weak positive correlation with the amplitude of these magnetic fluctuations and the normalized heat flux magnitude (Wilson et al., 2013). It has also been observed that the electron distributions at the time of observation satisfied the whistler heat flux instability threshold, the majority of events with $T_{halo,\parallel}/T_{halo,\perp} > 1.01$ (Gary et al., 1994). These results imply that whistler waves may be regulating the electron heat flux and the halo temperature anisotropy and thus have significant implications for strahl electron scattering. Particularly, if the apparent scattering is brought about by enhancements in wave amplitude or electron densities due to the presence of an interplanetary shock, as the scattering effects would likely be more pronounced at larger radial distances from the Sun due to the increased occurrence of interplanetary shocks at larger radial distances (Luhmann, 1995). Finally, there have also been observations of enhanced fluxes of suprathermal electrons resulting from co-rotating shocks reported by Ulysses beyond 2 AU (Gosling et al., 1993). These electrons are bi-directional in nature and it is thought that the remnants of the backstreaming beams may contribute significantly to the diffuse solar wind halo electron population.

2.2.8 Strahl and IMF Topology

Strahl is, by definition, strongly field-aligned and its constituent electrons have a high field-aligned velocity relative to the bulk plasma flow. As a consequence, strahl electrons travel at high relative speeds along the Parker spiral field. Hence, understanding uni- and bi- directional strahl trajectories can be used to determine large scale IMF topology and provide near-instantaneous indications of solar connectivity (e.g. Pilipp et al., 1987b,a; Owens et al., 2008). Bi-directional strahl are thought to be good indicators of newly-formed magnetic loops and have also been observed when suprathermal electrons are reflected at interplanetary shocks (e.g. Gosling et al., 1987; Owens and Forsyth, 2013). It has also been suggested that bi-directional electron heat flux events are one of the more consistent signatures of coronal mass ejections, particularly at 1 AU (e.g. Gosling et al., 1987). More recently, the key role strahl pitch angle distributions can play in the determination of IMF global topology was illustrated in a study by Li et al. (2016a), who used predictions of suprathermal pitch angle distributions to test the validity of a proposed IMF mapping technique.

The nature and heliospheric locations/conditions of the strahl scattering process(es) have significant implications for the applicability of strahl trajectories as tool for inferring IMF topology. For example, the bi-directional signature associated with IMF loops may often be scattered to the extent that is lost (e.g. Hammond et al., 1996; Maksimovic et al., 2005; Owens et al., 2008). This is particularly relevant for the sunward component of bi-directional strahl as it is travelling into regions or increasing magnetic field strength and therefore will experience broadening due to conservation of magnetic moment. Establishing the bounds of their utility for IMF topology determination through further investigation into the radial variability of strahl signatures is therefore highly desirable.

Chapter 3

Instrumentation & Methodology

In this body of work, suprathermal, field-aligned beams of solar wind electrons called strahl were investigated. The primary observations required to complete the studies presented in this thesis are of the solar wind electrons themselves and of the interplanetary magnetic field. The space missions, instruments and datasets used in this thesis are described within this chapter. These include the Cassini-Huygens, Advanced Composition Explorer (ACE), Wind, Cluster and Mars Express missions. The key analysis methods used and developed in this thesis are also described. These include Gaussian fitting to suprathermal pitch angle distributions; solar wind flux tube analysis; partial variance of increments; and interplanetary field line length estimation using solar energetic particle onset observations.

Figure 3.1: Photograph of the Cassini-Huygens launch (15/10/1997) on a Titan IVB/Centaur launch vehicle. This photograph was taken from Hangar AF on Cape Canaveral Air Force Station. The ship seen in the foreground is for solid rocket booster retrieval. Image credit: NASA.

3.1 The Cassini-Huygens Mission

The Cassini-Huygens mission to the Kronian System began on the 15th October 1997 when the spacecraft was launched in a Titan IVB/Centaur from Cape Canaveral, Florida (Figure 3.1). The Cassini-Huygens mission came to an end on the 15th July 2017, one month short of twenty years in space, when it was deliberately plunged into Saturn, to ensure that the planet's moons remain uncontaminated for future exploration. During its lifetime the Cassini-Huygens mission completed 294 orbits of Saturn and 162 moon flybys, collected 635 GB of scientific data and captured 453,048 images. Key mission discoveries include, and are certainly not limited to, the presence of liquid methane seas on Saturn's moon Titan and a global ocean that likely has hydrothermal activity within the moon Enceladus.

Figure 3.2: This photograph shows the tandem space probe Cassini-Huygens in the clean room of the Cape Canaveral, Florida, space center before its 1997 launch. The Huygens probe is contained within the flying-saucer-shaped heat shield coated in gold-coloured multi-layer insulation. Image credit: Associated Press.

The Cassini-Huygens mission consisted of the Cassini spacecraft and the Huygens probe, which was deployed at the Saturn's moon Titan in December 2004. Cassini-Huygens was one of the largest, heaviest and most complex interplanetary spacecraft ever built, with 18 different science instruments and a vast quantity of propellant (over 50% of the total mass). The Cassini spacecraft alone weighed

2,150 kg and was 6.7 m tall, approximately the same size as a newborn blue whale (Ruud, 1956). For more information on the Cassini-Huyens mission, see the relevant webpages (Cassini Science Communications Team, 2018). In this thesis, solar wind electron and magnetic field observations from Cassini's interplanetary journey to Saturn were examined, in order to investigate the heliocentric radial evolution of strahl electrons. The instruments used to do so were the low energy Electron Spectrometer (ELS), part of the Cassini Plasma Spectrometer (CAPS, Young et al., 1998) experiment, and the Fluxgate Magnetometer (FGM) part of the Cassini Dual Technique Magnetometer (MAG, Dougherty et al., 2004).

Cassini's journey to Saturn took approximately 7 years, during which time it travelled a distance of 3×10^9 km, until on the 1st July 2004 it became the first spacecraft to orbit Saturn. Figure 3.4 shows the spacecraft trajectory from launch until the end of 2004. During its interplanetary journey, the Cassini spacecraft performed both Earth and Jupiter flybys, during which scientific data from CAPS ELS and FGM were obtained. There are also intervals during the cruise phases between planetary observations during which CAPS and FGM were both acquiring data. Both instruments were required to obtain electron pitch-angle information. This is illustrated in Figure 3.4, which show the Cassini interplanetary trajectory projected onto the heliocentric inertial x-y plane. Sections marked in red show where the data necessary to conduct strahl beam width evolution observations were available. By making use cruise phase and fly-by data from a planetary mission, observations of suprathermal solar wind electrons were made over the largest heliocentric range to date ($\sim$ 1 to 9 AU).

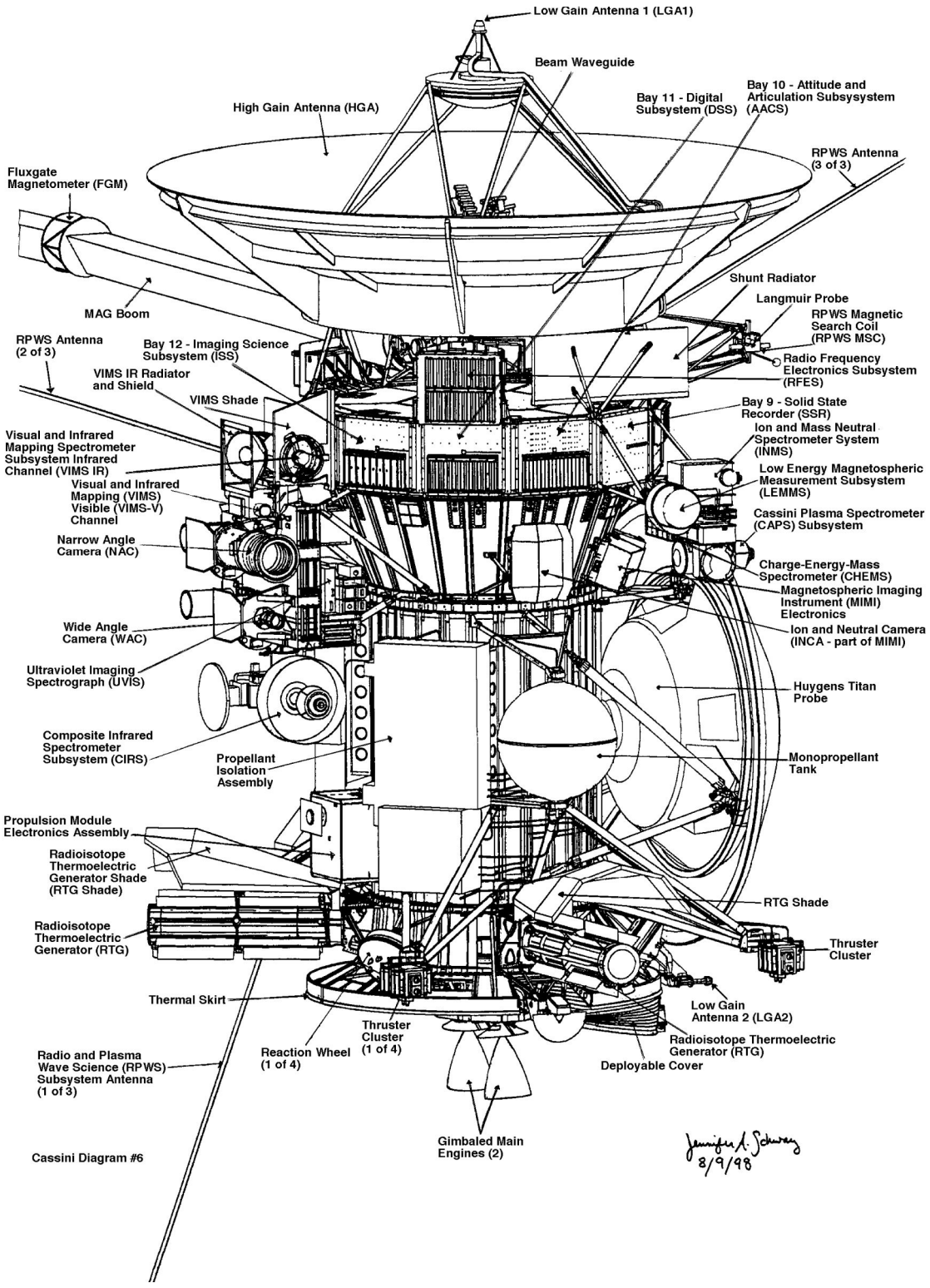

Figure 3.3: Cassini spacecraft schematic showing the location of scientific instruments included on the Cassini orbiter and the Huygens probe. Image credit: NASA.

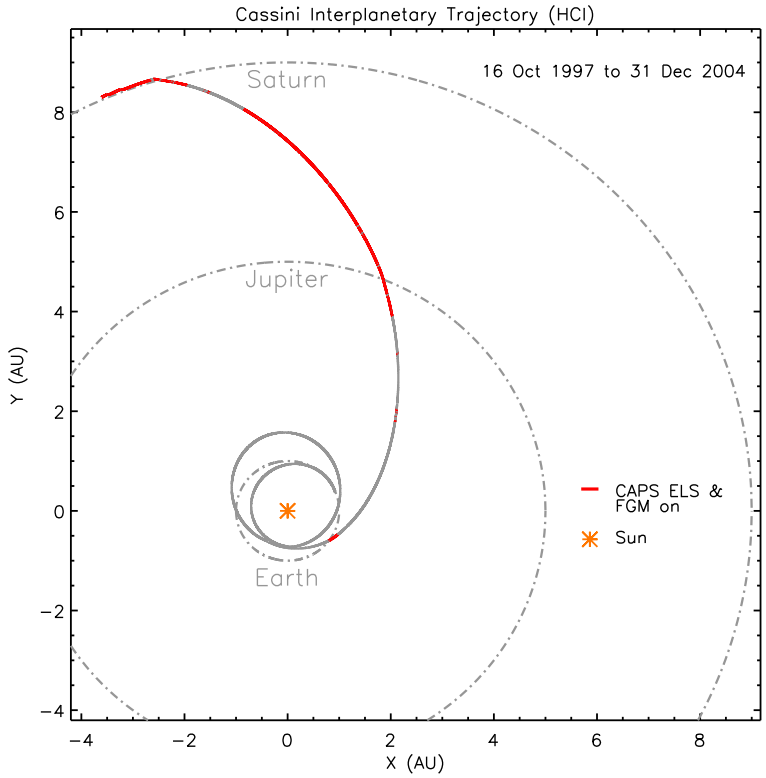

Figure 3.4: The trajectory of Cassini en route to Saturn from 16/10/1997 to 31/12/2004, as projected onto the Heliocentric Inertial (HCI) X-Y plane (Graham et al., 2017). The red line represents sections where and both CAPS ELS and MAG FGM were collecting data. The Sun is represented by a orange star and the approximate orbits for Earth, Jupiter and Saturn are shown by grey dash-dot lines. The Earth flyby (closest approach) took place on 18/08/1999, the Jupiter flyby (closest approach) took place on 30/12/2000 and the Saturn orbit insertion took place on 01/07/2004.

3.1.1 Cassini Electron Spectrometer

Electron measurements are provided by the ELS sensor for CAPS, which is a hemispherical top-hat electrostatic analyser (Young et al., 1998). A top-hat consists of two conducting, hemispherical plates which are mounted concentrically, with a small gap between them, and a top cap/circular collimator. An illustration of the generic geometry of a hemispherical top-hat electrostatic analyser is shown in Figure 3.5. In the case of an electron detector like ELS, the inner hemisphere is given a positive voltage with respect to the outer hemisphere, which is grounded.

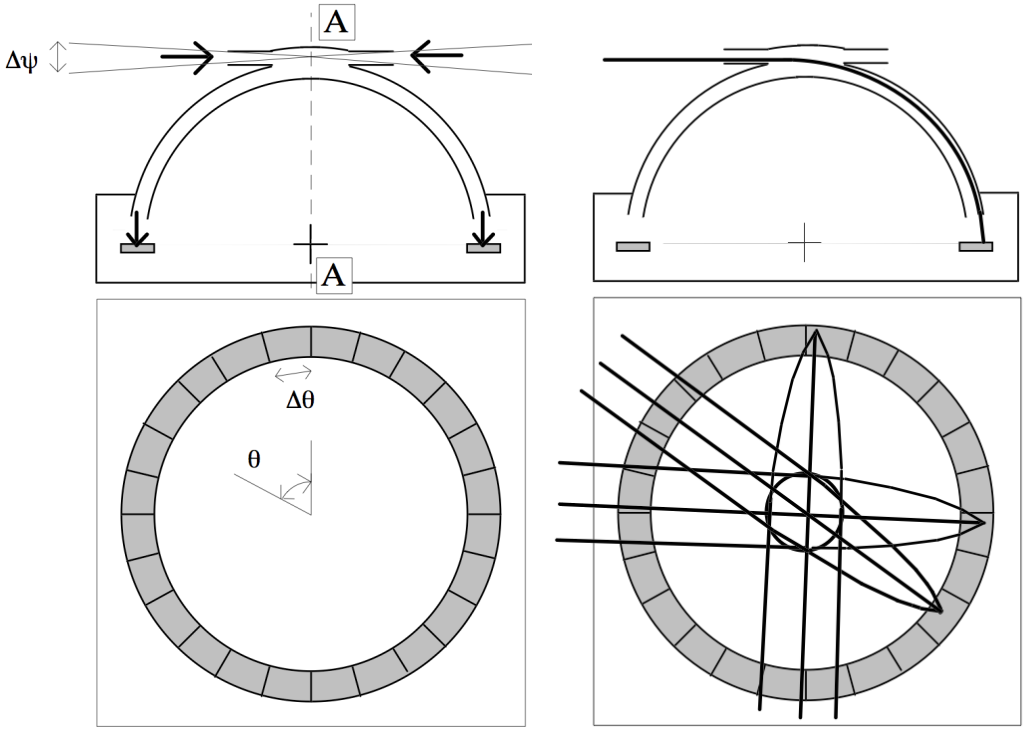

Figure 3.5: (a) An illustration of a top-hat electrostatic analyser (Paschmann and Daly, 1998). The upper part of the diagram shows a cross section of the analyser taken through a plane containing the rotational axis of symmetry (marked by the dashed line labelled AA). The top-hat consists of two conductive hemispheres mounted concentrically with a small gap between them. There is also a collimator section at the top-hat entry aperture which consists of parallel circular plates. The azimuthal acceptance angle for the collimator is shown by the thin grey lines and labelled $\Delta\psi$. Particles which do not have arrival paths lying within the fan bounded by these lines do not reach the detector plane. Particles that enter the aperture are rotated though 90° as they pass between the hemispheres and strike the detector (indicated by the grey rectangles). The bold arrows show the direction of particle trajectories at the entry aperture and the exit of the nested hemispheres. The lower part of the diagram shows the detector in plan view (i.e., looking down the axis AA). The detector in this diagram is divided into equal sectors, each associated with a different polar angle zone labelled $\Delta\theta$. (b) An illustration of the same top-hat electrostatic analyser with particle trajectories shown with thick black lines (Paschmann and Daly, 1998). The lower part of the diagram shows a projection of particle trajectories onto the plane containing the detector. Parallel beams arriving from three different polar angles are shown, the small, inner circle shows the entrance to the outer hemisphere though which the beams must pass. Particle beams are effectively focussed by the top-hat for all polar angles.

Electrons enter the outer hemisphere though the collimating parallel plates which only allow electrons from a finite azimuthal angle to enter the aperture. In the case of the Cassini ELS this azimuthal angle is 5.2° and the polar angle fan covers 160° (unlike in Figure 3.5 which has a full 360° polar fan). The polar angle is measured in the plane whose normal is parallel to the top-hat symmetry axis, labelled AA in Figure 3.5. Electrons approaching the aperture with trajectories that lie outside the aperture acceptance angle will strike one of the plates (N.B. ELS has a baffle system designed to reduce background arising from secondary photoelectrons and internal scattering). Electrons that enter the analyser are then deflected by the voltage applied between the two hemispherical plates. For a given potential difference, only electrons with a specific energy will be deflected in such a way that the trajectory passes though the gap between the two plates and impacts the detector. Electrons with energies that are too low (high) will impact the inner hemisphere (outer hemisphere or collimator). Thus by varying the voltage applied to the inner hemisphere, electrons with different energies can be observed.

Electrons that have the required energy to pass between the two hemispheres will strike the detector. In the case of ELS, the detector is divided into 8 polar angle sectors comprising of micro-channel plates (MCPs) mounted above 8 anodes. This provides an instantaneous field-of-view (FOV) of 5.2° in the azimuthal direction and $\pm 80°$ in elevation (20° per anode) (Linder et al., 1998). MCPs consist of thousands of microscopic glass lined pores orientated so that incident electrons will hit the walls of one of these pores (ELS makes use of a chevron pair of MCPs to achieve this). When an electron impacts the MCP wall, one or more secondary electrons are emitted. This process continues, resulting in an avalanche of electrons which then strike the surface of the anode. The surface of the anode becomes negatively charged and a count is registered in the detector electronics when a sufficient potential difference has been reached.

In order to observe over a range of electron energies, the voltage between the ELS hemispheres is 'swept' through a number of discrete voltage steps. ELS has an energy/charge response range of $\sim$ 0.5 - 27,000 eV/e (Linder et al., 1998). This is divided into 63 energy steps with a 31.25ms sampling time per energy level and a total cadence of 2s. However, the time and/or energy resolution of the data were sometimes reduced by summing over several energy sweeps and/or pairing energy bins if CAPS ELS was assigned low telemetry priority (Young et al., 2004; Arridge et al., 2009). For example, during the Earth flyby, the temporal cadence was limited to $\sim$ 10s (Rymer et al., 2001).

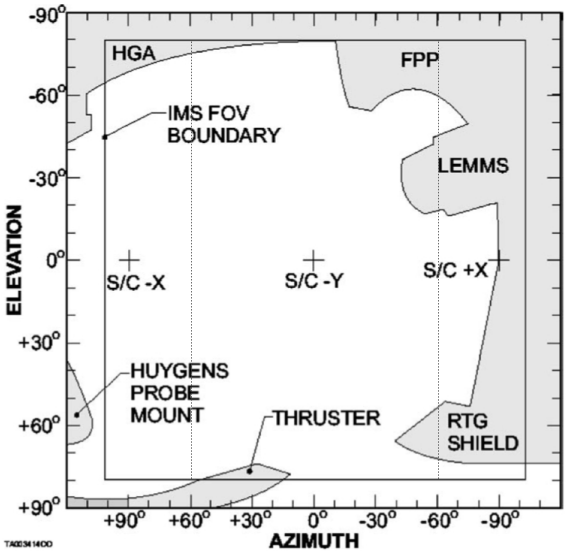

Figure 3.6: An approximate sketch of the physical blockages of the full CAPS FOV [Young et al., 2004]. The acronyms are as follows: HGA, High Gain Antenna; FPP, Fields and Particles Pallet; IMS, Ion Mass Spectrometer; LEMMS, Low Energy Magnetospheric Measurement Subsystem; RTG, Radioisotope Thermionic Generator. This figure is only approximate as it actually shows the FOV of the CAPS ion instrument mounted directly alongside the ELS. Also not included in the diagram are the multi-layer insulation blankets covering all spacecraft surfaces, adding a further 5cm thickness, or the presence of the Huygens probe mounted in the bottom left corner.

The ELS is mounted with the other CAPS sensors, on a rotating platform driven by a motor actuator, that is able to sweep through $\pm 104^{\circ}$ in the ELS azimuthal direction in 208s (Young et al., 2004). The full ELS FOV is shown in Figure 3.6. Although, it should be noted that this is the maximum actuation range and it is not always implemented. For example, during the Earth flyby, the actuator only sweeps through 120° and during the Jupiter encounter the actuator was fixed

at 0° for extended periods in the solar wind (Rymer, 2004). It should also be noted that other instruments on-board the Cassini spacecraft intrude upon the CAPS ELS FOV (see Young et al., 2004, for more details), in particular, the Huygens probe was not deployed until 2004. Hence, the usable FOV of ELS is reduced further as the obstructed regions must be removed from analysis. Finally, when using CAPS ELS data, the background count rate resulting from contamination via Cassini's radiation sources must also be taken into account. An investigation by Arridge et al. (2009) produced a model for this energy-independent, look-direction and time-dependent background count rate which can be used to subtract the background level from the ELS data. A summary of the key properties of CAPS ELS are shown in Table 3.1.

3.1.2 Fluxgate Magnetometer

Measurements of the interplanetary magnetic field strength and direction are provided by the Cassini MAG FGM (Dougherty et al., 2004). In particular, these observations are related to the concurrent ELS observations to determine electron pitch angle distributions.

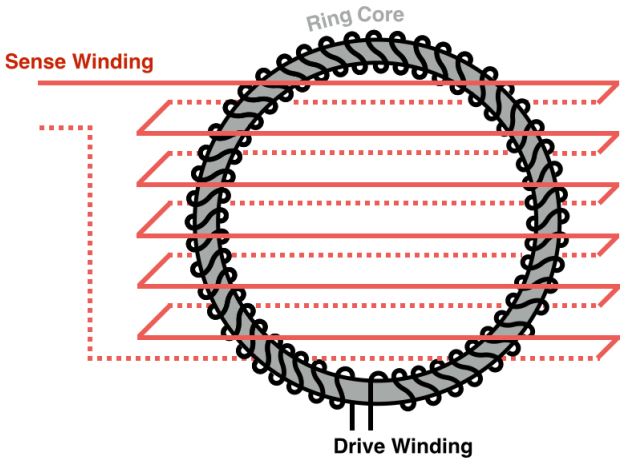

Figure 3.7: An illustration of a single fluxgate sensor. The drive winding (thick black lines) is toroidally wrapped around a high-permeability ring core (grey). This is mounted inside a rectangular sense winding (thick red lines) with its axis in the plane of the ring core. To observe the full 3D magnetic field, two other fluxgate sensors are required, mounted orthogonally to the first, so that the magnetic field strength is observed for all three components of the magnetic vector.

The FGM is mounted midway along the 11m magnetometer boom and we use 1s cadence data throughout this thesis. The FGM consists of three orthogonally mounted, single-axis fluxgate sensors. Each fluxgate sensor is a toroidally wound, high-permeability ring core mounted inside a rectangular sense winding with its axis in the plane of the ring core, see Figure 3.7. An alternating current is applied to the toroidal winding, driving the core through a magnetic saturation cycle

Cassini Instrument Properties	
CAPS ELS Parameter	Capability
Energy/Charge Response	
Range (eV/e)	0.6-28.75 $\times 10^3$
Resolution ($\measuredangle$ E/E)$_{FWHM}$	0.17
Energy-geometric Factor (cm^2 sr eV / eV)	1.4 $\times 10^{-2}$
Energy Sweep Time Resolution (s^{-1})	0.5
Angular Response	
FOV (AZ $\times$ EL)$_{FWHM}$	5.2°$\times$160°
Resolution (AZ $\times$ EL)$_{FWHM}$	5.2°$\times$20°
Actuator Angular Range	$\pm$104°
MAG FGM Parameter	Capability
Normal Downlink Data Rate (vec. s^{-1})	32
Dynamic Range (nT), Resolution (pT)	40, 4.9
	400, 48.8
	10,000, 1,200
	44,000, 5,400

Table 3.1: Summary of CAPS ELS Parameters (Young et al., 1998) and MAG FGM parameters (Dougherty et al., 2004). N.B.full-width-half-maximum (FWHM).

which continuously flips the polarity of the electromagnet. This flipping magnetic field then induces a corresponding alternating current in the sense winding. In the presence of an external magnetic field, the component of the field in the plane of the sense winding will distort the symmetry of the magnetic saturation cycle i.e., magnetic saturation will be reached more (less) easily when the external field is parallel (anti-parallel) to the ring core field. The output current will therefore be modulated by the external magnetic field, allowing the strength of the component of the external field in the plane of the sense winding to be determined. Hence, by combining three orthogonal fluxgate sensors, three-dimensional information about the magnetic field can be obtained. The Cassini FGM has four different operational ranges which are summarised in Table 3.1.

3.2 The Wind Mission

Wind, together with the Polar spacecraft, was originally part of the Global Geospace Science (GGS) programme in which the two spacecraft worked in tandem to observe how the solar wind drives changes in the magnetosphere. GGS itself was part of a larger initiative called the International Solar Terrestrial Physics (ISTP) program - a fleet of spacecraft including Geotail, the SoHO and Cluster, placed at a variety of locations in order to further understand the Sun-Earth system. The Wind spacecraft was launched from Cape Canaveral on the 1st Noverember 1994 in a Delta II rocket.

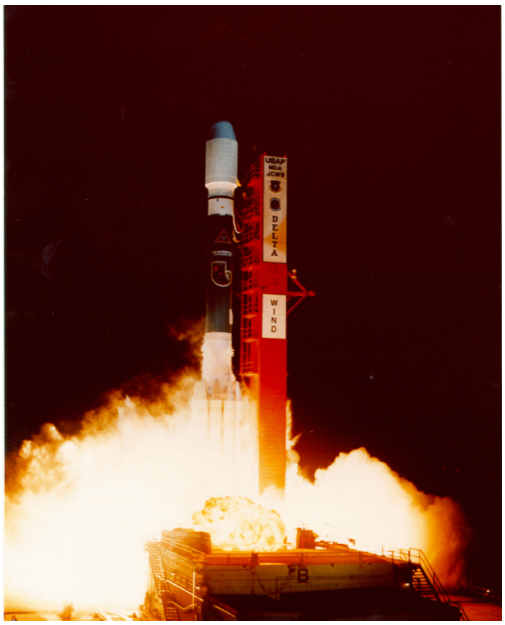

Figure 3.8: Photograph of the Wind launch (01/11/1994) on a Delta II launch vehicle from Cape Canaveral. Image credit: NASA.

During the first 2 years of the mission the Wind spacecraft completed several Earth orbits and was transferred to a halo orbit at the 1st Lagrange point (L1), becoming the 2nd ever spacecraft to do so, the International Sun-Earth Explorer-3 mission was the 1st (on November 20, 1978). Between 1996 and 2004 the Wind spacecraft travelled to a variety of different locations, observing both solar wind and magnetospheric plasma at different stages in its mission lifetime. Notably, when the solar wind monitor named ACE (Section 3.3) was placed in an L1 orbit, Wind was moved to L2, downstream of Earth and deep in the magnetotail. In 2004, the Wind spacecraft was permanently placed in a halo orbit at L1, in order to make continuous observations of the unperturbed solar wind upstream of Earth. The Wind spacecraft has spent over 20 years in space, data from the mission has been used in over 4000

scientific publications and, despite having a planned mission of 5 years, the Wind spacecraft has enough fuel for over 50 more years in space. For more information please see the relevant NASA web pages (Zell and Dunbar, 2017; Kovalick and Szabo, 2018; Wilson and Szabo, 2018).

Wind is a spin stabilized spacecraft with its spin axis normal to the ecliptic plane and a spin rate of 20 rpm. The Wind spacecraft has a number of different scientific instruments, shown in Figure 3.9. In this thesis, solar wind electrons and other interplanetary phenomena are examined using the Wind spacecraft, in order to investigate the evolution of strahl electrons from the Sun to 1 AU. The instruments used to do this were: the 3D Plasma (3DP) Electron Electrostatic Analysers (EESA); the 3DP Solid State Telescopes (SST); the Energetic Particles: Acceleration, Composition, and Transport (EPACT) instrument, specifically, the Low Energy Matrix Telescopes (LEMT); and the Magnetic Field Investigation (MFI).

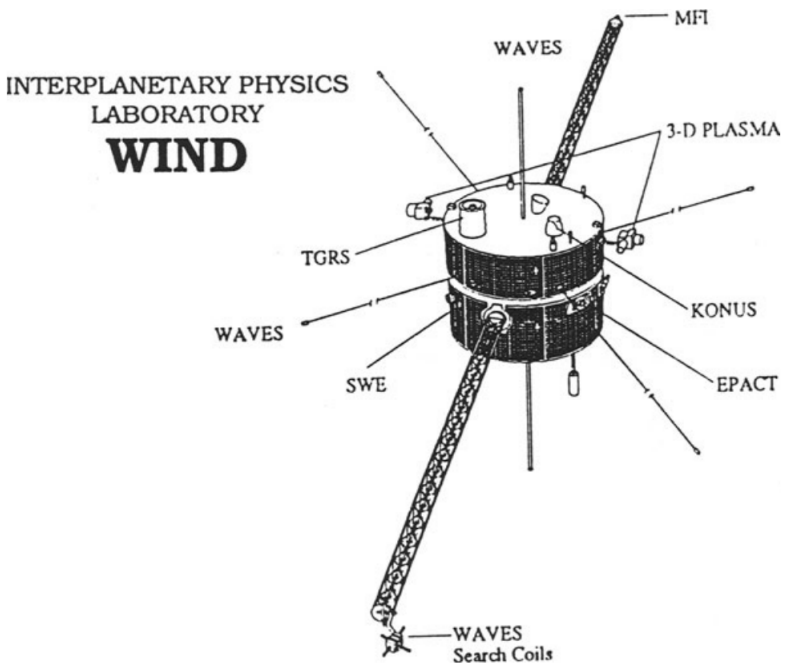

Figure 3.9: Wind spacecraft schematic (Desch et al., 1999) showing the location of the scientific instruments included on the Wind spacecraft.

3.2.1 Wind 3D Plasma Experiment

Wind 3DP (Lin et al., 1995) makes observations of the full 3D distributions of suprathermal ions and electrons and is capable of observing from the solar wind particle populations to low energy cosmic rays. The solar wind electrons examined in this thesis are observed using the Electron Electrostatic Analysers (EESA), which are two top-hat symmetrical spherical section electrostatic analysers, which measure high and low electron fluxes (high energy Electron Electrostatic Analyser (EESA-H) and low energy Electron Electrostatic Analyser (EESA-L) respectively). A description of how a top-hat electrostatic analyser operates is given in Section 3.1.1. The EESA sensors have an energy range of 3 eV - 30 keV and complete 32 or 64 energy sweeps per $\sim$3s spacecraft spin (Lin et al., 1995). The sensors are also mounted on a boom to reduce the effects of spacecraft potential (see Figure 3.9. EESA-H and EESA-L have an instantaneous FOV of 360 x 90° and 180 x 14° respectively, full sky coverage can thus be obtained for one half or one full spacecraft spin.

Higher energy solar energetic particle (SEP) electrons are investigated using the Wind 3DP Solid State Telescopes (SST, Lin et al., 1995). SST is made up of three pairs of double-ended telescopes. Each double-ended telescope contains either a pair or triplet of closely sandwiched semi-conductor detectors. In one look direction of the double ended telescope, the detector is covered with a thin foil whose thickness was chosen to stop protons of energy up to the energy of electrons ($\sim$ 400 keV) which penetrate the detector. In the opposite look direction, a broom magnet sweeps away electrons below $\sim$ 400 keV. The foil in one direction leaves the electron spectrum essentially unchanged and the broom magnet in the opposite direction does not affect the protons. Thus, in the absence of higher energy particles, the foil detectors count only electrons while the magnet detectors count only protons. The output of each detector is taken in anti-coincidence with the detector behind it in order to achieve a low background.

Higher energy electrons ($\sim$ 400 keV to 1 MeV) and protons (6-11 MeV) are identified by the pair of double-ended telescopes containing the triplet detector sandwich, which has a third thicker semi-conductor detector in the centre. The majority of $>$ 400 keV electrons penetrate the front detectors and are rejected by the

Wind 3DP Instrument Properties		
EESA Parameter	EESA-H Capability	EESA-L Capability
Particle Species & Energy Range	100 eV-30 keV e	3 eV-30 keV e
Geometric Factor (cm^2 sr)	0.1 E	1.3 E $\times 10^{-3}$
FOV (°)	360 x 90	180 x 14
Dynamic Range $eV(cm^2\ sr\ eV\ s)^{-1}$	1-10^8	10^2-10^9
SST Parameter	F Capability	FT Capability
Particle Species & Energy Range	25-400 keV e	400 keV-1 MeV e
Geometric Factor (cm^2 sr)	1.7	0.36
FOV (°)	180 x 20	72 x 20
Dynamic Range $eV(cm^2\ sr\ eV\ s)^{-1}$	0.1-10^6	10^{-2}-10^6

Table 3.2: Summary of 3DP EESA-H, EESA-L, SST Foil (F) and SST Foil with the thicker central detector (FT) parameters (Lin et al., 1995).

anti-coincidence with the adjacent detector, however some 400 keV electrons stop in the front detector. Electrons from $\sim$ 400 keV to $>$ 1 MeV are cleanly measured by the sum of the front and centre detector outputs of the triplet (foil or magnet) when they are in coincidence. Protons up to $\sim$ 6 MeV stop in the front detectors and $\sim$ 6-11 MeV protons are detected by the combination of the front and centre (magnet) detectors in the triplet. Each double-ended telescope has two 36 x 20° FOVs and hence, five telescopes cover a 180 x 20° slice for magnet detectors and an analogous slice for foil detectors. As the spacecraft rotates through 360°, each slice sweeps out the full sky.

A summary of the key properties of 3DP EESA and SST is given in Table 3.2. It should be noted that, the time resolution of the available data for both EESA and SST varies depending on the instrument mode available at the time of observation.

Wind MFI Instrument Properties	
Parameter	Capability
Normal Downlink Data Rate (vec. s^{-1})	44 (snapshot), 10.87 (standard)
Dynamic Range (nT)	$\pm$ 4, $\pm$ 16, $\pm$ 64, $\pm$ 256, $\pm$ 1024, $\pm$ 4,096, $\pm$ 16,384, $\pm$ 65,536
Digital resolution (12-bit A/D) (nT)	$\pm$ 0.001, $\pm$ 0.004, $\pm$ 0.016, $\pm$ 0.0625, $\pm$ 0.25, $\pm$ 1.0, $\pm$ 4.0, $\pm$ 16.0

Table 3.3: Summary of MFI parameters (Lepping et al., 1995).

3.2.2 The Magnetic Field Investigation

The Magnetic Field Investigation (MFI, Lepping et al., 1995) provides measurements of the interplanetary magnetic field. It is a twin tri-axial fluxgate magnetometer mounted on a 12 m boom on the Wind spacecraft see Figure 3.9. A description of how a fluxgate sensor works is given in Section 3.1.2. MFI has eight different operational ranges which are summarised in Table 3.3.

3.2.3 The Low Energy Matrix Telescopes

The EPACT investigation (Von Rosenvinge et al., 1995) consists of multiple telescopes designed to observe energetic particle populations. LEMT has three identical solid-state detector telescopes which use the dE/dx by E method of particle identification. Each telescope has 16 surface barrier detectors (or dE/dx elements) arrayed on a spherical dome in order to minimize path-length variations. The residual energy detector is mounted under the dome and subdivided into five strips on each side, strips on opposite sides being orthogonal to each other. Behind the residual energy detector is an anti-coincidence detector to reject particles penetrating through the residual energy detector. The look directions of the three LEMT telescopes combined with the spin of the spacecraft permit near omnidirectional viewing (Telescope A is canted 25° below the spacecraft X - Y plane, Telescope B looks directly into the X - Y plane, and Telescope C is canted 25° above the X - Y plane). In this thesis, Helium ions were investigated using EPACT LEMT, which has an

Wind EPACT LEMPT Instrument Properties	
Parameter	Capability
Energy range	
Hydrogen (MeV)	1.4-10
Helium (MeV nuc^{-1})	1.4-10
Iron (MeV nuc^{-1})	2.5-50
Geometry factor (cm^2 sr)	3 x 17

Table 3.4: Summary of EPACT LEMPT parameters (Von Rosenvinge et al., 1995).

energy range of 1.4-10 MeV/nuc and data that is generally available at a time resolution of 5 mins (Von Rosenvinge et al., 1995). A summary of the key properties of EPACT LEMT is given in Table 3.4.

3.3 The ACE Mission

Figure 3.10: Photograph of the ACE launch (25/08/1997) on a Delta II launch vehicle from Cape Canaveral. Image credit: NASA.

ACE was launched on the 25th of August 1997 from Cape Canaveral on a Delta II launch vehicle. The primary aims of the mission were to examine the composition of the corona, interstellar medium and galactic matter. However, the spacecraft was also placed in an L1 orbit and hence, the in-situ instruments inboard ACE can provide near-continuous observations of the solar wind. In this body of work, we use only the solar wind velocity information derived from Solar Wind Electron, Proton, and Alpha Monitor (SWEPAM, McComas et al., 1998) data and interplanetary magnetic field observations provided by the magnetometer (MAG, Smith et al., 1998), in order to compare solar wind observations to those of the Cassini spacecraft during its Earth Flyby. MAG is a set of twin, triaxial flux-gate magnetometers which was originally a flight spare for the Wind mission (see Section 3.2). SWEPAM is made up of the modified spare solar wind electron and ion sensors from the Ulysses mission and designed to observe electrons from $\sim$ 1 - 900 eV and ions from $\sim$ 0.26 - 35 keV in three dimensions. Both the ion and electron instruments are electrostatic analysers with a fan shaped aperture (see Section 3.1.1 for a description of electrostatic analysers) and make 3D observations for every 64s spacecraft spin.

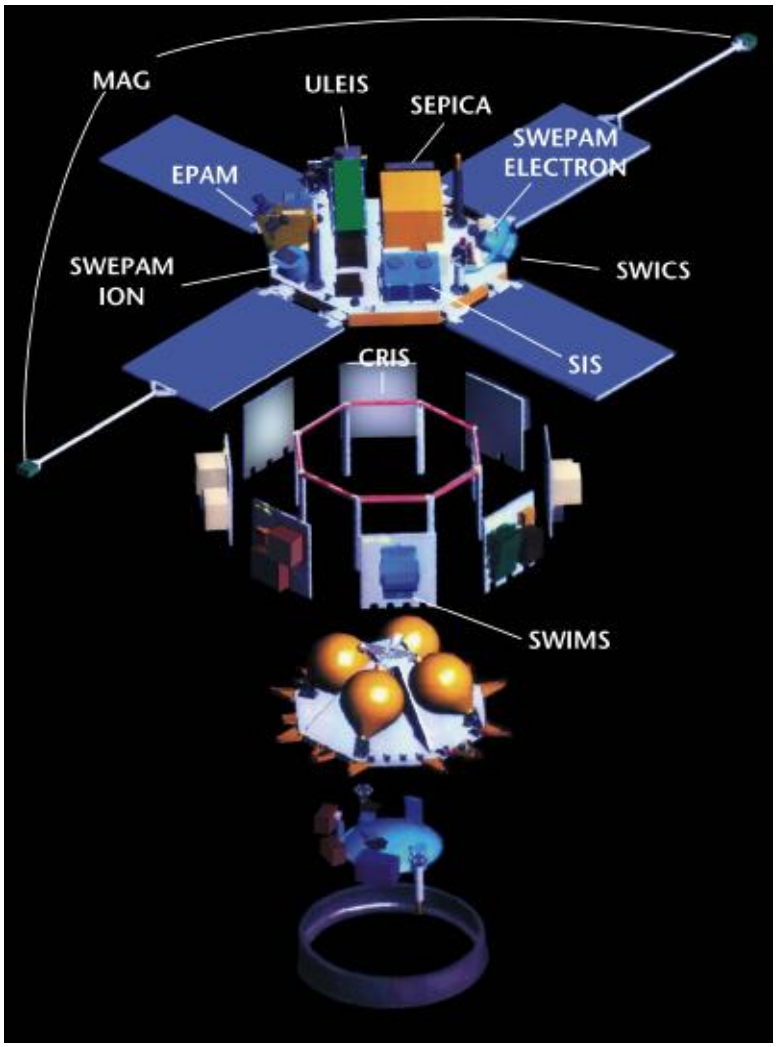

Figure 3.11: Exploded view of the ACE spacecraft structure (Stone et al., 1998) showing the location of the scientific instruments on board ACE.

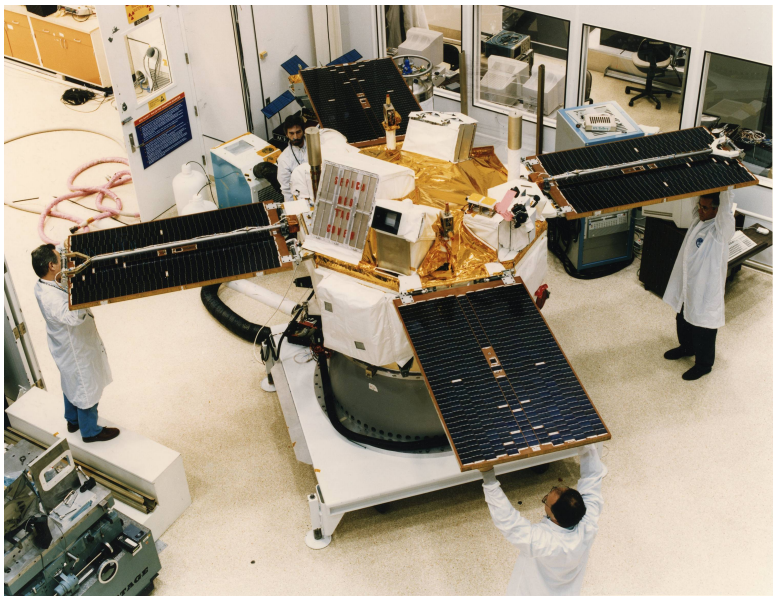

Figure 3.12: Engineers hold the solar panels in place during an examination of the ACE spacecraft in a cleanroom at the Johns Hopkins University Applied Physics Laboratory in Laurel, Maryland, where ACE was designed and built. Image credit: NASA/JHU-APL.

3.4 The Cluster Mission

The Cluster mission consists of a quartet of spinning spacecraft designed to observe the three-dimensional, small-scale structures within and in regions near to Earth's magnetosphere (Escoubet and Schmidt, 2000). The Cluster spacecraft achieve this by flying in close formation while making simultaneous observations, thereby enabling the quartet to distinguish between spatial and temporal changes. Importantly, the three-dimensional Cluster observations also mean that current densities can be measured without assuming the observed current sheets are elongated in a specific direction. The original Cluster quartet was due for launch in 1996 on the first test flight of the Ariane-5 booster. However, the launch vehicle's maiden flight lasted just 37 s before the automatic self-destruct system was initiated, and the remains of the Cluster I spacecraft were unceremoniously scattered over the nearby mangrove swamps.

Figure 3.13: Photograph of the launch of the first two Cluster II spacecraft (16/07/2001) on a Soyuz-U launch vehicle from Baikonur Cosmodrome, in Kazakhstan. The second pair of Cluster spacecraft where launched in August of the same year. Image credit: ESA/Starsem-S.Corvaja.

Happily, and in just 4 years, the Cluster mission was rebuilt. The four Cluster II spacecraft where launched in pairs on the 16th of July 2000 and the 9th of August 2000, both in Soyuz launch vehicles from the Cosmodrome in Kazakhstan. The Cluster mission has been extended several times since its original end-of-mission date in 2004. At the time of writing this thesis, the completion of the Cluster mission has had preliminary confirmation for a 2019-2020 extension, taking the Cluster

spacecraft to 20 years spent in space. The Cluster mission has contributed pioneering observations of the magnetospheric and interplanetary environments, that have shaped our understanding of the Sun-Earth connection. Major scientific highlights of the Cluster mission include: the first 3D observations of a magnetic reconnection null-point; observing the mysterious origins of dark aurora; and the discovery of huge, planet-scale Kelvin-Helmholtz vortices at the boundary between the Earth's magnetosphere and the solar wind.

Cluster Instrument Properties		
PEACE Parameter	LEEA Capability	HEEA Capability
Energy Range	0.59 eV - 26.4 keV	0.59 eV - 26.4 keV
Energy Resolution (FWHM)	0.127±0.006	0.165±0.007
Energy sweeps/spin	16, 32, or 64	16, 32, or 64
FOV (°)	179.4 x (2.79±0.14)	179.4 x (5.27±0.20)
Polar Angular Resolution (°)	3.75, 15	3.75, 15
Geometric Factor per 15 (°) zone (m^2 sr eV/eV)	1.6×10^{-8}	6×10^{-8}
Maximum Total Count Rate Over All Anodes (s^{-1})	$> 10^7$	$> 10^7$
FGM Parameter	Capability	
Dynamic Range (nT)	-64 to +63.992, -265 to +255.97, -1024 to +1023.9, -4096 to +4095.5, -5536 to +65528	
Digital Resolution (nT)	7.813 x 10^{-3}, 3.125 x 10^{-2}, 0.125, 0.5, 8	

Table 3.5: Summary of PEACE and FGM parameters (Johnstone et al., 1997; Balogh et al., 1997).

In this thesis, Cluster observations of solar wind electrons and the interplanetary magnetic were examined, in order to investigate the use of strahl beams as a tool for magnetic orientation. The instruments used to do so were the Plasma Elec-

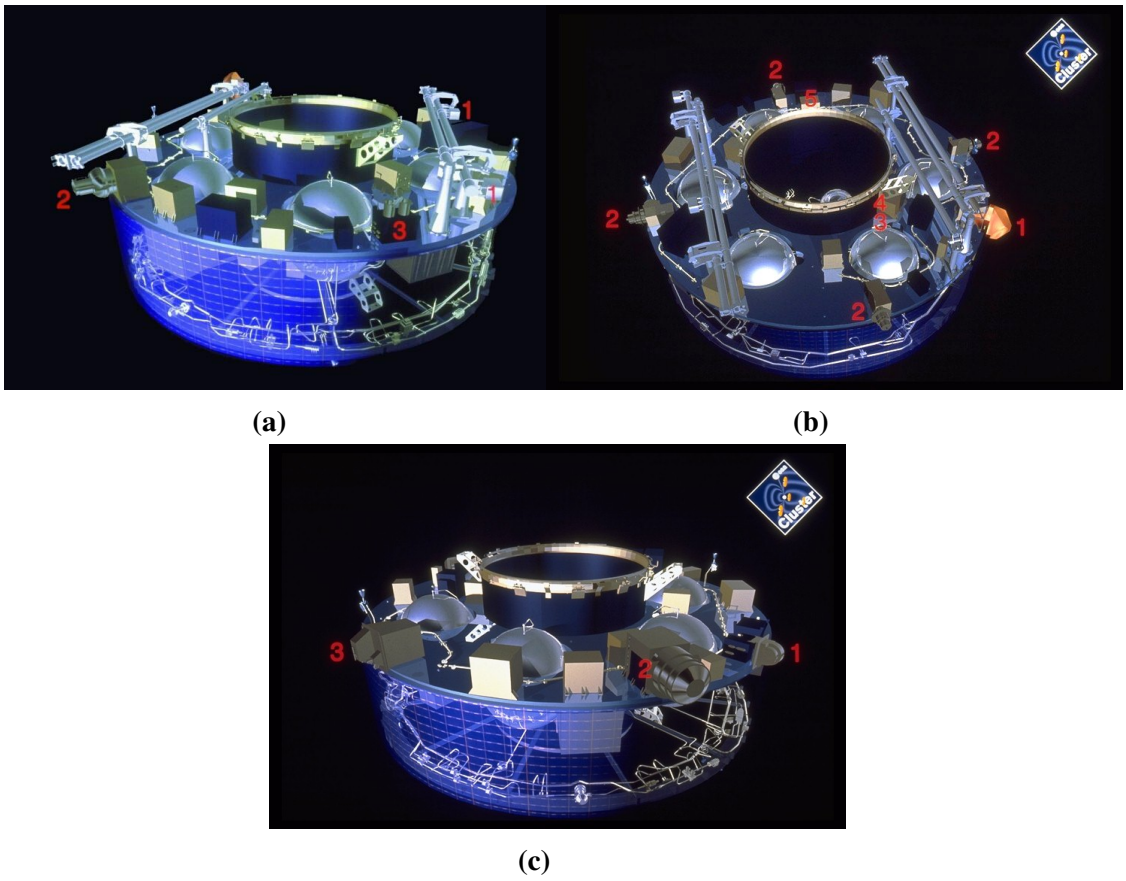

(a) (b)

(c)

Figure 3.14: (a) Cutaway of Cluster spacecraft main equipment platform, showing the FGM (1), EDI (2) and ASPOC (3) instruments. (b) Cutaway of Cluster spacecraft main equipment platform, showing the STAFF (1), EFW (2), DWP (3), WHISPER (4) and WBD (5) instruments.(c) Cutaway of Cluster spacecraft main equipment platform, showing the PEACE (1), CIS (2) and RAPID (3) instruments. Image Credit: ESA.

tron And Current Experiment (PEACE, Johnstone et al., 1997) experiment, and the Flux-Gate Magnetometer (FGM, Balogh et al., 1997). For a general description of how a fluxgate magnetometer work see Section 3.1.2. Cluster PEACE is a dual-sensor, top-hat electrostatic analyser, the design of which was modified for use on the Cassini mission (see Section 3.1.1). Each Cluster spacecraft has two top-hat sensors that are mounted on opposite sides. Each of the PEACE sensors have an energy range of 0.59 eV to 26.4 keV which is divided into 88 energy bins. The energy range observed by each PEACE sensor during an energy sweep, and the number of bins within that range, varies depending on the instrument mode chosen.

The two top-hat sensors on a Cluster spacecraft generally observe different, overlapping energy ranges and are thus called the Low Energy Electron Analyser (LEEA) and the High Energy Electron Analyser (HEEA). LEEA has an instanta-

neous FOV of 180° x 2.8° and HEEA has an instantaneous FOV of 180° x 5.3°. The 180° fan in each case is in the polar direction, parallel to the spacecraft spin axis, whereas the smaller azimuthal angular coverage is measure in the spin plane. Over the course of a spacecraft spin each PEACE sensor sweeps out a full 360° in the azimuthal direction, thus PEACE observes a full 3D distribution in 4s, or in 2s in the case of an overlapping LEEA and HEEA energy range. It should also be noted that the azimuthal resolution of the PEACE sensors varies depending on the number of energy sweeps that are completed during a spacecraft spin. The duration of a spacecraft spin is longer if a larger number of energy bins within a given range are selected, thus there is a trade off between higher resolution energy observations and angular resolution in the azimuthal direction.

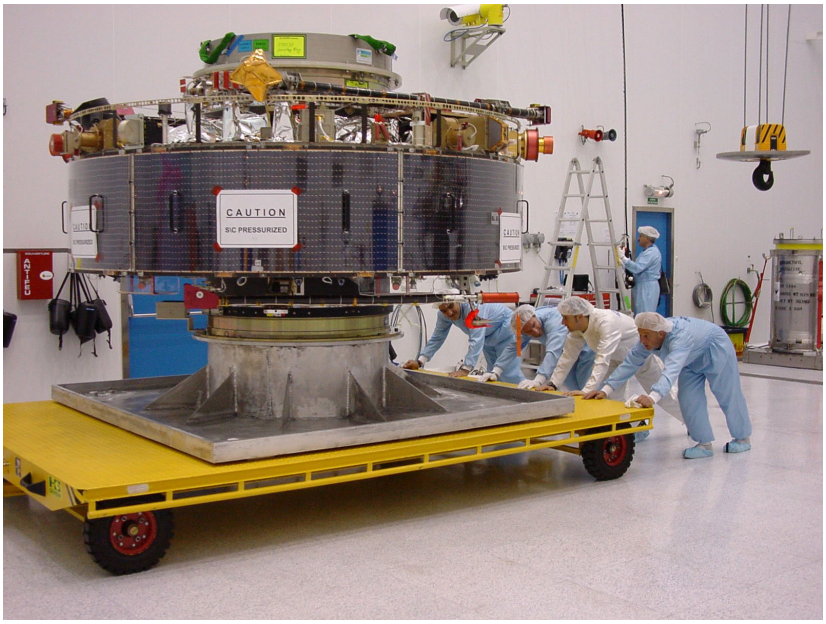

Figure 3.15: The Cluster spacecraft were transferred with a special trolley from the Hazardous Processing Facility (HPF) clean room to the Upper Composite Integration Facility (UCIF) clean room in Baikonur, Kazakhstan. Image credit: ESA.

3.5 Mars Express

Mars Express (MEX) began its interplanetary journey on a Soyuz/Fregat launch vehicle at the Cosmodrome in Kazakhstan on the 2nd June 2003. Named after the impressive rapidity and efficiency with which it was built, Mars Express has doubly appropriate nomenclature as it was launched when the positions of Earth and Mars allowed for the shortest possible route and it arrived at the Red Planet after approximately six months. MEX was initially inserted into a highly elliptical capture orbit and was later manoeuvred into its operational near polar orbit in January 2004.

Figure 3.16: Photograph of the Mars Express launch (02/06/2003) on a Soyuz/Fregat launch vehicle at the the Baikonur Cosmodrome in Kazakhstan. Image credit: ESA/STARSEM-S. CORVAJA 2003.

Six days before orbit insertion, MEX successfully ejected the Beagle 2 lander. Named after the HMS Beagle, aboard which Charles Darwin famously formulated his revolutionary (evolutionary) theories about life on Earth, it was hoped that Beagle 2 would inspire similarly great leaps in our knowledge of life on Mars. Unfortunately, the Beagle 2 lander never made contact and a crash landing seemed a likely possibility. However, analysis of images taken by the Mars Reconnaissance Orbiter revealed that Beagle 2 had in fact landed successfully on the surface of Mars, but that a partially deployed solar panel, pehaps due to damage of electrical systems on landing, likely resulted in a loss of communication with MEX (Bridges et al., 2017).

Whereas Beagle 2 was tantalisingly close to complete success, there is no doubt that the MEX spacecraft has fulfilled its mission expectations, providing observations of the Martian subsurface, surface, atmosphere and solar

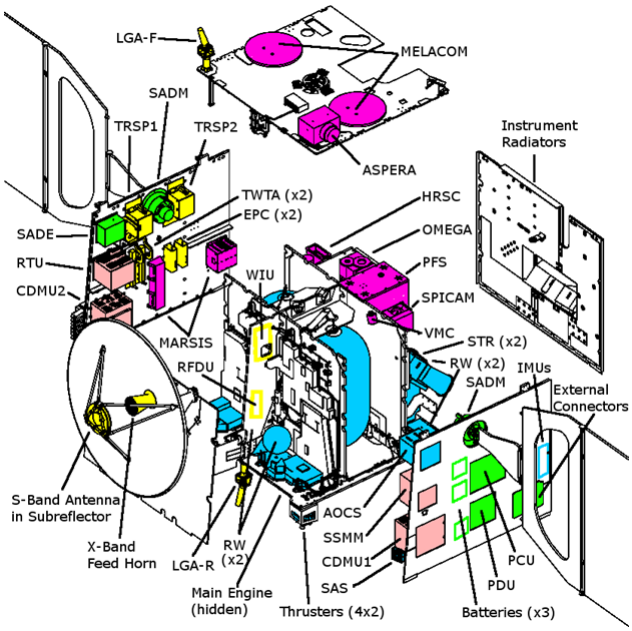

Figure 3.17: Diagram of the Mars Express spacecraft showing scientific payload and subsystems. Image credit: ESA.

wind-atmosphere interaction. Mission highlights include detection of methane in the Martian atmosphere, potentially with subsurface microorganisms as a source (Formisano et al., 2004), and the discovery of water ice in the South Polar ice cap (Bibring et al., 2004).

In this thesis, MEX observations of solar wind electrons were examined, in order to investigate the use of strahl beams as a tool for magnetic orientation. The instrument used to do so was the Analyser of Space Plasma and Energetic Atoms (ASPERA-3, Barabash et al., 2004) electron spectrometer (ELS). ASPERA-3 ELS is a standard top-hat electrostatic analyser mounted on a scanning platform that enables full-sky coverage. Electrons with an energy range of 0.01 - 20 keV are measured, with a maximum time resolution of one energy sweep per 4 s. The ELS has 16 anodes that observe 360°, so that the full angular distribution of electrons is measured during each platform scan from 0° to 180°.

Mars Express Instrument Properties	
ASPERA-3 ELS Parameter	Capability
Energy Range (keV/e)	0.01 - 20
Energy Resolution ($\Delta E/E$)	0.08
Energy sweeps/spin	16, 32, or 64
FOV (°)	10 x 360
Angular Resolution (°)	10 x 22.5
Geometric Factor per Pixel (cm^2 sr eV/eV)	5×10^{-4}
Actuator Angular Range (°)	180
Time Resolution Full 3D (s)	32

Table 3.6: Summary of ASPERA-3 ELS parameters (Barabash et al., 2004).

Figure 3.18: Photograph of Mars Express having its mass measured after spacecraft integration (08/1/2003). Image Credit: ESA.

3.6 Gaussian Fitting to Suprathermal Pitch Angle Distributions

A key part of the work in this thesis is the characterisation of strahl beam width. This is achieved by examining the pitch angle distributions of solar wind suprathermal electrons and determining the pitch angle width of the strahl. Pitch angle is described in more detail in Chapter 2, Section 1.4. In order to determine solar wind electron pitch angle distributions, electron observations are related to the concurrent magnetic field direction. The pitch angle of the centre of each anode is determined using the the orientation of the anode relative to the magnetic field direction. In general, the count rate measurements of the anodes are then averaged into pitch angle bins, the size of these bins varies between instruments with different resolutions.

In this thesis, strahl beam widths were determined by fitting a function consisting of the sum of two Gaussians, one centred on 0° pitch angle and the other on 180°, and a constant background term. The full-width-half-maximum (FWHM) of each Gaussian peak was then used as a measure of the width of the parallel (0°), anti-parallel (180°) or bi-streaming strahl beam while the constant term represents an isotropic halo population. This is a method which has been implemented in multiple previous observational studies (e.g. Hammond et al., 1996; Anderson et al., 2012) and strahl pitch angle distributions have been shown to be approximately Gaussian in theory (Horaites et al., 2017). An illustration of the strahl fitting technique is shown Figure 3.19.

The assumption that the halo is an approximately isotropic population means that the fitting method employed does not consider potential halo anisotropies. In order to minimise the effects of ambiguous pitch angle distributions, only strahl fitting results where the peak is at least 2 times greater than that of the background examined (e.g., Anderson et al., 2012; Graham et al., 2017). It is also required that the FWHM of the peak must be $< 180^\circ$ in order to be considered a strahl beam, as larger widths represent an almost isotropic distribution (e.g., Hammond et al., 1996; Anderson et al., 2012).

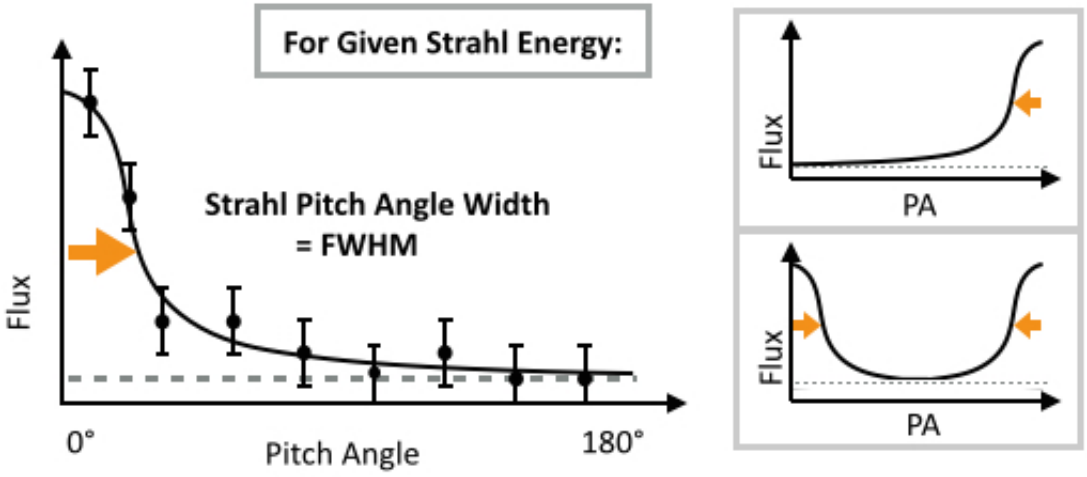

Figure 3.19: Illustration of fitting to average electron pitch angle distribution for a single suprathermal energy bin in the case of parallel (left), anti-parallel (right, upper) and bi-directional strahl(right, lower). Strahl beam width is given by the FWHM of the Gaussian peak at either 0° pitch angle or 180° depending on the IMF orientation. The data points are an illustration of the typical data examined and do not represent real data. The grey dashed line represents the constant background term.

3.7 Examining the IMF

In Chapter 4 a study of strahl evolution from 1 to 9 AU using the solar wind observations made by the Cassini spacecraft en-route to Saturn is presented. Reliable measurement of strahl beam width requires that two key criteria are fulfilled. Firstly, the observations were made while Cassini was in the 'pure' solar wind. Secondly, the selected suprathermal electron pitch angle distributions must cover the full range of 0 - 180°, such that any strahl beam can be clearly resolved. The first condition was fulfilled by removing times when Cassini is behind a planetary bow shock from the data set. For details of when Cassini was not in the solar wind we refer the reader to Rymer (2004), Arridge et al. (2006) and Achilleos et al. (2006). The Cassini electron instrument was not designed with the study of solar wind strahl electrons as a key science goal and, for reasons explained in more detail within this section, it was necessary to find a method to determine suitable periods within the solar wind for strahl pitch angle width observations to fulfil the second requirement.

Electron measurements are made by CAPS ELS (see Section 3.1.1). ELS comprises of a fan of 8 anodes, providing an instantaneous FOV of 5.2° in the azimuthal direction and ±80° in elevation (20° per anode). ELS is mounted on

actuating platform that can sweep through $\pm 104^{\circ}$ in the ELS azimuthal direction in 208s. However, as noted previously, this is the maximum actuation range and it is not always implemented. It should also be noted that, although the ELS instrument can sweep though its energy range in 2s, the time and/or energy resolution of the data were sometimes reduced by summing over several energy sweeps and/or pairing energy bins if CAPS ELS was assigned low telemetry priority.

The ELS FOV coverage in the solar wind is variable, for one energy sweep, or even one actuation, the observed electron distribution may not always contain the full electron pitch angle range required to determine the characteristics of the strahl component. This concept is illustrated in Figure 3.20 which provides examples of the approximate pitch angle ranges observed for different magnetic field orientations relative to the instrument FOV. In order to assemble full and representative 180° pitch angle distributions using CAPS ELS, it was necessary to identify individual parcels of relatively consistent solar wind, in which the CAPS ELS sensor has sufficient time to sample the full pitch angle distribution whilst the plasma parameters remained comparatively steady.

It has been suggested (Borovsky, 2008) that the solar wind is made up of a network of entangled magnetic 'flux tubes', each containing a distinct solar wind plasma population, and that these flux tubes are fossil structures originating from the solar corona. In this scenario, there should be limited changes in the plasma properties or behaviour within a particular flux tube. Hence, the electron data recorded between the flux tube boundaries should be suitable for averaging over the longer periods of time required to obtain a distribution which covers the full pitch angle range. This approach is a means of minimising the potential aliasing of the measured properties of two or more distinct plasma populations.

Borovsky (2008) showed that detection of large changes in the magnetic field direction and/or solar wind velocity can be used as a method for determining spacecraft crossing of a flux tube wall. However, due to limitations of the FOV outlined above, it is not always possible to determine the solar wind bulk parameters using Cassini CAPS. Thus, in order to perform our study of strahl over large heliospheric distances, only the magnetic criterion described in Borovsky (2008) are applied to identify periods in which we might expect relatively steady electron populations.

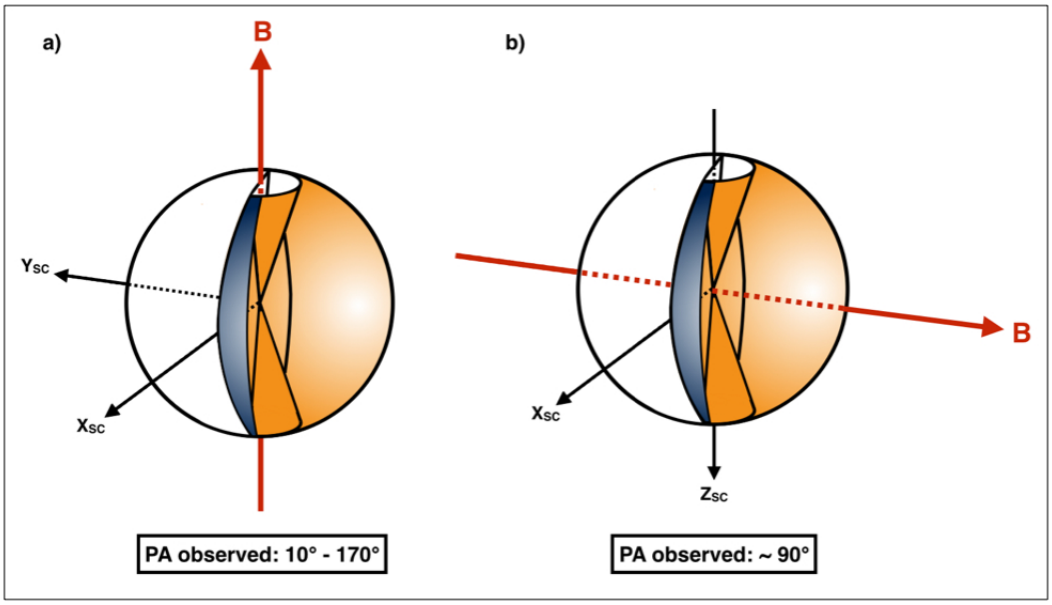

Figure 3.20: Sketch of the area of sky covered by the ELS anodes in respect to the spacecraft frame. The blue area represents the $\sim 10°$azimuthal x 160° elevation region covered in 1 energy sweep (for the telemetry mode used during the Earth flyby). The orange (+ overlapping blue) area represents approximate region covered in 1 actuation. (a) Shows an example of the total pitch angle range observed during one energy sweep for an unvarying magnetic field antiparallel to the spacecraft Z-axis. (b) Shows an example of the total pitch angle range observed during one energy sweep for an unvarying magnetic field antiparallel to the spacecraft Y-axis.

Neugebauer and Giacalone (2015) suggested that magnetic field magnitude changes are associated with tangential discontinuities more likely to originate in solar corona and therefore be associated with flux tube walls as opposed to rotational discontinuities that are associated with turbulence. Hence, an ancillary magnetic field magnitude criterion taken from Neugebauer and Giacalone (2015) is also implemented.

In the Borovsky (2008) investigation, solar wind angular discontinuities over $\sim 60°$ were found to be part of a population of large changes and interpreted to be crossings of the interfaces between flux tubes. Small changes, below $\sim 25°$, were interpreted to be a result of angular fluctuations associated with MHD turbulence. It was also found that significant changes in the properties of the plasma, such as alpha-to-proton ratio, occurred across these large angular discontinuities, or

flux tube boundaries, evidence that these boundaries are likely to originate at the Sun rather than forming in-transit within the solar wind. In the Neugebauer and Giacalone (2015) investigation sharp changes in energetic particle flux where identified and it was found that at least 68% of these boundaries where associated with significant plasma and magnetic field discontinuities which were be said to be unambiguously tangential if there was a magnitude change >20%. The criteria used in this thesis for flux tube wall determination based on changes in the magnetic field are as follows:

$$\Delta\theta \quad = \quad \cos^{-1}\left(\frac{\bar{\mathbf{B}}_{inst} \quad \cdot \quad \bar{\mathbf{B}}_{av}}{|\,\bar{\mathbf{B}}_{inst}\,||\,\bar{\mathbf{B}}_{av}\,|}\right) \quad > \quad 60^{\circ} \tag{3.1}$$

$$\frac{|\,\bar{\mathbf{B}}_{inst} - \bar{\mathbf{B}}_{av}\,|}{|\,\bar{\mathbf{B}}_{inst}\,|} > 0.2 \tag{3.2}$$

Where $\Delta\theta$ is the angular change in the magnetic field vector, $\bar{\boldsymbol{B}}_{inst}$ is the instantaneous 1s resolution magnetic field vector, and $\bar{\boldsymbol{B}}_{av}$ is the calculated running average for the time period required for the actuator to sweep through $\sim 180^{\circ}$. Further analysis was completed in order to determine the shortest periods of data accumulation within a flux tube and therefore produce as many statistically valid pitch angle distributions within a flux tube and hence between 1 and 9 AU as the dataset could support. The details of this work are presented in Chapter 4.

It should be noted that some studies that have argued that these "flux tube boundaries" are more likely to be structures that develop in-transit due to turbulence (e.g. Owens et al., 2011). However, whether the boundary forms in the corona or develops further out into interplanetary space is not critically important for our analysis. We simply use these IMF discontinuities in order to identify regions in which large changes in the electron populations are not expected and can therefore support the longer-term averaging needed to derive full pitch angle distributions from Cassini.

Another method that can be used to identify significant changes in the IMF is called partial variance of increments (PVI). PVI establishes a quantitative connection between large variations in scale and intermittency (Greco et al., 2009). This means that identification of intermittent events, such as such as current sheets be-

tween solar wind flux tubes, can be found by PVI exceeding a particular threshold value. PVI is given by the following equation (Osman et al., 2014):

$$PVI = \frac{|\,\Delta\mathbf{B}\,|}{\sqrt{<|\,\Delta\mathbf{B}\,|^2>}} \tag{3.3}$$

Where $\Delta\boldsymbol{B}$ is the change in magnetic field between measurements and the average is taken over 30 mins, which corresponds roughly to the time scale where solar wind turbulent fluctuations become uncorrelated (Osman et al., 2014). PVI is implemented in the work shown in Chapter 5, in order to examine the the magnetic variation during both solar wind electron and solar energetic particle observations.

3.8 Using Solar Energetic Particles to Estimate IMF Length

In Chapter 5 of this thesis, methodology developed in Solar Energetic Particle studies is used to estimate the path length travelled by the field aligned SEPs. Thereby enabling the estimation of path length travelled along the same field lines by strahl from the Sun to 1 AU. This method is implemented in order to examine the change in strahl width with distance travelled along the IMF, as opposed to examining the radial trend as in Chapter 4. Further details regarding the motivation for this type of investigation are presented in Chapter 4. SEPs are intermittent bursts of very high energy particles (electrons and ions) which are produced by acceleration at solar flare sites and interplanetary shocks. They are typically divided into two categories - gradual and impulsive. A visual summary of the two types of SEP are shown in Figure 3.21 .

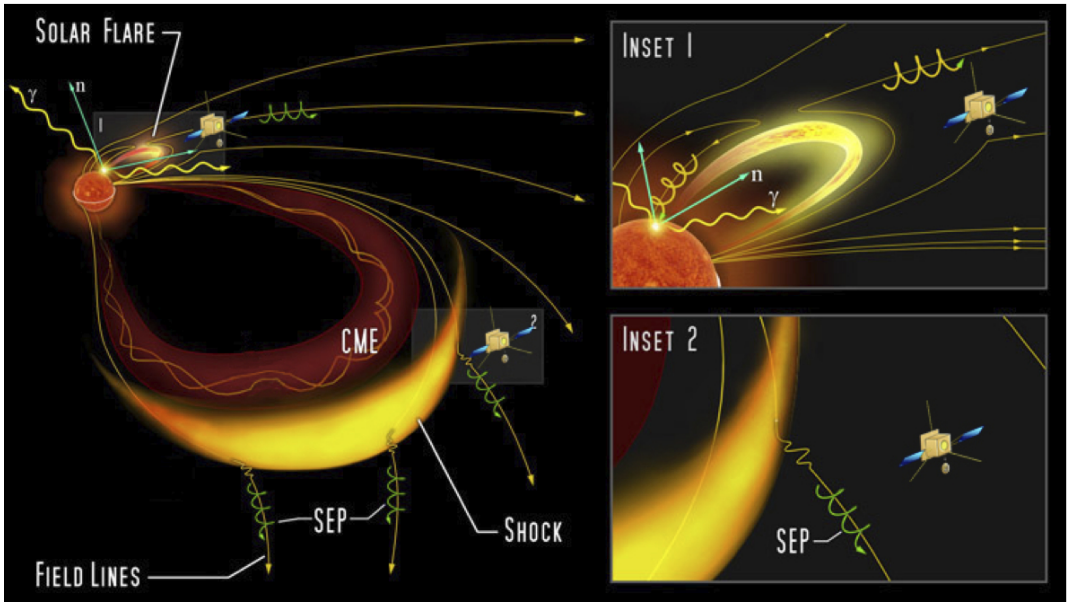

Figure 3.21: Illustration of an impulsive and gradual SEP event and associated phenomena (Lin and Szabo, 2006). Gradual SEPs are accelerated at interplanetary shocks, see inset 2. Gradual events are spatially extensive and associated with type II radio bursts. Impulsive SEPs are accelerated at solar flares, see inset 1. Impulsive events are spatially compact and associated with type III radio bursts. Both types of SEP propagate through the heliosphere along open IMF.

Within this body of work, only impulsive SEP events were selected for analysis as, in general, they are spatially and temporally less extensive than gradual events. For example, Reames (1999) estimated a 'source longitude' spread of $\pm 20^{\circ}$ for flux tubes containing promptly arriving impulsive SEPs, compared to that of the entire surface of the Sun for gradual events. In particular, ions accelerated in solar flares are observed to be well confined to flux tubes connected to the reconnection site (Mazur et al., 2000). It has also been observed that impulsive SEPs are associated with solar flares and with reconnection with open magnetic field lines that are magnetically well connected to the observer (Reames, 2013, and references within).

Some of these studies also found that impulsive SEPs are associated with type III radio bursts related to the transport of accelerated 10 keV-1MeV electrons. Type III radio bursts can be a useful proxy for the 'start time' of the SEP event (Tan et al., 2013). It is important to note that impulsive SEPs from the same source have been observed to have a spread of $> 130^{\circ}$ (Wiedenbeck et al., 2011), implying that SEPs may experience significant perpendicular transport. However, a recent investigation into an impulsive SEP event, in which the two Solar TErrestrial RElations Observatory (STEREO) spacecraft observed SEPs on opposite polarity field lines, found that the most likely explanation was particle propagation along non-radial magnetic field towards both spacecraft magnetic solar foot points (Klassen, 2017). Hence, widely spread impulsive SEPs may be a result of complex reconnection topology on the Sun as opposed to scattering effects. Hence, with careful examination of the events, SEPs can be used to estimate IMF path length.

In order to find the onset times for SEP events, the automated method outlined in the Krucker et al. (1999) study is implemented. For each species and for each energy, the particle flux is normalized relative to the background flux in units of standard deviation. This enables clear observation of any increase in energetic particle flux associated with the type III radio burst. An upper, or latest, limit for the onset time is then determined by locating the time at which the particle flux increases to 6σ above the background level, at any time beyond this limit the SEP event has definitely begun (Krucker et al., 1999). The onset time is then taken to be the first preceding time, relative to the upper limit, at which the normalised flux rises above the background level (Krucker et al., 1999). The difference between the up-

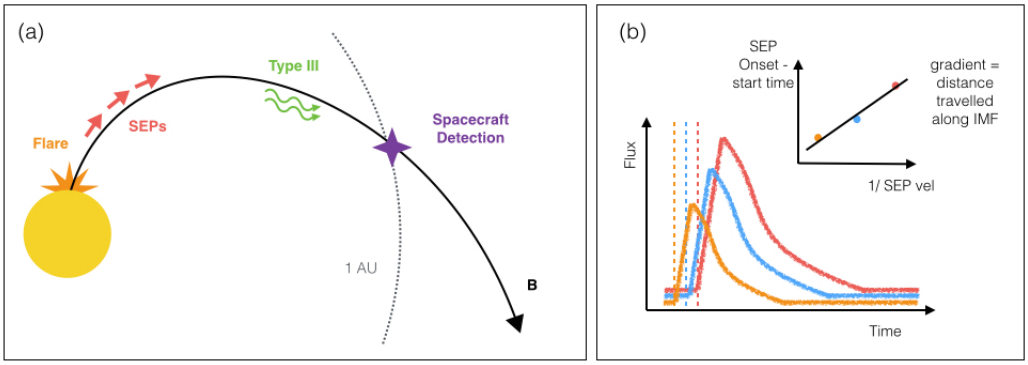

Figure 3.22: (a) Illustration of an impulsive SEP event and associated phenomena (Graham et al., 2018). SEPs are accelerated on an open Earth-directed IMF line, travel along the IMF, and are detected by the spacecraft at 1 AU. (b) Illustration of the observed increase in energetic particle flux at 1AU for three different energies (Graham et al., 2018): low (red), medium (blue), and high (orange). The dashed lines show the SEP onset times. The top corner inset shows an illustration of these onset times as a function of inverse SEP velocity. This inset shows the expected velocity dispersion, with faster particles arriving at the observer first.

per limit and the onset time can then be used as an estimate of the onset uncertainty. In the original Krucker et al. (1999) study, all onset times and uncertainties were also determined by eye for each individual event and it was found that the results were consistent with the automated method developed by Krucker et al. (1999).

Once the onsets for each species and for each energy were determined, velocity dispersion analysis (VDA) can be perfomed in order to estimate the IMF path length travelled by the particles, as shown schematically in Figure 3.22. VDA makes use of the different time-of-flight of different velocity SEPs (of the same species), with the assumption that they are released at the same time and location. The gradient of onset time as a function of the inverse of the particle velocity can then be used as an estimate of the length along the IMF travelled by the SEPs (e.g., Tan et al., 2013). This method also assumes that the first SEPs to arrive travel scatter-free (i.e., mean free path $>$ 1AU) to the observation point, resulting in enhancements in particle flux that display velocity dispersion.

Chapter 4

The Evolution of Strahl Electrons from 1 to 9 AU

Cassini observations of strahl pitch angle width evolution as a function of radial distance and electron energy are presented in this chapter. The majority of this work has been published previously in Graham et al. (2017), The evolution of solar wind strahl with heliospheric distance, Journal of Geophysical Research: Space Physics, 122(4), pp.3858-3874.

Strahl beams observed in the near-Earth solar wind have been shown to have a pitch angle width that is larger than predicted for adiabatic focussing to be the sole effect experienced by the strahl in-transit (e.g., Anderson et al., 2012). Average strahl width has also been observed to increase with radial distance from $\sim$ 1 to 2.5 AU (Hammond et al., 1996) and the strahl fraction of the total electron density has been observed to decrease relative to that of the halo population with heliospheric distance (e.g., Stverak et al., 2009). These findings imply that strahl electrons must be subject to some form of scattering process as they travel outward from the Sun. In particular, it seems likely that strahl electrons continue to be scattered as they travel outward away from the Sun, until eventually they form part of the diffuse halo population. The solar wind is too tenuous for Coulomb collisions to produce the scattering effect necessary to match all suprathermal electron observations (e.g., Vocks et al., 2005). Thus, numerous studies have concluded that the strahl scattering mechanism(s) must involve electron interaction with plasma waves rather than

via collisions (e.g., Saito and Gary, 2007; Pagel et al., 2007). Understanding the evolution of strahl electrons is key to unravelling what in-transit processes affect strahl, where and how frequently these mechanisms affect the strahl, and what the initial characteristics of the strahl electron population are likely to be at their solar origins.

The findings reported in the Hammond et al. (1996) of average strahl width with radial distance from the Sun demonstrated that strahl width increases with heliocentric distance for all observed strahl energies out to $\sim$2.5 AU. Beyond this distance, to $\sim$ 3.5 AU, the observations suggest that this increase in width may not continue, although the results within this distance range are fewer and were obtained over a large heliolatitude range. It has been demonstrated that in the presence of a constant scattering rate, independent of time heliocentric distance, and electron energy, the geometric effect of a Parker spiral IMF can, to a certain extent, explain why adiabatic focussing dominates closer to the Sun (within $\sim$20 R_S), whereas at larger heliocentric distances pitch angle scattering becomes more influential (Owens et al., 2008). This is because, for a Parker field line, the IMF becomes less radial at greater heliocentric distances and thus for a given unit of time/unit distance along an IMF line, a field-aligned electron further away from the Sun experiences a smaller decrease in magnetic field strength but the same constant scattering rate. The balance between adiabatic effects and scattering thereby explaining the apparent linear increase in strahl width observed from 1 to 2.5 AU.

It has also been demonstrated that time-of-flight effects could account for some of the apparent energy dependence of strahl pitch angle distribution broadening described by Hammond et al. (1996), who found that the strahl broadening per AU in radial distance from the Sun decreased with strahl energy. A less steep, but similar energy relation is obtained by time-of-flight effects in the presence of constant scattering rate, as electrons with greater velocities travel further along the IMF in a given unit of time and therefore experience a larger decrease in magnetic field strength and greater adiabatic focussing effects (Owens et al., 2008). It has also been suggested that this effect should decrease with increasing heliolatitude, as the Parker IMF becomes less tightly wound with heliolatitude. A quasi-continuous strahl scattering rate that is constant with heliocentric distance fits well to the Hammond et al. (1996)

observations (although it does not fully explain the observed energy relation). However, indications of strahl electrons have been found as far out as $\sim$10 AU by Walsh et al. (2013) using the Cassini spacecraft. The estimated strahl pitch angle widths were narrower than predicted by extrapolation of the observations within 2.5 AU and it was therefore concluded that the rate of strahl scattering should decrease with increasing radial distance.

In order to reconcile the numerous previous studies of strahl made within 4 AU with those of Walsh et al. (2013) and investigate the likelihood of a strahl presence at 10 AU, it was necessary to make consistent measurements of suprathermal electron pitch angle distributions across the widest heliospheric distance range to date. Thus, data obtained by the Cassini spacecraft across its interplanetary voyage to the Kronian system were used to investigate the radial evolution of strahl. Not only did CAPS ELS and FGM data from Cassini's cruise phase and flybys provide the required electron and magnetic field observations from $\sim$1 to 9 AU, but Cassini observations were also made over a minimal helio-latitude range. Hence, it was possible to characterize strahl width while avoiding the effects of variable helio-latitude, which has been invoked as a potential influence on electron observations (e.g., Hammond et al., 1996; Owens et al., 2008). Using single spacecraft observations over a radial distance range of 8 AU also meant that it was possible to extend previous studies of strahl evolution without the additional complications of cross-calibrating multiple spacecraft datasets (e.g., Maksimovic et al., 2005).

4.1 The Cassini Earth Flyby

The Earth Flyby was used to examine the methodology employed when examining the Cassini CAPS ELS data, before making use of the full solar wind dataset obtained over its journey to Saturn. The Cassini Earth flyby was selected because ELS was switched on while in relatively close proximity to spacecraft orbiting Earth and L1. During the Cassini Earth flyby event IMP 8, Geotail and Wind were orbiting Earth, and ACE was orbiting L1. Figure 4.1 shows the spacecraft locations from 17th to 25th August 1999. Both Cassini and the spacecraft selected for comparison were required to be in the 'pure' solar wind i.e., outside the Earths magnetopause, bowshock and electron foreshock. ACE was chosen for comparison to Cassini as the spacecraft is in a halo orbit of L1 and makes almost continuous observations of the unperturbed solar wind. Key times in the Cassini Flyby are given in Table 4.1.

Event	Date	Time (UT)
ELS on	17/08/1999	13:30:00
Inbound Bowshock	18/08/1999	01:51:27
Outbound Bowshock	18/08/1999	10:47:40
ELS off	25/08/1999	00:23:17

Table 4.1: Key times for the CAPS ELS instrument during the Cassini Earth Flyby (Rymer, 2004)

Solar activity varied over the flyby and so Cassini was subjected to slow and fast solar wind, as well as the effects of a ICME. In fact, examination of the magnetic field data for Cassini shows that, from approximately 21:00 UT on 20th to 18:00 UT on 23rd, Cassini was within a magnetic cloud (see Figure 4.2). Magnetic clouds are a particular class of ICME, typically characterised by three properties at 1AU: a large smooth rotation of the magnetic field direction; higher than average magnetic field strengths; and lower than average proton temperatures (Burlaga, 2001). A smooth rotation is observed in the Cassini magnetometer data, shown in Figure 4.2. However, Cassini spacecraft limitations mean that the spacecraft body often blocks the direction looking into plasma flow and so Cassini does not have solar wind parameter data available at all times. ACE also passes through a magnetic cloud

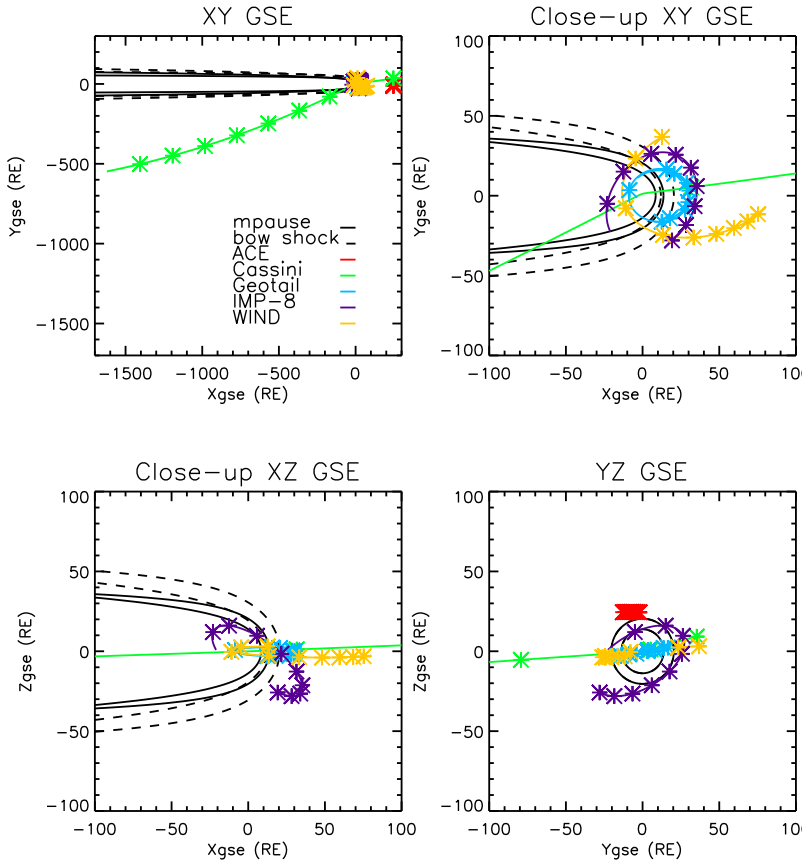

Figure 4.1: Showing locations of IMP 8, Geotail, Wind, ACE and Cassini for the Cassini Earth Flyby (17-25/08/1999). The upper left-hand panel shows the SC locations in the X-Y plane (GSE coordinates), the lower left-hand and upper right-hand panels show close-ups of SC orbiting the Earth in the X-Y and XZ planes respectively. The lower right-hand panel shows the spacecraft locations in the YZ plane i.e., looking face-on at the nose of the magnetosphere. The maximum and minimum extent of the Earth's bow shock (Chao et al., 2002, model calculated using ACE data) are represented by the dashed black lines. The maximum and minimum extent of the Earth's magnetopause (Shue et al., 1997, model calculated using ACE data) are shown by the solid black lines. The trajectories of IMP 8, Geotail, Wind, ACE and Cassini are shown by the purple, blue, yellow, red and green lines respectively. Crosses mark the start of each day.

during the Earth flyby event and, as a result of the very similar magnetic features observed by ACE and Cassini, it is concluded that both spacecraft observe the same magnetic cloud. It is also assumed that the solar wind parameters measured by ACE at the same time as a particular magnetic feature are approximately the same as those that were observed by Cassini. The proton temperature observed by ACE in the magnetic cloud can be seen to drop to approximately 10^4 K, which is a factor of 10 lower than average solar wind values at 1 AU.

In Chapter 3 Section 3.7 the variable nature of the Cassini electron spectrometer FOV is discussed. In particular, that the CAPS ELS FOV does not always observe the pitch angle range required to study strahl. It was therefore necessary to bin the ELS data over a longer time period, during which the observed magnetic field could be allowed to vary to a certain extent but during which Cassini must remain within a relatively steady plasma population. This enabled a larger pitch angle range to be observed, while also minimising the possible temporal aliasing of measured properties of distinct plasma populations. In the Earth fly-by analysis the 'flux tube boundary' method determined by Borovsky (2008) (discussed in Chapter 3 Section 3.7 was used to determine periods when the spacecraft was within an individual flux tube. Due to the FOV restrictions, Cassini did not always have solar wind velocity information and so it was not possible to use both of the criteria examined in Borovsky (2008). Instead, only the magnetic criteria for flux tube boundary identification was used, which assumes that an angular change in the magnetic field direction ($\Delta\theta$) of greater than 60° indicates a flux tube boundary.

On the 24th August 1999 the Cassini spacecraft was clear of any magnetospheric regions and the observations obtained by CAPS ELS and FGM are presented below. By comparing Cassini and ACE magnetometer data, and matching magnetic features by eye, it was estimated that Cassini was in solar wind with a speed of $\sim$ 400 km/s. Using the Borovsky (2008) magnetic criteria it was found that Cassini crosses through 6 suitable strahl observation periods during this time. Figure 4.3 shows $\Delta\theta$ with time, derived from Cassini magnetometer observations. Figure 4.4 shows electron data from within the 1st flux tube (01:50:14 to 03:11:09 UT). The time and anode averaged spectrogram for an hour within the flux tube shows that at energies of $\sim$ 70 to 1100 eV had significantly higher count rates for lower pitch

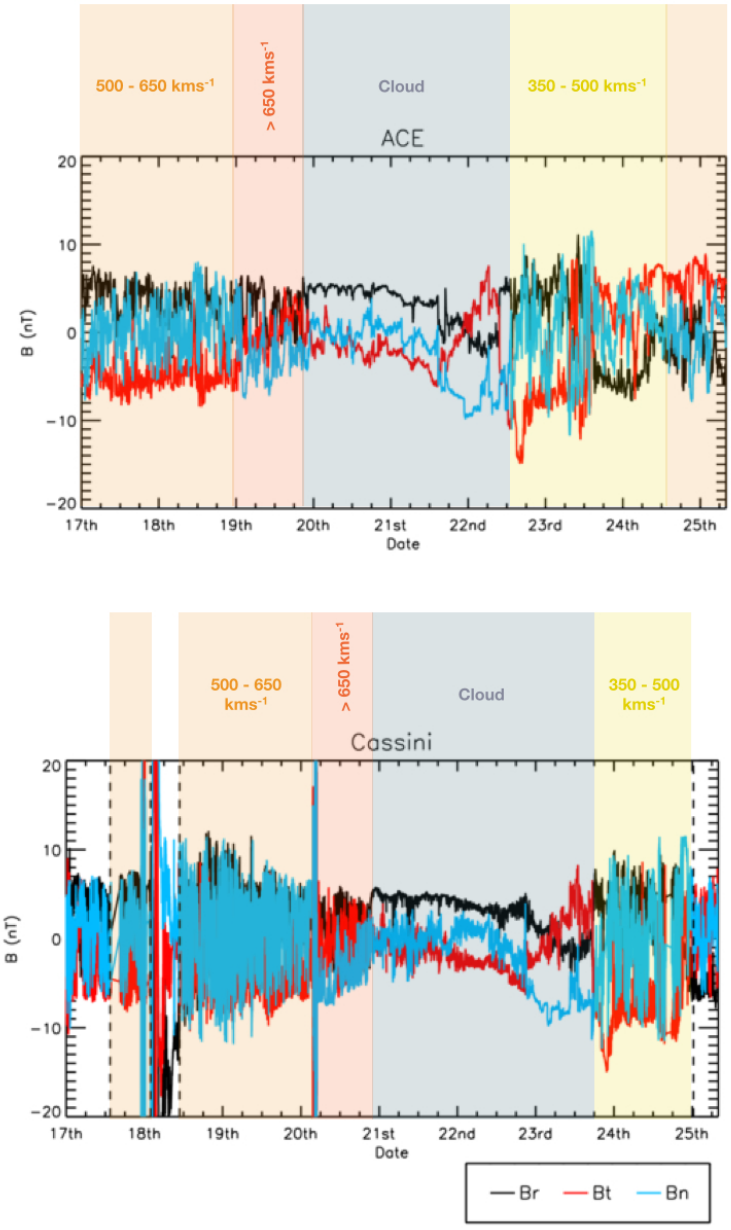

Figure 4.2: ACE (top) and Cassini (bottom) magnetic field vectors in RTN coordinates for Cassini Earth flyby (17-25/08/1999). The black, red and blue lines represent BR, BT and BN respectively. The dashed vertical lines correspond to the times listed in Table 3.2.2.1 and are for ELS on (13:30:00 UT 17/08/1999), bow shock crossing (01:51:27 UT 18/08/1999), magnetopause crossing (10:47:40 UT 18/08/1999) and ELS off (00:27:14 UT 25th). The large changes in magnetic field at approximately 24:00 UT on 17/08/1999 and 06:00 UT on 20/08/1999 are artefacts of SC manoeuvres. The smooth rotation, observed by Cassini (ACE) during the relatively quiet period from approximately 21:00 (24:00) UT on 20/08/1999 (19/08/1999) to 18:00 (12:00) UT on 23/08/1999 (22/08/1999), suggests that both SC pass through a magnetic cloud. The colour blocks of red, orange and yellow represent solar wind with $>$650 kms^{-1}, 500-650 kms^{-1} and 350-500 kms^{-1} velocity ranges. The blue shaded area shows the region within the magnetic cloud.

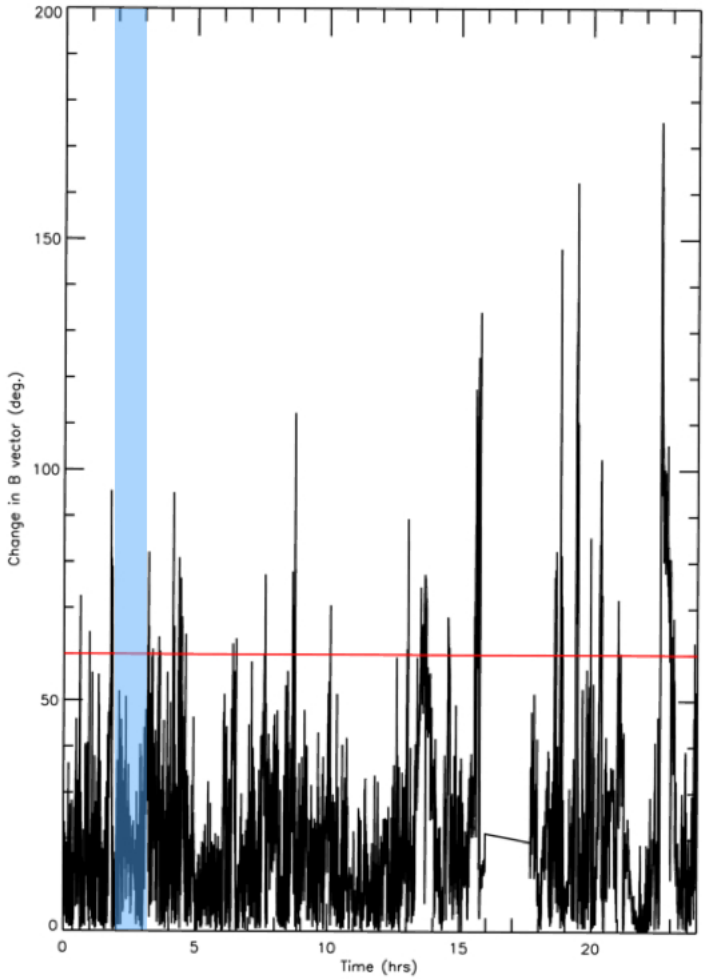

Figure 4.3: Showing the angular difference ($\Delta\theta$) between the instantaneous 1s resolution magnetic field vector, measured by the Cassini magnetometer, and the calculated 60 minute running average, for 24/08/1999. Any change of $>60^{\circ}$ is considered to indicate the presence of a flux tube boundary. 30, 10, 5 and 1 minute running averages were also analysed but are not included in this plot as they all in general agreement. Suitable strahl observation periods during this time are 01:50-03:11, 04:37-06:24, 06:32-07:35, 07:38-08:40, 08:46-10:06, and 10:06-13:01 UT. From $\sim$16:00 to $\sim$17:45 UT the magnetometer is not taking measurements and so the possible strahl observation period from 15:45:43 to 18:35:43 UT is not necessarily a single flux tube and cannot be treated as such. From $\sim$15:30 to $\sim$18:30 UT the actuating platform was not actuating. At $\sim$ 21:00 UT there is a large change in sun angle resulting from a spacecraft manoeuvre. The blue highlighted area is the 'flux tube' in which the example electron data presented this chapter was observed.

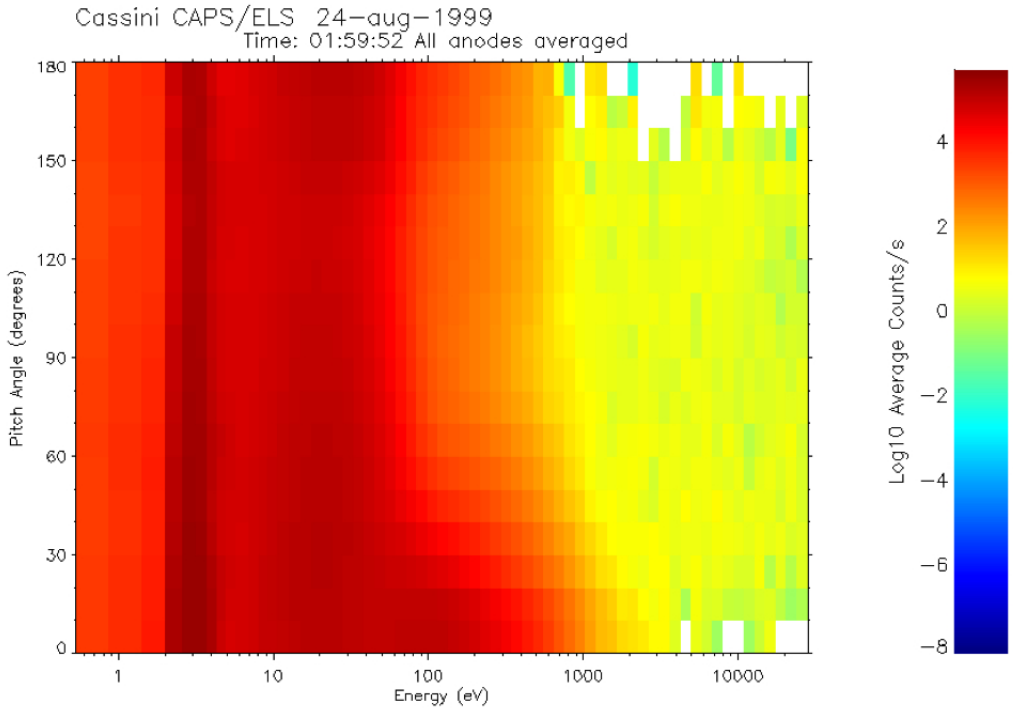

Figure 4.4: Cassini ELS observation of electron pitch angle against energy from 01:59:52 UT for 337 energy sweeps (≈1hr) on 24/08/1999. The colour scale represents the average number of raw counts/s detected by the ELS instrument for each pitch angle/energy bin [CASSPA plotting utility].

angle values, indicating a field aligned population of suprathermal electrons.

Examination of pitch angle distributions for a single suprathermal energy also show a clear strahl presence. Figure 4.5 shows an example pitch angle distribution for 67.15 eV (upper plot) and 200.9 eV. The 200.9 eV distribution has a distinct strahl peak with a FWHM of about 30°. The 67.15 eV distribution also has a strahl peak, although it is broader with a FWHM of about 70°. For both energies there also appears to be a small, broad secondary peak in the anti-field aligned direction. This suggests that the possible presence of back-scattered anti-strahl or perhaps an anisotropic halo distribution.

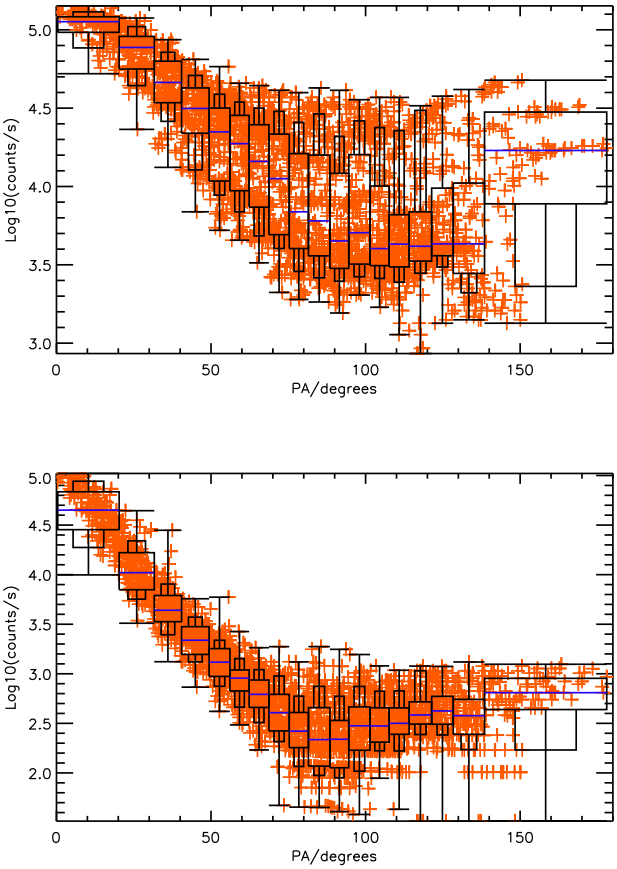

Figure 4.5: Log of the Electron count rate against pitch angle for the CAPS ELS energy bin with central energy of 67.15 eV (upper) and 200.9 eV (lower). Orange crosses are the instantaneous count rate for an individual anode and pitch angle of the centre of that anode. A box and whisker plot is fitted to the distribution, each pitch angle bin contains the same number of data points and so they vary in width. The primary boxes represent the upper and lower quartiles of the count rate data and the secondary, thinner boxes represent the 10th and 90th percentiles.

4.2 Characterising Strahl Width from 1 to 9 AU

4.2.1 Pitch Angle Distributions within a 'Flux Tube'

The 'flux tube boundary' criteria, described in Chapter 3 Section 3.7, were used to identify solar wind flux tube boundaries observed by Cassini for all time periods where both FGM and ELS data were available in the solar wind during its inter-planetary journey (see Figure 3.4). Once appropriate solar wind time periods had been identified, the look-direction and time-dependent background level count rate (as determined by Arridge et al. (2009)) was subtracted from the ELS data within each flux tube and the data from obstructed parts of the FOV were removed (as was done on Walsh et al. (2013)). No spacecraft potential information was available, and so no photoelectron contamination correction was made to the data. However, photoelectron contamination is unlikely at suprathermal energies, and so this is not expected to affect the results (Walsh et al., 2013). For each ELS measurement the pitch angle of the centre of each anode was determined using the the orientation of the anode relative to the magnetic field direction. These count rate measurements were then averaged into 10° wide pitch angle bins within each flux tube over the given time period detailed below. In order to achieve reasonable counting statistics while maintaining acceptable errors, the ELS data within each 10° pitch angle bin was subjected to a count rate criterion; all pitch angle bins must contain a sufficient number of individual count rate observations to produce an error for the mean count rate observation of $\leqslant 10\%$. The percentage propagated error ($\sigma_{\%prop}$) for the mean count rate for each bin was calculated as follows,

$$\sigma_{\%prop} = \frac{1}{m} \sqrt{\sum_{m=1} (\frac{\sigma}{x})^2} \tag{4.1}$$

where m is the number of observations, x is measured count rate, and σ is the count rate error (equivalent to the Poisson error on the count rate). The required number of observations (m_{req}) for each 10° pitch angle bin is therefore given by,

$$m_{req} = 10 \sqrt{\sum_{m=1} (\frac{\sigma}{x})^2} \tag{4.2}$$

In this way, the shortest periods of data accumulation within a flux tube which are able to satisfy the criterion were determined and individual observations within these periods could be averaged to produce as many statistically valid pitch angle distributions within a flux tube, and hence between 1 and 9 AU, as the data set could support. It should be noted that if the entire time within the flux tube was not enough to satisfy this criterion, then data obtained within this flux tube were rejected from any further analysis. Finally, data from periods with telemetry modes resulting in reduced time resolution of CAPS ELS were included, but no data were used from periods with reduced energy resolution, in order to maintain consistent energy bins.

For each event that satisfied the magnetic boundary (Chapter 3 Section 3.7) and count rate criteria (above), fits to the differential energy flux as a function of pitch angle were made for each suprathermal electron energy bin, as discussed in Chapter 3 Section 3.6. The function chosen for fitting consisted of the sum of two Gaussians, one centered on 0° pitch angle and the other on 180°, and a constant background. The FWHM of each Gaussian peak was then used as a measure of the width of the parallel (0°) and anti-parallel (180°) poulations, while the constant term represents an isotropic halo population, a method which has been implemented in multiple previous studies(e.g., Hammond et al., 1996; Anderson et al., 2012).

In the case where a bi-directional strahl was found using the fitting technique, the most intense strahl beam was chosen for use in the analysis. This choice was made as it is likely that broader strahl in a counter-streaming event has travelled either along the longer path of a closed IMF loop, along an IMF loop in the Sunward direction and therefore experienced adiabatic broadening, or has been reflected back off of an upstream shock (Gosling et al., 1993). Hence, the more intense strahl beam in a counter-streaming event was compared to those events with unidirectional strahl. It is possible that the strahl beams may have been exposed to different scattering regimes along the different legs of a closed IMF loop. Hence, a future investigation that solely examined the radial evolution of bi-directional strahl would be informative. However, this would be challenging due to the relatively low occurrence of bi-directional strahl which are generally observed $\sim$10% of the time in the solar wind whereas a single strahl beam is observed $\sim$65% of the time (Anderson et al., 2012).

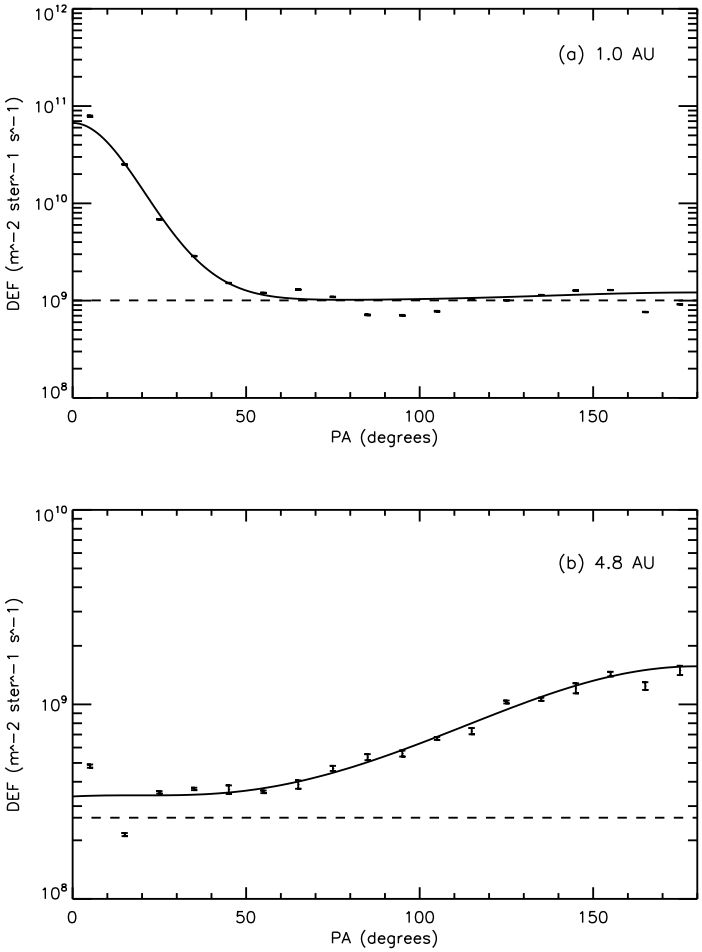

Figure 4.6: Electron pitch angle distributions observed at a heliocentric radial distance of (a) 1.0 AU and (b) 4.8 AU, plotted in units of $eVm^{-2}sr^{-1}s^{-1}eV^{-1}$ (Differential energy flux), for the CAPS ELS energy bin with central energy of 235.0 eV (Graham et al., 2017). Each data point represents the mean DEF determined for a 10° pitch angle bin. The solid line is a double Gaussian (one centred at 0° pitch angle and the other at 180°) plus a constant background term, fitted to the data using a non-linear least-squares fit method (Markwardt, 2009).

Two representative electron pitch angle distributions that fulfilled the analysis criteria and demonstrate the fitting technique are shown in Figure 4.6. Both example distributions are for the CAPS ELS energy bin with a central energy of 235.0 eV. The upper plot (a) shows field-aligned strahl observed at ∼1.0 AU, and the lower plot (b) shows broader, anti-field-aligned strahl observed at ∼4.8 AU.

4.2.2 Strahl width as a function of Radial Distance

In order to characterise the evolution of strahl beam width with heliocentric radial distance the criteria and fitting technique specified above were applied to all periods during Cassini's interplanetary journey for which both ELS and FGM data were available. Figure 4.7 shows the median strahl electron pitch angle width, and median absolute deviation, as a function of radial distance for CAPS ELS energy bins with central energies ranging from ∼70 to 600 eV. The upper bound of this energy range was chosen as count rates for ELS were too low to construct statistically acceptable pitch angle distributions above ∼600 eV. Particularly at large radial distances due to the decrease in electron density with distance from the Sun. The lower energy bound was chosen to allow direct comparison with observations made in previous strahl investigations (e.g., Hammond et al., 1996). The median value was obtained from radial distance bins of 0.5 AU width and was chosen over the mean to reduce the influence of skewed data and/or statistical outliers. Most observations made beyond ∼5.5 AU were not suitable for analysis because they did not fulfil the measurement criteria outlined above (see Section 4.2.1). Therefore, the rate of pitch angle scattering beyond this distance remains unknown. It should also be noted that some radial distances were omitted due to a lack of available data.

Examination of Figure 4.7 shows that, in general, strahl width increases with radial distance from ∼1 to 5.5 AU, in agreement with previous pitch angle width trends determined using Ulysses observations from ∼1 to 2.5 AU (Hammond et al., 1996). This implies that strahl is subjected to pitch angle scattering throughout the radial distances sampled by Cassini. Although, no conclusions can be drawn as to whether scattering is a relatively continuous or intermittent process, as only the general trends of electron evolution were investigated. A number of the results shown in Figure 4.7 diverge from a linear increase in pitch angle width with radial distance after ∼3 AU. Some energies, such as ∼320 eV, display variable median pitch angle width and others, such as ∼380 eV, display a more asymptotic trend. This variation with energy could be due to the presence of more than one scattering mechanism acting on the electrons with different mechanisms being more dominant at different radial distances. However, it should also be noted that although the IMF is generally well described by the Parker model (e.g., Burlaga et al., 1998;

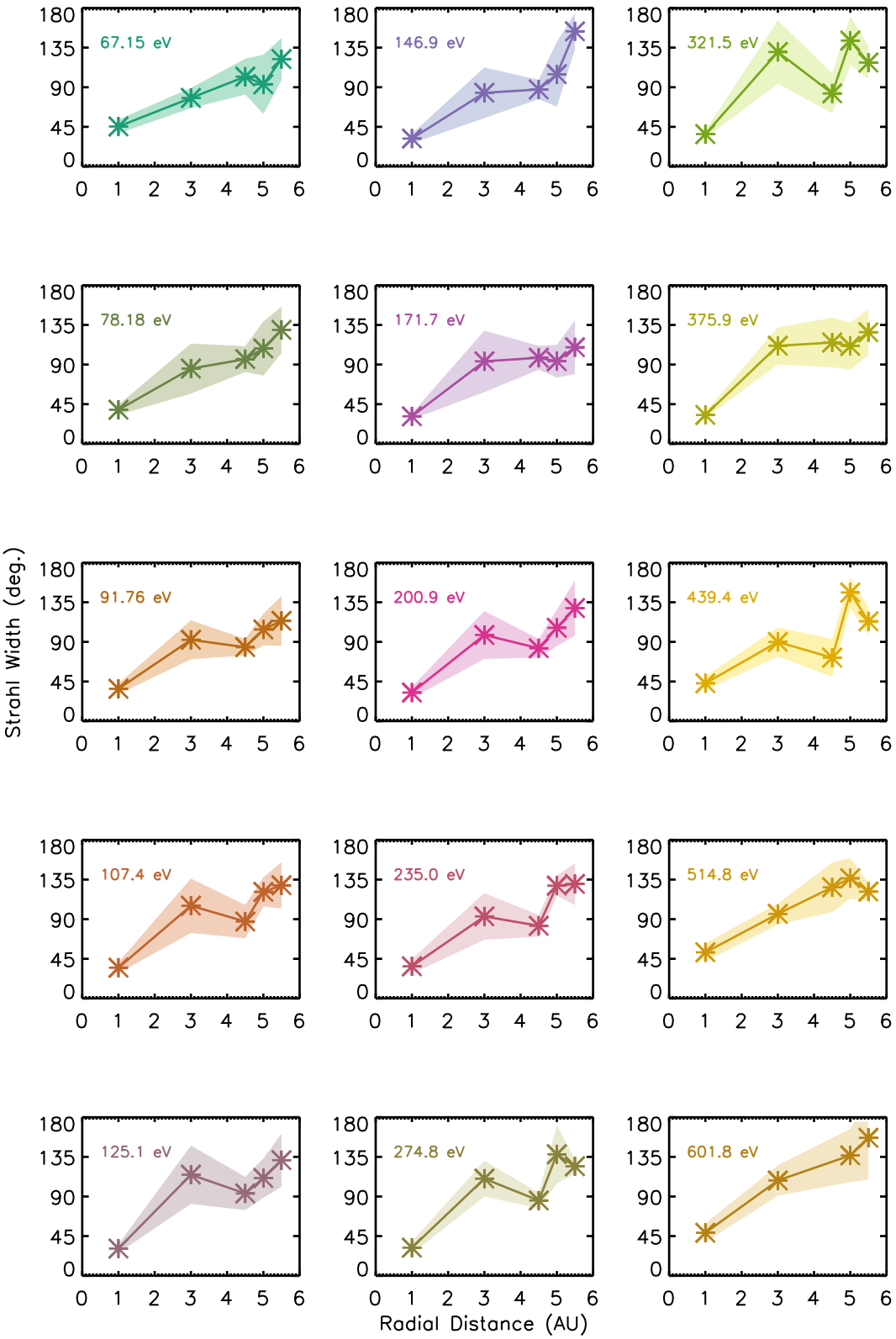

Figure 4.7: Strahl electron pitch angle width as a function of radial distance for CAPS ELS energy bins with central energies ranging from 67.15 to 601.8 eV (Graham et al., 2017). The plot shows median strahl width against radial distance for 0.5 AU bins. The colour-filled polygons represent the median absolute deviation.

Forsyth et al., 1996a), the magnetic field orientation can also deviate significantly (e.g., Borovsky, 2010). Hence, there could be implications for the consistency of adiabatic focussing experienced by the electrons observed by Cassini, as a more radial (less radial) IMF would result in greater (lesser) narrowing of the strahl beam per unit radial distance, as the change in field strength per unit radial distance is greater for a more radial field (e.g., Owens et al., 2008).

4.2.3 Strahl width as a function of Energy

The variation of strahl beam width with electron energy for a given radial distance is shown in Figure 4.8. From top to bottom, Figure 4.8 presents the median strahl width as a function of electron energy for radial distances of 5.5, 5, 4.5, 3, and 1 AU, normalized to the maximum value observed at that radial distance. At both 1 and 4.5 AU two relatively clear energy relationships can be observed: for lower electron energies ($\sim$70-150 eV), there appears to be an inverse relationship between strahl width with electron energy, whereas for higher energies ($\sim$200-600 eV), strahl widths increase with electron energy. The results obtained at 3 AU are less clear, although there is a sharp increase in strahl width observed for the lowest strahl energies (up to $\sim$120 eV), beyond this there is an approximately uniform strahl width with energy. Strahl width is approximately constant for higher energies at 5 AU and across all energies at 5.5 AU. There may be that some slight peaks for particular strahl energies at 3 and 5 AU ($\sim$300 and $\sim$100 eV respectively) that may indicate slight preferential scattering for particular strahl energies.

It is important to note that the inherent variability of strahl has resulted in quite large uncertainties. Hence, these relationships are merely indicative and quantitative conclusions could not be made based on these relationships. The variation in energy relations observed and the significant uncertainties found do suggest that there are likely multiple scattering mechanisms affecting the strahl population in the solar wind. These mechanisms are likely to produce competing effects on the energy relation of strahl width. This is in line with statistical findings at 1 AU which demonstrated that, at any given time, it was equally probable to observe strahl that either broadened or narrowed with electron energy (Anderson et al., 2012).

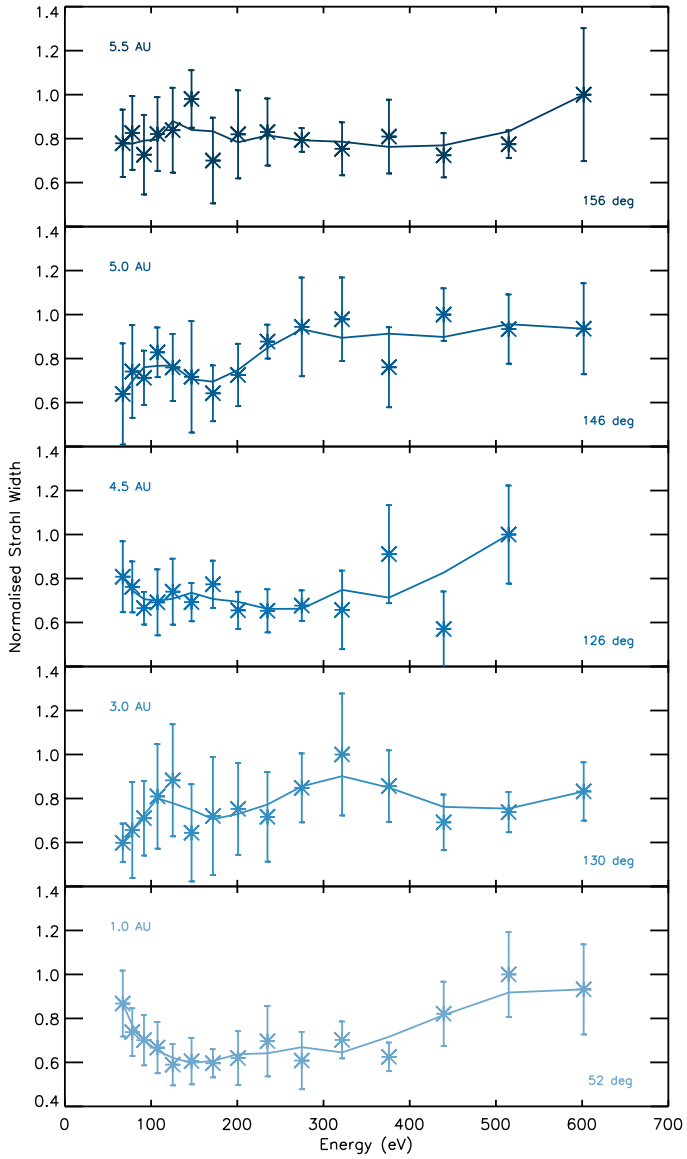

Figure 4.8: Strahl electron pitch angle width as a function of electron energy for 1 AU (bottom) to 5.5 AU (top) (Graham et al., 2017). The error bars plotted represent the median absolute deviation. The solid lines are a 3 point smooth of the data and are used only to highlight the trends observed. The values are normalised to the maximum strahl pitch angle width at each radial distance, the values of which are written in the bottom right of each panel.

4.2.4 Comparison to previous Strahl Evolution Studies

Previous observations of the evolution of strahl beam width made using the Ulysses spacecraft displayed indications that the increase in strahl width may fall off with radial distance (Hammond et al., 1996). The strahl width observations obtained using Cassini extend beyond the range of the previous study to 5.5 AU and demonstrate that strahl pitch angle widths continue to increase. A direct comparison between previous Ulysses results (Hammond et al., 1996) and the results obtained in this study are shown in Figure 4.9. The radial changes in strahl pitch angle width determined in this investigation were fitted by a linear function using a least squares fit method. Examination of the fits revealed that a linear increase in median strahl pitch angle with radial distance was appropriate for all compared energies. The Cassini results lie within the errors of previous estimates of strahl pitch angle width evolution, although it should be noted that previous errors (grey-filled area) are somewhat larger than those calculated within this study.

Discrepancies between the two strahl evolution studies could be due to a number of factors, one of which being the large uncertainties, particularly for the (Hammond et al., 1996) linear fits. Physical reasons for the contrasting results could also be due to the differences in spacecraft location during observation. The Ulysses observations were made in the fast solar wind, whereas Cassini observations were likely made in a mixture of solar wind regimes (see Section 4.2.6). It is also reported that the IMF becomes less tightly wound (more radial) as helio-latitude increases (Forsyth et al., 2002). Therefore, a change in helio-latitude could affect the adiabatic focussing experienced by strahl electrons (Owens et al., 2008), narrowing the expected strahl widths at higher helio-latitudes. The Ulysses data were obtained over a large helio-latitude range of $+30^{\circ}$ to -50°. Whereas, due to Cassini's near-equatorial trajectory, the observations reported in this study were obtained with minimal latitudinal variation.

A comparison with previous results of the change in strahl width with radial distance as a function of energy is shown in Figure 4.10. The Cassini results are shown (black solid line + blue errors) together with the relations derived observationally (red dashed line) by Hammond et al. (1996) and via modeling (orange dashed line) by Owens et al. (2008). The Cassini results were fitted with a linear

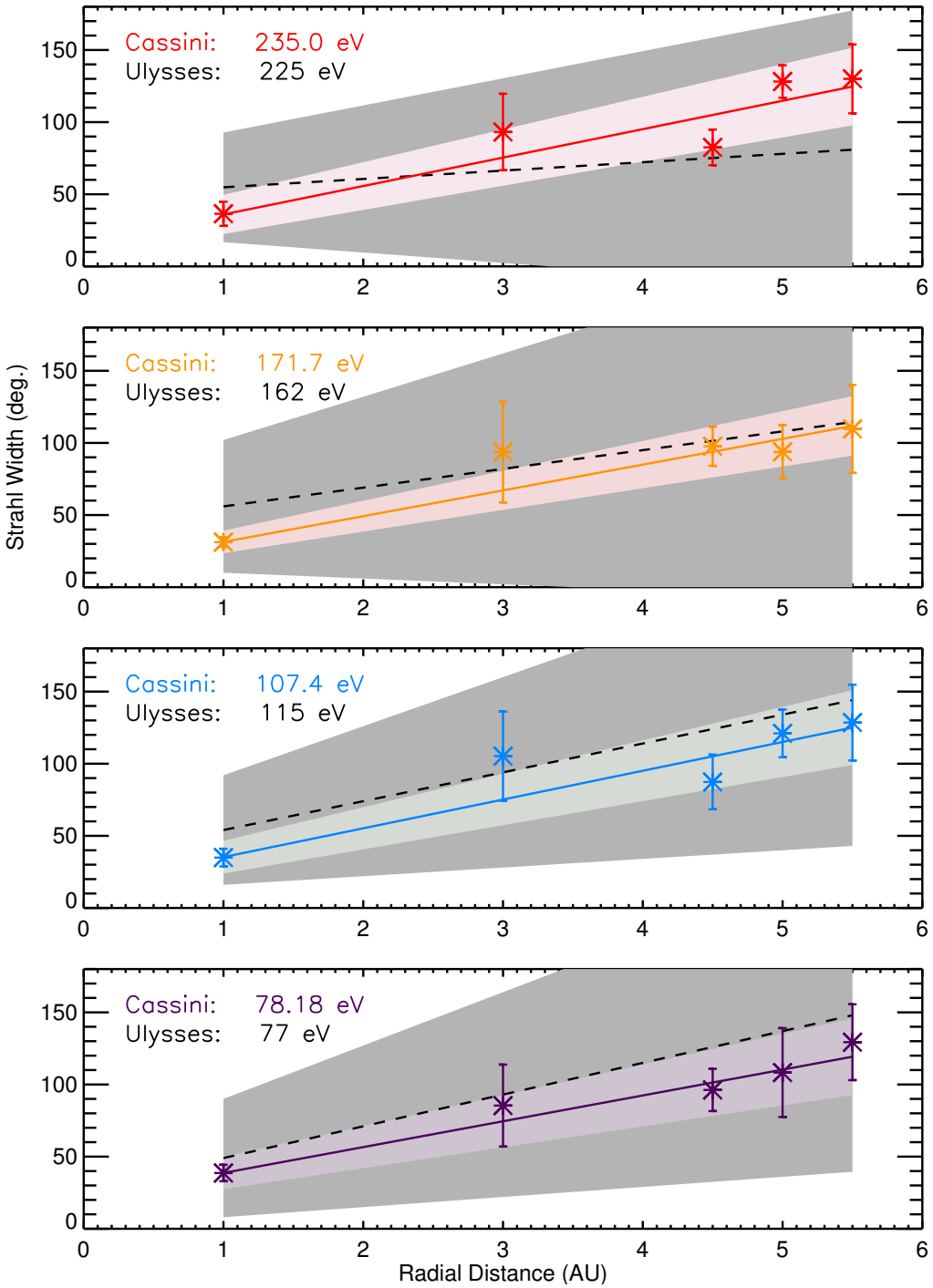

Figure 4.9: Strahl electron pitch angle width as a function of radial distance for CAPS ELS energy bins with central energies 78.18 (purple), 107.4 (blue), 171.7 (orange) and 235.0 eV (red) (Graham et al., 2017). Each panel shows median strahl width vs. radial distance for 0.5 AU bins. The error bars plotted represent the median absolute deviation, the solid lines are a linear fit to the results and the colour-filled polygons show the 1σ errors for the linear fits. The dashed lines represent the extrapolated Ulysses results for 77, 115, 162 and 225 eV from Hammond et al. (1996) and the grey-filled polygons represent their reported errors.

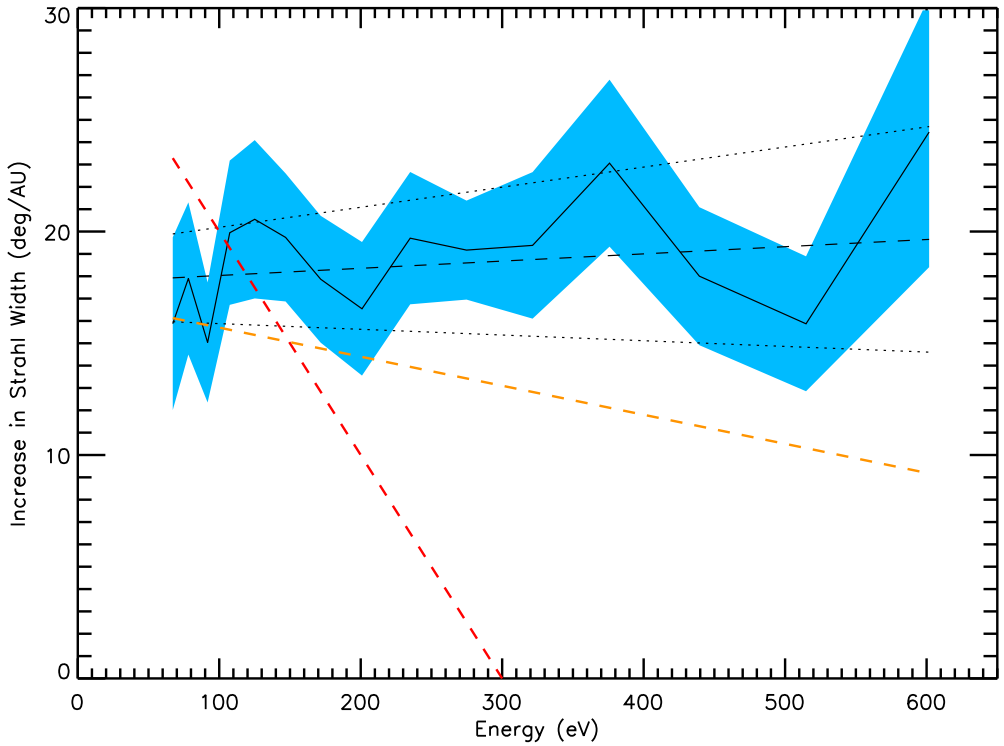

Figure 4.10: Variation in strahl width per unit distance as a function of electron energy, obtained from the linear fits to the strahl width vs. radial distance distributions (Graham et al., 2017). The results from this study are represented by the solid black line and the blue-filled polygon shows the 1σ errors for the linear fits. The red dashed line represents the extrapolated Ulysses results reported by Hammond et al. (1996). The orange dashed line represents the extrapolated Owens et al. (2008) results obtained through an empirical model based on the Hammond et al. (1996) observations. The black dashed line is a linear fit to the results from this study and the black dotted line represents the 1σ error for the fit.

function using a least squares fit method as previously detailed (black dashed line + black dotted errors). It was found that there is a slight increase in strahl pitch angle scattering rate with increasing electron energy. This is in contrast to the results of Hammond et al. (1996) and Owens et al. (2008), which showed an increase in width with radial distance that monotonically decreased with electron energy. It should also be noted that observational results obtained by Hammond et al. (1996) have a significantly steeper decrease with energy than the modelling results obtained by Owens et al. (2008).

The modelled results of Owens et al. (2008) shown in Figure 4.10 are based upon empirical fits to data within 2.5 AU presented in Hammond et al. (1996). However, unlike the Hammond et al. (1996) observations, the model demonstrated

that the effect of adiabatic focusing in a Parker spiral magnetic field, combined with a constant pitch angle scattering rate (constant with time, radial distance and electron energy), produces a weak energy dependence for strahl widths with radial distance (as shown in Figure 4.10 by the orange dashed line). This can be explained by time-of-flight effects, as faster field-aligned electrons travelling outwards along a Parker spiral field will experience a larger decrease in magnetic field strength per unit time/distance. Hence, in the presence of a constant pitch angle scattering rate, the effects of adiabatic focussing are stronger for more energetic electrons.

The increase in strahl pitch angle width with distance obtained by Owens et al. (2008), for $\sim$ 80 eV strahl is approximately the same as the observational results obtained in this study for the same energy, which in turn is of course consistent with the results of Hammond et al. (1996). Extrapolation of the modelled results for $\sim$ 80 eV gives a strahl pitch angle width of $\sim 100^{\circ}$ at 5 AU, which is in agreement with our median strahl pitch angle widths found at this distance using Cassini ($\sim 110^{\circ}$). However, at higher energies our observations diverge from the Owens et al. (2008) model, as higher energy strahl were found to broaden significantly more per AU than their lower energy counterparts. Hence, the results suggest that there is a dominant scattering mechanism with an intrinsic energy relation that extends beyond simple time-of-flight effects.

In Chapter 2, Section 2.2.6, a number of the different possible scattering mechanisms for strahl elections in the solar wind are discussed. One aspect to note here, is the hypothesis that resonant scattering could occur due to strahl interaction with broadband whistler fluctuations resulting from turbulent cascade (Saito and Gary, 2007). This study demonstrated that higher energy strahl were scattered more than lower energy strahl and thus this could explain why higher energy strahl would experience greater pitch angle broadening in the solar wind. It has also been shown that observations of this energy relation occur in conjunction with periods of enhanced magnetic field fluctuations in the whistler frequency range (Pagel et al., 2007) and that whistler-like fluctuations are often observed in the solar wind (e.g., Lacombe et al., 2014). Hence, the results from the Cassini strahl investigation suggest that, although there are likely multiple strahl scattering mechanisms present in the solar wind, a broadband spectrum of whistler mode waves could play a dominant

role in the radial evolution of strahl pitch-angle distributions.

4.2.5 Coverage of the Investigation

The Cassini spacecraft covered a radial range of ∼1 to 9 AU however, there were very few events beyond 5.5 AU that fulfilled the necessary acceptance criteria. This can be seen in of Figure 4.11 which shows the proportion of events that were considered acceptable for examination because they fulfilled the count rate criteria (a) and the beam-like distribution criteria (b), for each central energy, as a function of radial distance. Panel (a) of Figure 4.11 shows that the majority of events examined were during the Earth and Jupiter Flybys. It can also be seen that, for higher energy electrons, the percentage of total events examined drops off more rapidly with radial distance, most likely because of low count rates. Panel (b) of Figure 4.11 shows that the fraction of pitch angle distributions examined which have a FWHM $< 180^{\circ}$ also falls with radial distance, e.g., dropping from $\sim$ 0.95 to 0.60 by 5.5 AU for $\sim$ 120 eV. Hence, it was only possible to derive median strahl pitch angles for $\sim$ 1 - 5.5 AU and it was concluded that, at larger radial distances, the strahl is most likely completely scattered to form part of the halo population. This is consistent with previous observations of pitch angle width broadening with radial distance from $\sim$ 1 - 2.5 AU (Hammond et al., 1996) and observations of halo to strahl relative number density increasing with radial distance (e.g., Maksimovic et al., 2005; Stverak et al., 2009).

There is a notable decrease in the number of beam-like distributions at $\sim$ 5 AU, which is particularly pronounced for higher electron energies, and suggests that solar wind conditions at this distance may have been favourable for strahl scattering. Further analysis to find estimations of the prevailing solar wind conditions experienced at the time, including a detailed analysis of the magnetic fluctuations observed, may provide some insight into this deviation. The gradual increase of median pitch angle width over a large radial range also has implications regarding the formation of the halo. The implication being that, for an approximately isotropic halo to be observed at 0.3 AU (e.g., Stverak et al., 2008) to be solely a result of scattering of a suprathermal beam, much stronger scattering affects would need to be acting closer to the Sun. Extrapolation of linear fits to the data from Figure 4.8

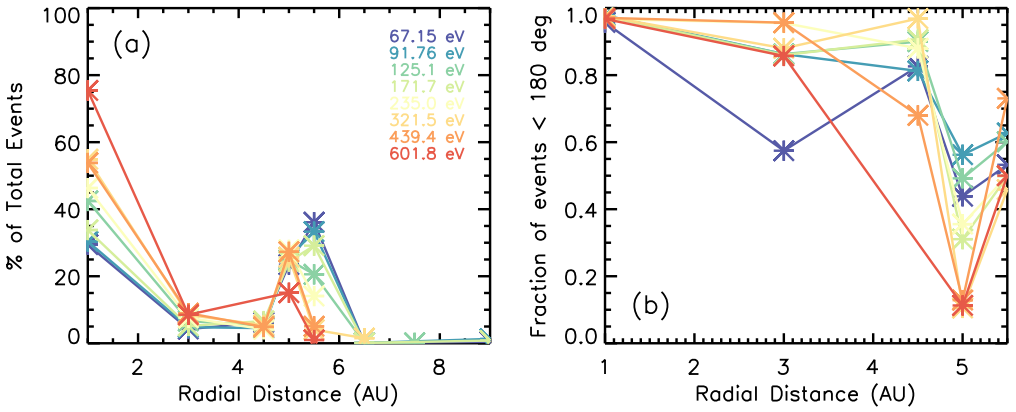

Figure 4.11: Panel (a) shows the percentage of total events examined (i.e., that pass the acceptance criteria specified in Section 3.2) for each central energy as a function of radial distance. Each energy is represented by a different colour ranging from 67.15 eV (purple) to 601.8 eV (red) (Graham et al., 2017). Panel (b) shows the fraction of events examined at each radial distance that have a pitch angle width $\leq 180^{\circ}$, and therefore can be considered to be a beam, against radial distance. Each central energy is represented by a the same colour as in panel (a).

suggests that by 10 AU, the majority of strahl would have been scattered to pitch angle widths $> 180^{\circ}$. This implies that indications of strahl found at $\sim$ 10 AU (Walsh et al., 2013) are more likely to be the result of a halo temperature anisotropy, than any field-aligned electron beam. However, it should be noted that this analysis was concerned with average strahl behaviour, whereas the results obtained at 10 AU are from an extended case study. Hence, the findings for average behaviour do not completely discount the possibility that strahl, subjected to fewer scattering events than average, may have been observed at 10 AU during the four day interval considered by Walsh et al. (2013). In order to further investigate the possibility of strahl at 10 AU, a number of Cassini solar wind intervals in which the full pitch angle range is observed could be examined.

4.2.6 Assumptions and Limitations of the Investigation

In order to derive clear strahl signatures using Cassini CAPS ELS, several assumptions were required. Most importantly, it was assumed that the solar wind can be considered to be made up of a tangled network of fossil flux tubes, that originate in the corona and expand outwards with the solar wind flow (e.g., Borovsky, 2008; Neugebauer and Giacalone, 2015). Some studies that have argued that these 'flux

tube boundaries' are more likely to be structures that develop in-transit due to turbulence (e.g., Owens et al., 2011). However, whether the boundary forms in the corona or develops further out into interplanetary space was not critically important for the presented analysis. The IMF discontinuities were simply used to distinguish between regions which had relatively steady electron populations and could therefore support the longer-term averaging needed to derive full pitch angle distributions from Cassini.

Identifying IMF discontinuities is not the only method of finding flux tube boundaries, observed changes in other parameters, such as solar wind bulk velocity (Borovsky, 2008) are often used in conjunction with magnetic field information. Since Cassini CAPS has a limited FOV, the derivation of accurate solar wind bulk parameters, such as density, temperature and velocity is more often than not impossible or else relies heavily on assumptions (e.g., Paschmann et al., 1998; Rymer, 2004; Lewis et al., 2008) and so no solar wind bulk parameters were examined in this investigation. This also means that different solar wind regimes have not been considered within this study, in which differing scattering mechanisms could potentially be invoked. The slow solar wind is often reported to have a broader strahl pitch angle distribution for a given energy than the fast solar wind (e.g., Feldman et al., 1978; Fitzenreiter et al., 1998; Anderson et al., 2012). It is also worth noting that in a Parker spiral IMF, slower wind would result in a less tightly wound magnetic field and thus strahl electrons would experience less adiabatic focusing effects per unit radial distance travelled. However, no conclusions on the radial dependence of strahl that separate any potential effects of the fast and slow solar wind on the evolution of electron pitch angle distributions were made using the Cassini dataset. Adiabatic focussing effects are also more significant within 1 AU, which is outside the range covered by the Cassini dataset.

4.2.7 Potential Strahl Scattering Mechanisms

A number of different possible strahl scattering mechanisms were discussed in Section 2.2.6. The variation in energy relations observed and the significant uncertainties found within the investigation within this chapter, suggest that there are likely multiple scattering mechanisms affecting the strahl population in the solar wind. This is in agreement with previous statistical findings which demonstrated that, at any given time, it was equally probable to observe strahl that either broadened or narrowed with electron energy (Anderson et al., 2012).

One particular scattering mechanism to note at this point is due to resonant interaction with a broadband spectrum of Whistler fluctuations resulting from turbulent cascade (Saito and Gary, 2007). The modelled results for this scattering mechanism result in strahl pitch angle width that broadens with increasing strahl energy and the results presented in Section 4.2.4 found that higher energy strahl broaden more per AU than their lower energy counterparts (see Figure 4.10). Therefore it seems likely that there may be a dominant strahl pitch-angle scattering mechanism in the solar wind and a broadband spectrum of whistler mode waves provides an energy dependence that can account for greater pitch angle broadening per unit radial distance for higher energy electrons. This idea is examined in more detail in Section 5.3 of Chapter 5.

Chapter 5

Using Solar Energetic Particles to Study Strahl within 1 AU

Wind spacecraft observations of strahl pitch angle width as a function of IMF path length and electron energy are presented in this chapter. The majority of this work has been published previously in Graham et al. (2018), Investigating the Effect of IMF Path Length on Pitch-angle Scattering of Strahl within 1 AU, The Astrophysical Journal, 855(1), p.40.

Observations of strahl beam width in the solar wind at 1 AU reveal strahl that are frequently too broad to be due solely to expansion effects (e.g., Owens et al., 2008; Anderson et al., 2012; Graham et al., 2017). Thus, solar wind suprathermal electrons must be subject to some form of scattering process, or processes, most likely via wave-particle interactions (e.g., Saito and Gary, 2007; Pagel et al., 2007; Smith et al., 2012; Landi et al., 2012; Pavan et al., 2013). In general, strahl width increases with heliospheric radial distance beyond 1 AU (e.g., Hammond et al., 1996; Graham et al., 2017). These findings imply that suprathermal electrons are subjected to in-transit scattering processes throughout the heliosphere. In this investigation, strahl evolution within 1 AU is examined via a novel technique that makes use of estimates of the IMF length.

Narrow strahl features ($< 20^{\circ}$) are most commonly observed in the coronal hole solar wind (e.g., Fitzenreiter et al., 1998; Anderson et al., 2012) and it has

been shown that, in general, strahl pitch angle widths are narrower in the fast solar wind than the slow solar wind (e.g., Feldman et al., 1978). This suggests that the strahl has either undergone a lesser degree of scattering in-transit within the fast solar wind than the slow wind, or that the different origins of the slow and fast solar wind result in different electron velocity distributions. However, it should also be noted that proximity to IMF sector boundaries may have a more significant effect on strahl width than wind speed, producing a strahl pitch angle broadening effect that is independent of electron energy (Pilipp et al., 1987b).

It has also been shown that narrow strahl features are fractionally more likely to occur for bi-directional strahl associated with closed magnetic field loops within an ICME than in the solar wind as a whole (e.g., Anderson et al., 2012). ICMEs and the fast solar wind do not generally originate from similar source regions (Schwenn, 2007, and references within). However, ICMEs frequently experience over-expansion as they propagate away from the Sun i.e., the magnetically isolated ejected material expands faster than the surrounding solar wind (Gosling et al., 1994; Richardson and Cane, 1995). In addition, the fast solar wind generally has more radial IMF than the slow solar wind. Therefore it is likely that both ICMEs and fast solar wind have a greater decrease in IMF strength per unit distance along the IMF direction than the slow solar wind; thereby providing a greater adiabatic focusing effect for the strahl scattering mechanism to overcome (e.g., Anderson et al., 2012). Therefore, it seems likely that the topology of the IMF and, specifically, the path length travelled by the strahl electron, should have a significant effect on the width of the strahl observed at 1 AU. If an average IMF length along which the strahl has travelled can be reliably estimated, then information pertaining to the strahl scattering mechanisms in relation to electron energy and distance can be obtained, which then takes into account the effect of the IMF topology and adiabatic focusing experienced by the electrons.

On average the IMF topology agrees with the Parker solar wind model, but observations have also shown that the in-ecliptic magnetic field angle can significantly deviate from the expected spiral field direction, sometimes by 90° (e.g., Forsyth et al., 1996b; Owens et al., 2008; Borovsky, 2010; Owens and Forsyth, 2013). This means a Parker model IMF on its own is not sufficient for the accurate

estimation of field line length required in this type of investigation. As an aside, the variation in observed magnetic field direction compared to the Parker modelled angles may also partly explain why, although strahl width is generally broader in the slow wind, there is no direct correlation between solar wind speed and strahl width (Pilipp et al., 1987b). However, it is possible to use the onset time of SEP events to find the IMF length travelled by energetic particles along the field (e.g., Krucker et al., 1999). Hence, in this Chapter the methodology developed in SEP studies was used to determine the path length travelled by the field aligned SEPs. From this, an estimate of the path length travelled along the same field lines by strahl from the Sun to 1 AU. The relation of the IMF estimates to the average observed width of the strahl was then examined.

5.1 Solar Energetic Particle Methodology

5.1.1 Determining Solar Energetic Particle Onsets

An independently derived list of 69 SEP events and associated phenomena originally studied by Nitta et al. (2006) was used as the starting point of the investigations presented in this chapter. These 69 SEP events were determined to be impulsive rather than gradual, with associated observed type III radio bursts. Hence, the SEPs from these events likely had a limited spatial extent and it could be assumed that the SEPs for each event had the same source time and location. In addition, Nitta et al. (2006) also investigated the source regions of the SEP events and found that $\sim$ 80% of the events were in close proximity to source regions with open magnetic flux and were thus likely to have be magnetically well connected to the observer. The Nitta et al. (2006) events were visually inspected to verify the location of the Wind spacecraft with respect to the different plasma regions surrounding the Earth. A number of the Nitta et al. (2006) events were then discarded from our analysis, as examination of spacecraft position and plasma parameters suggested that the Wind spacecraft was either situated in the magnetosphere or that there was ambiguity regarding the purity of the solar wind observed, for example due to proximity to the foreshock.

High energy electron and helium SEP fluxes for the days associated with each catalogued type III radio burst from Nitta et al. (2006) where examined for onsets. Two different particle species were chosen as electrons behave differently from ions as they resonate with different wave modes. Thus, by comparing path lengths estimated using both, the possible role of wave-particle interactions affecting IMF length estimates could be investigated. In order to find the onset times for the SEP events, the method as outlined in the Krucker et al. (1999) study, described in Section 3.8, was implemented. Briefly, for each species and for each energy, the particle flux is normalized relative to the background flux and the onset time is then taken to be the first time at which the normalised flux rises above, and then continues to rise significantly over, the background level. Examples of SEP onset times obtained are shown in Figure 5.1.

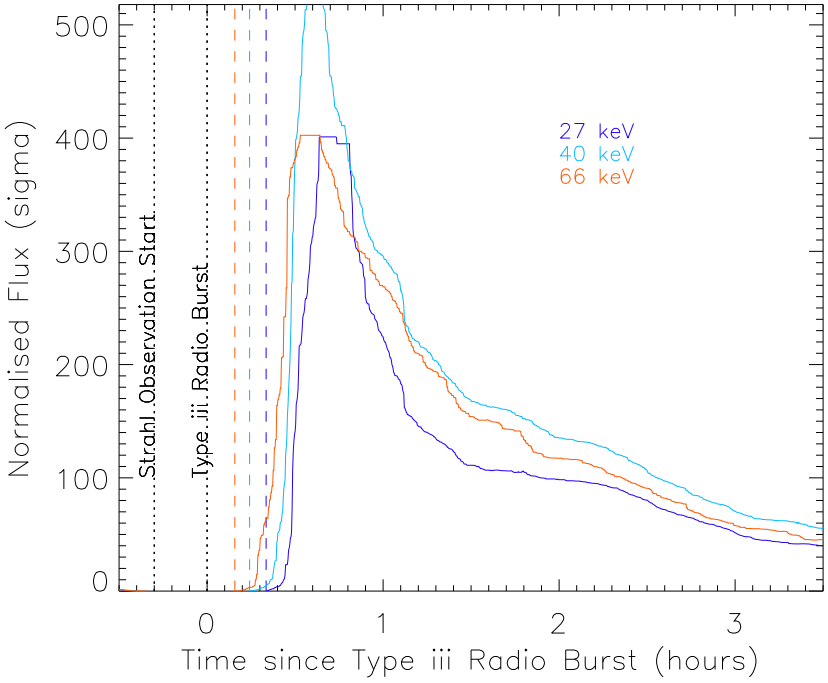

Figure 5.1: An example of SEP onset time detection for electron SEPs with energies of ∼ 27, 40 and 66 keV (Graham et al., 2018). The plot shows normalised SEP electron flux as a function of time since the associated type III radio burst onset. The SEP electron flux is normalised in units of standard deviation relative to the background flux for each energy. Onset times for each energy are marked by the vertical dashed lines in the corresponding colour. The type III radio burst onset time is marked by a dotted and labelled line. The average strahl pitch angle width (see Section 3.6) is found for the 20 minutes before the observed type III radio burst onset.

5.1.2 Estimating IMF Path Length

Once the onsets for each species and for each energy were determined, VDA was performed to estimate the IMF path length travelled by the particles, as described in Section 3.8. Previous studies have found that ion VDA generally produces reasonable estimates of IMF path length but VDA for electron SEPs can result in unphysically short path lengths (i.e., < 1 AU) (Tan et al., 2013). It has been suggested these short path lengths may be an effect of energy deposition in the solid state telescopes on the Wind spacecraft, which would result in apparent increase in flux for the lower energy bins earlier than expected and shorten the path length estimate (Tan et al., 2013). However, energy deposition should not be an issue if the intensities are high enough (Haggerty and Roelof, 2002). Hence, before conducting analysis using the electron SEP onset times, the SST observations were first com-

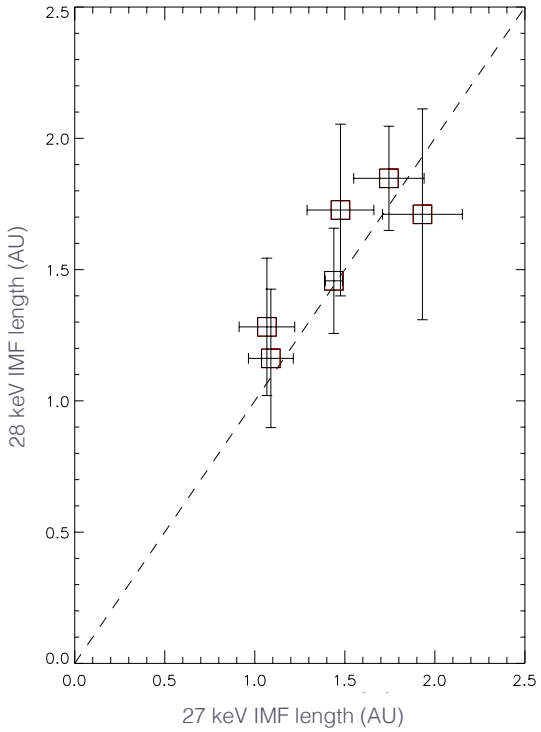

Figure 5.2: Estimated IMF path length for ∼28 keV electron SEPs derived using onsets detected by Wind EESA against estimated IMF path length for ∼27 keV electron SEPs derived using onsets detected by Wind SST. Estimated IMF path lengths were found using the method which assumes that the time between the onset of type III radio burst (proxy for SEP start times) and onset of the electron SEPs, is the time taken for the field-aligned electron SEPs to travel along the IMF path length.

pared to those of the EESA observations for the overlapping electron SEP energy bin, see Figure 5.2. It was found that for events where both instruments detected clear onsets, the path lengths agreed well and therefore short path lengths were not likely to be an instrumental effect.

Another possible explanation for an unphysically short path length estimate may be that higher energy SEP electrons are subject to scattering effects and therefore arriving later than expected. Previous studies have shown that this effect may be due to the transition from a 'scatter-free' to 'diffusive' regime (in which particle motion across flux-tubes can occur) as the electron SEP energy approaches relativistic values (e.g., Tan et al., 2011). It has been shown that higher energy SEP electrons, approaching the diffusive regime, are scattered more than lower energy electrons and that the boundary between the two regimes varies from event to event (e.g., Tan et al., 2013). Hence, it was decided that VDA would not be used to estimate the IMF path length using electron SEPs. Instead the IMF path length was estimated using the time taken for electron SEPs of $\sim$ 27 keV to travel from the Sun to $\sim$ 1 AU. It is possible to estimate the "start time" the SEP event as type III radio bursts are related to the transport of accelerated 10-1000 keV (Tan et al., 2013). Thus it can be assumed that the time taken for the field-aligned electron SEPs to travel along the IMF path length is the time difference between the onset of the type III radio burst and the onset of the $\sim$ 27 keV electron SEPs.

The VDA method for helium ion SEPs and the travel time method for electron SEPs and type III bursts were used to calculate IMF path length estimates for each event. Any IMF path length estimates that resulted in large errors (found from fitting in the VDA case, and propagated through in the travel time case) were visually inspected and any errors that exceeded 1 AU or 0.3 times the calculated IMF path length were excluded from further analysis. Any estimates with a non-physical, negative IMF length were also excluded. Using this criteria results pertaining to unclear onset determination or to unclear velocity dispersion are removed from analysis. Key reasons for these unclear VDA distributions include: high energy SEPs arriving later than expected relative to lower energy SEPs; potential overlapping SEP events; unclear or absence of onset detection for some or all energies.

5.1.3 Determining Strahl Beam Width

The average electron pitch angle distribution, for each suprathermal energy bin, was determined for 20 minutes before each radio burst detection. Strahl beam widths were determined by Gaussian fitting to the strahl beam, as outlined in Section 3.6 and used previously in the research described in Chapter 4 and Graham et al. (2017). The estimated IMF path length for both the ions and the electrons was compared to the average strahl width. Figure 5.3 shows an illustration of the methods used in this Chapter. In particular, Figure 5.3(d) illustrates the expected trend if there is a clear relationship between strahl beam width and distance travelled along the IMF. This could occur if the scattering rate is constant with time and distance from the Sun. The shorter distance along the field, d2, means that strahl would take a shorter time to travel the same radial distance as the longer distance along the field, d1. Hence, the strahl electrons would experience the same adiabatic focusing but may undergo a greater scattering effect.

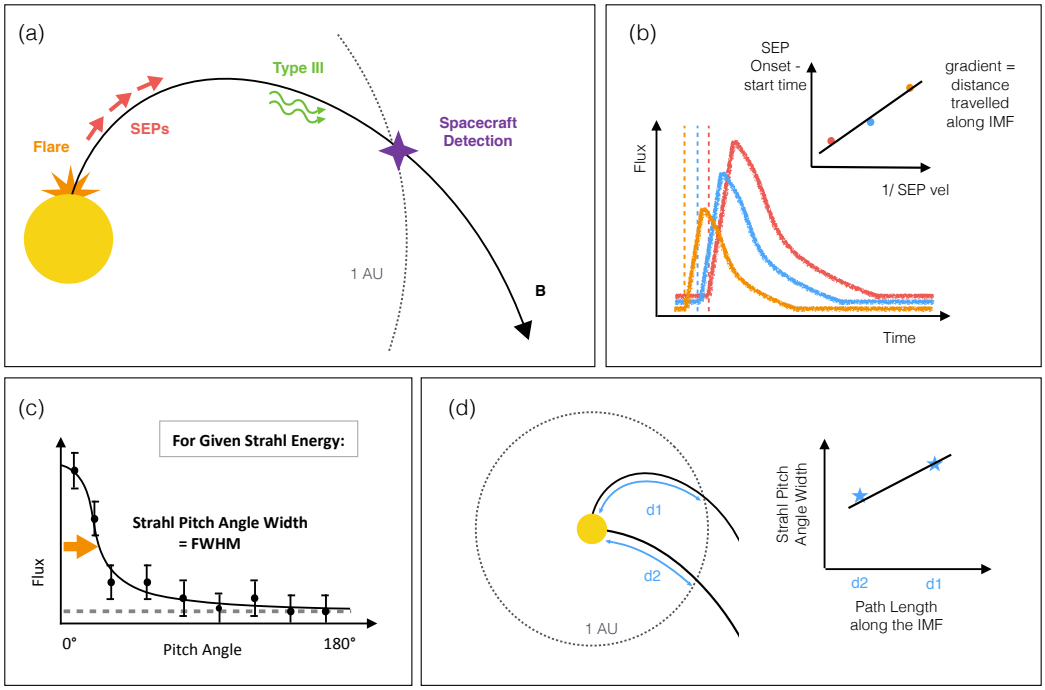

Figure 5.3: Key aspects of the methods used to determine SEP onset times, estimate IMF length and compare with average strahl width (Graham et al., 2018). (a) Illustration of an impulsive SEP event and associated phenomena. SEPs are accelerated on an open Earth-directed IMF line, travel along the IMF, and are detected by the spacecraft at 1 AU. (b) Illustration of the observed increase in energetic particle flux against time at 1AU for three different energies: low (red), medium (blue), and high (orange). The dashed lines show the SEP onset times. The top corner inset shows an illustration of these onset times as a function of inverse SEP velocity. This inset shows the expected velocity dispersion, with faster particles arriving first. (c) Illustration of fitting to average electron pitch angle distribution for one suprathermal energy bin. Strahl beam width is given by the FWHM of the Gaussian peak at either 0° pitch angle or 180° depending on the IMF orientation. The grey dashed line represents a constant background. (d) Illustration of the expected trend if there is a clear relationship between strahl beam width and distance travelling along the IMF path length i.e. if the scattering rate is constant with time and distance travelled along the field away from the Sun. The shorter distance d2 means that strahl would take a shorter time to travel the same radial distance as d1. Hence, field-aligned strahl electrons on d2 would experience the same adiabatic focusing but lesser scattering effects.

5.2 Examination of Strahl Width in Conjunction with IMF Length

5.2.1 Strahl width Variation with IMF Length

Average strahl pitch angle width as a function of estimated IMF path length for suprathermal energy bins ranging from $\sim$ 140 to 1300 eV is shown in Figure 5.4. The left panel shows the results for IMF estimates from the travel time method for $\sim$ 27 keV electron SEPs and type III bursts. The right panel shows the results for IMF estimates obtained using the VDA method for helium ion SEPs. The electron SEP travel time method results display an increase in average strahl width with estimated IMF length, this can be seen for all strahl energies, with higher energy strahl displaying a more pronounced relationship. Although, there may be an exception in the highest strahl energy channel, in which there is potentially a separation into two strahl populations; one with broader pitch angle widths, and another with significantly narrower beam widths. There is also an event with a high estimate of IMF length but narrow strahl that is observed in all energy channels. This event is for a solar wind speed of $\sim$ 500 kms^{-1} and a relatively low median PVI of $\sim$ 0.46, but no evidence of any unusual solar wind conditions or ejecta were present. The ion SEP VDA method also displays an increase in average strahl width with IMF length, although the relationship is less clear than for the electron SEP travel time method.

It should be noted that for the lowest strahl energy channel, for both the ion VDA and electron travel-time IMF length estimation methods, a weaker trend is observed than for the higher energies and further observations would be required to resolve this ambiguity. These two methods also produce some high values for IMF length i.e. $>$ 2 AU. However, even if these high values are excluded, an increase in strahl width with estimated IMF length would be observed using both methods. However, both the ion VDA and electron travel-time methods give reasonable values for the IMF path length, which is in line with the previous results of Tan et al. (2013) and Mazur et al. (2000). Finally, the increase in average strahl width with IMF length observed in both cases suggests that strahl on longer IMF path lengths is subject to greater scattering effects en route from the Sun. This suggests that the

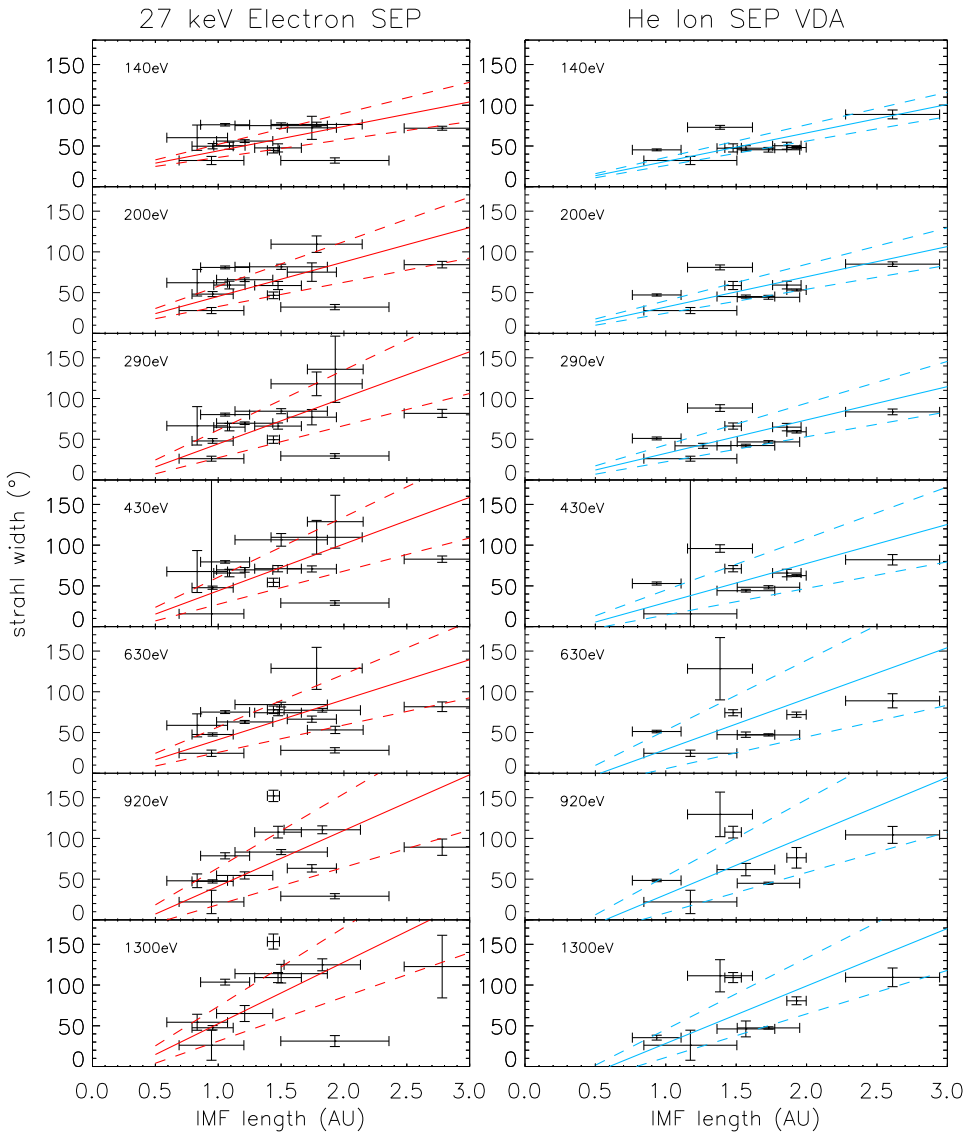

Figure 5.4: Average strahl pitch angle width as a function of estimated IMF path length (Graham et al., 2018). (Left) IMF path length found using the estimation method that assumes that the time between the onset of type III radio burst (proxy for SEP start times) and onset of the 27 keV electron SEPs, is the time taken for the field-aligned 27 keV electron SEPs to travel along the IMF path length. (Right) IMF path length estimated using He ion VDA. Each panel, for both the left and right plots, represents a different strahl electron energy, from top to bottom: $\sim$ 140, 200, 290, 430, 630, 920 and 1300 eV. The solid lines are a linear fits to the data obtained using reduced major-axis regression and the dashed lines are the calculated uncertainties for the linear fits (Isobe et al., 1990).

strahl is subjected to scattering effects continuously or quasi-continuously throughout its journey from the Sun and that the strahl widths observed do not simply reflect the latest strahl scattering interaction.

5.2.2 Strahl Width Relation with Energy

The strahl width as a function of energy observed at a given time for each interval studied produced a variety of results. Events for which the average strahl width broadened with energy, decreased with energy and events with unclear or no energy relation were observed. This is in line with the variable nature of strahl reported by previous studies, particularly Anderson et al. (2012), which found that for any time, the strahl width may broaden or narrow with energy. The increase in average strahl pitch angle width per unit distance along the IMF was obtained from linear fits to strahl width as a function of IMF path length, shown in Figure 5.4. This is shown as a function of suprathermal electron energy in Figure 5.5. The relationship shown in red (diamonds) is found using the IMF path length estimation method that assumes that the time between the onset of type III radio burst (proxy for SEP start times) and onset of the 27 keV electron SEPs, is the time taken for the field-aligned 27 keV electron SEPs to travel along the IMF path length. The relationship shown in blue (asterisks) is found using the IMF path length estimation method that uses helium ion VDA.

In both cases, it is observed that strahl width broadening per unit distance along the IMF path is greater for higher strahl energies. The general trend for increase in strahl width per AU for both methods are within error of each other, with a range of $\sim 30 - 80^{\circ}/AU$. The increase in strahl broadening per AU along the IMF path length with increasing strahl energy suggests that pitch angle scattering is likely greater for higher energy strahl electrons. Although, it should be noted that the errors associated with the estimates of change in strahl width per unit distance are large. The increase in beam broadening per unit distance is also much clearer for lower energy electrons, beyond $\sim$ 400 eV it is possible to interpret the trend as flat rather than increasing. However, even if the distribution is flat, the increase in strahl width is still larger than can be explained by a constant scattering rate in a simple time-of-flight model (Owens et al., 2008) or by kinetic modelling of strahl evolution to 1 AU (Horaites et al., 2017).

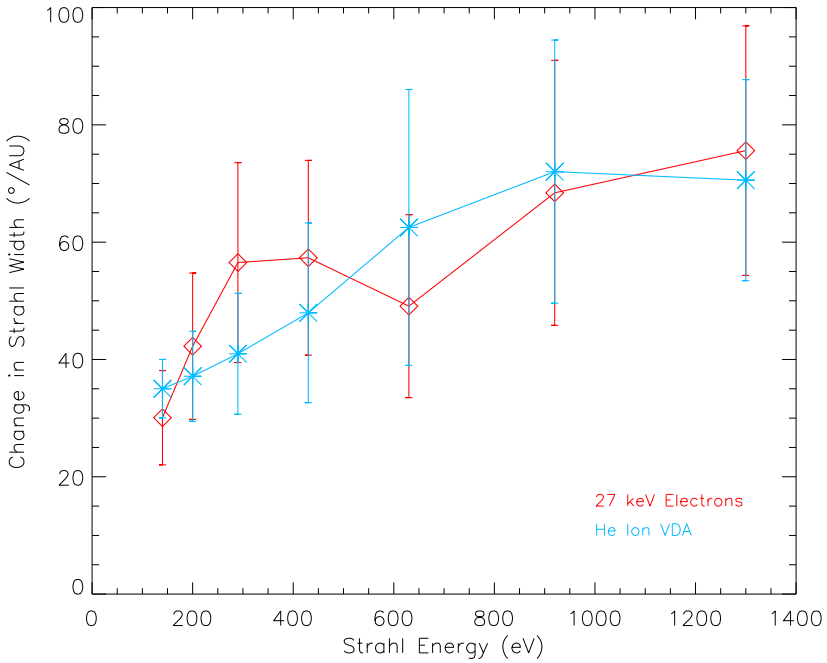

Figure 5.5: Change in strahl pitch angle width per unit distance as a function of electron energy, obtained from linear fits to strahl width as a function of IMF path length in Figure 5.4 (Graham et al., 2018). The relationship shown in red (diamonds) is found using the IMF path length estimation method that assumes that the time between the onset of type III radio burst (proxy for SEP start times) and onset of the 27 keV electron SEPs, is the time taken for the field-aligned 27 keV electron SEPs to travel along the IMF path length. The relationship shown in blue (asterisks) is found using the IMF path length estimation method that uses He ion VDA. The error bars show the calculated uncertainties for the linear fits.

5.2.3 Solar Wind Conditions

The IMF topology, solar wind type and IMF variation may all play a role in solar wind strahl width and so each of these was examined, in order to understand possible global or local effects on the strahl beam. To provide context for the conditions under which the events were observed, histograms of the general solar wind/IMF properties of the events are shown in Figures 5.7 and 5.8.

Figure 5.7 Panel (a) shows the model Parker spiral length calculated using observed average solar wind speed. The solid line represents the spiral length for a solar wind speed of 400 kms^{-1}, which is the average solar wind speed in the ecliptic (e.g., Hundhausen et al., 1970). In general, there is a difference of $\sim 30\%$ between IMF lengths calculated using the Parker model and the IMF estimates calculated using the travel time method for electron SEPs. In general, there is a difference of $\sim 40\%$ between IMF lengths calculated using Parker model and the IMF estimates calculated using the VDA method. A comparison of IMF length estimates and theoretical Parker spiral lengths for each event is shown in Figure 5.8. Here it can be seen that the results of the two aforementioned methods are reasonably similar even though there are low statistics. The IMF estimates calculated using the travel time method for electron SEPs are often lower than the theoretical Parker spiral lengths. However, in general, and for both methods, the IMF length estimated is larger than the Parker length.

The Parker angle calculated using average solar wind speed was also compared to average observed IMF angle. A peak was found centred on the expected Parker angle but also some significant deviations were observed, in which the average field direction is nearly radial or tangential. Such intervals have been previously observed in the solar wind (e.g., Forsyth et al., 1996b; Borovsky, 2010; Owens and Forsyth, 2013). For the probability distribution functions for IMF angle from 1965 to 2012 see Owens and Forsyth (2013), reported in Section 2.1.3, where it is shown that generally the ideal Parker spiral values agree well with observations but that IMF direction is variable.

The difference between the Parker values and the SEPs estimates is perhaps illustrated more clearly in figure Figure 5.9. This figure shows the IMF lengths calculated using the Parker model against the IMF estimates calculated using the travel time method for electron SEPs (red) and the IMF estimates calculated using the VDA method (blue). If we compare the Parker IMF values, calculated using the average solar wind velocities during the strahl observation interval, to the strahl widths observed then there is no clear correlation. The range of IMF lengths obtained is also much smaller ($\sim$1.0-1.3 AU) than those estimated using IMF. Both SEPs and strahl are populations that travel along the IMF at high velocities com-

pared to that of the bulk solar wind. They are subject to the geometry of the IMF which can deviate from the expected spiral field direction, sometimes by 90° (e.g., Forsyth et al., 1996b; Owens et al., 2008; Borovsky, 2010; Owens and Forsyth, 2013). Strahl in particular can be observed travelling in the sunward direction during intervals of folded magnetic flux. This means a Parker model IMF may not be sufficient for the accurate estimation of field line length required in an investigation that is concerned with the effect of the length of path travelled by the strahl. As stated previously, the variation in observed magnetic field compared to the Parker model may also partly explain why, although strahl width is generally broader in the slow wind, there is no direct correlation between solar wind speed and strahl width (Pilipp et al., 1987b). Further investigation into strahl scattering within this regain (¡ 1 AU) and the possible cross-field transport of SEPs are required to make conclusive statements about the difference between the path length travelled by strahl electrons and the average IMF geometry.

Panel (b) of Figure 5.7 shows the average observed solar wind speed during each of the events. The average solar wind speed during these events varies from $\sim$ 300-600 kms^{-1}. The mean, median and standard deviation for an event wind speed in this in this study is 416 kms^{-1}, 402 kms^{-1} and 82 kms^{-1} respectively. The solid line represents the spiral length for a solar wind speed of 400 kms^{-1}, which is the average solar wind speed in the ecliptic (e.g., Hundhausen et al., 1970). No direct relationship between strahl beam width and solar wind speed was observed. The average solar wind speed for events with clearly detectable strahl versus those that did not fulfil the criteria specified in Section 3.6 was also examined.

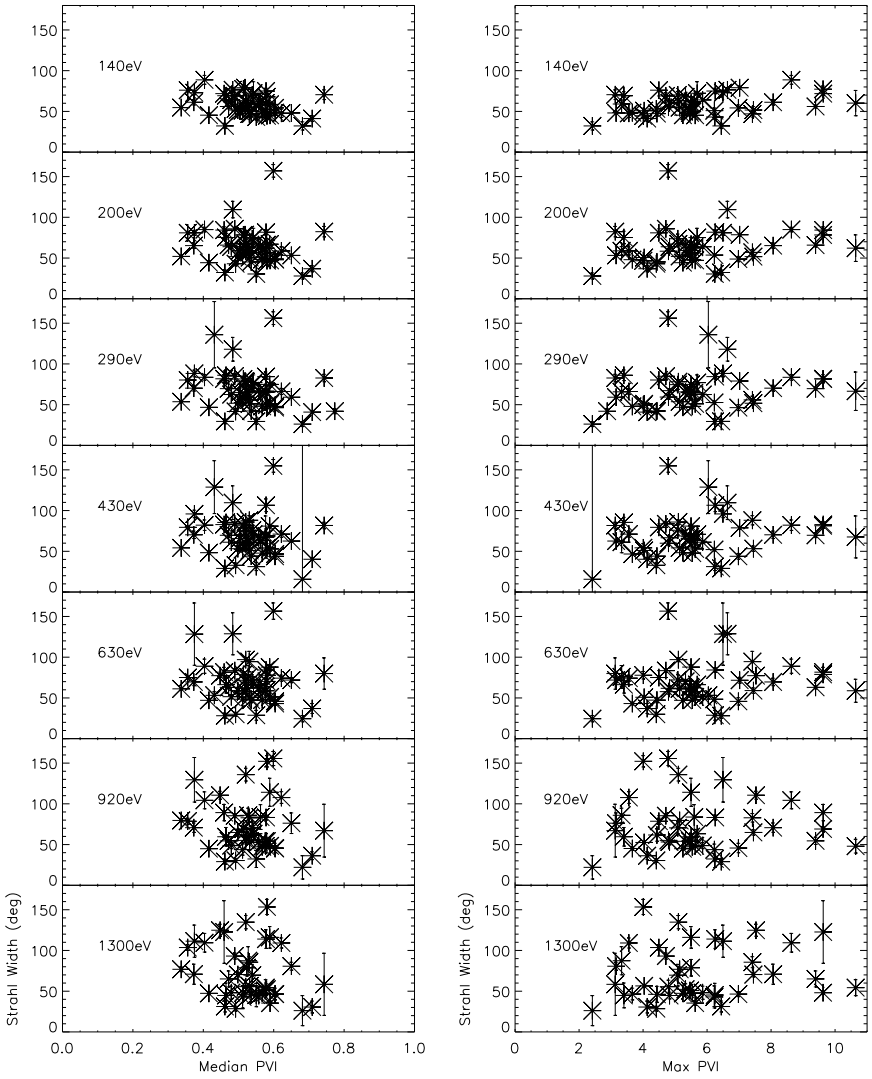

Figure 5.6: Strahl width against median (left) and maximum (right) PVI found for strahl observation period for each of the events investigated.

The magnetic variation during both the strahl observations and during the entire period in which SEP onsets are observed was also examined, in order to investigate possible effects related to magnetic fluctuations. PVI, as defined in Section 3.7, was used for this purpose. It should be noted that the PVI was calculated using 3s magnetometer observations and thus, can not provide information on intermittent features at kinetic scales which may result in electron scattering. However, the observations may provide useful information with regard to: possible blurring of the strahl distribution due to magnetic field fluctuations during strahl observation periods; or strahl scattering resulting from coherent non-Gaussian magnetic field

structures such as current sheets between solar wind flux tubes.

Panel (c) of Figure 5.7 shows the calculated median PVI values for each strahl observation period. The median values for PVI were found to be low (i.e. below 1.0) for the strahl observation periods (Osman et al., 2014). The average strahl width for each event showed no clear relationship with either median and maximum values of PVI observed during each event, as can be seen in Figure 5.6. The median and maximum values of PVI during SEP onset observation were also examined. No relationship was observed between the resulting IMF estimate and PVI. The lack of a clear relation between average strahl width and PVI values suggests that the observed increase in strahl width with IMF path length is related to in-transit effects in the solar wind between the Sun and 1 AU, and that the average strahl widths observed for our events are not strongly related to local magnetic variation effects at the time of observation. However, the possibility of local fluctuations on the kinetic scale affecting the strahl widths observed, such as the intense, bursty strahl electron scattering to form a proto-halo population observed by Gurgiolo et al. (2012), can not be ruled out.

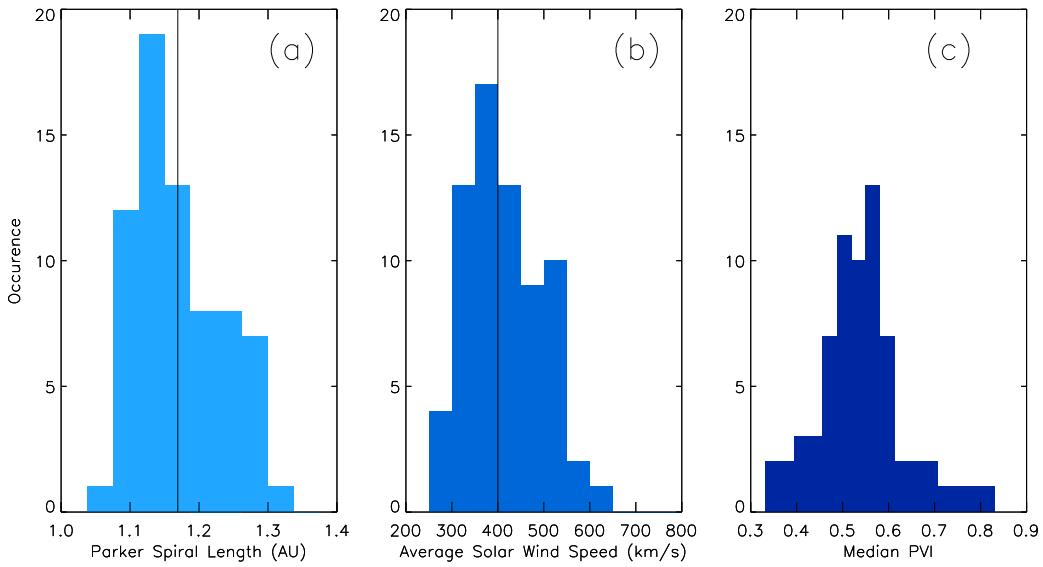

Figure 5.7: Histogram for all events investigated (Graham et al., 2018), showing (a) Parker spiral length calculated using observed average solar wind velocity. The solid line represents the spiral length for a solar wind speed of 400 kms^{-1}, which is the average solar wind speed in the ecliptic (Hundhausen et al., 1970). (b) the average solar wind speed observed. (c) the median PVI found for strahl observation time for each of the events investigated, PVI values below 1 are considered to have minimal fluctuations (Osman et al., 2014).

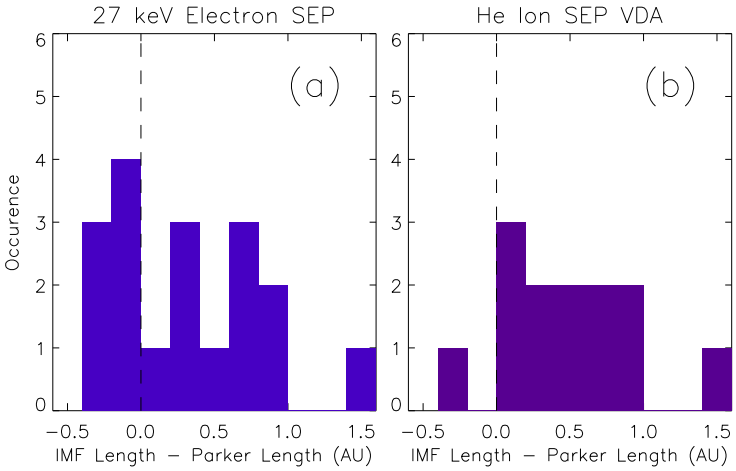

Figure 5.8: Histogram for all events (Graham et al., 2018), showing (a) Difference between the estimates of IMF path length using the travel time method for electron SEPs and type III bursts and the Parker spiral length calculated using observed average solar wind velocity. (b) Difference between the estimates of IMF path length using the VDA method for helium ion SEPs and the Parker spiral length calculated using observed average solar wind velocity.

5.2.4 Assumptions and Limitations of the Investigation

It is important to note that it was not possible to reliably estimate strahl width and IMF length for all of the initial 69 events, nor do all events have an IMF estimate from both of the methods investigated. After applying the fitting criteria for strahl observations and after removing IMF length estimates that had large errors or non-physical results, it was only possible to determine an estimate of both IMF length and strahl width for a subset of the initial list of events. The results in Figure 5.4 consist of 18 valid IMF estimates for the IMF lengths calculated using the travel time method and 13 valid IMF estimates for the VDA method. IMF estimates from both methods can be obtained for 4 events and two of these events render very similar IMF path lengths whereas two do not. Given that there are only 4 events with results for both methods, no quantitative assessment is made on the agreement of the two methods used to determine IMF path length.

The possibility of there being spatial effects leading to errors in the results for IMF path length should also be considered. Mazur et al. (2000) found that He ions in impulsive events were well confined to “flux tubes”. These flux tubes had an average estimated cross-section of $\sim$0.03 AU and a maximum cross-section of $\sim$0.15 AU. It is possible that as these flux tubes are convected outwards from the

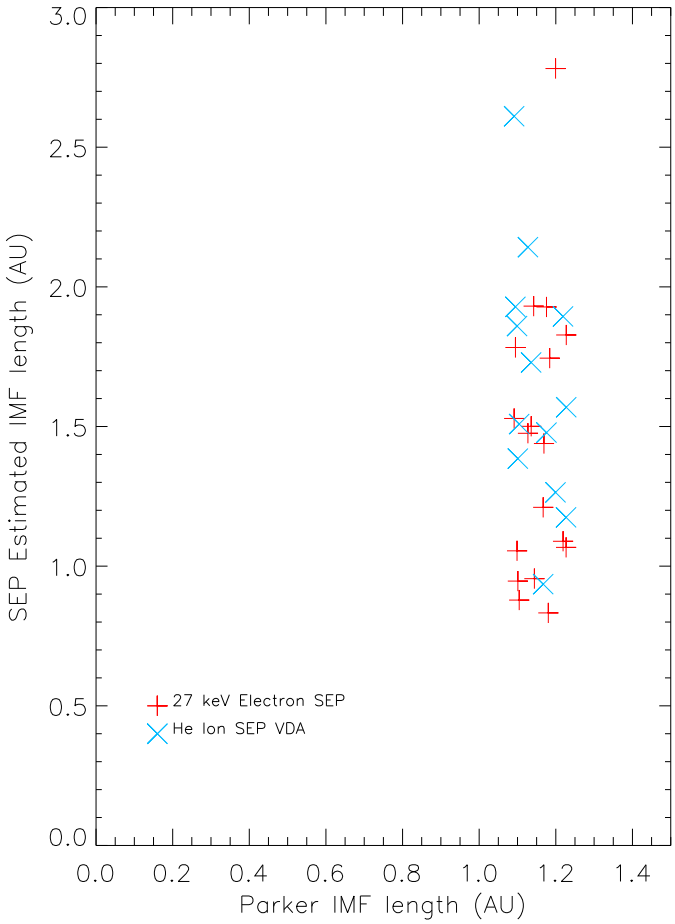

Figure 5.9: IMF lengths calculated using the Parker model against the IMF estimates calculated using SEP onset observations. The relationship shown in red is found using the IMF path length estimation method that assumes that the time between the onset of type III radio burst (proxy for SEP start times) and onset of the 27 keV electron SEPs, is the time taken for the field-aligned 27 keV electron SEPs to travel along the IMF path length. The relationship shown in blue is found using the IMF path length estimation method that uses He ion VDA. The the calculated uncertainties are not shown but are the same as shown in previous figures within this chapter.

Sun, they become tangled in-transit with flux tubes with footpoints that are not connected to what will be the SEP acceleration site. Thus, as flux tubes convect across the spacecraft during an SEP event, "empty" flux tubes may be observed that could effect the VDA. For each of the events, a length scale was calculated by

dividing the time between the first and last observed SEP onsets by the average solar wind speed. The maximum value of this length scale was ∼0.08 AU. Hence, spatial effects cannot be completely ruled out, although no relationship between calculated length scale and large estimates of IMF path length was found, so it seems unlikely to have significantly affected the results obtained for IMF path length.

In the research presented in this chapter, a novel strahl width analysis technique was tested and implemented using an independently studied list of events as a starting point. A larger number of events would provide improved statistics and allow more substantial claims regarding strahl broadening. However, the results do provide a good indication of the processes effecting the strahl within 1 AU and a testable strahl width energy relation for both future inner heliospheric missions, which will be able to observe the strahl and its energy relations within 1 AU directly, and further investigations that make use of a greater number of SEP events.

5.3 Comparison to Previous Investigations

Previous observational investigations into the evolution of strahl pitch angle distributions, including those presented in the previous chapter, found that, in general, strahl width increases with heliospheric radial distance and that strahl must be subjected to in-transit scattering effects (Hammond et al., 1996; Graham et al., 2017). Increase in strahl width with radial distance was also successfully reproduced by an empirical model which assumed a pitch-angle scattering rate that was constant with time, distance and electron kinetic energy (Owens et al., 2008). However, all three of the studies above produced different energy relations for strahl broadening per unit radial distance. Hammond et al. (1996) observed that strahl broadening per AU steeply decreased with increasing strahl energy, Graham et al. (2017) (Chapter 4) observed that strahl broadening per AU slightly increased with increasing strahl energy and the Owens et al. (2008) model produced strahl broadening per AU slightly decreased with increasing strahl energy. The energy relation found in this investigation does not agree with those of Hammond et al. (1996) or Owens et al. (2008) and although, like the Graham et al. (2017) study, an increase in strahl broadening per AU with electron energy is observed, the increase observed is much steeper. In fact, this study indicates that, for ∼70-600 eV strahl, broadening per AU within 1

AU is approximately double that of the 1 to 5.5 AU range.

When comparing the results of these four studies, it is important to consider the possibility that slow and fast solar wind may produce differences in the strahl pitch-angle distribution, either due to in-transit processing or their solar origins. Some previous investigations have found that strahl beams are generally broader in the slow solar wind than the fast (e.g., Fitzenreiter et al., 1998) and it has also been shown that strahl width is greater when in proximity to IMF sector boundaries (Pilipp et al., 1987b). However, proximity to IMF sector boundaries is observed to result in strahl pitch angle broadening that is independent of electron energy (Pilipp et al., 1987b), and therefore cannot explain the energy relation found in this investigation. Both the Hammond et al. (1996) observations and the Owens et al. (2008) model were made in fast solar wind streams. However, the Hammond et al. (1996) observations were made over a range of heliosphere latitudes, whereas the Owens et al. (2008) model assumed a constant heliolatitude. The Graham et al. (2017) observations were for unknown, but likely mixed, solar wind speeds obtained from 1999-2004. The results from this study were obtained from 1999-2002 and had average solar wind speeds ranging from $\sim$ 300-600 kms^{-1}. Both the observations made in this investigation, and those of the previous chapter, were for approximately constant heliolatitude, in the equatorial plane. Thus, it is likely that the average solar wind conditions seen in Chapter 4 and this investigation were more similar to each other than those of Hammond et al. (1996) and Owens et al. (2008).

The energy relation produced by the Owens et al. (2008) model is solely a result of the suprathermal electrons having different velocities. The modelled scattering rate used in Owens et al. (2008) was constant with time, distance and electron kinetic energy. Hence, the faster strahl electrons travel further along the modelled field in a given time and experience the same quantity of scattering but a greater adiabatic focussing effect. The observational results obtained in this investigation, Hammond et al. (1996) and Graham et al. (2017), which differ from the model and each other, cannot be explained solely by strahl time-of-flight effects. This relation suggests that the scattering mechanism or mechanisms for solar wind strahl may have an inherent energy dependence. Finally, we should note that Parker field line length estimates were not thought to be sufficient for the purpose of this current

investigation, whereas the Owens et al. (2008) empirical model assumed Parker geometry. Thus further work in which this model was altered to allow for heliospheric field lines that are longer or shorter than the predicted Parker values is needed to match strahl observations.

Although the results obtained in this investigation agree with the those presented in Chapter 4, it is important to note the differences between the methods used in each case. This is particularly important as the results herein display a stronger strahl width broadening per AU than reported in Graham et al. (2017). In this current investigation, we find strahl width broadening per AU as a function of distance along the IMF path length by estimating the path length travelled by the strahl along the IMF from the Sun to 1 AU. In contrast, in Chapter 4 it was found the strahl width broadening per AU as a function of radial distance by fitting to the observed radial trends of strahl beam width from $\sim$ 1 - 5.5 AU. In a Parker spiral field, the distance along the IMF path increases with radial distance from the Sun. For example, for solar wind with a speed of 500 kms^{-1}, the IMF path length would be 2.8 and 5.2 AU at radial distances of 2 and 3 AU from the Sun respectively. Hence, if the Chapter 4 results were measured in terms of IMF path length as opposed to radial distance, it is likely that the broadening per AU would be an even lower value than when given in terms of radial distance. Thus, the difference in methods used does not explain the difference in results.

The observed strahl width broadening per AU in Chapter 4 was also thought to be relatively constant with heliospheric radial distance. Hence, if results were measured in terms of IMF path length as opposed to radial distance, this conversion would also result in a broadening per AU along the IMF path length that decreased with radial distance from the Sun. It is expected that the effect of adiabatic focussing on the strahl beam will decrease with radial distance, due to the longer path length travelled along the IMF by the electrons for a given change in radial distance and hence in interplanetary magnetic field strength. Therefore, the approximately constant radial broadening of strahl beam width with radial distance may be due to the strahl scattering mechanism decreasing with radial distance in conjunction with the effect of adiabatic focussing. Hence, comparison of the energy relation for strahl broadening per AU found in this investigation and Chapter 4, suggests that

the dominant scattering mechanism, resulting in the observed energy relation, may have a stronger effect within 1 AU than it does beyond it.

As discussed in Sections 2.2.6 and 4.2.7, resonant interaction with broadband whistler fluctuations is thought to result in higher energy strahl experiencing greater pitch angle broadening (e.g., Vocks et al., 2005; Saito and Gary, 2007; Pagel et al., 2007). Hence, this scattering mechanism may explain the greater broadening per AU for higher energy strahl observed in this paper and Graham et al. (2017). The effectiveness of whistler-mode scattering depends on the available wave power below the electron gyrofrequency (Vocks et al., 2005) and the wave power and the electron gyrofrequency decrease with radial distance (Hu et al., 1999). Hence, decrease in scattering effects with radial distance may also be consistent with whistler-mode wave interaction as the primary strahl pitch angle scattering mechanism. It has been shown that whistler-like fluctuations are present in the solar wind up to 10% of the time (e.g., Lacombe et al., 2014). However, we should also note that whistler-mode waves are certainly not the only possible scattering mechanism for strahl and thus further investigation into the effectiveness and occurrence of wave-electron interactions in the solar wind is required.

A number of alternative possible strahl scattering mechanisms were also discussed in Section 2.2.6. These included a core electron temperature anisotropy (where $T_{\perp}/T_{\parallel} > 1$) which could result the excitation of the whistler anisotropy instability, thereby producing enhanced whistler fluctuations which then resonantly interact with strahl electrons, resulting in beam width that decreases with strahl energy. Anisotropies of this kind have been observed to be relatively common at a number of different radial distances (between ~ 0.3 and 4 AU) and hence this mechanism could be a source of strahl scattering though out the heliosphere (Stverak et al., 2008). In addition, observations at 1 AU of strahl pitch-angle widths that decrease with increasing electron energy may be evidence that this mechanism may occur in the solar wind (e.g., Feldman et al., 1978; Pilipp et al., 1987a; Fitzenreiter et al., 1998). However, both the energy relation for broadening per AU found within this study and that of Chapter 4 suggest that the dominant strahl scattering mechanism should result in greater scattering for higher energy strahl. Thus, although this mechanism may contribute to strahl broadening, it seems likely that it

does not have a dominant effect on the average strahl evolution. At least, not within the mixed (mainly slow) speed solar wind observed in the ecliptic.

The strahl itself could also be a driver for for instabilities that can result strahl scattering. For instance, whistler-mode waves generated by the electron heat flux instability could be a potential source for scattering (Gary et al., 1994). However, observations of the solar wind heat flux made by the Ulysses spacecraft from $\sim$1 - 5.5 AU revealed that there was no correlation between scaled electron heat flux and enhanced whistler-frequency fluctuations. Although, it is worth noting that all interplanetary shock intervals were excluded from this investigation and that whistler waves downstream of shocks have been observed to demonstrate a weak positive correlation with the normalised heat flux magnitude (Wilson et al., 2013) and may result in strahl scattering upstream of shocks. Fluctuations resulting from the electron firehose instability (where $T_{\perp}/T_{\parallel} < 1$) are another possible source of strahl scattering, as this anisotropy has also been found to be relatively common at a number of different radial distances (between $\sim$ 0.3 and 4 AU, Stverak et al., 2008). For example, the Hellinger et al. (2014) study found that this instability eventually resulted in whistler-mode waves that were then rapidly damped, resulting in perpendicular electron heating. Although, no explicit relation is given with regard to the electron energies that experience damping.

Strahl-generated Lagmuir waves offer another possibility for a self-induced scattering mechanism. In particular, it has been shown that at 1 AU this type of wave-particle interaction produces significant broadening, with lower energy strahl displaying greater pitch-angle widths higher than their higher energy counterparts (Pavan et al., 2013). Finally, anisotropy of the strahl electron velocity distribution can also result in a core-strahl system that is unstable to lower hybrid waves and results in pitch-angle diffusion of the strahl (Shevchenko and Galinsky, 2010). It is worth noting at this point, that all modelled results need to be evaluated carefully when examining them in conduction with observations strahl evolution and considering their implications with regard to strahl scattering. Firstly, because many studies chose to neglect one or more of the electron populations (e.g., Gary et al., 1994; Stverak et al., 2008; Hellinger et al., 2014). Secondly, because many models consider only the time evolution of a given electron distribution and therefore neglect

the effect that adiabatic focussing will have on the development of instabilities and scattering effects (e.g., Shevchenko and Galinsky, 2010; Pavan et al., 2013). Thus, simulations that include all three populations and the effect of adiabatic focussing are required to effectively model strahl evolution.

In this Chapter, and in Chapter 4, it is concluded that resonant interaction with broadband whistler fluctuations resulting from turbulent cascade is a likely candidate for the dominant strahl scattering mechanism. In particular, because simulations have shown that this mechanism should produce strahl beam width that increases with strahl energy (Saito and Gary, 2007). However, another candidate for strahl scattering which could also result from turbulent cascade is obliquely propagating KAWs, which may be able to interact with the field-aligned strahl via Landau damping. An argument for KAWs, in favour of whistler fluctuations is the number of observations of KAWs at appropriate scales (e.g., Salem et al., 2012; Chen et al., 2013b; Kiyani et al., 2012; Lacombe et al., 2017). This scattering mechanism may also produce the energy relation required to match our observations, as strahl broadening with increasing energy is a natural consequence of a turbulent spectrum with greater wave-power for longer wavelengths (Saito and Gary, 2007). However, it should be noted that both KAW and whistler-mode waves may be present at electron scales, with relative ratios that vary depending on the solar wind conditions. Thus, it has been suggested that simulations that allow initial spectrum to cascade into both modes are required to model the effects on the strahl distribution (Gary et al., 2008).

Finally, with regard to the modelled radial evolution of strahl width and its associated energy relation, it is worth noting two things. Firstly, the Owens et al. (2008) modelled results are for an ideal Parker Spiral, in fast, constant-speed solar wind and has a constant, ‘add-hoc scattering rate. It is worth noting that the original purpose of this model was to illustrate the effect that large-scale IMF geometry can have on the strahl population, not to determine the precise strahl scattering mechanism. Thus, examining the effect of variable wind speeds, with a spread of allowable spiral lengths based on observed values, and using scattering rates based on simulations of wave-particle interactions would allow for the model to be more effectively employed in examination of the possible strahl scattering mechanisms. Secondly,

kinetic modelling investigations of strahl evolution, such as Horaites et al. (2017), can explain the formation of a narrow strahl beam in fast solar wind streams and illustrate the potential importance of the effect of collisions within the solar wind. However, for the variability and broadness of strahl widths to be fully accounted for, it seems likely that these models will need to include the effect of wave-particle interactions a source of strahl scattering in the future. Particularly, as small-scale fluctuations resulting from solar wind turbulence are both ubiquitous and a highly likely candidate for strahl scattering.

Chapter 6

Determining Magnetic Field Orientation using Strahl Obervations

Estimates of interplanetary magnetic field orientation obtained from Cluster and Mars Express observations of strahl beams in the solar wind are presented in this chapter.

Strahl is, by definition, strongly field-aligned and consequently it serves as a useful tracer of IMF topology. In addition, since strahl electrons travel at high speeds relative to the bulk plasma flow, strahl can act as a near-instantaneous indication of changes in magnetic connection to the Sun (e.g. Pilipp et al., 1987a,b; Owens et al., 2008). Thus, while highly accurate information about the local magnetic field can be provided by a magnetometer, observations of suprathermal electrons can provide IMF information on a more global scale.

Strahl electrons are typically observed to travel along the IMF in the anti-sunward direction, in either the parallel or anti-parallel magnetic field direction, depending on the IMF polarity (e.g., Feldman et al., 1978; Pilipp et al., 1987b). For particular IMF topologies however, strahl can also be observed in the sunward direction. For example, electron beams are observed in both the parallel and anti-parallel magnetic field direction simultaneously in newly-formed IMF loops with both foot-points connected to the solar surface (e.g., Gosling et al., 1987) and local sunward strahl has also been observed as a result of folded IMF topologies (e.g., Owens and Forsyth, 2013, and references within). Bi-directional strahl have also been observed

when suprathermal electrons are reflected at interplanetary shocks (e.g. Owens and Forsyth, 2013) and it has been suggested that bi-directional strahl are one of the more consistent signatures of CMEs, particularly at 1 AU (e.g. Gosling et al., 1987). It should be noted that periods in which there is no clear strahl population also occur in the solar wind (e.g., Anderson et al., 2012), particularly during slow solar wind observations (e.g., Gurgiolo and Goldstein, 2017).

The key role strahl beams can play in the determination of IMF topology is illustrated in a number of recent studies that made use of observed suprathermal electrons. For example, strahl pitch angle distributions have been used to test the validity of a new IMF mapping technique (Li et al., 2016a,b) and also to investigate the solar sources of solar wind observed at 1 AU, particularly with regard to regions in which interchange reconnection is likely to have occurred (Fazakerley et al., 2016). The concept of 'Strahl confusion zones', regions of strahl-less solar wind banded by weak, intermittent, and/or intermittently bi-directional strahl, have also been used to identify magnetic sector reversal regions for use in solar wind type categorization (Xu and Borovsky, 2015). In addition, strahl has also been employed as an identifier of different IMF topologies in work examining the total open solar flux in the heliosphere (Owens et al., 2017).

In this Chapter, 3D observations of suprathermal electrons were used to determine strahl beam and thus, IMF orientation, with aim of investigating whether strahl observations could be used to provide relible confirmation of magnetometer observations, or to provide an alternative measurement of IMF orientation if the magnetometer is not in operation or if there is no onboard magnetometer.

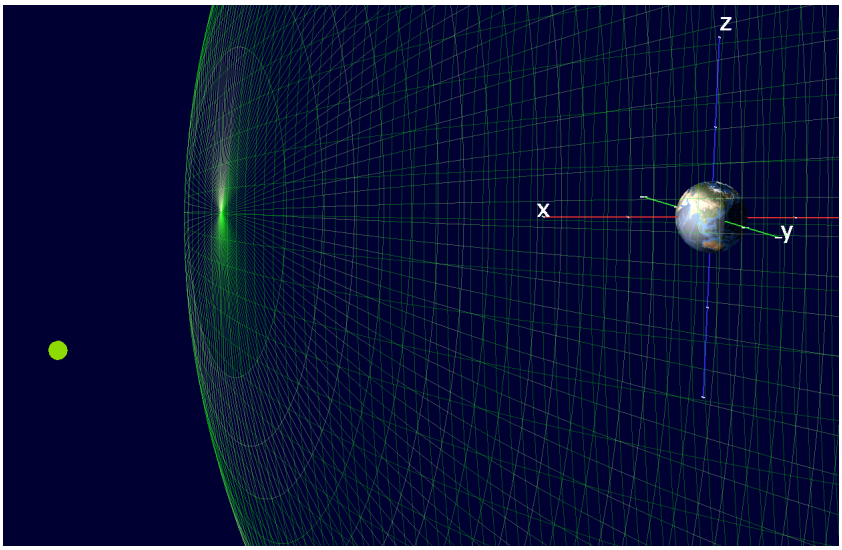

Figure 6.1: The location of the Cluster spacecraft quartet during the examined solar wind interval (08:52:05 to 10:19:29 UT on 02/03/2004) in GSE coordinates. The spacecraft quartet, represented by the green sphere, is located approximately 20 R_E from Earth. The modelled location of the Earth's bow shock is represented by the green mesh. This 3D Plot was obtained using the NASA Satellite Situation Centre (SSC) 4D Orbit Viewer. The SSC software uses a modified version of the Fairfield (1971) model to calculate the location of the bow shock, which changes in response to solar wind and IMF conditions.

6.1 Cluster Trial: High Resolution Observations of Narrow Strahl

The Cluster PEACE instrument was selected to trial the concept of strahl beam fitting as a method of estimating IMF orientation, as the spacecraft periodically make observations in the solar wind and are capable of providing 3D electron distributions at high cadence and angular resolution. The available Cluster PEACE electron distributions depend on the bandwidth constraints of the downlinked data. This varies between spacecraft as Cluster 2 (C2) and Cluster 4 (C4) both have inoperative instruments (CIS and EDI respectively). This allows the PEACE instruments on board C2 and C4 to have a higher bandwidth allocations than on C1 and C3.

A solar wind interval, free of electron foreshock contamination (Private communication, Owen, 2017), in which a clear strahl presence was observed and for which the C2 PEACE LEEA sensor was in a high resolution 'burst' mode was selected for this investigation. Specifically, the data product available during this interval was medium angular resolution (MAR) 3DX. This data product provides 3D electron observations with full polar resolution but with a reduced azimuthal and

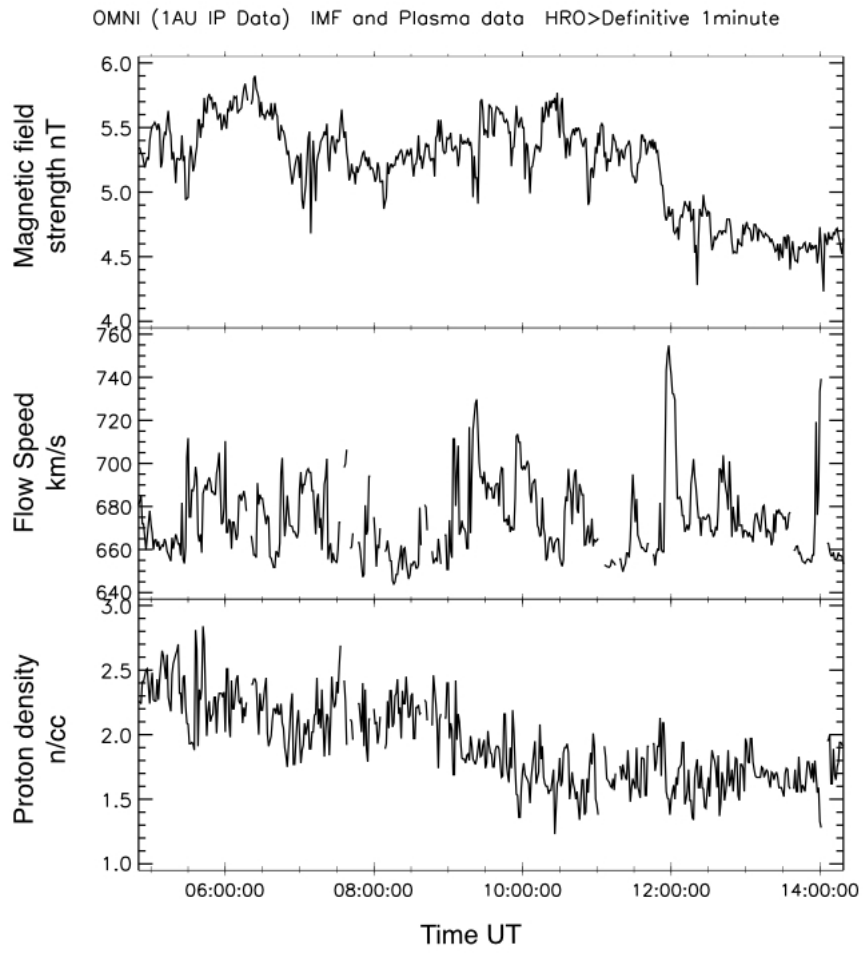

Figure 6.2: Solar wind magnetic field strength, speed and density from 04:50 to 14:20 UT on 02/03/2004. These plots were obtained using NASA/GSFC's OMNI data set through OMNIWeb. During the examined solar wind interval (08:52:05 to 10:19:29 UT on 02/03/2004), the average magnetic field strength was $\sim$ 5.4 nT, the solar wind speed was $\sim$ 670 kms^{-1} and the proton density was $\sim$ 2.1 cm^{-3}. The ranges covered were $\sim$ 4.9 to 5.7 nT, $\sim$ 640 to 730 kms^{-1} and $\sim$ 1.4 to 2.5 cm^{-3}.

energy resolution, produced by summing pairs of azimuth and energy bins. In other words, the data product has 12 polar bins, 32 (as opposed to 64) azimuth bins and 30 (as opposed to 60) energy bins. The energy range for LEEA during this period was $\sim$ 2,880 to 4.7 eV. Only the LEEA sensor was in operation during this interval and so the cadence of the 3D electron distributions is that of the spacecraft spin ($\sim$ 4s). Full resolution magnetic field data from the Cluster FGM (67 samples per second) were available for this time period. The location of the spacecraft quartet during the studied interval (08:52:05 to 10:19:29 UT on 02/03/2004) is shown in Figure 6.1 and the solar wind density, speed and magnetic field strength are shown in Figure 6.2.

6.1.1 Method

In this investigation, a range of suprathermal electron energies were examined using PEACE energy bins with central energies equal to $\sim$ 70, 90, 110, 140, 170, 220 and 270 eV. For each chosen energy bin, the 3D electron flux, divided into 32 azimuth and 12 polar bins, was obtained for the full resolution 4s cadence data. The 3D data within each angular bin were also summed to produce 1 min and 5 min cadence data for the chosen interval. The approximate location of the strahl peak was located by assuming it was the angular bin with the greatest flux of suprathermal electrons. If the strahl peak was located above 315° or below 45° in the azimuthal direction then the FOV was rotated 90° before fitting to the beam, to avoid cutting off part of the distribution. If the strahl beam was found to be located above 135° or below 45° in the polar direction then the FOV was rotated 90° in the polar direction to avoid smearing due to projection effects.

The data were then interpolated and re-binned using inverse distance weighting. The data are then fitted with a function consisting of a 2D Gaussian, for which the peak position and FWHM provides the location and width of the strahl beam in the FOV of the Cluster PEACE instrument. The 4s, 1 min and 5 min average magnetic field orientation was calculated and then converted to its equivalent azimuth and polar position in the Cluster PEACE FOV and compared to the results obtained by fitting to strahl, in order to examine the effectiveness of this technique.

An example of this process is shown in Figure 6.3. The upper panel shows an example of 1 min resolution Cluster PEACE electron data (PSD), divided into angular bins with an azimuthal and polar size of 11.25° and 15° respectively. The middle plot shows the electron data from the upper panel after a rotation of by 90 degrees and re-binning to to avoid FOV projection smearing. The lower panel illustrates fitting a 2D Gaussian function to the strahl beam after rotation. For plotting purposes, in each panel, a linear scaling function has been applied to the electron PSD to give the normalised colour scale with a range of 0 to 255.

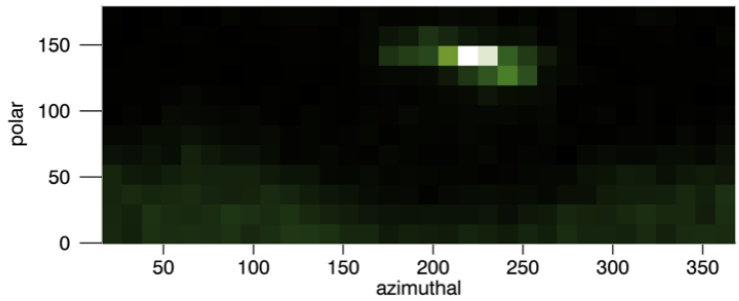

(a)

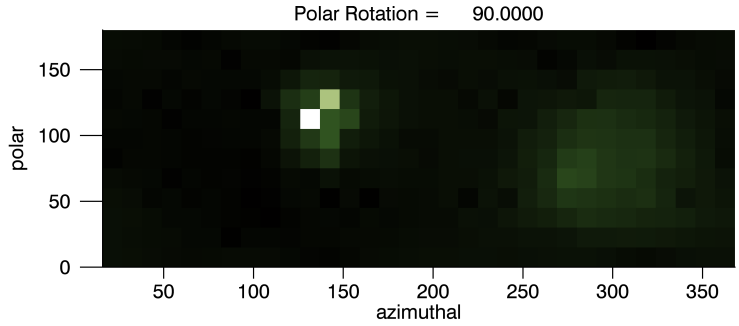

(b)

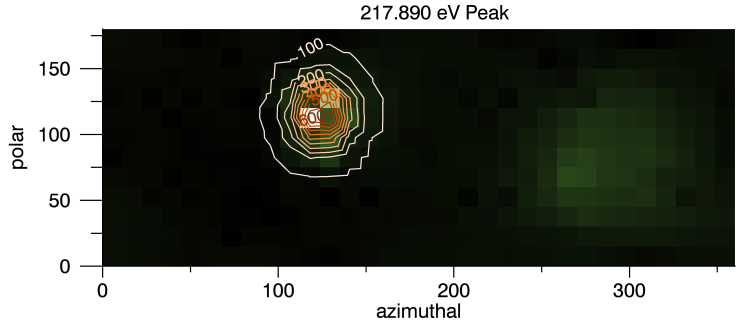

(c)

Figure 6.3: (a) Example of 1 min resolution Cluster PEACE electron data, shown in the instrument FOV. PSD of the electrons is divided into angular bins with an azimuthal and polar size of 11.25° and 15° respectively. The input 2D image is scaled into full colour dynamic range of 0 to 255 with a linear scaling function. (b) Rotation of the 1 min electron data shown in (a) in order to avoid FOV projection smearing. The electron data have been rotated 90 degrees in the polar direction and re-binned using an inverse distance method of interpolation. (c) Fitting to the rotated data shown in (b). The data are fitted by a 2D Gaussian function, of which the peak location and FWHM are used to determine the strahl beam direction and width.

6.1.2 Results

Figures 6.4 and 6.5 show the observed average magnetic field direction and strahl beam direction in terms of the azimuthal and polar angles for the PEACE FOV. The strahl beam directions in Figures 6.4 and 6.5 were determined by the fitting procedure outlined above (Section 6.1.1) using PEACE electron bins with central energies of $\sim$ 70 and 270 eV respectively. Examination of Figure 6.4 shows that, in general, the centre of the lower energy ($\sim$70 eV) strahl beam 'tracks' the magnetic field direction very closely for the 4s, 1 min and 5 min data. Examination of Figure 6.5 shows that, for the higher energy strahl ($\sim$270 eV), the centre of the beam still corresponds to the magnetic field direction the majority of the time but that there are a much larger number of differences between the observed field and fitted beam, particularly in the polar direction.

This comparison can be seen more clearly in Figures 6.6 and 6.7, which show the difference between the average magnetic field and the strahl beam direction in the azimuthal and polar FOV directions respectively. It can be seen that, for all observed energies and cadences, the strahl beam generally produces a good agreement with the magnetic field data, with the majority of fitting results within 30° of the magnetic field estimate. However, there are also a number observations in which there is a significant difference between the observed field and the strahl fitted estimate. Interestingly, many of these large differences have values that are close to 180° in the azimuthal direction or 90° in the polar direction. It should be noted that, unlike in the azimuthal direction, the majority of larger polar differences between the observed field and the strahl fitted estimate are positive. There is also more scatter in the values for the difference between the observed field and the strahl estimate in the polar direction than in the azimuthal direction. Finally, examination of Figures 6.6 and 6.7 also shows that lower energies have fewer large differences between the average magnetic field and the strahl beam direction.

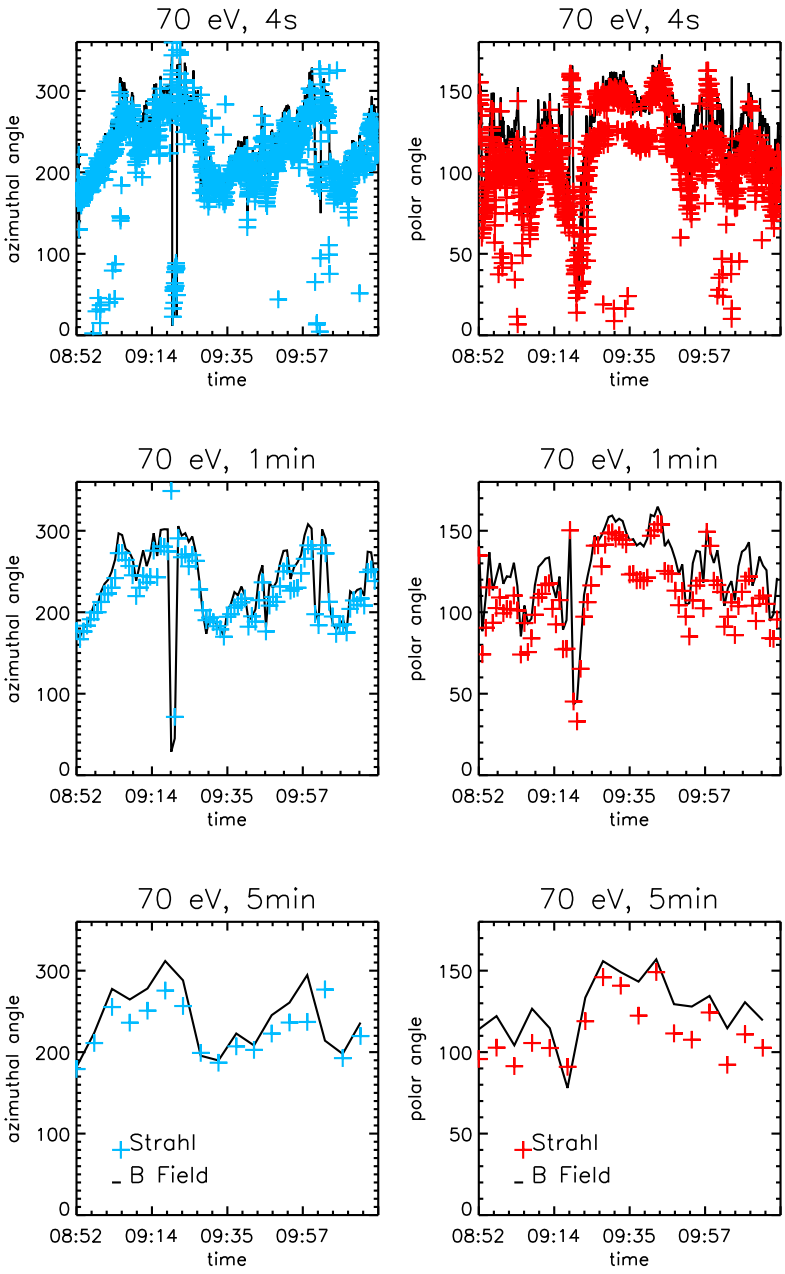

Figure 6.4: Magnetic field observations (black line) and strahl field orientation estimates (coloured crosses) against time for the azimuthal (left) and polar (right) direction in the Cluster PEACE FOV. Each vertical panel shows the results for the different (4 s, 1 min and 5 min) cadences examined. These observations are from the PEACE energy bin with a central energy of $\sim$ 70 eV.

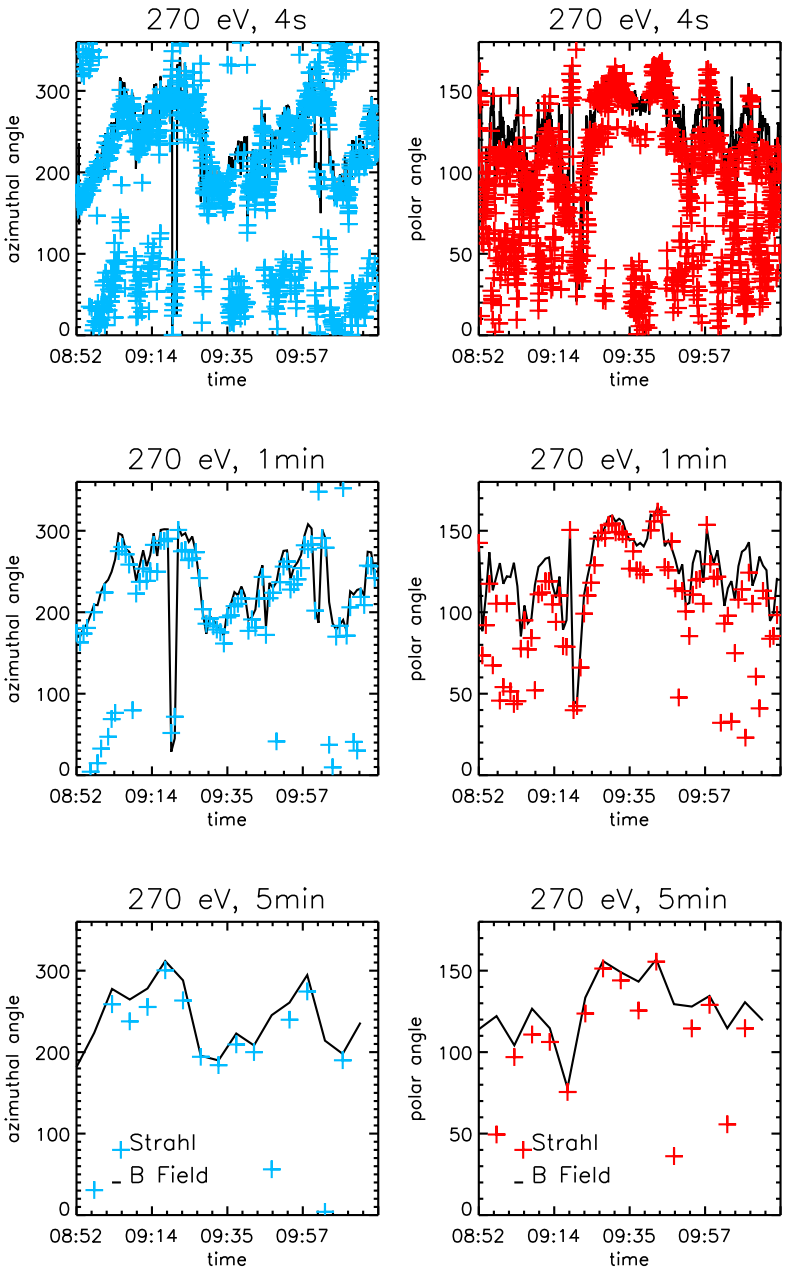

Figure 6.5: Magnetic field observations (black line) and strahl field orientation estimates (coloured crosses) against time for the azimuthal (left) and polar (right) direction in the Cluster PEACE FOV. Each vertical panel shows the results for the different (4 s, 1 min and 5 min) cadences examined. These observations are from the PEACE energy bin with a central energy of $\sim$ 270 eV.

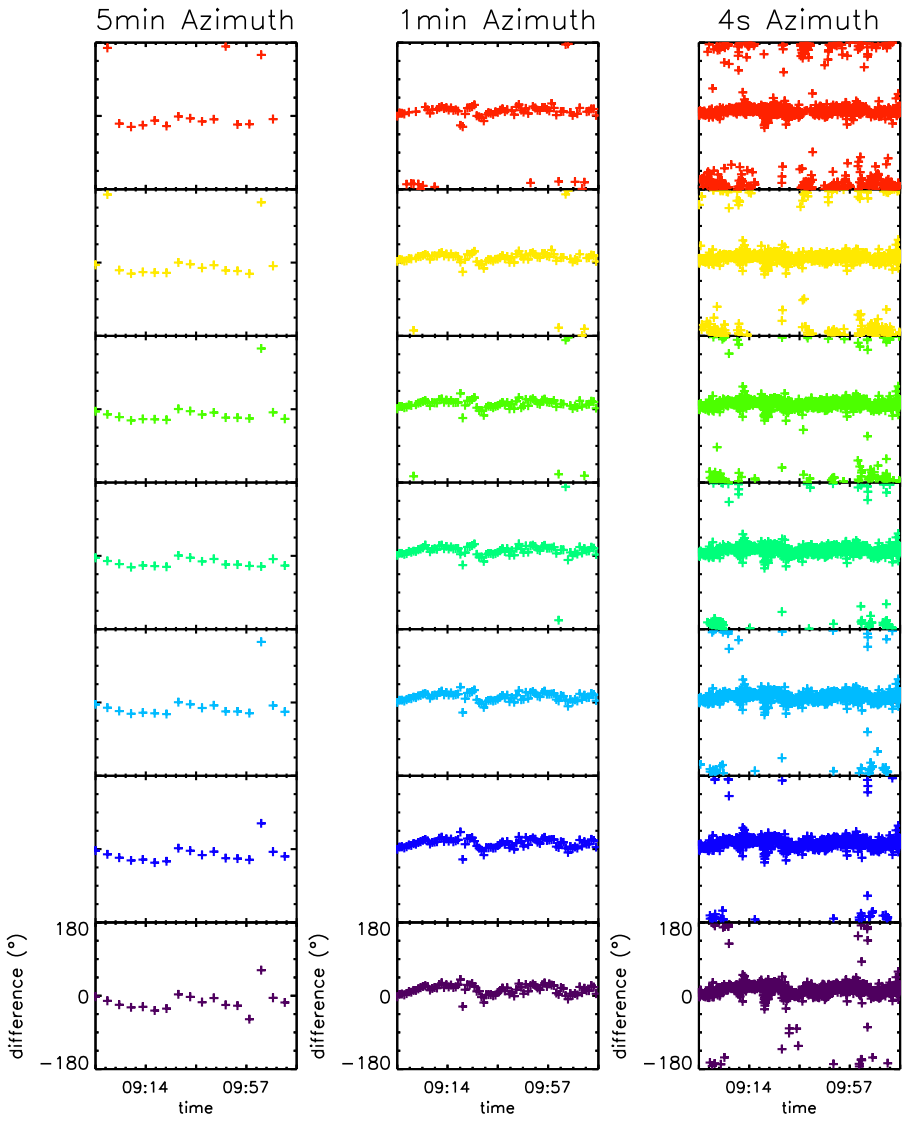

Figure 6.6: Difference between magnetic field observations and strahl field orientation estimates against time for the azimuthal direction in the Cluster PEACE FOV. Each panel shows the results for different cadences examined, from left to right, 5 min, 1 min and 4 s. The different colours represent the different strahl energies examined: 70 (purple), 90 (dark blue), 110 (light blue), 140 (dark green), 170 (light green), 220 (yellow) and 270 (red) eV.

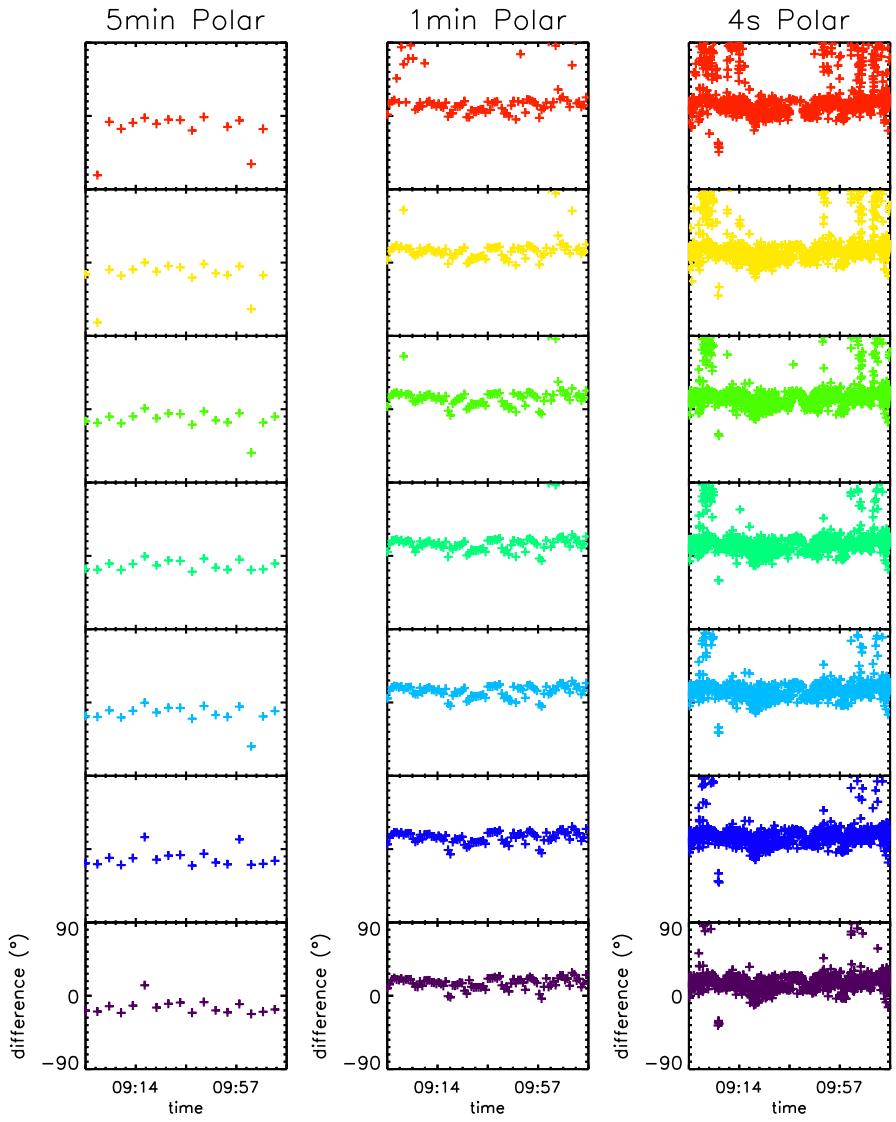

Figure 6.7: Difference between magnetic field observations and strahl field orientation estimates against time for the polar direction in the Cluster PEACE FOV. Each panel shows the results for different cadences examined, from left to right, 5 min, 1 min and 4 s. The different colours represent the different strahl energies examined: 70 (purple), 90 (dark blue), 110 (light blue), 140 (dark green), 170 (light green), 220 (yellow) and 270 (red) eV.

These larger differences observed may be a result of: a significant change in the magnetic field direction during an electron measurement; larger uncertainty in the strahl beam direction due to broader strahl, either inherently or possibly as a result of blurring during the observation due to a changing magnetic field; or confusion between the strahl beam direction and anti-strahl direction. The smaller number of large differences between the average magnetic field and the strahl beam direction observed for lower strahl energies may be a result of lower number densities for higher energy strahl and thus fitting to less intense strahl beams or due to strahl widths for the higher energy strahl being broader during this particular interval. To investigate these possibilities the changes in magnetic field direction and strahl width relations were examined. The results are shown in Figures 6.8, 6.9, 6.10 and 6.11.

Figures 6.8 and 6.9 show the difference between the average magnetic field and the strahl beam direction in the azimuthal and polar FOV directions respectively, compared to the standard deviation of the magnetic field observations during each interval. It can be seen that, for all observed energies and cadences, the variation in the magnetic field data does not seem to have a strong influence on the difference between the observed field direction and the strahl fitted estimate of the field direction. Thus, the strahl beam observations match the average magnetic field direction relatively closely without being effected significantly by the fluctuations of the field away from the average direction during the observation interval.

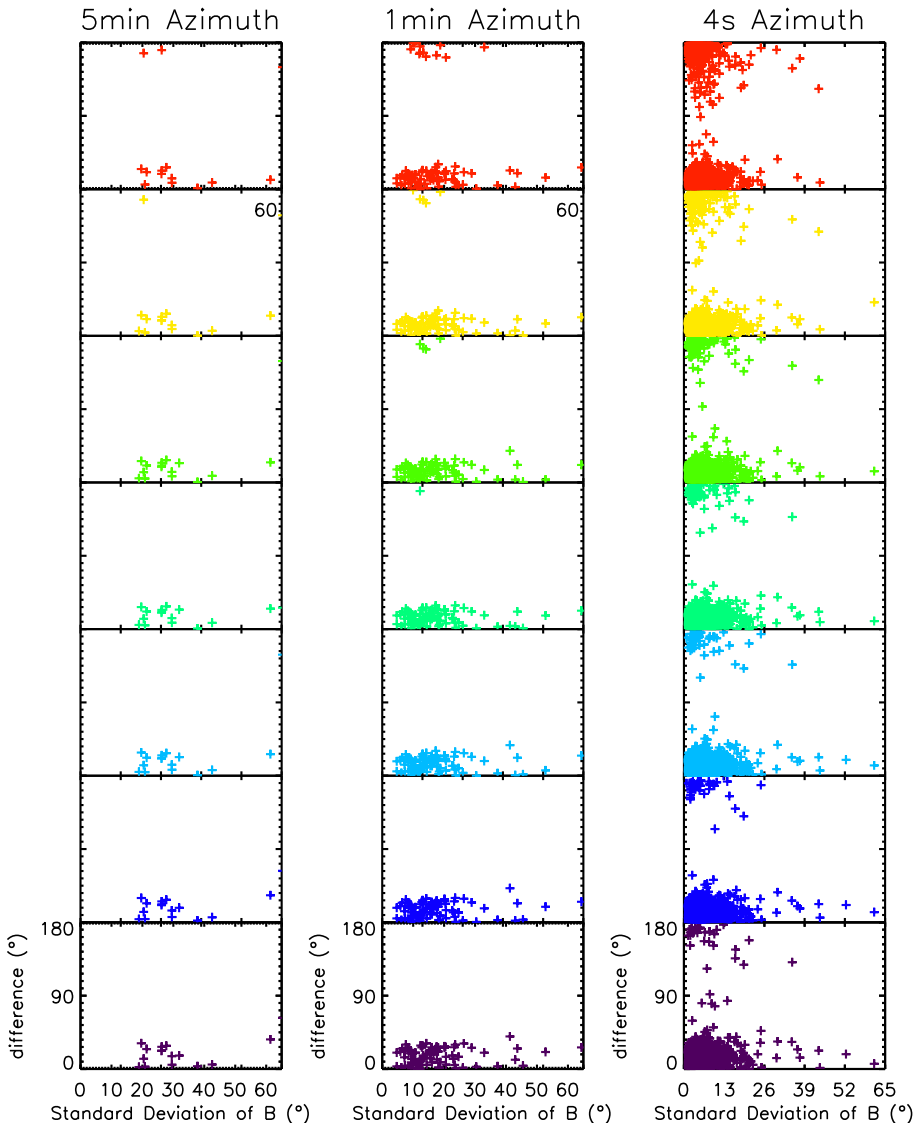

Figure 6.8: Difference between magnetic field observations and strahl field orientation estimates against the standard deviation in the magnetic field direction for the azimuthal direction in the Cluster PEACE FOV. Each panel shows the results for different cadences examined, from left to right, 5 min, 1 min and 4 s. The different colours represent the different strahl energies examined: 70 (purple), 90 (dark blue), 110 (light blue), 140 (dark green), 170 (light green), 220 (yellow) and 270 (red) eV.

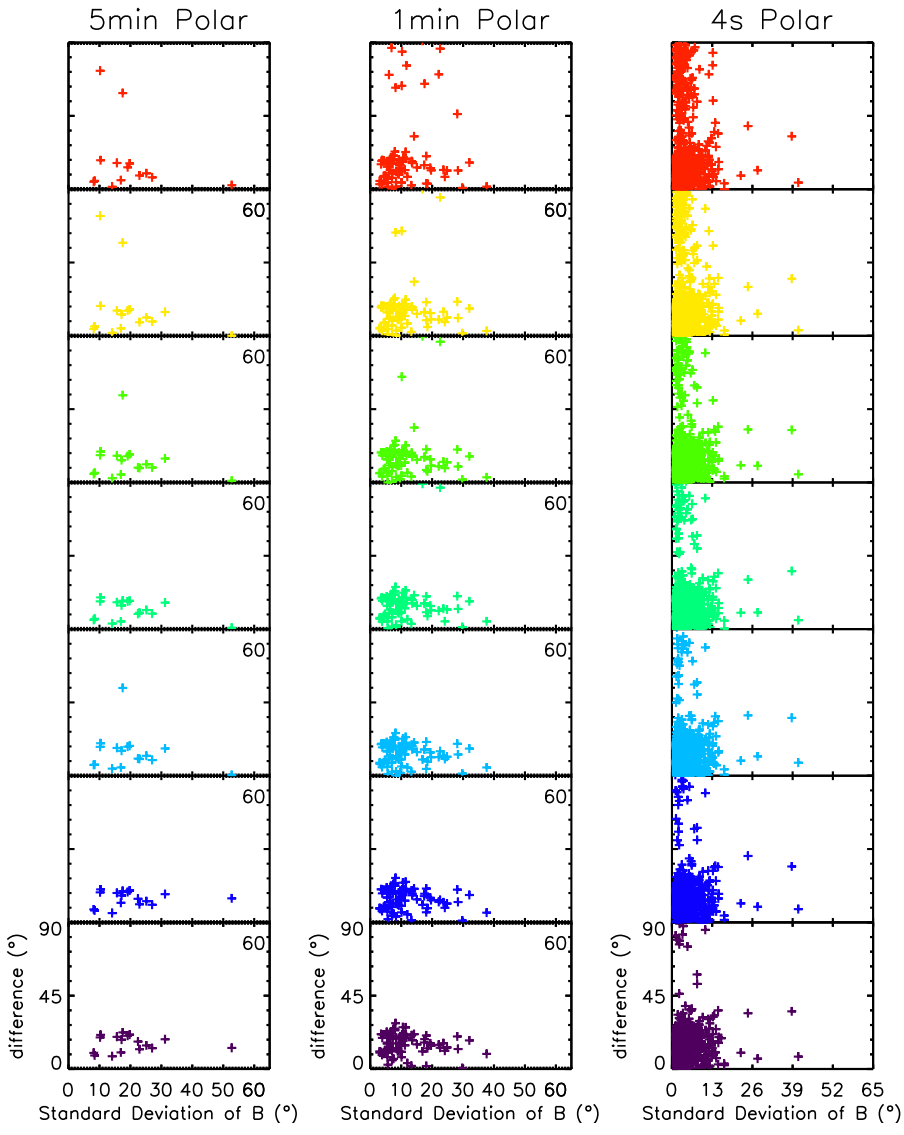

Figure 6.9: Difference between magnetic field observations and strahl field orientation estimates against the standard deviation in the magnetic field direction for the polar direction in the Cluster PEACE FOV. Each panel shows the results for the different cadences examined, from left to right, 5 min, 1 min and 4 s. The different colours represent the different strahl energies examined: 70 (purple), 90 (dark blue), 110 (light blue), 140 (dark green), 170 (light green), 220 (yellow) and 270 (red) eV.

Figures 6.10 and 6.11 show the difference between the average magnetic field and the strahl beam direction in the azimuthal and polar FOV directions respectively compared to the strahl width observed during the interval. It can be seen that, in both the azimuth and polar directions the differences between observed field and strahl estimate can be separated into two clear groups. The first, a closely clustered group, made up of strahl with widths that are generally below $\sim 40^{\circ}$ and that have a good agreement with the magnetic field direction. The second, much more spread group, made up of strahl with widths that are generally above $\sim 40^{\circ}$ and have much larger differences between the observed field direction and the strahl estimate. It can also be observed that strahl widths from the first group display a general decrease with strahl energy. In contrast, for the second group, there are a greater number of larger strahl widths for higher energy strahl but no clear energy trend.

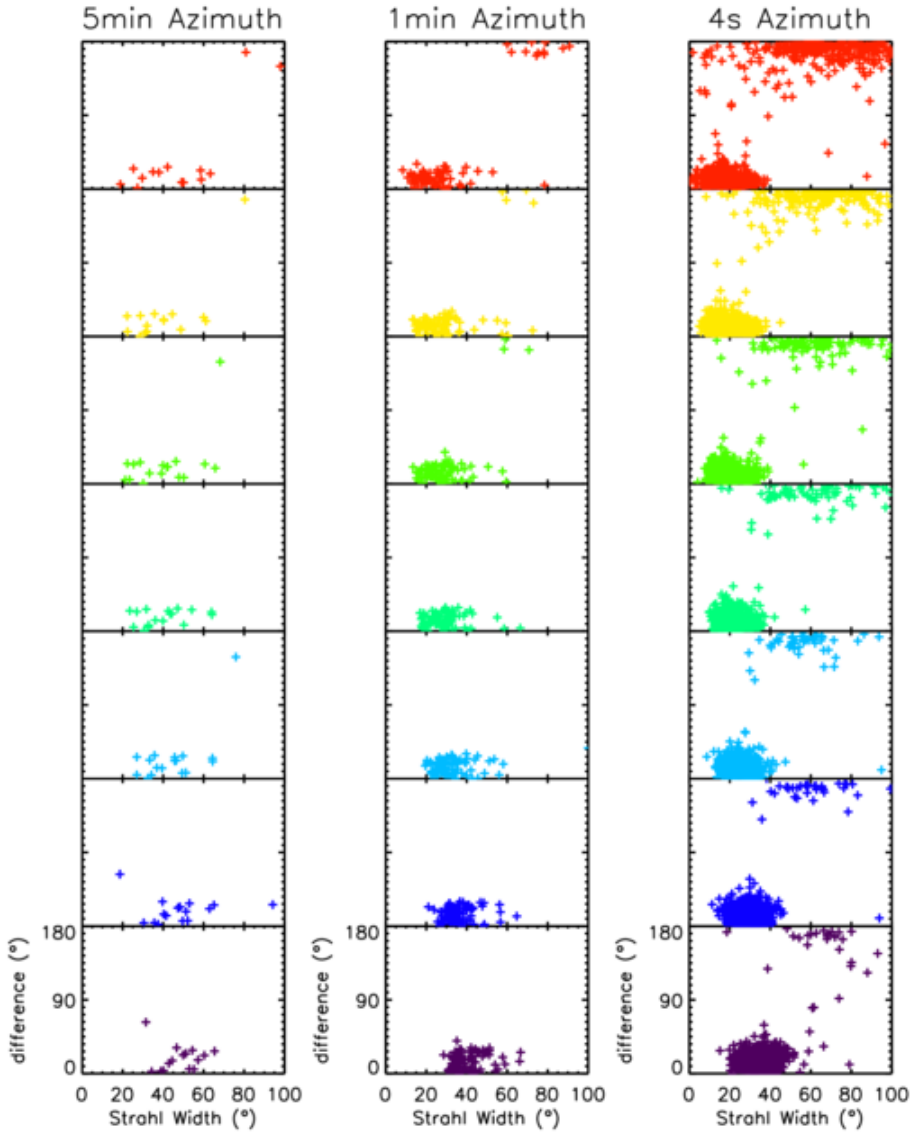

Figure 6.10: Magnitude of the difference between magnetic field observations and strahl field orientation estimates against strahl width for the azimuthal direction in the Cluster PEACE FOV. Each panel shows the results for different cadences examined, from left to right, 5 min, 1 min and 4 s. The different colours represent the different strahl energies examined: 70 (purple), 90 (dark blue), 110 (light blue), 140 (dark green), 170 (light green), 220 (yellow) and 270 (red) eV.

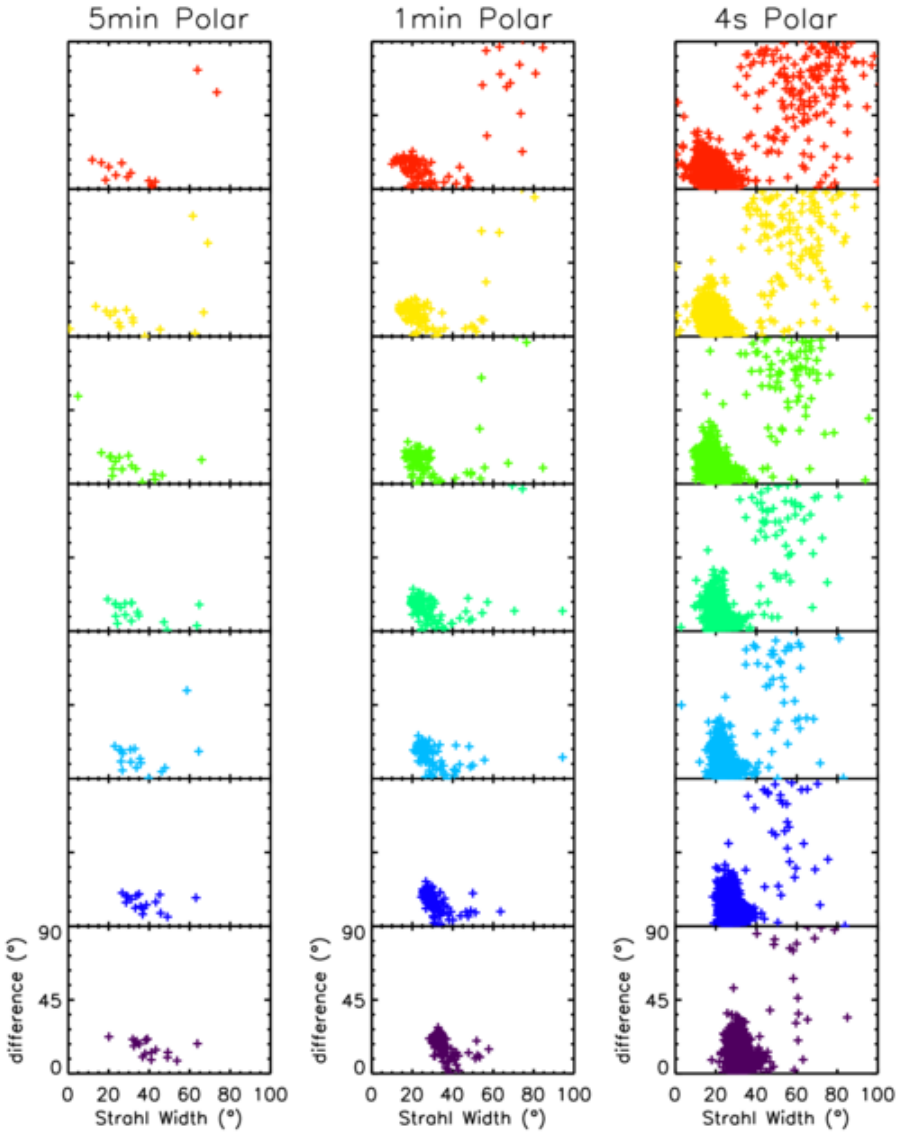

Figure 6.11: Magnitude of the difference between magnetic field observations and strahl field orientation estimates against the strahl width for the polar direction in the Cluster PEACE FOV. Each panel shows the results for different cadences examined, from left to right, 5 min, 1 min and 4 s. The different colours represent the different strahl energies examined: 70 (purple), 90 (dark blue), 110 (light blue), 140 (dark green), 170 (light green), 220 (yellow) and 270 (red) eV.

Thus, strahl beam width likely has a significant impact on the precision of the field orientation estimate, and the number of beam orientation estimates that give a value approximately opposite to the magnetic field direction suggests that during the fitting procedure the strahl beam may be confused with the electrons in the anti-strahl direction. In order to investigate this possibility the observations were re-examined, in particular, by comparing beam fitting in the strahl and anti-strahl direction, This was achieved by blocking the first fitted beam and fitting a second 2D Gaussian to the observations, shown in Figure 6.12. The observations for which the 'anti-strahl' width (2nd fitting result) was less than the 'strahl' width (1st fitting result) where removed from the dataset, as in these cases it seems likely that the strahl and anti-strahl directions had been confused during the fitting procedure.

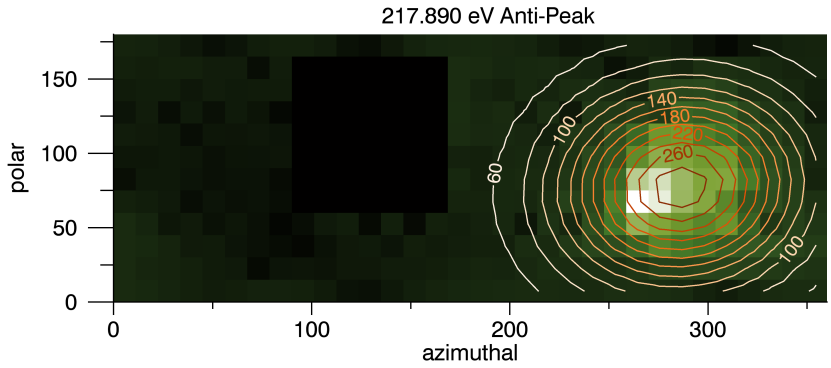

Figure 6.12: Example of 1 min resolution Cluster PEACE electron data, shown in the instrument FOV. This is for the same event as shown in Figure 6.3 and is in the same format with angular bins with an azimuthal and polar size of 11.25° and 15° receptively. The strahl beam that was fitted in (c) of Figure 6.3 has been blocked (PSD values in strahl bins have been replaced with the background value) and the remaining FOV has been fitted by a 2D Gaussian function.

Figures 6.13 and 6.14 show the observed average magnetic field direction and strahl beam direction in terms of the azimuthal and polar angles for the PEACE FOV for ~ 70 and 270 eV respectively (in the same format as Figures 6.4 and 6.5). In these Figures, the events for which distinction between the strahl and anti-strahl was not clear have been removed and it can be seen from comparison that the majority of very large differences between the magnetic field and the fitted beam have also been removed. This can be seen more clearly in Figures 6.15 and 6.16, which show the difference between the average magnetic field and the strahl beam direction in the azimuthal and polar FOV directions respectively.

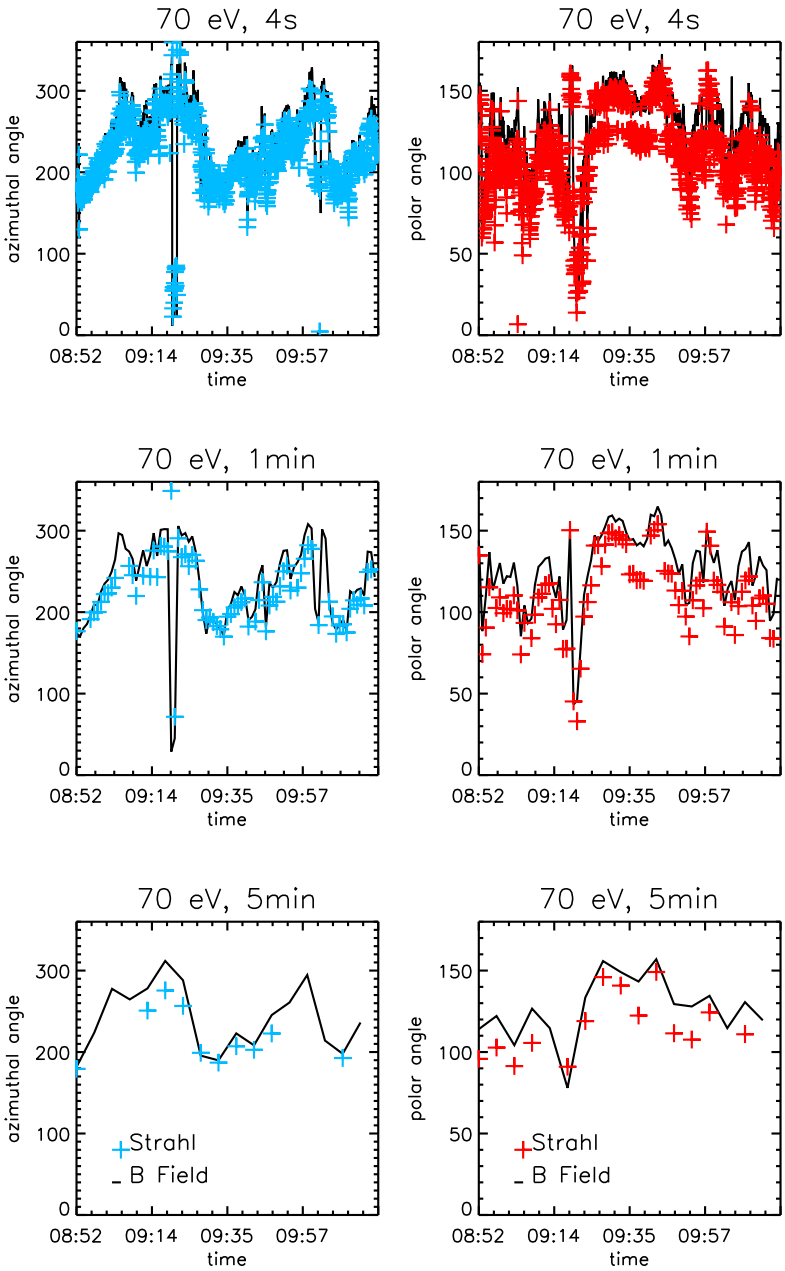

Figure 6.13: Magnetic field observations (black line) and strahl field orientation estimates (coloured crosses) against time for the azimuthal (left) and polar (right) direction in the Cluster PEACE FOV. Each vertical panel shows the results for the different (4 s, 1 min and 5 min) cadences examined. These observations are from the PEACE energy bin with a central energy of $\sim$ 70 eV.

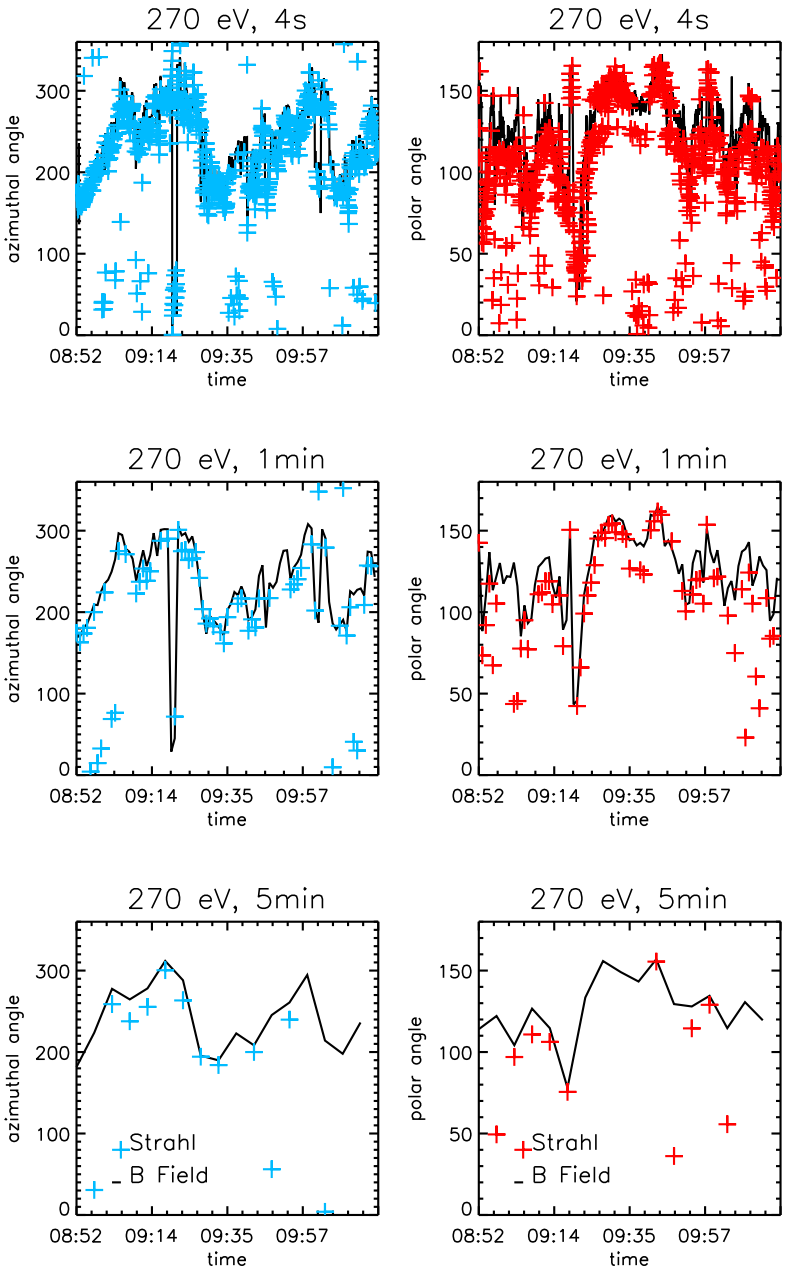

Figure 6.14: Magnetic field observations (black line) and strahl field orientation estimates (coloured crosses) against time for the azimuthal (left) and polar (right) direction in the Cluster PEACE FOV. Each vertical panel shows the results for the different (4 s, 1 min and 5 min) cadences examined. These observations are from the PEACE energy bin with a central energy of $\sim$ 270 eV.

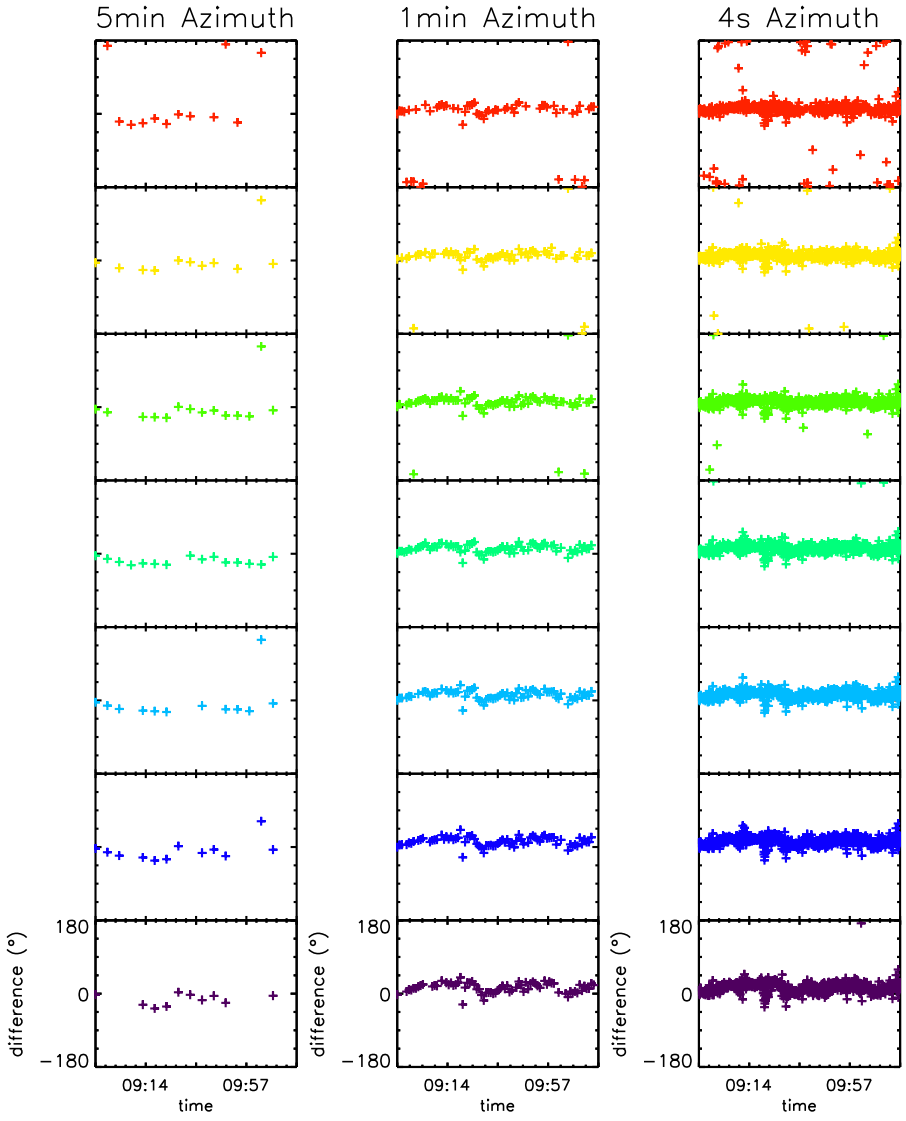

Figure 6.15: Difference between magnetic field observations and strahl field orientation estimates against time for the azimuthal direction in the Cluster PEACE FOV. Each panel shows the results for different cadences examined, from left to right, 5 min, 1 min and 4 s. The different colours represent the different strahl energies examined: 70 (purple), 90 (dark blue), 110 (light blue), 140 (dark green), 170 (light green), 220 (yellow) and 270 (red) eV.

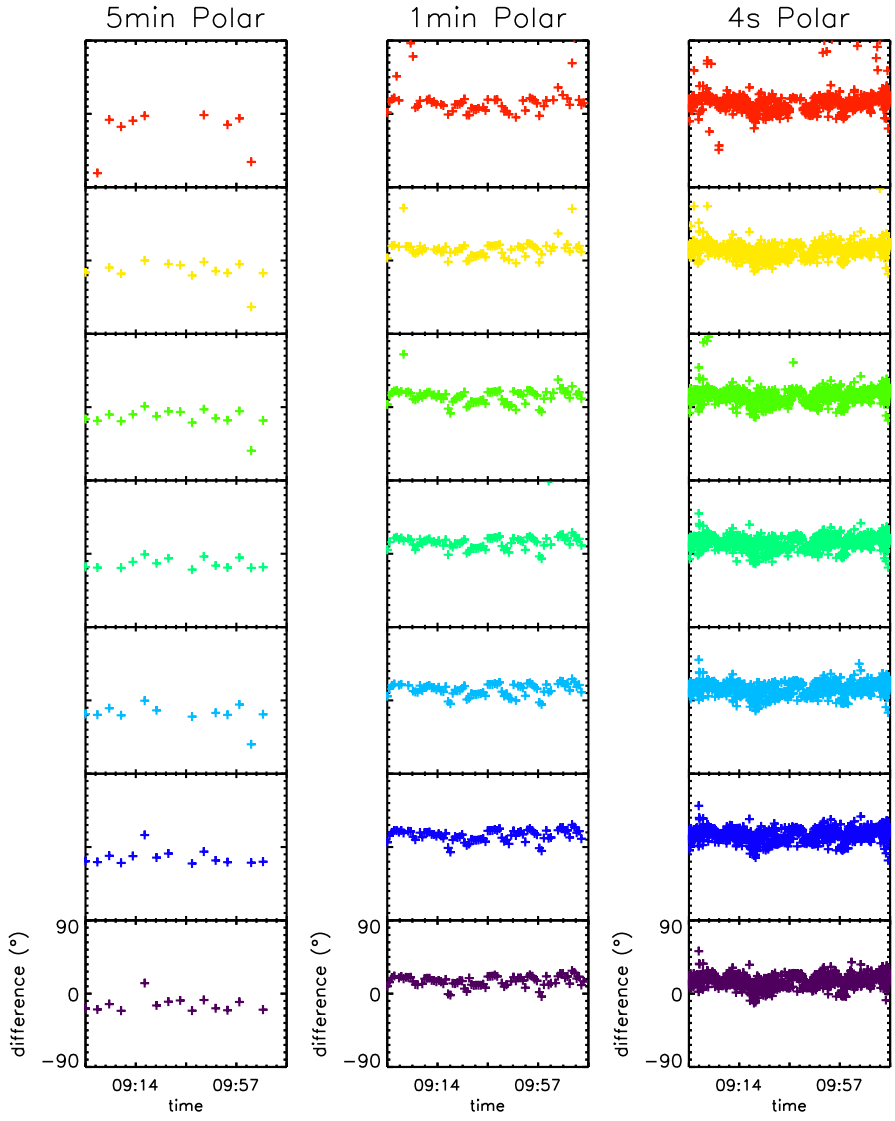

Figure 6.16: Difference between magnetic field observations and strahl field orientation estimates against time for the polar direction in the Cluster PEACE FOV. Each panel shows the results for different cadences examined, from left to right, 5 min, 1 min and 4 s. The different colours represent the different strahl energies examined: 70 (purple), 90 (dark blue), 110 (light blue), 140 (dark green), 170 (light green), 220 (yellow) and 270 (red) eV.

The strahl width relations of events for which clear strahl (without strahl-anti-strahl direction ambiguity) were examined, as before in Figures 6.10 and 6.11. Figures 6.17 and 6.18 show the difference between the average magnetic field and the strahl beam direction in the azimuthal and polar FOV directions respectively compared to the strahl width observed during the interval. It can be seen that, in both the azimuth and polar directions, the strahl width is generally less than 40° and only the largest electron energies observed retain a significant number of results with large widths. These large width values that remain are likely the result of beam-like distributions in both directions with similar widths or very broad strahl with a large associated error in beam position.

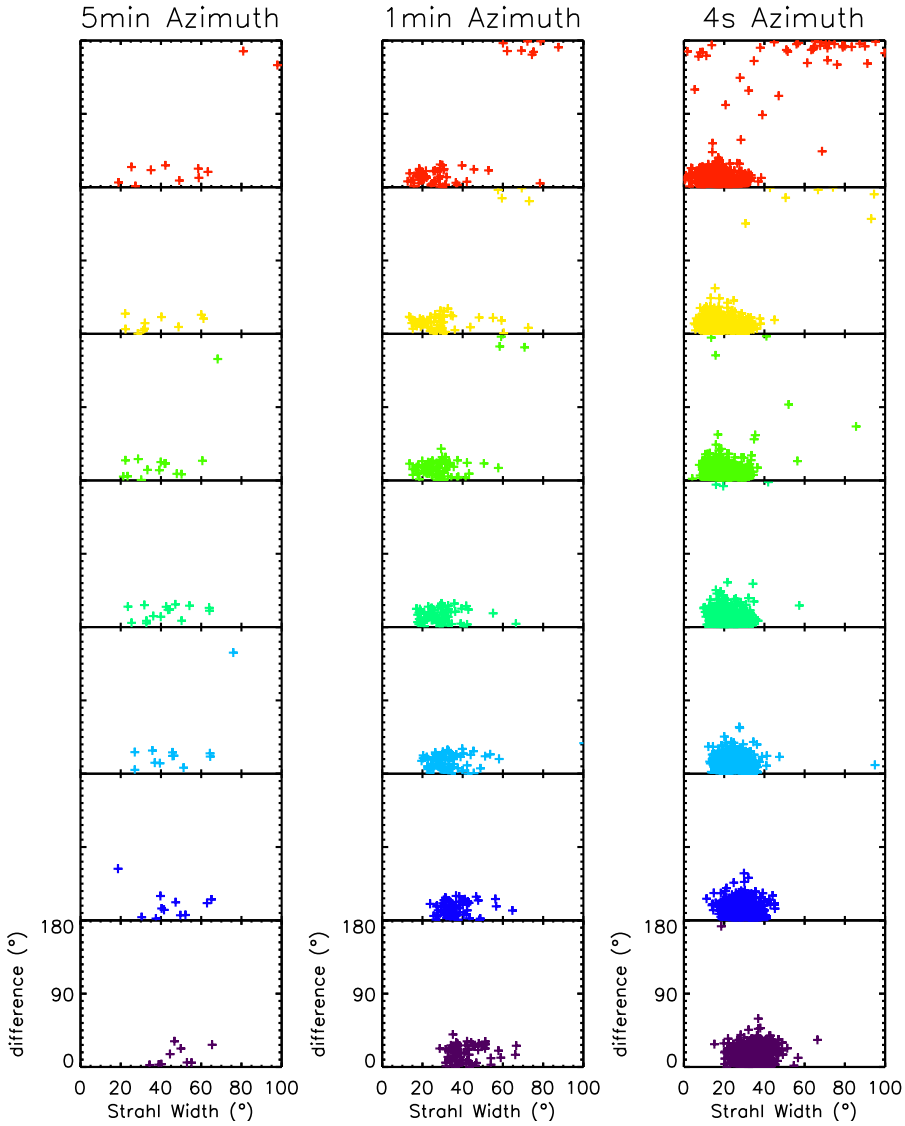

Figure 6.17: Magnitude of the difference between magnetic field observations and strahl field orientation estimates against strahl width for the azimuthal direction in the Cluster PEACE FOV. Each panel shows the results for different cadences examined, from left to right, 5 min, 1 min and 4 s. The different colours represent the different strahl energies examined: 70 (purple), 90 (dark blue), 110 (light blue), 140 (dark green), 170 (light green), 220 (yellow) and 270 (red) eV.

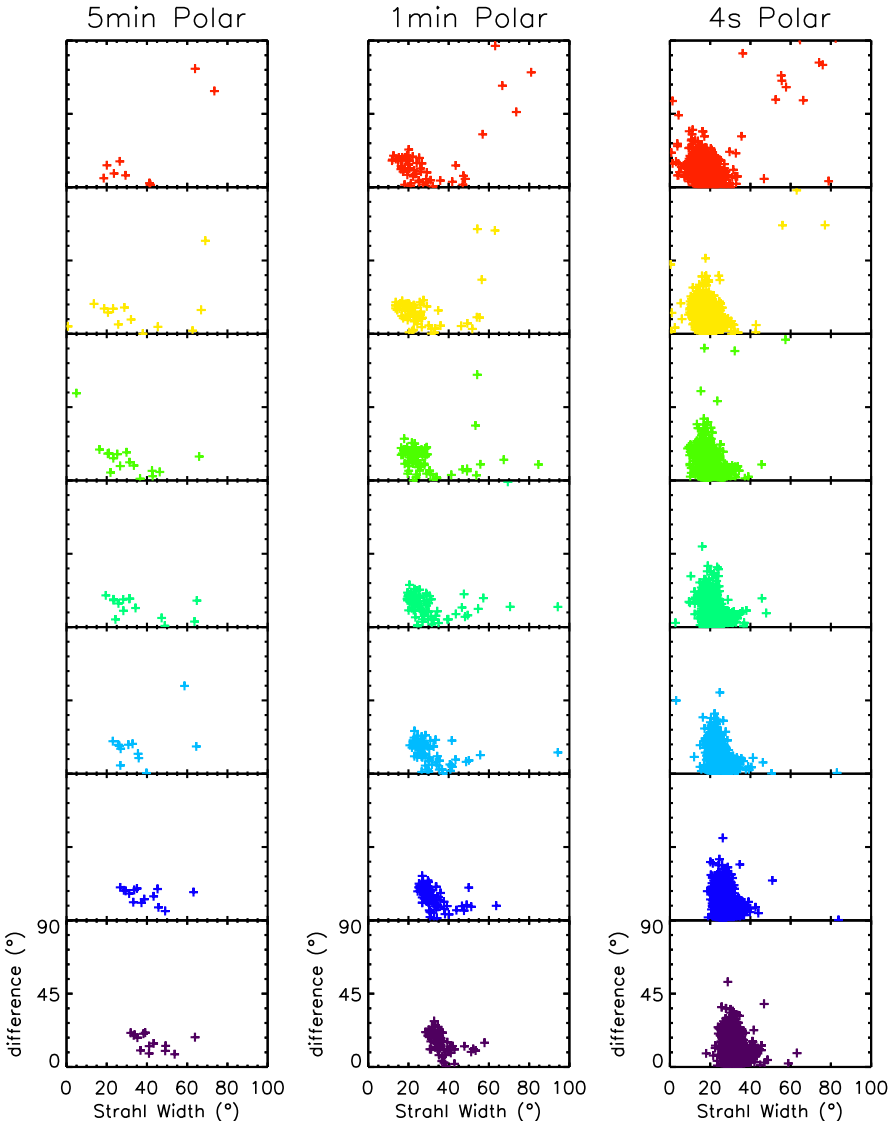

Figure 6.18: Magnitude of the difference between magnetic field observations and strahl field orientation estimates against the strahl width for the polar direction in the Cluster PEACE FOV. Each panel shows the results for different cadences examined, from left to right, 5 min, 1 min and 4 s. The different colours represent the different strahl energies examined: 70 (purple), 90 (dark blue), 110 (light blue), 140 (dark green), 170 (light green), 220 (yellow) and 270 (red) eV.

Figure 6.19 shows the mean and median difference between magnetic field observations and strahl field orientation estimates against strahl energy for only the narrow ($< 40^\circ$) strahl. In the polar direction, it can be seen that the mean and the median values are close (within $\sim 1-4^\circ$) and that there is a general decrease in difference between observed field direction and strahl fitting estimate of the field direction with strahl energy. Thus, the higher energy strahl, which were generally more narrow for this particular solar wind interval, provide a slightly more accurate estimate of the field orientation. In the azimuthal direction, it can be seen that the mean and the median values, for the 4s and 1 min cadence fitting, are close (within $\sim 1-3^\circ$) and that there is a flat or perhaps slightly decreasing difference between observed field direction and strahl fitting estimate of the field direction with strahl energy. For the 5 min cadence fitting there is no clear relation with energy. Figure 6.20 shows the percentage of observations with a difference between magnetic field observations and strahl field orientation that are less than $\leq 5^\circ$(blue), 10°(orange) and 20°(red). It can be seen that the majority of strahl observations provide an IMF orientation within 20° of the magnetic field observation, with the best results for strahl fitting for electron energies of $\sim$100-200 eV.

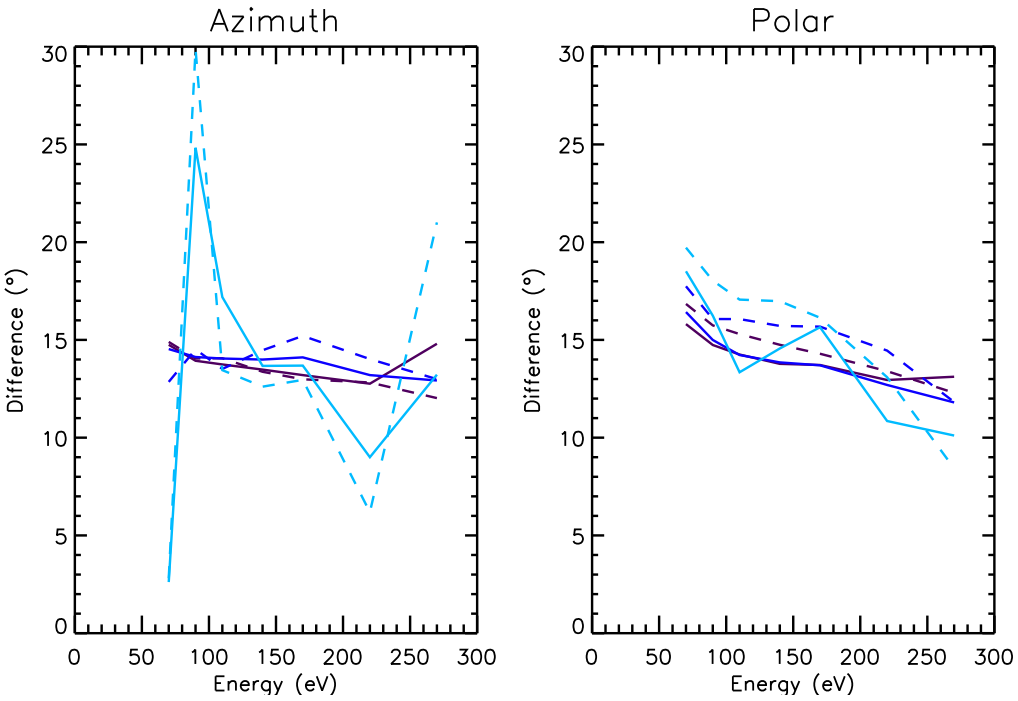

Figure 6.19: Difference between magnetic field observations and strahl field orientation estimates against strahl energy for azimuth (left) and polar (right) directions in the Cluster PEACE FOV. The mean and the median difference is shown by the solid and dashed lines respectively. The different colours represent the different cadences examined: 4s (purple), 1 min (dark blue) and 5 min (light blue).

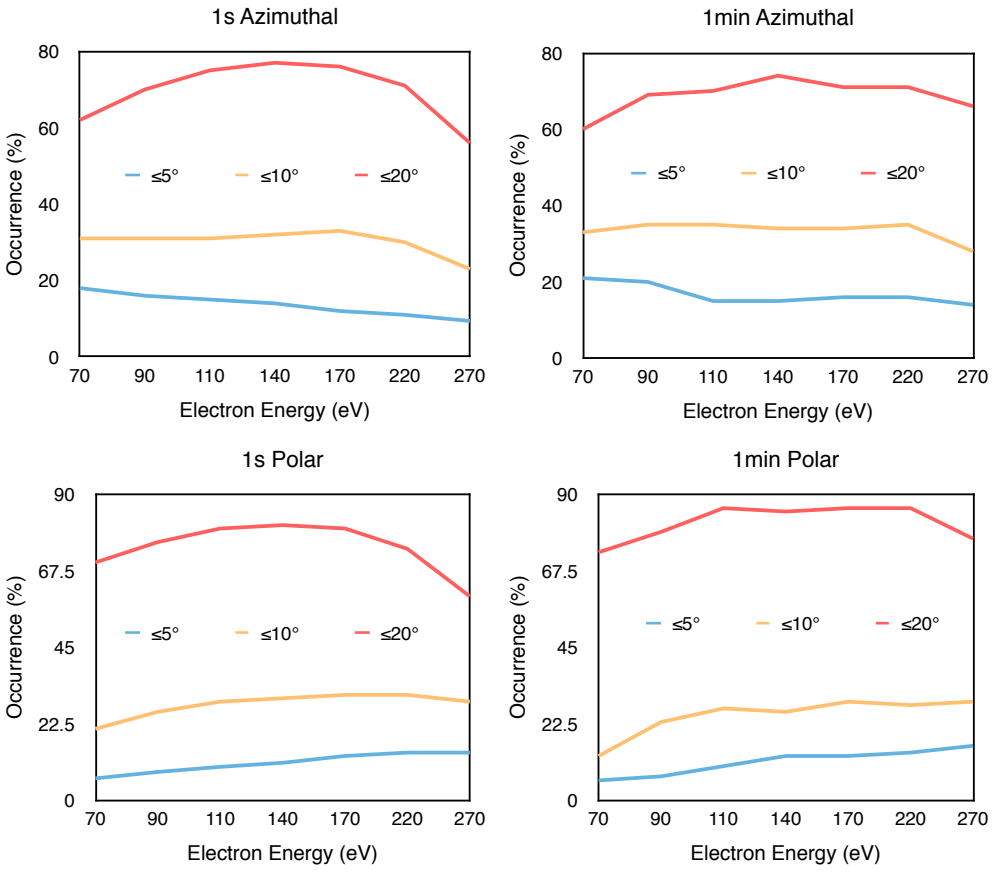

Figure 6.20: Percent of observations with a difference between magnetic field observations and strahl field orientation estimates of $\leq 5°$(blue), $10°$(orange) and $20°$(red). Percentage is plotted against strahl energy for 1 second (left) and 1 min (right) cadences for the azimuth and polar directions in the Cluster PEACE FOV.

As stated previously, the strahl widths display a clear general decrease with strahl energy. Interestingly however, there are more instances for higher energy strahl where electrons in the anti-strahl direction are beam-like enough to be selected over the strahl direction by the fitting procedure. This may be an indication that higher energy strahl have been backscattered more than their lower energy counterparts or that the halo component of the electrons at these higher energies is more strongly anisotropic. It has been shown that the halo temperature is often anisotropic, often with $T_{\parallel} > T_{\perp}$ in the fast solar wind (Pierrard et al., 2016). In as statistical study at 1 AU by Anderson et al. (2012) it was found that, although strahl cannot be characterized by a typical width at any energy, for widths $\leq 40°$ and $\geq 70°$ it is proportionally more likely to observe higher energy strahl. This energy subdivision is potentially reflected in our results, although further investigation into resolving the ambiguities between the strahl and anti-strahl direction is required.

6.2 Mars Express Test

The full-sky, relatively high angular resolution data observed by Cluster at 1 AU produces a good estimate of the magnetic field orientation. In this section, beam fitting was tested using using electron observations obtained by the MEX spacecraft. The MEX ASPERA-3 ELS has full-sky coverage when the scanning platform it is mounted on is in operation. However, it has lower angular resolution than the Cluster observations examined and, as Mars is $\sim$1.5 AU from the Sun, in general MEX will observe broader strahl than at 1 AU (Hammond et al., 1996; Graham et al., 2017). MEX was selected for this test as it is a more challenging task for strahl beam fitting, and a good test of its limitations, and because MEX has no magnetometer on board, and thus estimates of IMF orientation would be significantly beneficial.

An event examined by Edberg et al. (2009) during a period of high solar wind pressure observed by both Rosetta and Mars Express was selected for analysis. This period was originally investigated in order to examine how the Martian plasma environment is affected by high pressure solar wind. During this interval Mars express completed elliptical orbits that crossed the Martian bow shock on every orbit (inbound and outbound). The Martian bow shock crossings were identified by Edberg et al. (2009) using the MEX/ELS data as a sudden increase in electron fluxes on inbound passes (and vice versa). The solar wind and IMF downstream of Mars during this interval was observed by Rosetta.

The time periods chosen for the analysis presented in this chapter were bow shock crossings at $\sim$ 04.30 UT and $\sim$ 18.00 UT on the 25th February 2007 and $\sim$ 14.00 UT on the 26th February 2007. The scanning platform moves though 180° twice around the time of the bow shock crossings and is thus possibly making full 3D electron observations in the solar wind. Figure 6.21 shows a time series of MEX electron and ion spectra, ion density and solar wind velocity for 25th-27th February 2007. The interval of high pressure studied in Edberg et al. (2009) is marked by black lines, while the time periods chosen for analysis in this chapter are marked by orange lines.

For each of the intervals examined in this chapter, the scanning platform rotated though 180° twice, with each scan taking $\sim$ 3 mins 40 s. MEX ELS electron count rate observations for each polar anode and each energy sweep were averaged into 10° azimuthal bins using the position of the scanning platform at a given observation time. It was assumed that the counts were evenly distributed across the anode FOV, in order to calculate the fraction of the anode area within each bin, and weight the data value for that bin. In this way, a basic but testable full sky electron distribution was produced, to which the strahl beam fitting tool developed using Cluster PEACE data could be applied, in order to investigate the possibility of developing it further for MEX science requiring estimates of the magnetic field direction. The same procedure as described in Section 6.1.1 was then applied to all three MEX ELS intervals. Energies in the range $\sim$10-300 eV were examined. ELS measurements of electrons with energies below $\sim$ 10 eV are affected by the spacecraft potential and are not always reliable. However, as strahl energies are much higher, this did not present problems for the analysis.

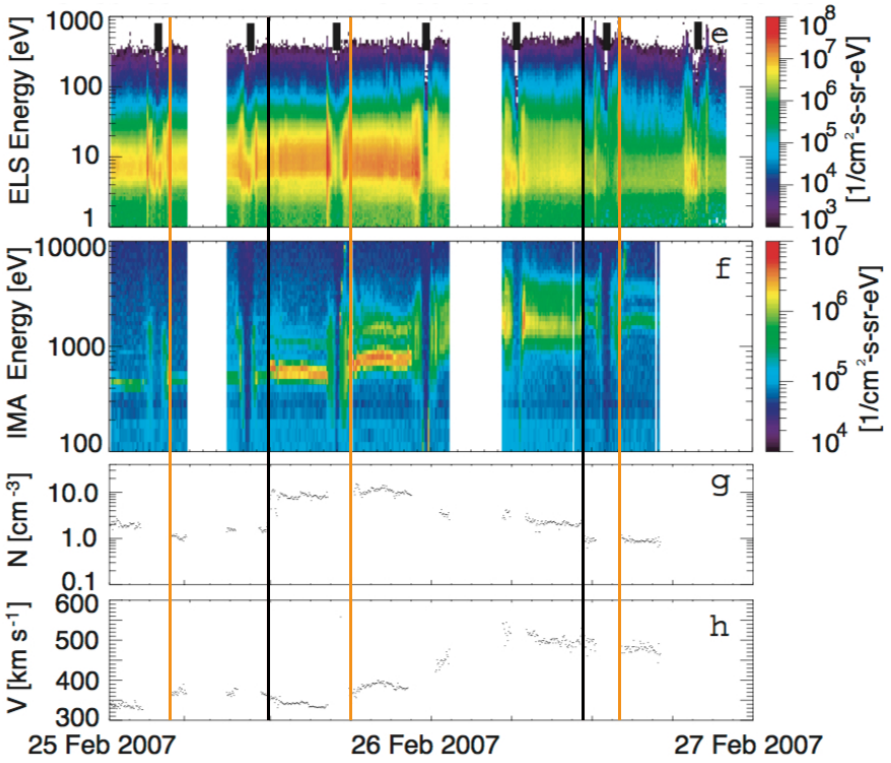

Figure 6.21: Figure taken from Edberg et al. (2009) showing a time series of MEX data for 25th-27th Jaunuary 2007. (e) MEX ELS omni-directional electron energy spectra, (f) MEX IMA omni-directional ion energy spectra as well as (g) MEX IMA ion density and (h) total velocity. The interval of high pressure studied in Edberg et al. (2009) is marked by black lines. The thick bars in panel (e) mark the closest approach of MEX during each orbit. The time periods chosen for analysis in this chapter are marked by orange lines.

6.2.1 Results

Panels (a), (b) and (c) of Figure 6.22 show the start and stop times of the scanning platform for the bow shock crossings on the 25th and 26th February 2007 and a time series of the average observed ∼20 eV electron flux. Each set of scans occur as the MEX spacecraft leaves the bow shock and enters the solar wind. However, examination of the electron flux for the three events shows that the first of each set of actuations occur within the bow shock, and that the same is true for the second actuation of (b) and (c). The second actuation for the event on the 25th shown in Panel (a), has a much lower flux relative to those observed in the bow shock for that event. However, it is still likely within the Martian bow shock. Panel (d) of Figure 6.22 shows the start and stop times of the scanning platform for the bow shock crossings on the 1st March 2007 superimposed on a time series of the average observed ∼20 eV electron flux. This time period was not initially considered as it occurs after the events analysed in the Edberg et al. (2009) study and does not have the associated Rosetta observations. However, the two MEX platform scans take place outside the Martian bow shock, as can be seen in Panels (d) of Figure 6.22.

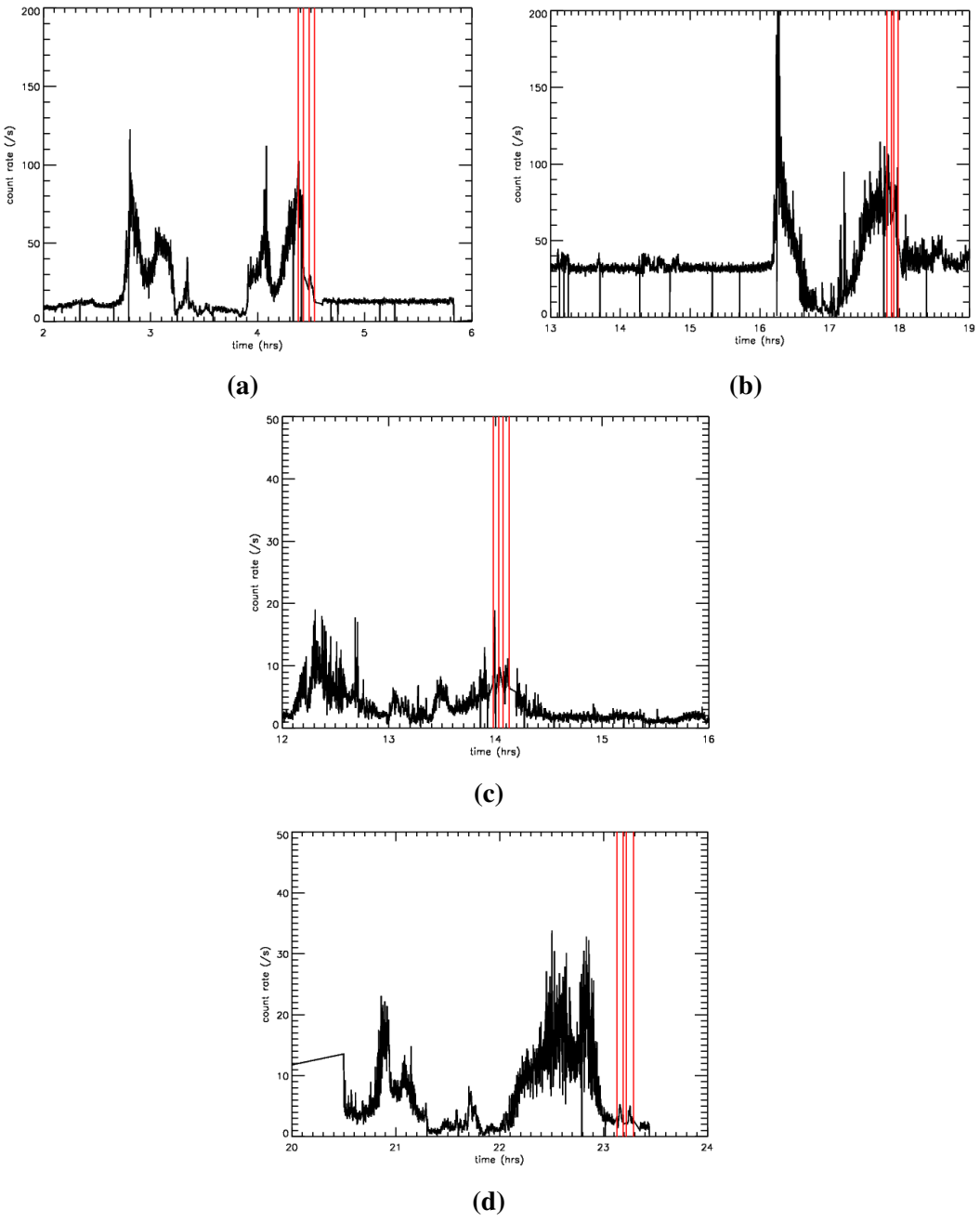

Figure 6.22: Time series of electron count rate for ∼20 eV electrons averaged over all anodes. The red vertical lines show the start and stop times for actuations made by the scanning platform. (a) 25th February 2007, scans from 04:23:03 to 04:26:42 UT and 04:28:39 to 04:32:17 UT. (b) 25th February 2007, scans from 17:49:27 to 17:53:05 UT and 17:55:03 to 17:58:41 UT. (c) 26th February 2007, scans from 13:58:41 to 14:02:19 UT, Act2 from 14:04:15 to 14:07:53 UT. (d) 1st March 2007, scans from 23:07:56 to 23:11:34 UT and 23:13:30 to 23:17:00 UT.

Figure 6.23 and Figure 6.24 show the full-sky FOV obtained by combining MEX ELS electron count rate observations for the 1st and 2nd actuations on the 25th from 17:49:27 to 17:53:05 UT and 17:55:03 to 17:58:41 UT respectively. Electron count rate is divided into angular bins with an azimuthal and polar size of 10.0° and 22.5° respectively, as described in Section 6.2. Each panel is for a different electron energy ranging from ∼10-300 eV. Examination of the results from the 1st actuation shows what appear to be beam-like populations from ∼ 40 to to ∼ 250 eV. Although, the beam widths are broader than those observed by Cluster at 1 AU and the observations are also generally less clear. Examination of the results from the 2nd actuation shows fewer beam-like populations, particularly for higher electron energies.

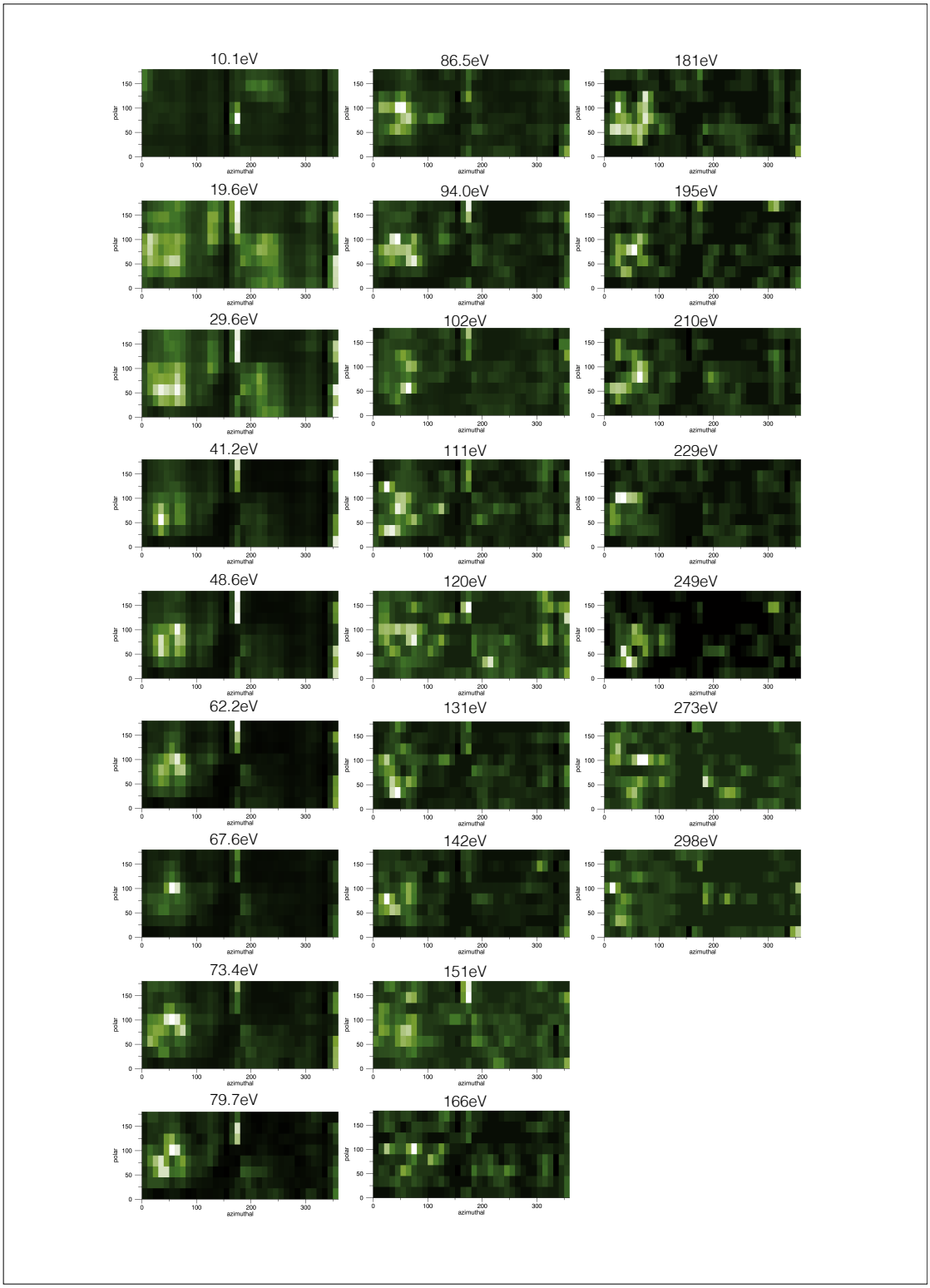

Figure 6.23: Full-FOV MEX ELS electron data from the 1st platform actuation on 25th February 2007 from 17:49:27 to 17:53:05 UT. Electron count rate is divided into angular bins with an azimuthal and polar size of 10.0° and 22.5° respectively. The input 2D image is scaled into full colour dynamic range of 0 to 255 with a linear scaling function. Each panel is for a different electron energy ranging from ∼10-300 eV.

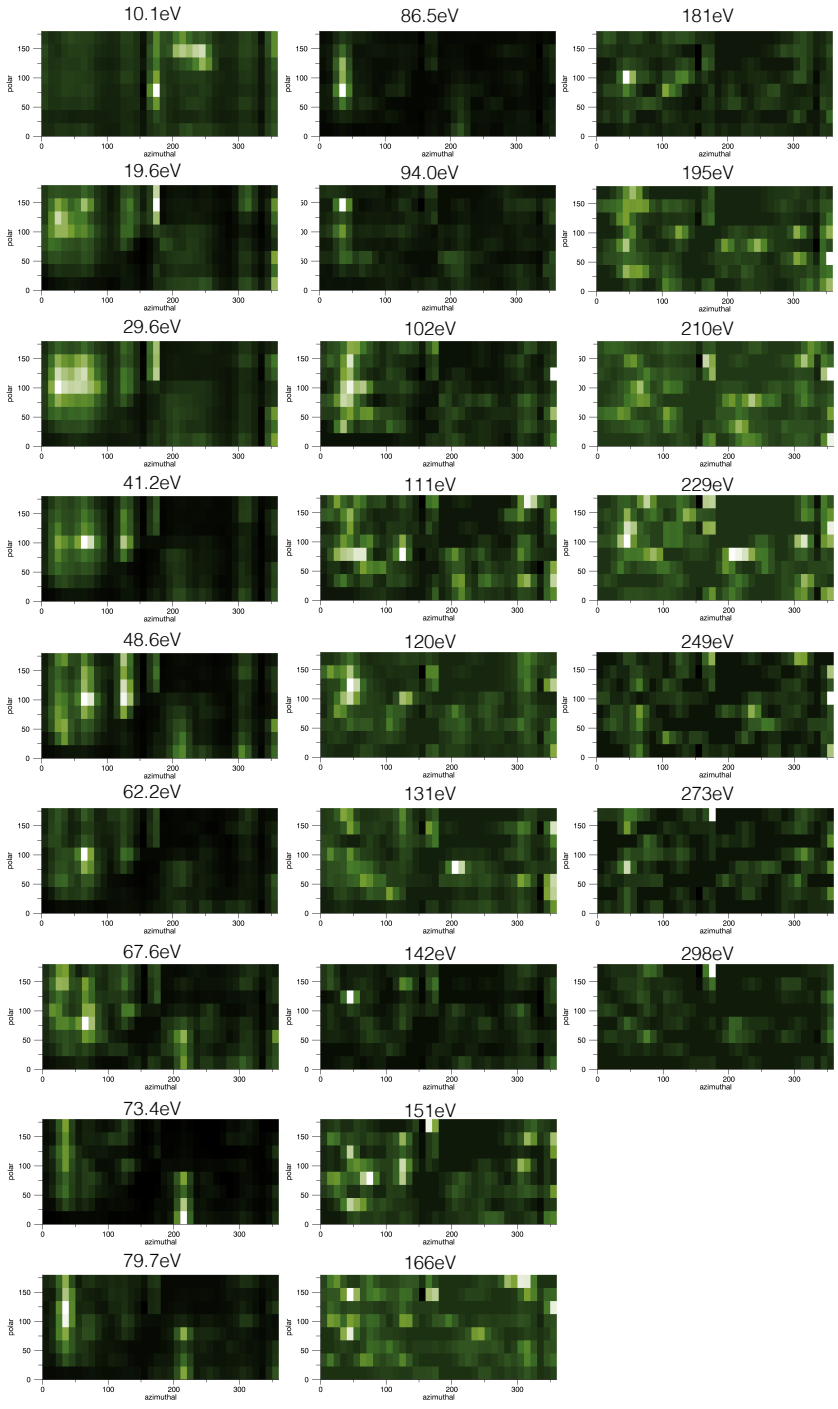

Figure 6.24: Full-FOV MEX ELS electron data from the 2nd platform actuation on 25th February 2007 from 17:55:03 to 17:58:41 UT. In the same format as Figure 6.23.

Beam widths were determined by Gaussian fitting to the beam, as outlined in Section 6.1.1. Only fitting results with a peak at least 2 times greater than that of the background and a FWHM of $< 180^{\circ}$ were to be considered a beam-like population (as described in Chapter 3.6). The locations of the centre of each fitted beam in the ELS full-sky FOV are plotted in Figures 6.25, 6.27, 6.29 and 6.31. Each panel shows the peak locations found over a platform scan, with each cross representing the result obtained for a MEX electron energy bin in the range $\sim$60 - 300 eV. The mean and median locations of the beam peaks for each actuation are represented by the diamond and triangle symbols respectively.

In Section 6.1.2 it was found that the beam fitting procedure could not always distinguish between the strahl and anti-strahl directions when two significantly beam-like distributions where observed. This is of particular relevance with regard to the MEX events examined within this Chapter, as a number of events are within or in close proximity to the Martian bow shock and may encounter regions in which electrons are back-streaming from the shock. The results in which a broader beam was selected over a narrower beam for fitting the 'strahl' were thus removed to account for this strahl-anti-strahl-direction ambiguity. These results are shown in Figures 6.26, 6.28, 6.30 and 6.32.

All of the beam fitting results from the first actuation for the event examined at $\sim$ 04:30 UT on the 25th have been rejected, as have half of the results from the second actuation (see Figure 6.26). The beam positions for the second actuation also remain spread over a wide range, although three of the four beam positions have azimuthal angles close to the median value of $\sim 54^{\circ}$. For the event examined at $\sim$ 18:00 UT on the 25th, most of the beam fitting results from the first and second actuation have been rejected (see Figure 6.28). The beam positions for the first actuation have similar values for both the azimuthal and polar angle, with median (mean) values of $\sim 48^{\circ}$ ($\sim 47^{\circ}$) and $\sim 78^{\circ}$ ($\sim 73^{\circ}$) respectively. The beam positions for the second actuation have azimuthal angles of $\sim 45^{\circ}$ and are split into two groups centred about $\sim$115° in the polar direction.

Most of the beam fitting results from the first and second actuation have been rejected for the event examined at $\sim$ 14:00 UT on the 26th (see Figure 6.30). However, the remaining beam positions for both the first and second actuation have

similar values for both the azimuthal and polar angle. The first actuation has beam positions in the azimuthal and polar direction with median (mean) values of $\sim$38° ($\sim$35°) and $\sim$94° ($\sim$89°) respectively. The second actuation has beam positions in the azimuthal and polar direction with median (mean) values of $\sim$41° ($\sim$45°) and $\sim$81° ($\sim$78°) respectively. For the event examined at $\sim$ 23:00 UT on the 1st, all but one of the beam fitting results from the first actuation have been rejected and only three results from the second actuation remain see Figure 6.32). The beam position for the first actuation is at $\sim$ 48° and $\sim$ 168°. The beam positions for the second actuation have beam positions in the azimuthal and polar direction with median (mean) values of $\sim$50° ($\sim$54°) and $\sim$79° ($\sim$69°) respectively.

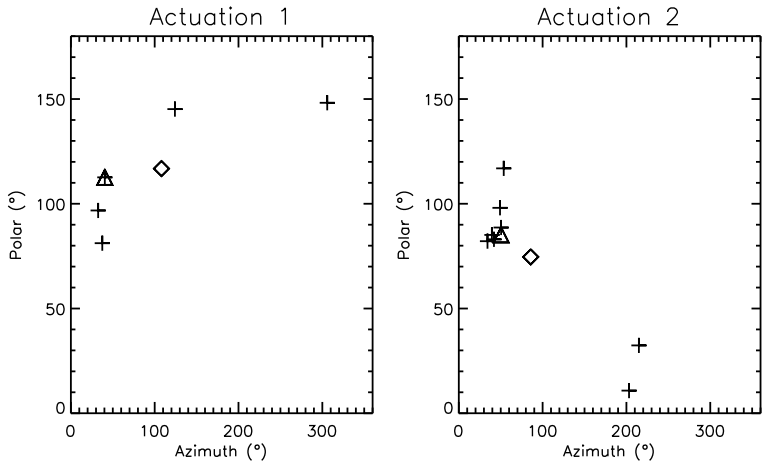

Figure 6.25: Location of the fitted peaks of the full sky FOV for MEX ELS electron data. The panel on the left is for the 1st actuation on the morning of 25th February 2007 from 04:23:03 to 04:26:42 UT. The panel on the right is for the 2nd actuation from 04:28:39 to 04:32:17 UT. Each cross represents the result obtained for a MEX electron energy bin in the range ∼60 - 300 eV. The triangle symbol shows the location of the median peak location over all energies. The diamond symbol shows the location of the mean peak over all energies.

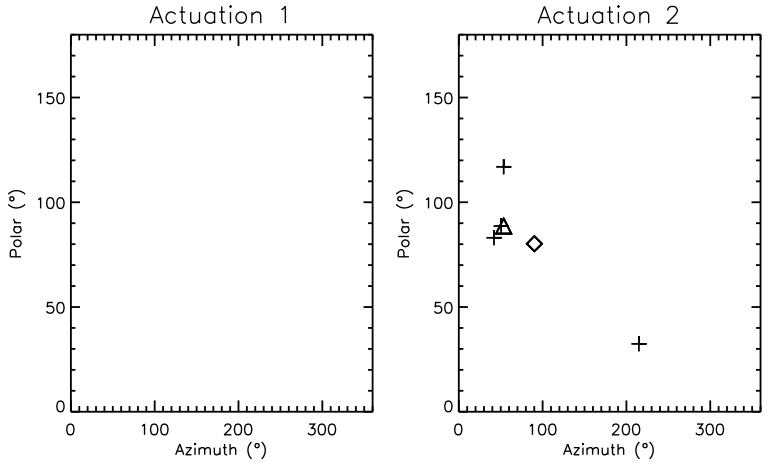

Figure 6.26: In the same format as Figure 6.25 except that events in which there was a clear strahl-anti-strahl-direction ambiguity, as discussed in Section 6.1.2, have been removed. The panel on the left is for the 1st actuation on the morning of 25th February 2007 from 04:23:03 to 04:26:42 UT. The panel on the right is for the 2nd actuation from 04:28:39 to 04:32:17 UT.

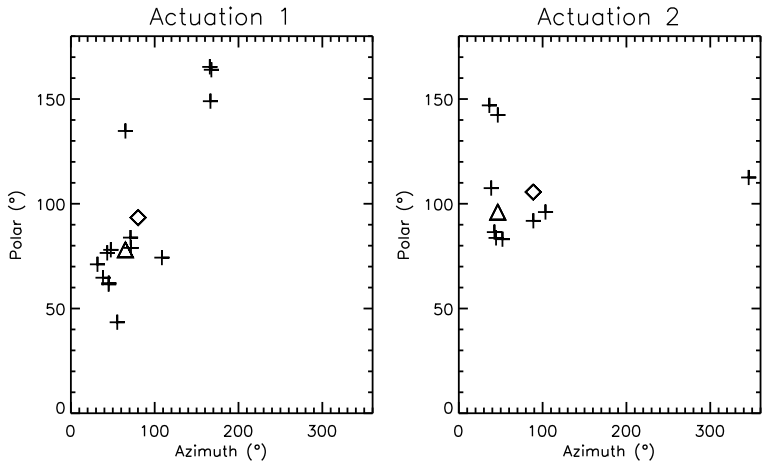

Figure 6.27: Location of the fitted peaks of the full sky FOV for MEX ELS electron data. The panel on the left is for the 1st actuation on the evening of 25th February 2007 from 17:49:27 to 17:53:05 UT. The panel on the right is for the 2nd actuation from 17:55:03 to 17:58:41 UT. Each colour (purple to red) represents a different electron energy (low to high) ranging from ∼60 - 300 eV. The triangle symbol shows the location of the median peak location over all energies. The diamond symbol shows the location of the mean peak over all energies.

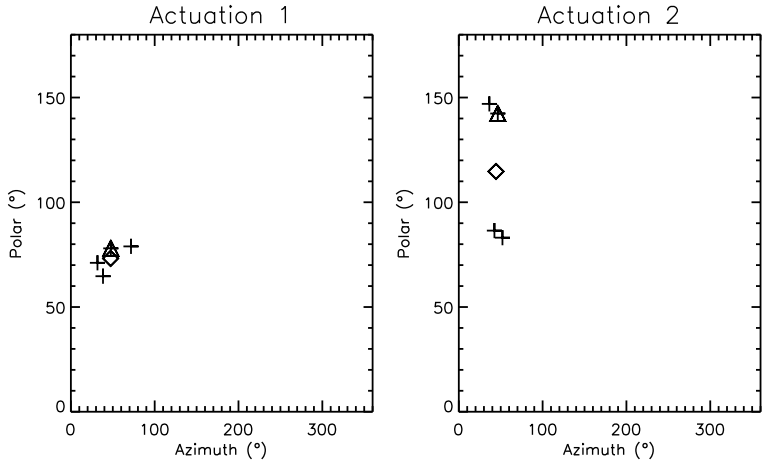

Figure 6.28: In the same format as Figure 6.25 except that events in which there was a clear strahl-anti-strahl-direction ambiguity, as discussed in Section 6.1.2, have been removed. The panel on the left is for the 1st actuation on the evening of 25th February 2007 from 17:49:27 to 17:53:05 UT. The panel on the right is for the 2nd actuation from 17:55:03 to 17:58:41 UT.

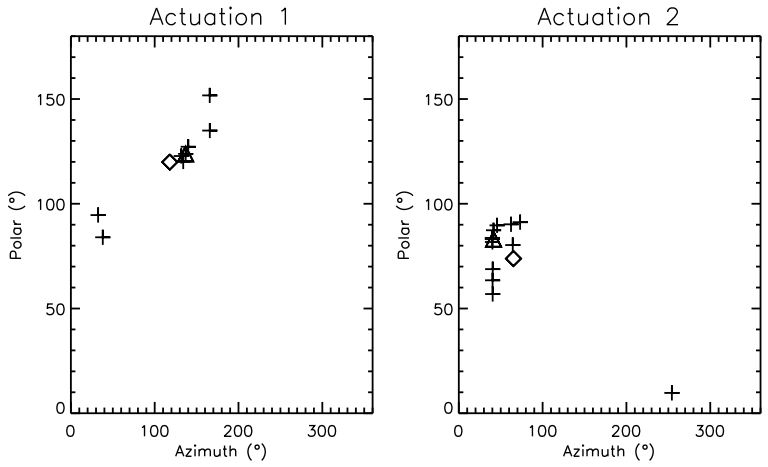

Figure 6.29: Location of the fitted peaks of the full sky FOV for MEX ELS electron data. The panel on the left is for the 1st actuation on 26th February 2007 from 13:58:41 to 14:02:19 UT. The panel on the right is for the 2nd actuation from 14:04:15 to 14:07:53 UT. Each cross represents the result obtained for a MEX electron energy bin in the range ∼60 - 300 eV. The triangle symbol shows the location of the median peak location over all energies. The diamond symbol shows the location of the mean peak over all energies.

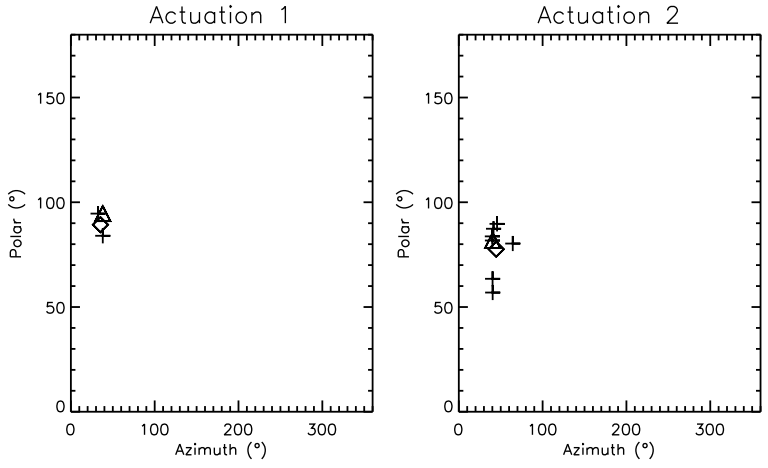

Figure 6.30: In the same format as Figure 6.25 except that events in which there was a clear strahl-anti-strahl-direction ambiguity, as discussed in Section 6.1.2, have been removed. The panel on the left is for the 1st actuation on 26th February 2007 from 13:58:41 to 14:02:19 UT. The panel on the right is for the 2nd actuation from 14:04:15 to 14:07:53 UT.

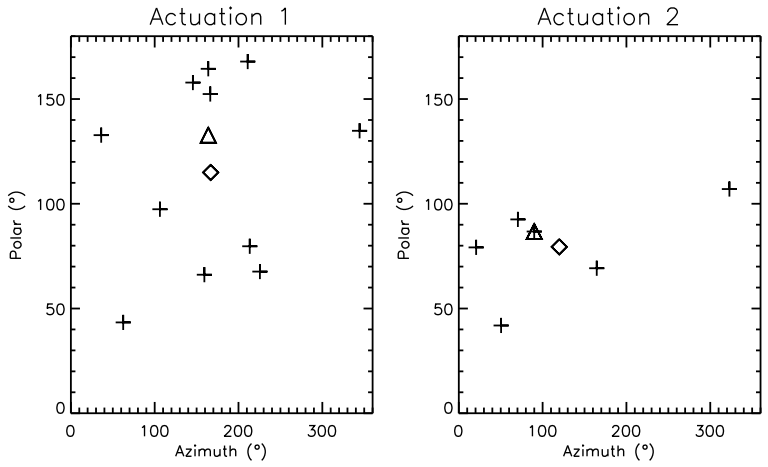

Figure 6.31: Location of the fitted peaks of the full sky FOV for MEX ELS electron data. The panel on the left is for the 1st actuation on 1st March 2007 from 23:07:56 to 23:11:34 UT. The panel on the right is for the 2nd actuation from 23:13:30 to 23:17:00 UT. Each cross represents the result obtained for a MEX electron energy bin in the range ∼60 - 300 eV. The triangle symbol shows the location of the median peak location over all energies. The diamond symbol shows the location of the mean peak over all energies.

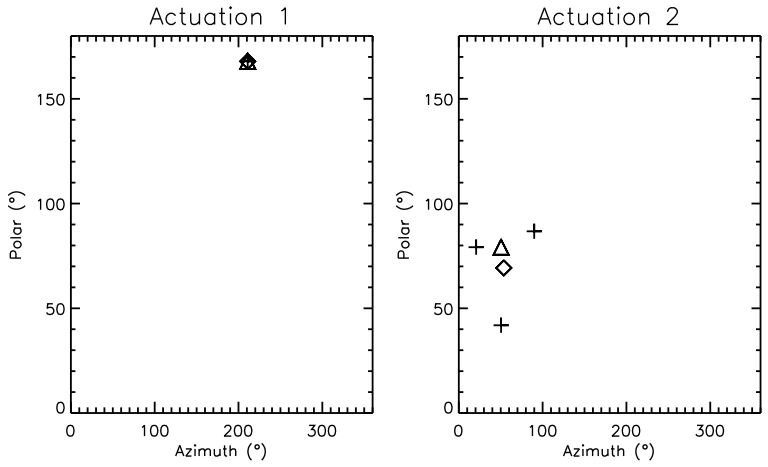

Figure 6.32: In the same format as Figure 6.25 except that events in which there was a clear strahl-anti-strahl-direction ambiguity, as discussed in Section 6.1.2, have been removed. The panel on the left is for the 1st actuation on 1st March 2007 from 23:07:56 to 23:11:34 UT. The panel on the right is for the 2nd actuation from 23:13:30 to 23:17:00 UT.

6.3 Discusion

In this chapter, a tool to estimate IMF orientation using strahl beam fitting was developed and tested using observations during a Cluster spacecraft solar wind interval. Full-sky suprathermal electron observations were examined at 4s, 1 min and 5 min cadences. The data were then fitted with a function consisting of a 2D Gaussian, for which the peak position and FWHM provides the location and width of the strahl beam in the FOV of the cluster instrument. The 4s, 1 min and 5 min average magnetic field orientation was calculated and then converted to its equivalent azimuth and polar position in the Cluster PEACE FOV and compared to the results obtained by fitting to strahl.

It was found that, for all observed energies ($\sim$ 70 and 270 eV) and cadences, the strahl beam generally produced a good agreement with the magnetic field data. However, there were also some observations in which there was a significant difference between the observed field and the strahl fitted estimate, many of which have values that were $\sim 180^\circ$ different in the polar direction or $\sim 90^\circ$ different in the polar direction. These large differences were thought to be either a result of: a significant change in the magnetic field direction during an electron measurement; larger uncertainty in the strahl beam direction due to broader strahl, either inherently, or possibly as a result of blurring during the observation due to a changing magnetic field; or confusion between the strahl beam direction and anti-strahl direction.

In order to investigate these possibilities, the changes in magnetic field direction and strahl width relations were examined. It was found that variation in the magnetic field (for the same time scales as the strahl observation period) did not have a strong influence on the estimate of the magnetic field orientation produced by strahl beam fitting and that the strahl beam observations match the average magnetic field direction relatively closely, despite fluctuations of the field during the observation interval. However, examination of the strahl width associated with each estimate revealed two clear groups. The first, a closely clustered group, made up of relatively narrow strahl that produced good estimates of the field direction. The second, a much more spread group, with broader strahl widths and much larger dif-

ferences between the observed field direction and the strahl estimate, a number of which gave a value approximately opposite to the magnetic field direction. It was therefore concluded that in some instances the procedure used to fit to the strahl beam could not distinguish between the strahl and anti-strahl directions due to a beam-like distribution in the anti-strahl direction.

In order to address this issue, a second 2D Gaussian was fitted to the electron distribution after the first fitted beam has been artificially blocked. The observations for which the anti-strahl width (2nd fitting result) was less than the strahl width (1st fitting result), clearly ambiguous events, were removed from the dataset. For the remaining strahl fitting results, it can be seen that, in both the azimuth and polar directions, the strahl width is generally less than 40°. Although, some larger widths were found for the higher electron energies, most likely due to strahl-anti-strahl ambiguity due to beam-like distributions in both directions with similar beam widths or very broad strahl with a large associated error in beam position.

It was observed that strahl beam width decreased with strahl energy but that there are more instances for higher energy strahl where electrons in the anti-strahl direction are beam-like enough to be selected over the strahl direction by the fitting procedure. It is possible that the latter may be a result of higher energy strahl having lower number densities, with a lower peak value to be fitted by a Gaussian. It may also be an indication that higher energy strahl have been backscattered more than their lower energy counterparts or that the halo component of the electrons at these higher energies is more strongly anisotropic. These results may also relate to the findings of Anderson et al. (2012), who found that, although strahl cannot be characterised by a typical width at any energy, for widths below $\sim$40° and above $\sim$70°, it is proportionally more likely to see higher energy strahl. Finally, it was found that, for strahl energies $\sim$100-200 eV, the majority ($>$70%) of strahl beam estimates of the IMF orientation were within 20° of the magnetic field observations. Lower and higher energy strahl still provided reasonable estimates ($>$50% within 20° of the magnetic field observations). However, for the purpose of an IMF orientation estimation tool, $\sim$100-200 eV is the most appropriate energy range for strahl beam fitting.

In this chapter, IMF orientation estimation using Gaussian fitting to electron observations was also tested using data obtained by MEX spacecraft. Unlike Cluster, MEX has no on board magnetometer thus estimates of IMF orientation would be greatly beneficial. Further complications include the lower time and angular resolution of the MEX ASPERA-3 ELS compared to Cluster PEACE; the limited number of intervals in which the scanning platform actuates through the full FOV; and that the strahl at $\sim$ 1.5 AU is generally broader than at Earth (Hammond et al., 1996; Graham et al., 2017).

The MEX intervals examined were initially chosen as they were part of a study that produced IMF estimates for the MEX spacecraft were found using time-shifted observations from the Rosetta spacecraft during its flyby of the planet. However, closer examination of the electron data revealed that MEX was likely within or on the edge of the Martian bow shock for the platform actuations available during this interval. Thus, a further event (1st March 2007) was also examined in which MEX platform actuations occur within the solar wind. This is of particular relevance, as close proximity to the Martian bow shock means that, not only will the observations be made within regions with energised electrons and increased wave activity, but also possibly within regions in which electrons are back-streaming from the shock (e.g. Skalsky et al., 1993; Acuna et al., 1998; Trotignon et al., 2000).

The fitting procedure tested using Cluster data was applied to all MEX ELS intervals. Only fitting results with a peak at least 2 times greater than that of the background and a FWHM of $< 180^{\circ}$ were to be considered a beam-like population (as described in Chapter 3.6). Beam-like electron populations were found for a number of suprathermal energies in all events. As expected, the beam widths observed were broader than those at 1 AU. The results in which a broader beam was selected over a narrower beam for fitting the 'strahl' were also removed to account for the strahl-anti-strahl-direction ambiguity found in the examination of Cluster data at 1 AU. This significantly reduced the number of accepted fitting results for the MEX ELS observations and thus, there are few clear uni-directional beam-like events.

More comprehensive analysis of the MEX data is required before the utility of applying this tool to MEX ELS observations can be decided. Firstly, a number of

events that are within the pure solar wind, or at least less proximal to the bow shock are required. Secondly, it should also be noted that count rates have been used for the MEX observations and results would likely be improved by further processing to produce MEX FOVs in terms of phase space as for the Cluster observations. Estimation of magnetic field orientations with MEX ELS was expected to be challenging and this is certainly verified by this initial test. However, for some of the ELS observations in this study a clear beam-like population can be seen and there are years of MEX ELS data to be examined. Thus, although in this investigation it must be concluded that no clear strahl is observed, the strahl-fitting tool may yet prove useful for future MEX analysis.

In conclusion, the initial test of strahl beam fitting to estimate IMF direction using Cluster data, which has good angular and time resolution, at 1 AU is very effective. Particularly as the strahl observed was a clear, relatively narrow beam. Thus, for missions with similar or better resolutions, at 1 AU or closer distances from the Sun, this method can be used to effectively estimate the average IMF orientation seen by the spacecraft. For missions such as the upcoming Solar Orbiter, it would be possible to use strahl observations to provide confirmation of magnetometer observations or provide a magnetic field orientation estimate if the magnetometer is not in operation. In addition, it may be possible to pair these strahl observations with heliospheric models, to predict what the average direction the magnetic field is likely to be. It was found that strahl beam fitting to MEX data is much more challenging and further investigation is required before the method can be used to make IMF orientation estimates. In addition, it may be possible to conduct a similar study using Venus Express (VEX) ASPERA-4 data, as ASPERA-4 is a replica of the ASPERA-3 on board MEX. VEX is closer to the Sun (with correspondingly narrower strahl) and VEX has an on board magnetometer. In general, the study of strahl beam fitting to estimate IMF direction could also be expanded by using Cluster data with different resolutions to test the capability of method, by examining the effect of different solar wind conditions, and investigating the effect of boundary crossings within the solar wind.

Chapter 7

Discussion & Conclusions

In this thesis the solar wind electron population known as strahl has been investigated in three separate studies. The first examined the evolution of strahl beam width with heliocentric radial distance beyond 1 AU, the second investigated the effect of IMF path length on strahl evolution within 1 AU, and the third explored the utility of strahl beams with regards to IMF observation.

Strahl is a solar wind electron population that consists of a field-aligned beam of suprathermal electrons. Strahl electrons travel in the anti-sunward direction, along the IMF, at high velocities relative to the bulk plasma flow. Strahl are observed in either the parallel or anti-parallel magnetic field direction, depending on the IMF polarity, but can also be bi-directional or sunward on a local scale for certain IMF topologies (e.g., Feldman et al., 1978; Pilipp et al., 1987a; Gosling et al., 1987; Owens and Forsyth, 2013, and references within). In addition, there may be times when the strahl population is absent, particularly within slow solar wind streams (e.g., Anderson et al., 2012; Gurgiolo and Goldstein, 2017).

Strahl electrons originate in the solar corona and, as these suprathermal electrons travel outward from the Sun, the collision frequency is reduced to the extent that both electron energy and magnetic moment are conserved (e.g., Pierrard et al., 2001). This means that the electrons experience strong adiabatic focussing as they move into regions of decreasing magnetic field strength, resulting in the formation of an electron beam (e.g., Owens et al., 2008). Strahl beams observed at 1 AU have pitch angle widths that are often significantly broader than expected to be due solely to the effects of expansion (e.g., Owens et al., 2008; Anderson et al., 2012).

In addtion, the suprathermal electron population known as the halo is observed to be present at all pitch angles. Thus, suprathermal electrons must be subject to some form of scattering process, or processes, as they travel outwards from the Sun. Solar wind plasma is too tenuous for Coulomb collisions to produce the scattering effect necessary to match suprathermal electron observations (e.g., Hammond et al., 1996; Vocks et al., 2005). As a consequence, these scattering mechanisms likely involve electron interaction with plasma waves (e.g., Saito and Gary, 2007; Pagel et al., 2007).

Previous observational investigations have examined the relationship between strahl width and electron energy in order to determine the nature of the strahl scattering mechanism(s), in particular the role of resonant wave-particle interactions. However, these studies found a number of variable, and often seemingly contradictory, energy relations. This implies that there may be multiple scattering mechanisms present in the solar wind. Accordingly, a variety of resonant and non-resonant wave-particle interactions have been proposed each with different possible drivers for these fluctuations.

Previous observational investigations also found that strahl beam width broadened with heliospheric radial distance from $\sim$ 1 to 2.5 AU (Hammond et al., 1996) and that the strahl population decreases relative to the halo population with heliospheric distance from $\sim$ 0.3 to 1.5 AU (e.g., Maksimovic et al., 2005; Stverak et al., 2009). These observations suggest that strahl continues to be subject to scattering throughout the solar wind and may eventually be scattered to form part of the halo electrons. However, indications of strahl width found at $\sim$ 10 AU by Walsh et al. (2013) using Cassini observations implied that scattering may in fact fall off with distance. Thus, the starting point for the first project presented within this thesis was the aim to expand the radial range of strahl evolution, in order to determine how strahl scattering varies with heliocentric distance.

In Chapter 4 observations of strahl pitch angle width evolution as a function of radial distance and electron energy were examined over a radial distance of $\sim$ 1 - 5.5 AU. This was achieved by making use of data obtained by the Cassini spacecraft during its interplanetary voyage to the Saturnian system. Cassini observations allowed for the characterisation of changes in the strahl distribution to be made

over a heliocentric radial range that was significantly wider than previously studied (e.g., Hammond et al., 1996). Cassini observations also had the advantage of minimizing any effects due to variable heliospheric latitudes, which had been previously invoked as a potential influence on electron observations (e.g., Hammond et al., 1996; Owens et al., 2008). In addition, the use of a single spacecraft meant that there were no challenges associated with the inter-calibration of multiple spacecraft datasets, which had been necessary to overcome in previous investigations of electron evolution (e.g., Maksimovic et al., 2005).

The CAPS ELS instrument on board Cassini spacecraft had a FOV with variable coverage during the interplanetary and planetary flyby observations. This meant that the ELS did not always cover a full electron pitch angle distribution during the measurement period. In order to find clear strahl signatures, it was therefore necessary to find times when Cassini was observing solar wind electron populations that could support the longer-term averaging needed to observe full pitch angle distributions. Thus, a key assumption used in this investigation was that the solar wind can be considered to be made up of a tangled network of flux tubes that originate in the corona and expand outwards with the solar wind flow (e.g., Borovsky, 2008; Neugebauer and Giacalone, 2015). IMF discontinuities were used to identify these regions, within which the solar wind plasma could be considered to be relatively steady compared to the magnetic field and plasma parameter changes associated with the flux tube boundaries.

It has also been argued that these flux tube boundaries are more likely to be structures that develop in-transit due to turbulence (e.g., Owens et al., 2011). However, whether the boundary forms in the corona or develops further out into interplanetary space was not critically important for this particular investigation. This is because these IMF discontinuities were only used to distinguish between regions in which full pitch angle distributions could be obtained by CAPS ELS without the risk of dramatically different plasma populations becoming averaged together. It should also be noted that identifying IMF discontinuities is not the only method of finding flux tube boundaries and that observed changes in other parameters, such as solar wind bulk velocity can also be used along side the magnetic field information (Borovsky, 2008). However, since Cassini CAPS has a limited FOV, the derivation

of accurate solar wind bulk parameters, such as density, temperature and velocity is either impossible or relies heavily on assumptions (e.g., Paschmann et al., 1998; Rymer, 2004; Lewis et al., 2008). This missing information also means that the strahl beams observed were not separated by solar wind type and, therefore, no conclusions could be made on the radial dependence of strahl which separates the potential effects of fast and slow solar wind streams on the evolution of electron pitch angle distributions.

In general, strahl pitch angle width was found to increase with heliocentric radial distance from $\sim$ 1 - 5.5 AU, in keeping with previous observations of strahl pitch angle width from $\sim$ 1 - 2.5 AU (Hammond et al., 1996). Critically, this implies that strahl was subjected to pitch angle scattering throughout the radial range sampled by Cassini. This is in good agreement with the Owens et al. (2008) model for suprathermal electron evolution, for which it was demonstrated that a constant pitch angle scattering rate (constant with time, radial distance and electron energy) combined with the effect of adiabatic focussing in a Parker spiral magnetic field, produced strahl widths that become broader with radial distance. This is due to the spiral field becoming more tightly wound with heliocentric radial distance, thereby reducing the change in magnetic field strength per unit distance and hence, reducing the effect of adiabatic focussing at larger distances.

Previous observations of strahl pitch angle width with heliocentric distance did not report the same trend beyond $\sim$ 2.5 AU. Instead, it was found that the increase strahl width appeared to fall off and it was expected that strahl width may remain approximately constant beyond a certain distance (Hammond et al., 1996). This apparent divergence from the results obtained within in thesis may be explained by a key difference between the datasets. The previous investigation used Ulysses observations over a large helio-latitude range whereas this investigation relied on Cassini data with very minimal changes in helio-latitude. The IMF becomes less tightly wound (more radial) as helio-latitude increases (Forsyth et al., 2002). Therefore, any change in helio-latitude would affect the the adiabatic focussing experienced by strahl electrons (Owens et al., 2008), narrowing the expected strahl widths at higher helio-latitudes.

Although this investigation ranged across 1 to 9 AU, there were very few events beyond 5.5 AU that fulfilled the count rate and beam-like distribution acceptance criteria. It was therefore concluded that, at larger radial distances, the strahl is most likely scattered to form part of the halo population. This is consistent with previous observations of strahl broadening with radial distance from $\sim$ 1 - 2.5 AU (Hammond et al., 1996) and observations of the proportion of halo and strahl electrons increasing and decreasing with radial distance respectively (e.g., Maksimovic et al., 2005; Stverak et al., 2009). The gradual increase in pitch angle width observed by Cassini beyond 1 AU also has implications regarding the formation of the halo population within 1 AU. This is because in order for an approximately isotropic halo to be observed at 0.3 AU (e.g., Stverak et al., 2008) to be solely a result of scattering of a suprathermal beam, much stronger scattering affects (than those observed within this investigation beyond 1 AU) would need to be acting closer to the Sun.

In this investigation, the relationship between strahl pitch angle width and electron energy at different radial distances was also examined, in order to investigate the possibility of scattering via resonant interactions with waves. In previous studies, it had been observed that strahl pitch angle width narrowed with increasing strahl energy at 1 AU (e.g Feldman et al., 1978; Pilipp et al., 1987b; Fitzenreiter et al., 1998). This is a finding consistent with the theoretical proposal of resonant interaction with whistler-mode waves generated via a core electron temperature anisotropy as the strahl pitch angle scattering mechanism (Saito and Gary, 2007). However, strahl width that broadens with increasing energy had also previously been reported during periods of enhanced turbulence within the low-frequency whistler regime at 1 AU (Pagel et al., 2007). This was theorised to correspond to resonant scattering due to enhancements in the broadband spectra of whistler fluctuations that persist in the solar wind (Vocks et al., 2005; Saito and Gary, 2007). The Cassini observations revealed strahl width energy relations at different radial distances were highly variable; either increasing, decreasing or displaying no trend with electron energy. Implying that there are likely multiple different resonant and non-resonant scattering mechanisms in the solar wind, that have a variable presence and are likely to produce competing effects on the energy relation of strahl width. This is in line with statistical findings at 1 AU which demonstrated that

it was equally probable to observe strahl that either broadened or narrowed with electron energy (Anderson et al., 2012).

The relationship between increase in strahl pitch angle width with radial distance and electron energy was also examined. Cassini observations revealed that higher energy strahl beams broadened slightly more per unit distance than for lower energies. This is in contrast to the previous Ulysses findings for which a steep decrease in strahl broadening per unit distance was observed. However, both the Cassini and Ulysses observations were found to differ from modelled results, which found a weak decrease in strahl broadening per unit distance (Owens et al., 2008). The weak energy relation produced by the model was a result of time-of-flight effects, as faster field-aligned electrons travelling outwards along a Parker spiral field will experience a larger decrease in magnetic field strength per unit time/distance. Thus the energy relations found using Cassini observations implies that whatever processes are competing, there must be an explicit energy dependence in the dominant pitch-angle scattering mechanism that accounts for greater pitch angle broadening per unit radial distance for higher energy electrons that expected for time-of-flight effects. A similar argument can also be made for the opposite energy relation found using Ulysses observations. It is therefore important to consider the possibility that slow and fast solar wind may produce differences in the strahl pitch-angle distribution, either due to in-transit processing or their solar origins. Both the Hammond et al. (1996) Ulysses observations and the Owens et al. (2008) model were for fast solar wind streams. In addition, the Hammond et al. (1996) observations were made over a wide range of helio-latitudes, whereas the Cassini observations were for unknown, but likely, mixed solar wind speeds obtained over an approximately constant heliolatitude, in the equatorial plane.

The investigation discussed above and presented in Chapter 4 covered a radial distance range of $\sim$ 1 - 5.5 AU. The second investigation presented in Chapter 5 of this thesis probed the evolution of strahl electrons within 1 AU. This was achieved, not using spacecraft data obtained within 1 AU, but by estimating the IMF path length travelled by the strahl on their journey from the Sun to 1 AU. Thus, it was possible to obtain average strahl broadening in relation to electron energy and distance, while also taking into account the general effect of IMF topology and adia-

batic focusing experienced by the strahl. This was achieved with Wind spacecraft observations of strahl and SEPs in the solar wind.

The two different methods used to determine the IMF path length had been developed in previous investigations of impulsive-type SEP onsets at $\sim$ 1 AU, which are associated with reconnection events on the Sun. The first made use of velocity dispersion of ion SEPs, for which it is assumed that the accelerated ions have the same source location and time. The more energetic SEPs will therefore arrive at the measurement point faster than the less energetic SEPs. This enables the path travelled by the SEPs along the IMF to be found by measuring the velocity dispersion of the observed SEP onsets. The second method made use of electron SEPs, the acceleration of which is associated with type III radio bursts. Thus, observations of the type III radio bursts can provide a proxy for the start time of an SEP event. This can be combined with observations of electron SEP onset for a particular energy/velocity, to provide the time taken for the SEPs to travel along the IMF to the measurement point; thereby enabling the calculation of IMF path length. These calculated lengths could then be compared to the average strahl width observed just before the first SEP onset. This investigation involved implementing a novel strahl width analysis technique and the starting point was an independently studied list of a relatively small number (69) of events (Nitta et al., 2006). It was not possible to reliably estimate strahl width, onset and/or IMF length for all of these events as a large number of events failed the chosen beam fitting, onset detection and/or dispersion fitting criteria selected to ensure clear results. It was therefore concluded that, although the results from this investigation provide a good indication of the processes effecting the strahl within 1 AU, a larger number of events would provide improved statistics and allow more substantial claims regarding strahl broadening to be made.

It was found that both the ion VDA and the electron travel-time methods gave reasonable estimates of the IMF path length, which was in line with previous SEP investigations (Tan et al., 2013; Mazur et al., 2000). In addition, for both methods, it was found that average strahl width broadens with distance travelled along the IMF. This relationship implies that strahl is subject to scattering throughout the range examined, resulting in strahl on longer IMF path lengths being subject to greater

scattering effects en route from the Sun. This is in agreement with the previous findings, reported in Chapter 4, that strahl width increases with heliospheric radial distance and must therefore be subjected to in-transit scattering effects (Hammond et al., 1996; Graham et al., 2017). The results of this investigation also highlight the impact of Parker spiral geometry on strahl evolution, as a less-radial field is likely associated with greater exposure to scattering events for the same adiabatic focussing effect seen by a more radial field (Owens et al., 2008).

The Wind observations of strahl pitch angle width with electron energy during the events examined revealed variable energy relations, much like in previous strahl investigations at 1 AU (e.g., Anderson et al., 2012) and beyond (Hammond et al., 1996; Graham et al., 2017) . However, the investigation of strahl width with IMF path length revealed a strahl broadening per unit distance along the IMF that increased with electron energy. This implies that pitch angle scattering over the range observed was greater for higher energy strahl electrons. This energy relation does not agree with those of Hammond et al. (1996) or Owens et al. (2008) which found a strong and weak decrease in strahl broadening per unit distance respectively. However, it does agree with the Cassini observations presented in Chapter 4 and Graham et al. (2017), in the sense that both investigations observe an increase in strahl broadening per unit distance. Although, the increase observed in this investigation was found to be much steeper than reported in Chapter 4. This result implies that there is a dominant strahl pitch-angle scattering mechanism with an inherent energy relation and that it is perhaps more dominant within 1 AU than beyond.

It is important to note that, although the results reported in Chapter 4 agree with those reported in Chapter 5, the methods used in each case were very different. In the former study, strahl width broadening as a function of distance along the IMF path length was investigated. In the latter, strahl width broadening as a function of heliocentric radial distance was investigated. However, if the energy relation for strahl width broadening per unit radial distance was found in terms of IMF path length, it is likely that the broadening per unit distance would be an even lower value. Therefore the difference in methodology used was found not to explain the difference in the strahl broadening per unit distance energy results.

The observed strahl width broadening per unit radial distance in the Cassini investigations was also thought to be relatively constant with heliospheric radial distance. However, if these results were measured in terms of IMF path length, it would likely result in a broadening per unit distance along the IMF that decreased with heliocentric radial distance from the Sun. The effect of adiabatic focussing should also decrease with radial distance as a result of the IMF becoming less radial. Hence, the approximately constant radial broadening of strahl beam width with radial distance out to $\sim$ 5.5 AU may be due to strahl scattering decreasing with radial distance in conjunction with adiabatic focussing effects. This is in agreement with the previous assertion that the scattering mechanism which results in the observed energy relation may have a stronger effect within 1 AU.

The solar wind speeds observed by the Wind spacecraft during this investigation range from $\sim$ 300-600 kms^{-1} and were obtained obtained from 1999-2002. The strahl observations made by Cassini were for unknown, but likely, mixed solar wind speeds obtained from 1999-2004. Both the observations made by Wind, and those of Cassini, were for approximately constant heliolatitude, in the equatorial plane. Thus, it seems likely that the average solar wind conditions seen by the two investigations were similar. This may also explain the increase in strahl broadening per unit distance seen by Cassini and Wind in contrast to the decrease in strahl broadening per unit distance seen by Ulysses, as the latter's observations where only made in fast solar wind and often at high latitudes. Thus, it seems likely that the different energy relations are in some way related to the solar wind conditions, either as a result of differing in-transit processing of the strahl or different solar origins.

In Chapter 2.2.6 the large number of potential strahl scattering mechanisms was highlighted. It was established that resonant interactions with whistler-mode waves are frequently proposed (e.g., Fitzenreiter et al., 1998; Hammond et al., 1996; de Koning et al., 2006; Vocks et al., 2005; Pagel et al., 2007; Anderson et al., 2012), for which different energy relations for strahl scattering can be expected depending on the driver of the whistler-mode fluctuations (Saito and Gary, 2007, & references therein). This could perhaps explain the ostensibly conflicting energy dependence for strahl width observations. The strahl itself may also drive instabilities that produce waves which can interact with and scatter the strahl. For instance,

whistler-mode waves generated by the electron heat flux instability (Gary et al., 1994), strahl-generated Lagmuir waves, or lower hybrid waves resulting from the core-strahl anisotropy (Shevchenko and Galinsky, 2010) could all be a potential source for scattering (Pavan et al., 2013). Finally, obliquely propagating kinetic Alfvén waves also may be able to interact with the field-aligned strahl via Landau damping.

The observations of variable strahl width relations presented in Chapters 4 and 5 suggest that there are likely multiple strahl scattering mechanisms present in the solar wind. However, the increase in strahl broadening per unit distance with electron energy observed for both investigations suggests that there is a pitch angle scattering mechanism that plays a dominant role in the radial evolution of strahl pitch-angle distributions and that it has an inherent energy relation. A scattering mechanism candidate that can account for higher energy strahl experiencing greater pitch angle broadening is resonant interaction with broadband whistler fluctuations, themselves resulting from turbulent cascade (e.g., Vocks et al., 2005; Saito and Gary, 2007; Pagel et al., 2007). The findings presented in Chapters 4 and 5 also imply that this dominant scattering mechanism may have a stronger effect within 1 AU and reduce with heliocentric distance. This finding is consistent with whistler-mode wave interaction as the primary strahl pitch angle scattering mechanism, since, as stated previously, the effectiveness of whistler-mode scattering depends on the available wave power below the electron gyrofrequency, and both wave power and the electron gyrofrequency decrease with radial distance (Hu et al., 1999; Vocks et al., 2005). However, KAWs could also be a candidate for the dominant strahl scattering mechanism, as it is likely that strahl broadening with increasing energy is a natural consequence of a turbulent spectrum with greater wave-power for longer wavelengths (Saito and Gary, 2007). In addition, there have been several observations of KAWs at appropriate scales in the solar wind at 1AU (e.g., Lacombe et al., 2017). Further modelling is required to confirm this proposition, in particular to evaluate the effect that local solar wind conditions can have on the potentially variable and competitive presence of KAWs and whistler-mode waves at these scales (Gary et al., 2008).

The final research project presented in Chapter 6 focussed not on further understanding of strahl evolution, but on what information can be obtained from strahl based on current understanding. As stated above, strahl is strongly field-aligned and its constituent electrons have a high velocity relative to the bulk plasma flow. Consequently, strahl can serve as tracer of IMF topology and provide near-instantaneous indications of solar connectivity (e.g., Pilipp et al., 1987b,a; Owens et al., 2008). A number of recent investigations have made use of strahl in this manner; these include the study by Fazakerley et al. (2016) which used strahl distributions to investigate the solar sources of solar wind observed at 1 AU and, the work by (Owens et al., 2017) that made use of strahl as an identifier of different IMF topologies in order to examine the total open magnetic flux in the heliosphere. In Chapter 6, 3D observations of suprathermal electrons were used to determine strahl beam direction and the strongly field-aligned nature of strahl was then exploited to determine average IMF orientation.

The dataset used for development and testing of IMF orientation estimation was a Cluster spacecraft solar wind interval in which a clear strahl beam was observed. The Cluster PEACE electron data had high angular resolution and produced a full 3D electron distribution every 4s. Thus, in order to investigate the effect of longer cadences averaged 1 min and 5 min data were also examined. For each suprathermal energy bin, each 3D electron distribution was fitted with a function consisting of a 2D Gaussian. The peak position and FWHM of which provided the location and width of the strahl beam in the FOV of the cluster PEACE instrument. The beam direction was then compared to the average magnetic field orientation during each observation.

It was found that the strahl beam generally produced a close agreement with the magnetic field data but that there were also observations in which there was a large difference between the observed field and the strahl fitted estimate. One possibility for this discrepancy was that a significant change in the magnetic field direction during an electron measurement was producing an average magnetic field orientation that was very different from the average strahl orientation, potentially due to strahl 'blurring' as it is dragged across the FOV by the magnetic field. However, it was found that variation in the magnetic field direction did not have a strong

influence on the estimate of the field orientation produced by strahl beam fitting and that the strahl beam observations matched the average magnetic field direction relatively closely, despite fluctuations of the field during the observation interval.

Another possibility was that broader strahl produced larger uncertainty in the strahl beam direction or that the strahl beam direction and anti-strahl direction could not be distinguished the fitting procedure, due to the presence of a beam-like distribution in the anti-strahl direction. Thus, the beam width associated with each IMF orientation estimate was examined. It was found that the majority of observations were of narrow strahl in close agreement with the magnetic field observations but that, particularly for higher strahl energies, a number of observations had much broader strahl widths with an orientation estimate approximately opposite to the magnetic field direction. This issue was addressed by fitting a second 2D Gaussian to the electron distribution after the first fitted beam had been artificially blocked. The observations for which the 2nd fitting result was less than the 1st fitting result were considered to be observations in which the strahl and anti-strahl direction were ambiguous.

The remaining strahl fitting results provided IMF orientation estimates that closely agreed with the magnetometer observations, generally within $\sim 10-20^{\circ}$, for all energies and cadences observed. The strahl width was found to be generally less than 40° and that strahl beam width decreased with strahl energy. However, a small number of observations with larger beam widths and large differences between field and strahl orientation remained. These were most likely due to very broad strahl with a large associated error in beam position or due to strahl-anti-strahl ambiguity resulting from beam-like distributions in both directions with similar widths.

Interestingly, it was also observed that, although strahl beam width decreased with strahl energy, there were more instances for higher energy strahl where electrons in the anti-strahl direction are beam-like enough to be selected over the strahl direction by the fitting procedure. This may be a result of higher energy strahl having lower number densities, with a lower peak value to be fitted by a Gaussian. However, it may also be an indication that, for this solar wind interval, higher energy strahl had been scattered more than their lower energy counterparts or that the halo

component of the electrons at these higher energies was more strongly anisotropic. These results may be in agreement with the findings of Anderson et al. (2012), who found that for widths below $\sim 40^{\circ}$ and above $\sim 70^{\circ}$ it is proportionally more likely to see higher energy strahl.

In Chapter 6, an additional trial was also conducted using data obtained by MEX spacecraft which, unlike Cluster, has no on board magnetometer and therefore would greatly benefit from estimates of IMF orientation. The MEX ASPERA-3 also provided further challenges when compared to Cluster PEACE as it has lower time and angular resolution; a limited number of intervals in which the full FOV is observed, due to scanning platform restrictions; and that the strahl at $\sim$ 1.5 AU is generally broader than at 1 AU (Hammond et al., 1996; Graham et al., 2017).

Four MEX intervals in which the scanning platform was in operation were examined. The first three events were all found to have actuation within or on the edge of the Martian bowshock. The fourth event was found to have actuations within the solar wind but in close proximity to the Martian bow shock. This is significant, as the observations were likely made within regions containing energised electrons, increased wave activity and back-streaming electrons (e.g. Skalsky et al., 1993; Acuna et al., 1998; Trotignon et al., 2000). Beam-like electron populations were found for a number of suprathermal energies for all examined events. These beam widths observed were generally broader than those observed at 1 AU. Events with clear strahl-anti-strahl-direction ambiguity were removed in the same manner as the Cluster data, which significantly reduced the number of accepted fitting results. Thus only a few clear uni-directional beam-like events were observed.

The initial test of strahl beam fitting to estimate IMF direction using Cluster data at 1 AU was very effective. In can therefore be concluded that for missions with similar or better resolutions, at 1 AU or closer distances from the Sun, this method could be used to estimate the average IMF orientation observed by the Spacecraft. Strahl beam fitting to MEX data was much more challenging and it was concluded that further investigation would be required before the method can be used to make IMF orientation estimates in the near-Mars solar wind. The use of strahl within the research presented in Chapter 6 and SEPs within Chapter 5 has demonstrated the ability of particle populations to provide information on IMF geometry. The

study of strahl beam fitting to estimate IMF direction, described in Chapter 6, could be expanded by using Cluster data with different resolutions to test the capability of method and by examining the effect of different solar wind conditions and boundary crossings within the solar wind. In addition, it may be possible to conduct a similar study using VEX ASPERA-4 data, as ASPERA-4 is a replica of the ASPERA-3 on board MEX but VEX is closer to the Sun (with correspondingly narrower strahl) and VEX has an on board magnetometer. This magnetic field orientation tool may also be developed for other beam like populations, for example, those observed within magnetospheres.

7.1 Future Work

Understanding the formation and evolution of solar wind electron populations is a key aspect of Sun-solar wind science and the suprathermal, field-aligned strahl is a particularly informative component. Strahl evolution is affected by both global scale IMF geometry and local kinetic effects, and it can thus provide information on heliospheric magnetic field topology and solar connectivity, as well as the small scale interactions which occur within the solar wind. Both the former and the latter can provide context for in-situ observations and thereby aid the linking of in-situ measurements with remote sensing observation of the Sun. This is necessary for the investigation of solar wind source regions and evolution. Strahl may be particularly useful in identification of regions in which interchange reconnection has likely occurred and could also contribute to the understanding of solar wind transients, such as the internal structure and solar connectivity of interplanetary coronal mass ejections. Solar wind electrons are also known to play a key role in solar wind dynamics. In particular, suprathermal electrons are responsible for determining the electric field required to maintain zero net charge in the solar wind and for carrying the heat flux conducted into the solar wind from the corona. The formation and evolution of these suprathermals thus has large scale implications. In particular, they have potential to reveal information about the wave or reconnection mechanisms that heat the corona and accelerate the solar wind.

There are a number of different mechanisms that can be invoked to explain the generation of suprathermal election populations within the corona and their existence within the solar wind. Thus the coronal origins and evolution of both the field-aligned strahl and the quasi-isotropic halo remain unclear. In order to better understand these suprathermal electrons, it is necessary to determine first what processes affect the solar wind electrons in-transit. The work presented within this thesis provides some of the answers needed to address this issue. Strahl evolution beyond 1 AU was examined across the largest radial range to date and strahl evolution within 1 AU was investigated using a method that considered the effect of IMF geometry. The former provides clear constraints on field-aligned electron dynamics, and the electromagnetic waves that they interact with, and the latter provides

indications of how these may differ closer to the Sun. However, there is no doubt that further understanding of the heliospheric evolution of strahl electron beams is required before a complete picture of solar wind strahl can be assembled.

One particular consideration is that strahl beam widths are likely influenced by the different solar wind type that they exist within and possibly even the changing conditions within a particular solar wind stream. Narrow strahl features are most commonly observed in the coronal hole solar wind. This suggests that the strahl has either undergone a lesser degree of scattering in-transit within the fast solar wind than the slow, or that the different origins of the slow and fast solar wind result in different electron velocity distributions. The topology of the IMF and specifically the path length travelled by the strahl electrons has been shown to have a significant effect on the width of the strahl. The slow and fast solar wind also display very different properties when observed in-situ, in particular, the observed temperature anisotropies and turbulent evolution. In addition, the in-ecliptic solar wind is region divided and disrupted by streamer interaction regions and coronal mass ejections, both of which can result in shock formation; whereas the polar wind flows relatively smoothly into the heliosphere. It thus seems likely that the type and heliolatitude of the solar wind could result in conditions that favour the existence of differing wave generation and therefore strahl scattering mechanisms. The different origin for the slow solar wind streams from the fast, either from streamer belt region plasma that has undergone interchange reconnection or plasma from the edge of coronal holes that has undergone super radial expansion, or both, may also produce suprathermal electron distributions that are different before they are subject to interplanetary interactions.

The observations of variable strahl width relations presented in Chapters 4 and 5 suggest that there are likely multiple strahl scattering mechanisms present in the solar wind and support the suppositions above. In order to separate out these different mechanisms and unambiguously determine the electromagnetic fluctuations responsible for strahl scattering, it is necessary to conduct further studies of individual strahl scattering events, such as the high time and angular resolution investigations of (Gurgiolo et al., 2012) using Cluster data. It may also be possible to further exploit the Cassini observations by deriving approximate solar wind speed

estimations, by making use of the Cassini MIMI instrument, that would allow for the separation of slow and fast solar wind strahl evolution and more comprehensive 'flux tube' analysis. Further information may also be gained by attempting to characterise the core and halo electron distributions and observe the temperature anisotropies associated with the strahl width evolution measurements, although the presence of photoelectrons resulting from the spacecraft potential would make this challenging. Finally, more detailed investigation of the magnetic boundaries and fluctuations associated with the Cassini strahl observations may provide further clues as to strahl scattering, both in terms of the general changes with radial distance and individual observations at different radial distances during time periods with particularly good strahl coverage and/or enhanced magnetic fluctuations.

Finally, observations within 1 AU are key to fully understanding solar wind strahl. In particular, particle observations at different radial distances within 1 AU allows for the study of their evolution before they have been subject to significant in-transit processing. Hence, not only could strahl evolution be characterised for this region but it may also be possible to place constraints on the possible coronal electron distributions. The energy relation result for strahl pitch-angle broadening found in Chapter 4 and 5 indicated that their may be a dominant strahl scattering mechanism with an inherent energy relation, which has a greater impact on the strahl distribution within 1 AU than beyond. Examining the energy relation associated with strahl observations over a range within 1 AU could therefore refute or validate this indication. In addition, flux tube evolution could be examined in conjunction with the electrons at closer distances to the sun. This would allow investigation into whether these structures evolve with the solar wind or if they are fossil coronal features that have propagated out with the solar wind, or possibly a mixture of both, depending on the associated solar wind origins. If they are indeed coronal fossil features then examining electron populations within these tubes may even allow the nature of coronal electrons to be probed on a fine scale. The precise nature of the strahl scattering processes, and the heliospheric locations and conditions for which they occur, have significant implications for the applicability of strahl trajectories as tool for determining IMF topology. For example, bi-directional strahl signatures associated with closed IMF loops could be scattered to the extent that they are lost

before observation (e.g., Hammond et al., 1996; Maksimovic et al., 2005; Owens et al., 2008). Establishing the bounds of strahl utility for IMF topology inference through further investigation into the radial variability of strahl signatures is therefore also highly desirable.

In 2018 and 2020 respectively, the Parker Solar Probe and Solar Orbiter spacecraft will be launched, providing a whole new set solar wind observations within 1 AU. Parker Solar Probe will provide measurements to within 10 solar radii, enabling the study of plasma particles and magnetic field to be conducted in the nascent solar wind. The Solar Orbiter spacecraft will provide measurements within 0.3 AU which, with its comprehensive suits of remote-sensing and in-situ instruments, and orbits that are planned to extend out of the ecliptic, has the potential to dramatically improve our understanding of the source regions of the solar wind. In addition, radial and spiral IMF conjunctions between the spacecraft will allow direct observations of the evolution of different components the solar wind in addition to average trends. The data returned by Parker Solar Probe and Solar Orbiter have the potential, not only to allow for significant expansion of the solar wind strahl investigation presented within this thesis, but also to dramatically improve our understanding of the heliosphere.

Bibliography

Achilleos, N., Bertucci, C., Russell, C. T., Hospodarsky, G. B., Rymer, A. M., Arridge, C. S., Burton, M. E., Dougherty, M. K., Hendricks, S., Smith, E. J., and Tsurutani, B. T. (2006). Orientation, location, and velocity of saturn's bow shock: Initial results from the cassini spacecraft. *Journal of Geophysical Research: Space Physics*, 111(A3):n/a–n/a. A03201.

Acuna, M., Connerney, J., Wasilewski, P. a., Lin, R., Anderson, K., Carlson, C., McFadden, J., Curtis, D., Mitchell, D., Reme, H., et al. (1998). Magnetic field and plasma observations at mars: Initial results of the mars global surveyor mission. *Science*, 279(5357):1676–1680.

Alfvén, H. (1942). Existence of electromagnetic-hydrodynamic waves. *Nature*, 150(3805):405.

Alfvén, H. (1945). Magneto-hydrodynamic waves and sunspots. *Monthly Notices of the Royal Astronomical Society*, 105(1):3–16.

Alfvén, H. and Lindblad, B. (1947). Granulation, magneto-hydrodynamic waves, and the heating of the solar corona. *Monthly Notices of the Royal Astronomical Society*, 107(2):211–219.

Anderson, B. R., Skoug, R. M., Steinberg, J. T., and McComas, D. J. (2012). Variability of the solar wind suprathermal electron strahl. *Journal of Geophysical Research: Space Physics*, 117(A4):n/a–n/a. A04107.

Antiochos, S., Mikić, Z., Titov, V., Lionello, R., and Linker, J. (2011). A model for the sources of the slow solar wind. *The Astrophysical Journal*, 731(2):112.

Arridge, C. S., Achilleos, N., Dougherty, M. K., Khurana, K. K., and Russell, C. T. (2006). Modeling the size and shape of saturn's magnetopause with variable dynamic pressure. *Journal of Geophysical Research: Space Physics*, 111(A11):n/a–n/a. A11227.

Arridge, C. S., Gilbert, L. K., Lewis, G. R., Sittler, E. C., Jones, G. H., Kataria, D. O., Coates, A. J., and Young, D. T. (2009). The effect of spacecraft radiation sources on electron moments from the cassini {CAPS} electron spectrometer. *Planetary and Space Science*, 57(7):854 – 869.

Astrom, E. (1951). On waves in an ionized gas. *Arkiv for Fysik*, 2(5):443–457.

Bale, S., Pulupa, M., Salem, C., Chen, C., and Quataert, E. (2013). Electron heat conduction in the solar wind: Transition from spitzer-härm to the collisionless limit. *The Astrophysical Journal Letters*, 769(2):L22.

Balogh, A., Dunlop, M., Cowley, S., Southwood, D., Thomlinson, J., Glassmeier, K., Musmann, G., Lühr, H., Buchert, S., Acuna, M., et al. (1997). The cluster magnetic field investigation. *Space Science Reviews*, 79(1):65–91.

Balogh, A., Marsden, R. G., and Smith, E. J. (2001). *The heliosphere near solar minimum: The Ulysses perspective*. Springer Science & Business Media.

Barabash, S., Lundin, R., Andersson, H., Gimholt, J., Holmström, M., Norberg, O., Yamauchi, M., Asamura, K., Coates, A., Linder, D., et al. (2004). Aspera-3: Analyser of space plasmas and energetic ions for mars express. In *Mars Express: The Scientific Payload*, volume 1240, pages 121–139.

Baumjohann, W. and Treumann, R. A. (2012). *Basic space plasma physics*. World Scientific Publishing Company.

Bibring, J.-P., Langevin, Y., Poulet, F., Gendrin, A., Gondet, B., Berthé, M., Soufflot, A., Drossart, P., Combes, M., Bellucci, G., et al. (2004). Perennial water ice identified in the south polar cap of mars. *Nature*, 428(6983):627.

Boldyrev, S., Horaites, K., Xia, Q., and Perez, J. C. (2013). Toward a theory of

astrophysical plasma turbulence at subproton scales. *The Astrophysical Journal*, 777(1):41.

Boldyrev, S. and Perez, J. C. (2012). Spectrum of kinetic-alfvén turbulence. *The Astrophysical Journal Letters*, 758(2):L44.

Borovsky, J. E. (2008). Flux tube texture of the solar wind: Strands of the magnetic carpet at 1 au? *Journal of Geophysical Research: Space Physics*, 113(A8):n/a–n/a. A08110.

Borovsky, J. E. (2010). On the variations of the solar wind magnetic field about the parker spiral direction. *Journal of Geophysical Research: Space Physics*, 115(A9):n/a–n/a. A09101.

Bridges, J., Clemmet, J., Croon, M., Sims, M., Pullan, D., Muller, J.-P., Tao, Y., Xiong, S., Putri, A., Parker, T., et al. (2017). Identification of the beagle 2 lander on mars. *Royal Society open science*, 4(10):170785.

Bruno, R. and Carbone, V. (2013). The solar wind as a turbulence laboratory. *Living Reviews in Solar Physics*, 10(1):2.

Burlaga, L. (1988). Magnetic clouds and force-free fields with constant alpha. *Journal of Geophysical Research: Space Physics*, 93(A7):7217–7224.

Burlaga, L. (2001). Magnetic fields and plasmas in the inner heliosphere: Helios results. *Planetary and Space Science*, 49(14-15):1619–1627.

Burlaga, L. and Ness, N. (1993). Large-scale distant heliospheric magnetic-field-voyager-1 and voyager-2 observations from 1986 through 1989. *JOURNAL OF GEOPHYSICAL RESEARCH-SPACE PHYSICS*, 98(A 10):17451–17460.

Burlaga, L. F., Ness, N. F., Wang, Y.-M., and Sheeley, N. R. (1998). Heliospheric magnetic field strength out to 66 au: Voyager 1, 19781996. *Journal of Geophysical Research: Space Physics*, 103(A10):23727–23732.

Cane, H. and Richardson, I. (2003). Interplanetary coronal mass ejections in the near-earth solar wind during 1996–2002. *Journal of Geophysical Research: Space Physics*, 108(A4).

Cassini Science Communications Team (2018). Cassini 1997-2017 legacy. *Online – https://saturn.jpl.nasa.gov/*.

Chao, J., Wu, D., Lin, C.-H., Yang, Y.-H., Wang, X., Kessel, M., Chen, S., and Lepping, R. (2002). Models for the size and shape of the earth's magnetopause and bow shock. In *Cospar Colloquia series*, volume 12, pages 127–135. Elsevier.

Che, H. and Goldstein, M. L. (2014). The origin of non-maxwellian solar wind electron velocity distribution function: Connection to nanoflares in the solar corona. *The Astrophysical Journal Letters*, 795(2):L38.

Chen, C. (2016). Recent progress in astrophysical plasma turbulence from solar wind observations. *Journal of Plasma Physics*, 82(6).

Chen, C., Bale, S., Salem, C., and Maruca, B. (2013a). Residual energy spectrum of solar wind turbulence. *The Astrophysical Journal*, 770(2):125.

Chen, C., Boldyrev, S., Xia, Q., and Perez, J. (2013b). Nature of subproton scale turbulence in the solar wind. *Physical review letters*, 110(22):225002.

Cranmer, S. R. (2008). On competing models of coronal heating and solar wind acceleration: The debate in'08. *arXiv preprint arXiv:0804.3058*.

Crooker, N. and Owens, M. (2012). Interchange reconnection: Remote sensing of solar signature and role in heliospheric magnetic flux budget. *Space science reviews*, 172(1-4):201–208.

de Koning, C. A., Gosling, J. T., Skoug, R. M., and Steinberg, J. T. (2006). Widths of suprathermal pitch angle distributions during solar electron bursts: Ace observations. *Journal of Geophysical Research: Space Physics*, 111(A4):n/a–n/a. A04101.

Desch, M., Ogilvie, K., and Franz, H. (1999). The wind program: 1998–2000. *Interball in the ISTP Program*, pages 29–39.

Dougherty, M., Kellock, S., Southwood, D., Balogh, A., Smith, E., Tsurutani, B., Gerlach, B., Glassmeier, K.-H., Gleim, F., Russell, C., Erdos, G., Neubauer, F.,

and Cowley, S. (2004). The cassini magnetic field investigation. In Russell, C., editor, *The Cassini-Huygens Mission*, pages 331–383. Springer Netherlands.

Eastwood, J., Phan, T., Øieroset, M., Shay, M., Malakit, K., Swisdak, M., Drake, J., and Masters, A. (2013). Influence of asymmetries and guide fields on the magnetic reconnection diffusion region in collisionless space plasmas. *Plasma Physics and Controlled Fusion*, 55(12):124001.

Edberg, N. J., Auster, U., Barabash, S., Bößwetter, A., Brain, D., Burch, J. L., Carr, C. M., Cowley, S., Cupido, E., Duru, F., et al. (2009). Rosetta and mars express observations of the influence of high solar wind pressure on the martian plasma environment. In *Annales Geophysicae*, volume 27, pages 4533–4545.

Escoubet, C. and Schmidt, R. (2000). Cluster ii: Plasma measurements in three dimensions. *Advances in Space Research*, 25(7-8):1305–1314.

Fairfield, D. H. (1971). Average and unusual locations of the earth's magnetopause and bow shock. *Journal of Geophysical Research*, 76(28):6700–6716.

Fazakerley, A. N., Harra, L. K., and van Driel-Gesztelyi, L. (2016). An investigation of the sources of earth-directed solar wind during carrington rotation 2053. *The Astrophysical Journal*, 823(2):145.

Feldman, W. C., Asbridge, J. R., Bame, S. J., Gosling, J. T., and Lemons, D. S. (1978). Characteristic electron variations across simple high-speed solar wind streams. *Journal of Geophysical Research: Space Physics*, 83(A11):5285–5295.

Feldman, W. C., Asbridge, J. R., Bame, S. J., Montgomery, M. D., and Gary, S. P. (1975). Solar wind electrons. *Journal of Geophysical Research*, 80(31):4181–4196.

Fitzenreiter, R. J., Ogilvie, K. W., Chornay, D. J., and Keller, J. (1998). Observations of electron velocity distribution functions in the solar wind by the wind spacecraft: High angular resolution strahl measurements. *Geophysical Research Letters*, 25(3):249–252.

Formisano, V., Atreya, S., Encrenaz, T., Ignatiev, N., and Giuranna, M. (2004). Detection of methane in the atmosphere of mars. *Science*, 306(5702):1758–1761.

Forsyth, R., Balogh, A., Horbury, T., Erdös, G., Smith, E., and Burton, M. (1996a). The heliospheric magnetic field at solar minimum: Ulysses observations from pole to pole. *Astronomy and Astrophysics*, 316:287–295.

Forsyth, R., Balogh, A., Horbury, T., Erdös, G., Smith, E., and Burton, M. (1996b). The heliospheric magnetic field at solar minimum: Ulysses observations from pole to pole. *Astronomy and Astrophysics*, 316:287–295.

Forsyth, R. J., Balogh, A., and Smith, E. J. (2002). The underlying direction of the heliospheric magnetic field through the ulysses first orbit. *Journal of Geophysical Research: Space Physics*, 107(A11):SSH 19–1–SSH 19–11. 1405.

Gary, G. A. (2001). Plasma beta above a solar active region: rethinking the paradigm. *Solar Physics*, 203(1):71–86.

Gary, S. P., Saito, S., and Li, H. (2008). Cascade of whistler turbulence: Particle-in-cell simulations. *Geophysical Research Letters*, 35(2).

Gary, S. P., Scime, E. E., Phillips, J. L., and Feldman, W. C. (1994). The whistler heat flux instability: Threshold conditions in the solar wind. *Journal of Geophysical Research: Space Physics*, 99(A12):23391–23399.

Gopalswamy, N., Lara, A., Lepping, R., Kaiser, M., Berdichevsky, D., and St Cyr, O. (2000). Interplanetary acceleration of coronal mass ejections. *Geophysical research letters*, 27(2):145–148.

Gosling, J., Bame, S., Feldman, W., McComas, D., Phillips, J., and Goldstein, B. (1993). Counterstreaming suprathermal electron events upstream of corotating shocks in the solar wind beyond 2 au: Ulysses. *Geophysical research letters*, 20(21):2335–2338.

Gosling, J. T., Baker, D. N., Bame, S. J., Feldman, W. C., Zwickl, R. D., and Smith, E. J. (1987). Bidirectional solar wind electron heat flux events. *Journal of Geophysical Research: Space Physics*, 92(A8):8519–8535.

Gosling, J. T., Bame, S. J., McComas, D. J., Phillips, J. L., Scime, E. E., Pizzo, V. J., Goldstein, B. E., and Balogh, A. (1994). A forwardreverse shock pair in the solar wind driven by overexpansion of a coronal mass ejection: Ulysses observations. *Geophysical Research Letters*, 21(3):237–240.

Graham, G. A., Rae, I. J., Owen, C. J., and Walsh, A. P. (2018). Investigating the effect of imf path length on pitch-angle scattering of strahl within 1 au. *The Astrophysical Journal*, 855(1):40.

Graham, G. A., Rae, I. J., Owen, C. J., Walsh, A. P., Arridge, C. S., Gilbert, L., Lewis, G. R., Jones, G. H., Forsyth, C., Coates, A. J., and Waite, J. H. (2017). The evolution of solar wind strahl with heliospheric distance. *Journal of Geophysical Research: Space Physics*, 122(4):3858–3874.

Greco, A., Matthaeus, W., Servidio, S., Chuychai, P., and Dmitruk, P. (2009). Statistical analysis of discontinuities in solar wind ace data and comparison with intermittent mhd turbulence. *The Astrophysical Journal Letters*, 691(2):L111.

Gurgiolo, C. and Goldstein, M. L. (2017). Absence of the strahl during times of slow wind. *Annales Geophysicae*, 35(1):71–85. Copyright - Copyright Copernicus GmbH 2017; Last updated - 2017-01-05.

Gurgiolo, C., Goldstein, M. L., Viñas, A. F., and Fazakerley, A. N. (2012). Direct observations of the formation of the solar wind halo from the strahl. *Annales Geophysicae*, 30(1):163–175.

Haggerty, D. K. and Roelof, E. C. (2002). Impulsive near-relativistic solar electron events: Delayed injection with respect to solar electromagnetic emission. *The Astrophysical Journal*, 579(2):841.

Hammond, C., Feldman, W., McComas, D., Phillips, J., and Forsyth, R. (1996). Variation of electron-strahl width in the high-speed solar wind: Ulysses observations. *Astronomy and Astrophysics*, 316:350–354. Provided by the SAO/NASA Astrophysics Data System.

Hellinger, P., Trávníček, P. M., Decyk, V. K., and Schriver, D. (2014). Oblique electron fire hose instability: Particle-in-cell simulations. *Journal of Geophysical Research: Space Physics*, 119(1):59–68.

Hénon, M. (1982). Vlasov equation. *Astronomy and Astrophysics*, 114:211.

Horaites, K., Boldyrev, S., Wilson III, L. B., Viñas, A. F., and Merka, J. (2017). Kinetic theory and fast wind observations of the electron strahl. *arXiv preprint arXiv:1706.03464*.

Horbury, T., Balogh, A., Forsyth, R., and Smith, E. (1995). Ulysses magnetic field observations of fluctuations within polar coronal flows. In *Annales Geophysicae*, volume 13, pages 105–107.

Howes, G., Bale, S., Klein, K., Chen, C., Salem, C., and TenBarge, J. (2012). The slow-mode nature of compressible wave power in solar wind turbulence. *The Astrophysical Journal Letters*, 753(1):L19.

Hu, Y. Q., Habbal, S. R., and Li, X. (1999). On the cascade processes of alfvn waves in the fast solar wind. *Journal of Geophysical Research: Space Physics*, 104(A11):24819–24834.

Hundhausen, A., Bame, S., Asbridge, J., and Sydoriak, S. (1970). Solar wind proton properties: Vela 3 observations from july 1965 to june 1967. *Journal of Geophysical Research*, 75(25):4643–4657.

Isobe, T., Feigelson, E. D., Akritas, M. G., and Babu, G. J. (1990). Linear regression in astronomy. *The astrophysical journal*, 364:104–113.

Johnstone, A., Alsop, C., Burge, S., Carter, P., Coates, A., Coker, A., Fazakerley, A., Grande, M., Gowen, R., Gurgiolo, C., et al. (1997). Peace: A plasma electron and current experiment. In *The Cluster and Phoenix Missions*, pages 351–398. Springer.

Kajdič, P., Alexandrova, O., Maksimovic, M., Lacombe, C., and Fazakerley, A. (2016). Suprathermal electron strahl widths in the presence of narrow-band whistler waves in the solar wind. *The Astrophysical Journal*, 833(2):172.

Kepko, L., Viall, N., Antiochos, S., Lepri, S., Kasper, J., and Weberg, M. (2016). Implications of l1 observations for slow solar wind formation by solar reconnection. *Geophysical Research Letters*, 43(9):4089–4097.

Kiyani, K. H., Chapman, S. C., Sahraoui, F., Hnat, B., Fauvarque, O., and Khotyaintsev, Y. V. (2012). Enhanced magnetic compressibility and isotropic scale invariance at sub-ion larmor scales in solar wind turbulence. *The Astrophysical Journal*, 763(1):10.

Klassen, A. (2017). Strong non-radial propagation of seps in the solar corona. 7th Solar Orbiter Workshop: Exploring the solar environs.

Kovalick, T. and Szabo, A. (2018). Global geospace science. *Online – https://www-istp.gsfc.nasa.gov/.*

Krucker, S., Larson, D. E., Lin, R. P., and Thompson, B. J. (1999). On the origin of impulsive electron events observed at 1 au. *The Astrophysical Journal*, 519(2):864.

Lacombe, C., Alexandrova, O., and Matteini, L. (2017). Anisotropies of the magnetic field fluctuations at kinetic scales in the solar wind: Cluster observations. *The Astrophysical Journal*, 848(1):45.

Lacombe, C., Alexandrova, O., Matteini, L., Santolk, O., Cornilleau-Wehrlin, N., Mangeney, A., de Conchy, Y., and Maksimovic, M. (2014). Whistler mode waves and the electron heat flux in the solar wind: Cluster observations. *The Astrophysical Journal*, 796(1):5.

Landi, S., Matteini, L., and Pantellini, F. (2012). On the competition between radial expansion and coulomb collisions in shaping the electron velocity distribution function: Kinetic simulations. *The Astrophysical Journal*, 760(2):143.

Lemons, D. S. and Feldman, W. C. (1983). Collisional modification to the exospheric theory of solar wind halo electron pitch angle distributions. *Journal of Geophysical Research: Space Physics*, 88(A9):6881–6887.

Lepping, R., Acũna, M., Burlaga, L., Farrell, W., Slavin, J., Schatten, K., Mariani, F., Ness, N., Neubauer, F., Whang, Y., et al. (1995). The wind magnetic field investigation. *Space Science Reviews*, 71(1-4):207–229.

Lewis, G., Andr, N., Arridge, C., Coates, A., Gilbert, L., Linder, D., and Rymer, A. (2008). Derivation of density and temperature from the cassinihuygens {CAPS} electron spectrometer. *Planetary and Space Science*, 56(7):901 – 912.

Li, B., Cairns, I. H., Gosling, J. T., Steward, G., Francis, M., Neudegg, D., Schulte in den Bäumen, H., Player, P., and Milne, A. (2016a). Mapping magnetic field lines between the sun and earth. *Journal of Geophysical Research: Space Physics*, 121(2):925–948.

Li, B., Cairns, I. H., Owens, M., Neudegg, D., Lobzin, V., and Steward, G. (2016b). Magnetic field inversions at 1 au: Comparisons between mapping predictions and observations. *Journal of Geophysical Research: Space Physics*, 121(11).

Lie-Svendsen, Ø., Hansteen, V. H., and Leer, E. (1997). Kinetic electrons in high-speed solar wind streams: Formation of high-energy tails. *Journal of Geophysical Research: Space Physics*, 102(A3):4701–4718.

Lin, R., Anderson, K., Ashford, S., Carlson, C., Curtis, D., Ergun, R., Larson, D., McFadden, J., McCarthy, M., Parks, G., et al. (1995). A three-dimensional plasma and energetic particle investigation for the wind spacecraft. *Space Science Reviews*, 71(1):125–153.

Lin, R. and Szabo, A. (2006). Solar sentinels: Report of the science and technology definition team. *NASA/TM*, 2006214137.

Linder, D. R., Coates, A. J., Woodliffe, R. D., Alsop, C., Johnstone, A. D., Grande, M., Preece, A., Narheim, B., and Young, D. T. (1998). *The Cassini CAPS Electron Spectrometer*, pages 257–262. American Geophysical Union.

Luhmann, J. (1995). Sources of interplanetary shocks. *Advances in Space Research*, 15(8):355 – 364. Proceedings of the D2.1 Symposium of COSPAR Scientific Commission D.

Maksimovic, M., Zouganelis, I., Chaufray, J.-Y., Issautier, K., Scime, E. E., Littleton, J. E., Marsch, E., McComas, D. J., Salem, C., Lin, R. P., and Elliott, H. (2005). Radial evolution of the electron distribution functions in the fast solar wind between 0.3 and 1.5 au. *Journal of Geophysical Research: Space Physics*, 110(A9):n/a–n/a. A09104.

Markwardt, C. B. (2009). Non-linear least squares fitting in idl with mpfit. *arXiv preprint arXiv:0902.2850*.

Mazur, J., Mason, G., Dwyer, J., Giacalone, J., Jokipii, J., and Stone, E. (2000). Interplanetary magnetic field line mixing deduced from impulsive solar flare particles. *The Astrophysical Journal Letters*, 532(1):L79.

McComas, D., Bame, S., Barker, P., Feldman, W., Phillips, J., Riley, P., and Griffee, J. (1998). Solar wind electron proton alpha monitor (swepam) for the advanced composition explorer. In *The Advanced Composition Explorer Mission*, pages 563–612. Springer.

McComas, D., Bame, S., Feldman, W., Gosling, J., and Phillips, J. (1992). Solar wind halo electrons from 1–4 au. *Geophysical research letters*, 19(12):1291–1294.

McComas, D., Elliott, H., Schwadron, N., Gosling, J., Skoug, R., and Goldstein, B. (2003). The three-dimensional solar wind around solar maximum. *Geophysical research letters*, 30(10).

McComas, D., Velli, M., Lewis, W., Acton, L., Balat-Pichelin, M., Bothmer, V., Dirling, R., Feldman, W., Gloeckler, G., Habbal, S., et al. (2007). Understanding coronal heating and solar wind acceleration: Case for in situ near-sun measurements. *Reviews of Geophysics*, 45(1).

Meyer-Vernet, N. (2007). *Basics of the solar wind*. Cambridge University Press.

Mullan, D. and Smith, C. (2006). Solar wind statistics at 1 au: Alfven speed and plasma beta. *Solar Physics*, 234(2):325–338.

Narita, Y., Nakamura, R., Baumjohann, W., Glassmeier, K.-H., Motschmann, U., Giles, B., Magnes, W., Fischer, D., Torbert, R., Russell, C., et al. (2016). On electron-scale whistler turbulence in the solar wind. *The Astrophysical Journal Letters*, 827(1):L8.

Neugebauer, M. and Giacalone, J. (2015). Energetic particles, tangential discontinuities, and solar flux tubes. *Journal of Geophysical Research: Space Physics*, 120(10):8281–8287. 2015JA021632.

Nitta, N. V., Reames, D. V., DeRosa, M. L., Liu, Y., Yashiro, S., and Gopalswamy, N. (2006). Solar sources of impulsive solar energetic particle events and their magnetic field connection to the earth. *The Astrophysical Journal*, 650(1):438.

Osman, K., Matthaeus, W., Gosling, J., Greco, A., Servidio, S., Hnat, B., Chapman, S. C., and Phan, T. (2014). Magnetic reconnection and intermittent turbulence in the solar wind. *Physical Review Letters*, 112(21):215002.

Owen, C. (2017).

Owens, M., Lockwood, M., Riley, P., and Linker, J. (2017). Sunward strahl: A method to unambiguously determine open solar flux from in situ spacecraft measurements using suprathermal electron data. *Journal of Geophysical Research: Space Physics*, 122(11).

Owens, M., Wicks, R., and Horbury, T. (2011). Magnetic discontinuities in the near-earth solar wind: Evidence of in-transit turbulence or remnants of coronal structure? *Solar Physics*, 269(2):411–420.

Owens, M. J., Crooker, N. U., and Schwadron, N. A. (2008). Suprathermal electron evolution in a parker spiral magnetic field. *Journal of Geophysical Research: Space Physics*, 113(A11):n/a–n/a. A11104.

Owens, M. J. and Forsyth, R. J. (2013). The heliospheric magnetic field. *Living Reviews in Solar Physics*, 10(5).

Pagel, C., Gary, S. P., de Koning, C. A., Skoug, R. M., and Steinberg, J. T. (2007).

Scattering of suprathermal electrons in the solar wind: Ace observations. *Journal of Geophysical Research: Space Physics*, 112(A4):n/a–n/a. A04103.

Parker, E. (1965). Dynamical theory of the solar wind. *Space Science Reviews*, 4(5-6):666–708.

Parker, E. N. (1958). Dynamics of the interplanetary gas and magnetic fields. *The Astrophysical Journal*, 128:664.

Paschmann, G. and Daly, P. W. (1998). Analysis methods for multi-spacecraft data.

Paschmann, G., Fazakerley, A. N., and Schwartz, S. J. (1998). Moments of plasma velocity distributions. *Analysis methods for multi-spacecraft data*, 1:125–157.

Pavan, J., Viñas, A., Yoon, P. H., Ziebell, L. F., and Gaelzer, R. (2013). Solar wind strahl broadening by self-generated plasma waves. *The Astrophysical Journal Letters*, 769(2):L30.

Pierrard, V., Lazar, M., Poedts, S., Štverák, Š., Maksimovic, M., and Trávníček, P. (2016). The electron temperature and anisotropy in the solar wind. comparison of the core and halo populations. *Solar Physics*, 291(7):2165–2179.

Pierrard, V., Maksimovic, M., and Lemaire, J. (2001). Self-consistent model of solar wind electrons. *Journal of Geophysical Research: Space Physics*, 106(A12):29305–29312.

Pilipp, W., Miggenrieder, H., Montgomery, M., Mühlhäuser, K.-H., Rosenbauer, H., and Schwenn, R. (1987a). Characteristics of electron velocity distribution functions in the solar wind derived from the helios plasma experiment. *Journal of Geophysical Research: Space Physics*, 92(A2):1075–1092.

Pilipp, W., Miggenrieder, H., Mühläuser, K.-H., Rosenbauer, H., and Schwenn, R. (1990). Large-scale variations of thermal electron parameters in the solar wind between 0.3 and 1 au. *Journal of Geophysical Research: Space Physics*, 95(A5):6305–6329.

Pilipp, W., Miggenrieder, H., Mühlhäuser, K.-H., Rosenbauer, H., Schwenn, R., and Neubauer, F. (1987b). Variations of electron distribution functions in the solar wind. *Journal of Geophysical Research: Space Physics*, 92(A2):1103–1118.

Pizzo, V. (1991). The evolution of corotating stream fronts near the ecliptic plane in the inner solar system: 2. three-dimensional tilted-dipole fronts. *Journal of Geophysical Research: Space Physics*, 96(A4):5405–5420.

Reames, D. V. (1999). Particle acceleration at the sun and in the heliosphere. *Space Science Reviews*, 90(3-4):413–491.

Reames, D. V. (2013). The two sources of solar energetic particles. *Space Science Reviews*, 175(1-4):53–92.

Richardson, I. G. and Cane, H. V. (1995). Regions of abnormally low proton temperature in the solar wind (19651991) and their association with ejecta. *Journal of Geophysical Research: Space Physics*, 100(A12):23397–23412.

Ruud, J. T. (1956). The blue whale. *Scientific American*, 195(6):46–51.

Rymer, A. M. (2004). *Analysis of Cassini plasma and magnetic field measurements from 1-7 AU*. PhD thesis, University of London, University College London (United Kingdom. Provided by the SAO/NASA Astrophysics Data System.

Rymer, A. M., Coates, A. J., Svenes, K., Abel, G. A., Linder, D. R., Narheim, B., Thomsen, M., and Young, D. T. (2001). Cassini plasma spectrometer electron spectrometer measurements during the earth swing-by on august 18, 1999. *Journal of Geophysical Research: Space Physics*, 106(A12):30177–30198.

Saito, S. and Gary, S. P. (2007). All whistlers are not created equally: Scattering of strahl electrons in the solar wind via particle-in-cell simulations. *Geophysical Research Letters*, 34(1):n/a–n/a. L01102.

Salem, C., Howes, G., Sundkvist, D., Bale, S., Chaston, C., Chen, C., and Mozer, F. (2012). Identification of kinetic alfvén wave turbulence in the solar wind. *The Astrophysical Journal Letters*, 745(1):L9.

Schwenn, R. (2007). Solar wind sources and their variations over the solar cycle. In *Solar Dynamics and Its Effects on the Heliosphere and Earth*, pages 51–76. Springer.

Scime, E. E., Bame, S. J., Feldman, W. C., Gary, S. P., Phillips, J. L., and Balogh, A. (1994). Regulation of the solar wind electron heat flux from 1 to 5 au: Ulysses observations. *Journal of Geophysical Research: Space Physics*, 99(A12):23401–23410.

Scudder, J. D. (1992). On the causes of temperature change in inhomogeneous low-density astrophysical plasmas. *The Astrophysical Journal*, 398:299–318.

Scudder, J. D. and Olbert, S. (1979). A theory of local and global processes which affect solar wind electrons, 1. the origin of typical 1 au velocity distribution functionssteady state theory. *Journal of Geophysical Research: Space Physics*, 84(A6):2755–2772.

Seough, J., Nariyuki, Y., Yoon, P. H., and Saito, S. (2015). Strahl formation in the solar wind electrons via whistler instability. *The Astrophysical Journal Letters*, 811(1):L7.

Shevchenko, V. and Galinsky, V. (2010). Stability of the strahl electron distribution function and its dynamics. *Nonlinear Processes in Geophysics*, 17(5):593.

Shue, J.-H., Chao, J., Fu, H., Russell, C., Song, P., Khurana, K., and Singer, H. (1997). A new functional form to study the solar wind control of the magnetopause size and shape. *Journal of Geophysical Research: Space Physics*, 102(A5):9497–9511.

Sitenko, A. and Stepanov, K. (1957). On the oscillations of an electron plasma in a magnetic field. *Soviet Phys. JETP*, 4.

Skalsky, A., Grard, R., Kiraly, P., Klimov, S., Kopanyi, V., Schwingenschuh, K., and Trotignon, J. (1993). Simultaneous plasma wave and electron flux observations upstream of the martian bow shock. *Planetary and space science*, 41(3):183–188.

Smith, C. W., L'Heureux, J., Ness, N. F., Acuña, M. H., Burlaga, L. F., and Scheifele, J. (1998). The ace magnetic fields experiment. *Space Science Reviews*, 86(1-4):613–632.

Smith, H. M., Marsch, E., and Helander, P. (2012). Electron transport in the fast solar wind. *The Astrophysical Journal*, 753(1):31.

Stansby, D., Horbury, T., Chen, C., and Matteini, L. (2016). Experimental determination of whistler wave dispersion relation in the solar wind. *The Astrophysical Journal Letters*, 829(1):L16.

Stix, T. H. (1992). *Waves in plasmas*. Springer Science & Business Media.

Stone, E. C., Frandsen, A., Mewaldt, R., Christian, E., Margolies, D., Ormes, J., and Snow, F. (1998). The advanced composition explorer. *Space Science Reviews*, 86(1-4):1–22.

Stverak, S., Maksimovic, M., Travnicek, P. M., Marsch, E., Fazakerley, A. N., and Scime, E. E. (2009). Radial evolution of nonthermal electron populations in the low-latitude solar wind: Helios, cluster, and ulysses observations. *Journal of Geophysical Research: Space Physics*, 114(A5):n/a–n/a. A05104.

Stverak, S., Travnicek, P., Maksimovic, M., Marsch, E., Fazakerley, A. N., and Scime, E. E. (2008). Electron temperature anisotropy constraints in the solar wind. *Journal of Geophysical Research: Space Physics*, 113(A3):n/a–n/a. A03103.

Tan, L. C., Malandraki, O. E., Reames, D. V., Ng, C. K., Wang, L., Patsou, I., and Papaioannou, A. (2013). Comparison between path lengths traveled by solar electrons and ions in ground-level enhancement events. *The Astrophysical Journal*, 768(1):68.

Tan, L. C., Reames, D. V., Ng, C. K., Shao, X., and Wang, L. (2011). What causes scatter-free transport of non-relativistic solar electrons? *The Astrophysical Journal*, 728(2):133.

Thomas, B. T. and Smith, E. J. (1980). The parker spiral configuration of the interplanetary magnetic field between 1 and 8.5 au. *Journal of Geophysical Research: Space Physics*, 85(A12):6861–6867.

Treumann, R. and Baumjohann, W. (1997). Basic space plasma physics.

Trotignon, J., Trotignon, A., Dubinin, E., Skalsky, A., Grard, R., and Schwingenschuh, K. (2000). Electron plasma waves beyond the mars' bow shock: The pws/phobos-2 observations. *Advances in Space Research*, 26(10):1619–1622.

Viñas, A. F., Wong, H. K., and Klimas, A. J. (2000). Generation of electron suprathermal tails in the upper solar atmosphere: Implications for coronal heating. *The Astrophysical Journal*, 528(1):509.

Vocks, C., Mann, G., and Rausche, G. (2008). Formation of suprathermal electron distributions in the quiet solar corona. *Astronomy & Astrophysics*, 480(2):527–536.

Vocks, C., Salem, C., Lin, R. P., and Mann, G. (2005). Electron halo and strahl formation in the solar wind by resonant interaction with whistler waves. *The Astrophysical Journal*, 627(1):540.

Von Rosenvinge, T., Barbier, L., Karsch, J., Liberman, R., Madden, M., Nolan, T., Reames, D., Ryan, L., Singh, S., Trexel, H., et al. (1995). The energetic particles: acceleration, composition, and transport (epact) investigation on the wind spacecraft. *Space Science Reviews*, 71(1-4):155–206.

Walsh, A. P., Arridge, C. S., Masters, A., Lewis, G. R., Fazakerley, A. N., Jones, G. H., Owen, C. J., and Coates, A. J. (2013). An indication of the existence of a solar wind strahl at 10au. *Geophysical Research Letters*, 40(11):2495–2499.

Wiedenbeck, M., Mason, G., Cohen, C., Nitta, N., Gómez-Herrero, R., and Haggerty, D. (2011). Observations of broad longitudinal extents of 3he-rich sep events. In *32nd International Cosmic Ray Conference*.

Wilson, L. B., Koval, A., Szabo, A., Breneman, A., Cattell, C. A., Goetz, K., Kellogg, P. J., Kersten, K., Kasper, J. C., Maruca, B. A., and Pulupa, M. (2013).

Electromagnetic waves and electron anisotropies downstream of supercritical interplanetary shocks. *Journal of Geophysical Research (Space Physics)*, 118:5–16.

Wilson, L. B. and Szabo, A. (2018). Wind spacecraft. *Online – https://wind.nasa.gov/*.

Xu, F. and Borovsky, J. E. (2015). A new four-plasma categorization scheme for the solar wind. *Journal of Geophysical Research: Space Physics*, 120(1):70–100. 2014JA020412.

Yang, S., Zhang, J., Jin, C., Li, L., and Duan, H. (2009). Response of the solar atmosphere to magnetic field evolution in a coronal hole region. *Astronomy & Astrophysics*, 501(2):745–753.

Young, D., Barraclough, B., Berthelier, J., Blanc, M., Burch, J., Coates, A., Goldstein, R., Grande, M., Hill, T., Illiano, J., et al. (1998). Cassini plasma spectrometer investigation. *Measurement Techniques in Space Plasmas: Particles*, pages 237–242.

Young, D., Berthelier, J., Blanc, M., Burch, J., Coates, A., Goldstein, R., Grande, M., Hill, T., Johnson, R., Kelha, V., et al. (2004). Cassini plasma spectrometer investigation. In *The Cassini-Huygens Mission*, pages 1–112. Springer.

Zell, H. and Dunbar, B. (2017). A solar wind workhorse marks 20 years of science discoveries. *Online – https://www.nasa.gov/content/goddard/solar-wind-workhorse-marks-20-years-of-science-discoveries*.

Zouganelis, I. (2008). Measuring suprathermal electron parameters in space plasmas: Implementation of the quasi-thermal noise spectroscopy with kappa distributions using in situ ulysses/urap radio measurements in the solar wind. *Journal of Geophysical Research: Space Physics*, 113(A8).